UNIVERSITY OF CALIFORNIA,
IRVINE

Theory and Applications of Exceptional Points of Degeneracy in Microwave and High Sensitive Applications

DISSERTATION

submitted in partial satisfaction of the requirements
for the degree of

DOCTOR OF PHILOSOPHY

in Electrical and Computer Engineering

by

Alireza Nikzamir

Dissertation Committee:
Professor Filippo Capolino, Chair
Professor Michael Green
Assistant Professor Hamidreza Aghasi

2024

DEDICATION

TO MY FAMILY AND IN MEMORY OF MY GRANDPARENTS

TABLE OF CONTENTS

LIST OF FIGURES

LIST OF TABLES

ACKNOWLEDGMENTS

I would like to express my sincere appreciation and gratitude to my PhD advisor, Professor Filippo Capolino, for his unwavering support over the past five years. I have learned a lot of things from Professor Capolino that helped to develop my way of thinking, such as asking myself questions to understand, being precise when I speak or write, and being patient in learning new topics and improving things. Without the guidance and persistent help of Prof. Capolino, this dissertation would not have been possible. I am also thankful to Professor Green for involving me in remarkable projects and providing opportunities to collaborate with outstanding colleagues, Dr. Behnam Moradi and Dr. Yaoyu Cao, furthering my aspirations in the field of medical devices. In addition, I would like to thank the committee members, Professor Michael Green and Professor Hamidreza Aghasi, who have provided helpful feedback and insights.

I would like to thank my colleagues who were involved in the research. I am grateful to Dr. Kasra Rouhi for his invaluable friendship and support throughout my Ph.D. journey. I would like to extend my gratitude to Miguel Saavedra-Melo, Nathaniel Furman and Albert Herrero Parareda for their invaluable support, friendship, and collaboration throughout my research. I thank Dr. Hamidreza Kazemi and Dr. Tarek Mealy for working with me and supporting me. I am happy and appreciative of that teamwork. I also thank all my lab mates, Robert Marosi, Amin Hakimi, Vanessa Yao and Benjamin Bradshaw.

I am also grateful for the funding from the National Science Foundation. The research work in this dissertation was mainly supported by NSF ECCS-1711975.

I would like to acknowledge Professor Hamid Djalilian, Professor Green and the donors for their financial support, which made this research possible. The funding provided not only facilitated the acquisition of essential resources but also allowed me the freedom to delve deeper into the subject matter.

Most importantly, I am deeply and sincerely grateful to my mom and dad, who were always there for me at every step and gave me the strength and confidence to pursue my goals. I want to express my thanks to my elder brothers, Amirhossein Nikzamir, and my sister in Law, Samira Mansouri, for their continuous support and love. It would have been very difficult to reach this accomplishment without my Family's support. Lastly, I want to convey my love to my grandparents, hoping they are proud of me for this achievement.

- The text of Chapter 2 of this dissertation is a reprint of the material as it appears in Alireza Nikzamir, and Filippo Capolino. Highly Sensitive Coupled Oscillator Based on an Exceptional Point of Degeneracy and Nonlinearity. Phys. Rev. Appl., 18, 054059, Nov 2022. The coauthor listed in this publication is Filippo Capolino. Filippo Capolino, who directed and supervised research which forms the basis for the dissertation.

- The text of Chapter 3 of this dissertation is a reprint of the material as it appears in

Hamidreza Kazemi, Alireza Nikzamir, Tarek Mealy, Ahmed Abdelshafy, and Filippo Capolino. High-Sensitive Parity-Time Symmetric Oscillator in Coupled Transmission Lines with Nonlinear Gain. IEEE Journal of Microwaves, vol. 2, no. 3, pp. 389-400, July 2022. The coauthors listed in this publication are Hamidreza Kazemi, Tarek Mealy, Ahmed Abdelshafy, and Filippo Capolino. Filippo Capolino directed and supervised research which forms the basis for the dissertation.

- The text of Chapter 5 of this dissertation is a reprint of the material as it appears in Alireza Nikzamir, Kasra Rouhi, Alexander Figotin, and Filippo Capolino. How to achieve exceptional points in coupled resonators using a gyrator or PT-symmetry, and in a time-modulated single resonator: high sensitivity to perturbations. EPJ Applied Metamaterials, vol. 9, p. 14, 2022. The coauthors listed in this publication are Kasra Rouhi, Alexander Figotin, and Filippo Capolino. Alexander Figotin and Filippo Capolino directed and supervised research which forms the basis for the dissertation.

- The text of Chapter 6 of this dissertation is a reprint of the material as it appears in Alireza Nikzamir, Kasra Rouhi, Alexander Figotin, and Filippo Capolino. Time Modulation to Manage and Increase the Power Harvested from External Vibrations. Applied Physics Letters 123, no. 21, 2023. The coauthors listed in this publication are Kasra Rouhi, Alexander Figotin, and Filippo Capolino. Alexander Figotin and Filippo Capolino directed and supervised research which forms the basis for the dissertation.

- The text of Chapter 7 of this dissertation is a reprint of the material as it appears in Alireza Nikzamir, and Filippo Capolino. Exceptional Point Degeneracy as Desirable Operation Point of Oscillator Array with Discrete Nonlinear Gain and Radiating Elements. Phys. Rev. Appl., 21, 024037, Feb 2024. The coauthor listed in this publication is Filippo Capolino. Filippo Capolino directed and supervised research which forms the basis for the dissertation.

VITA

Alireza Nikzamir

EDUCATION

Doctor of Philosophy in Electrical and Computer Engineering **2024**
University of California, Irvine *Irvine, California, USA*

Masters of Science in Electrical and Computer Engineering **2022**
University of California, Irvine *Irvine, California, USA*

Bachelor of Science in Electrical and Computer Engineering **2019**
Sharif University of Technology, Iran *Tehran, Iran*

RESEARCH EXPERIENCE

Graduate Research Assistant **2020–2024**
University of California, Irvine *Irvine, California*

TEACHING EXPERIENCE

Teaching Assistant **2020–2024**
University of California, Irvine *Irvine, California*

Teaching Assistant/Tutor **2015–2019**
Sharif University of Technology, Iran *Tehran, Iran*

JOURNAL PUBLICATIONS

[1] **Nikzamir, A.**, Rouhi, K., Figotin, A., and Capolino, F., "Time modulation to manage and increase the power harvested from external vibrations, "in Appl. Phys. Lett., 123 (21): 211701, 2023.

[2] **Nikzamir, A.**, and Capolino, F., "Exceptional Point Degeneracy as Desirable Operation Point of Oscillator Array with Discrete Nonlinear Gain and Radiating Elements,"in Phys. Rev. Applied, 2024.

[3] **Nikzamir, A.**, Rouhi, K., Figotin, A., and Capolino, F.,"Demonstration of Exceptional Points of Degeneracy in Gyrator-Based Circuit for High-Sensitivity Applications,"in arXiv preprint arXiv:2107.00639, 2021.

[4] **Nikzamir, A.**, Rouhi, K., Figotin, A., and Capolino, F., "Highly How to achieve exceptional points in coupled resonators using a gyrator or PT-symmetry, and in a time-modulated single resonator: high sensitivity to perturbations", in EPJ Applied Metamaterials, 9, 14, 2022.

[5] **Nikzamir, A.**, and Capolino, F., "Highly Sensitive Coupled Oscillator Based on an Exceptional Point of Degeneracy and Nonlinearity,"in Phys. Rev. Applied, 2022.

[6] Kazemi, H., **Nikzamir, A.**, Mealy, T., Abdelshafy, A. and Capolino, F., "High-Sensitive Parity-Time Symmetric oscillator in Coupled Transmission Lines With Nonlinear Gain,"in IEEE Journal of Microwaves, 2022. [7] Mohseni, F., **Nikzamir, A.**, Cao, H., and Capolino, F.,"One-transmitter Multiple-receiver Wireless Power Transfer System Using an Exceptional Point of Degeneracy,"in arXiv preprint arXiv:2204.10928, 2022.

[8] Rouhi, K., **Nikzamir, A.**, Figotin, A., and Capolino, F.,"Exceptional point in a degenerate system made of a gyrator and two unstable resonators,"Physical Review A, 105(3), 032214, 2022,

[9] Yazdi, F., **Nikzamir, A.**, Mealy, T., Nada, M. Y., and Capolino, F., "Triple Ladder Lumped Circuit With Sixth Order Modal Exceptional Degeneracy,"in IEEE Transactions on Circuits and Systems I: Regular Papers, 69(5), 1910-1918, 2022.

[10] Rouhi, K., **Nikzamir, A.**, Figotin, A., and Capolino, F., "High-sensitivity in various gyrator-based circuits with exceptional points of degeneracy,"in EPJ Applied Metamaterials, 9, 8, 2022.

[11] Oshmarin, **Nikzamir, A.**, Green, M. M., and Capolino, F., "Pulse Generation Based on a Microstrip Circuit with Fourth Order Degenerate Band Edge,"in arXiv preprint arXiv:2206.13564, 2022.

[12] Oshmarin, D., Abdelshafy, A. F., **Nikzamir, A.**, Green, M. M., and Capolino, F., "Experimental demonstration of a new oscillator concept based on degenerate band edge in

microstrip circuit, "in arXiv preprint arXiv:2109.07002, 2021.

[13] Yazdi, F., Mealy, T., **Nikzamir, A.**, Marosi, R., and Capolino, F, "Third order modal exceptional degeneracy in waveguides with glide-time symmetry,"in Physical Review A 105, no. 5, 2022.

[14] Kazemi, H., Nada, M. Y., **Nikzamir, A.**, Maddaleno, F., and Capolino, F., Experimental demonstration of exceptional points of degeneracy in linear time periodic systems and exceptional sensitivity,"in Journal of Applied Physics, 131(14), 144502, 2022.

[15] Abdelshafy, A. F., Mealy, T., Hafezi, E., **Nikzamir, A.**, and Capolino, F., "Exceptional degeneracy in a waveguide periodically loaded with discrete gain and radiation loss elements,"Applied Physics Letters, 118(22), 224102, 2021.

[16] Yazdi, F., Oshmarin, D., Mealy, T., Almutawa, A. T., **Nikzamir, A.**, and Capolino, F., "Sixth-Order Degenerate Band Edge in Coupled Microstrip Waveguides,"in PhysRevApplied, 17 (6), 064049, 2022.

CONFERENCE PUBLICATIONS

[1] **Nikzamir, A.**, and Capolino, F., "Quasi PT-symmetric Nonlinear System With Exceptional Point of Degeneracy Leads to Highly Sensitive Oscillatory Regime,"in 2023 IEEE USNC-URSI Radio Science Meeting (Joint with AP-S Symposium), Portland, OR, USA, 2023, pp. 33-34.

[2] **Nikzamir, A.**, Marosi, R., Mealy, T., Yazdi, F., and Capolino, F., "Parity-Time Glide-Symmetry and Third Order Exceptional Degeneracy in a Three-Way Microstrip Waveguide,"in 2022 16th European Conference on Antennas and Propagation (EuCAP) (pp. 1-4). IEEE.

[3] **Nikzamir, A.**, N. Furman, A. Herrero, T. Mealy, and F Capolino, F., "Exceptional Points of Degeneracy in Waveguides with or without Loss and Gain,"in 2022 Sixteenth International Congress on Artificial Materials for Novel Wave Phenomena (Metamaterials), pp. 326-328. IEEE, 2022.

[4] **Nikzamir, A.**, Rouhi, K., Figotin, A., and Capolino, F., "Exceptional Points of Degeneracy in Gyrator-Based Coupled Resonator Circuit,"in 2021 Fifteenth International Congress on Artificial Materials for Novel Wave Phenomena (Metamaterials) (pp. 302-304). IEEE.

[5] **Nikzamir, A.**, Kazemi, H., Mealy, T., and Capolino, F., "Highly Sensitive Exceptional Degeneracy in Coupled Transmission Lines With Balanced Gain and loss,"in 2022 United States National Committee of URSI National Radio Science Meeting (USNC-URSI NRSM).

[6] **Nikzamir, A.**, Rouhi, K., and Capolino, F., "Exceptional Points of Degeneracy in Nonlinear Systems: Two Coupled Oscillators and Arrays of Oscillators,"in 2024 Eighteenth International Congress on Artificial Materials for Novel Wave Phenomena (Metamaterials)

(pp. 1-3). IEEE.

[7] Rouhi, K., **Nikzamir, A.**, Figotin, A., and Capolino, F., "Exceptional Points of Degeneracy Induced by Time-Periodic Modulation,"in 2023 Seventeenth International Congress on Artificial Materials for Novel Wave Phenomena (Metamaterials), Chania, Greece, 2023, pp. X-312-X-314.

[8] Rouhi, K., **Nikzamir, A.**, Figotin, A., and Capolino, F., "Enhanced Sensitivity of Gyrator-based Circuit at Exceptional Point Composed of Unstable Resonators,"in 2022 United States National Committee of URSI National Radio Science Meeting (USNC-URSI NRSM).

[9] Rouhi, K.,**Nikzamir, A.**, Figotin, A., and Capolino, F., "Two resonators with negative and positive reactive components to achieve an exceptional point of degeneracy,"in 2022 Sixteenth International Congress on Artificial Materials for Novel Wave Phenomena (Metamaterials), pp. X-374. IEEE, 2022.

[10] Rouhi, K., **Nikzamir, A.**, Figotin, A., and Capolino, F.,"Second-Order Exceptional Point of Degeneracy in Two Directly Coupled Resonator,"in 2024 United States National Committee of URSI National Radio Science Meeting (USNC-URSI NRSM) (pp. 263-263). IEEE.

[11] Mealy, T., **Nikzamir, A.**, Abdelshafy, A. F., Nada, M. Y., and Capolino, F., "Waveguides with Exceptional Points of Degeneracy of Order 2, 3, 4 and 6 without Loss and Gain,"in 2021 International Applied Computational Electromagnetics Society Symposium (ACES) (pp. 1-3). IEEE.

[12] Hafezi, E., Abdelshafy, A. F., Mealy, T., **Nikzamir, A.**, and Capolino, F., "Exceptional Points of Degeneracy in a Transmission Line Periodically Loaded with Gain and Radiation Loss ,"in 2021 United States National Committee of URSI National Radio Science Meeting (USNC-URSI NRSM) (pp. 52-53). IEEE.

[13] Nada, M. Y., Mealy, T., Hafezi, E., **Nikzamir, A.**, and Capolino, F. Sensing Via Exceptional Points in Space and Time Periodic Systems and in PT-Symmetric Systems,"in 2020 Fourteenth International Congress on Artificial Materials for Novel Wave Phenomena (Metamaterials) (pp. 042-044). IEEE.

[14] Mealy, T., Parareda, A.H., Furman, N., **Nikzamir, A.** and Capolino, F., "Lasing with multimode guided waves with exceptional degeneracy,"in Active Photonic Platforms 2022 (p. PC121961M). SPIE

[15] Mealy, T., **Nikzamir, A.**, Abdelshafy, A. F., and Capolino, F., "Exceptional Point of Degeneracy as a Desirable Point of Operation for Oscillator With Discrete Nonlinear Gain and Radiating Elements,"in 2022 United States National Committee of URSI National Radio Science Meeting (USNC-URSI NRSM).

[16] Saavedra-Melo M, Yao V, Bradshaw B, Rouhi K, De Leon A, **Nikzamir, A.**, Marosi R, and Capolino, F., "Exceptional Point of Degeneracy as a Desirable Point of Operation for Oscillator With Discrete Nonlinear Gain and Radiating Elements,"in 2024 IEEE International Symposium on Antennas and Propagation and INC/USNC-URSI Radio Science Meeting (AP-S/INC-USNC-URSI) (pp. 1963-1964). IEEE.

ABSTRACT OF THE DISSERTATION

Theory and Applications of Exceptional Points of Degeneracy in Microwave and High Sensitive Applications

By

Alireza Nikzamir

Doctor of Philosophy in Electrical and Computer Engineering

University of California, Irvine, 2024

Professor Filippo Capolino, Chair

Electromagnetic (EM) structures are essential in high-speed communications and radar systems. Enhancing the performance of these components can significantly impact applications requiring specific features such as ultra-high sensitivity, wireless power transfer, high-output power arrays, or precise oscillation frequency in periodic structures with high radiating power. The operational regime often constrains the performance of EM components. This dissertation presents a novel class of EM/Radio Frequency devices that utilize nonlinearity and dispersion engineering to exploit the operational condition known as the exceptional point of degeneracy (EPD). Operating in the EPD regime allows for pushing the performance boundaries of devices, especially within the millimeter and terahertz frequency ranges.

EPD refers to a singularity where two or more spectral components in the EM field distribution converge. This work investigates degeneracy conditions in microwave, optical, and radio frequency devices, examining the unique physical properties of devices operating under EPD conditions. The study focuses on various circuit configurations, including gyrator-based coupled resonators, PT-symmetric coupled resonators, single resonators with time-varying components, and periodic waveguide-based structures. Emphasis is placed on the high sensitivity of these circuits to variations in resistance, capacitance, and inductance, as well as

on their stability and instability conditions. Notably, it explores the advantageous use of instabilities in PT-symmetric circuits by introducing nonlinear gain, resulting in highly sensitive oscillators. Additionally, a proposed coupled-resonator system with EPD demonstrates extreme sensitivity to perturbations, even in broken PT-symmetry conditions. Another investigation shows how time modulation in a single resonator can enhance power extraction through EPD.

Finally, an oscillator array operating at an EPD in a waveguide, with discrete nonlinear gain and radiating elements is shown to achieve oscillations at the EPD frequency after saturation, and being resilient to changes in small-signal gain of the active elements.

These findings collectively pave the way for innovative applications, including high-sensitivity sensors, tunable oscillators, power harvesting systems, and high-power oscillating arrays.

Chapter 1

Introduction

1.1 Motivation of This Work

In this chapter, we focus on giving an introductory discussion along with a brief literature review of previous works relevant to the topics of this dissertation. We also introduce the organization and different chapters of this dissertation.

Electromagnetic (EM) and radio frequency (RF) components are crucial for high-speed communications and radar systems. This dissertation proposes a new class of EM and RF devices that exploit exceptional points of degeneracy (EPDs) to enhance performance. EPDs have been applied in various fields, including oscillators, amplifiers, delay lines, small antennas, pulse generators, high-Q resonators, sensors, and lasers. This work investigates the EPD condition and provides physics-based solutions for coupled resonators to enhance electronic reading sensitivity, as well as periodic waveguides with gain and loss to achieve stable oscillations. We also examine degeneracy conditions in time-varying systems to identify potential advancements in power harvesting and sensing applications.

EPDs are implemented in systems through different designs, leading to numerous applications, including ultra-sensitive PT-symmetric LC resonators, [6], stable oscillators [12], high-gain amplifiers [13, 14], and low-threshold lasers [15]. For instance, sensors operating at EPDs can achieve ultra-high sensitivity to perturbations. Traditional sensors experience changes in linewidth or frequency shifts proportional to perturbation strength. However, sensors designed to operate at EPDs exhibit enhanced sensitivity and achieve sharp resonances. Examples include a coupled cavity arrangement for Parity–time-symmetric coupled cavity systems [5], optical microcavity [16], and PT-symmetric RF sensor systems [17, 3, 6]. This dissertation, inspired by previous research on EPD in sensing applications, demonstrates that the EPD condition can be achieved in coupled resonators, gyrator-based circuits, and time-periodic resonators, leading to ultra-high sensitivity to the perturbation.

Oscillators play a vital role in microwave, terahertz (THz), and optical applications. Typically oscillators function as positive feedback systems with a gain device and frequency-selective reactive components. They generate continuous, single-frequency outputs by meeting Barkhausen's criteria [18] and require a self-sustaining mechanism to filter noise and create a stable periodic signal. Many RF oscillators use a single active device for simplicity and cost-effectiveness, as seen in Van der Pol and voltage-controlled oscillators [19]. Oscillators often incorporate an LC resonator with positive feedback and negative resistance, found in designs like Pierce, Colpitts, and cross-coupled transistor pairs [18, 20, 21]. While LC-resonator oscillators are the most common, other types—such as distributed [22, 23, 8], ring [24], and multimode oscillators—present unique advantages and challenges. In RF technology, there is significant interest in developing oscillators that provide stable oscillation frequency[25], high-quality factor[26], load independence [12], and high output power[27]. Thus, enhancement in oscillator specs is crucial for superior performance in RF and microwave sources. Recently, EPD-based oscillators have been a subject of study. Researchers have proposed EPD-based oscillators utilizing modal degeneracy, which offer relaxed oscillation thresholds, independence from loading conditions [12], and improved efficiency without

active output buffer stages [28]. EPDs can be achieved using spatial periodicity in coupled transmission lines, resulting in a coalescence of independent Bloch eigenmodes. Examples include oscillators based on exceptional points of degeneracy in periodic double-ladder circuits [7], periodically-loaded circular waveguiding structures [29], and backward-wave oscillators with distributed power extraction [30]. These designs highlight the advantages of EPDs in achieving high-performance oscillators with enhanced efficiency and stability, inspiring our work on EPD-based oscillators.

1.2 History of Exceptional Points of Degeneracy(EPD)

An Exceptional Point of Degeneracy (EPD) represents a unique condition in a system's parameter space where both eigenvalues and eigenvectors coalesce into a single eigenmode [31, 32, 33, 34, 35, 36, 37]. The term "exceptional point" (EP), used by Kato in 1966, describes a phenomenon where degeneracy goes beyond the usual case of coinciding eigenvalues, involving the coalescing of both eigenvalues and eigenvectors. EPDs specifically denote this merging of both eigenvalues and eigenvectors, emphasizing the unique, singular behavior of such a system state. The order of degeneracy reflects the number of eigenmodes that coalesce at the EPD, which leads to distinct responses in system behavior. For instance, the dispersion relation of electromagnetic eigenmodes in a waveguide with an EPD of order m exhibits the behavior $(\omega - \omega_e) \propto (k - k_e)^m$ near the EPD point (ω_e, k_e) [38, 39].

EPDs are important in non-Hermitian systems, particularly those exhibiting parity-time (PT) symmetry [40]. PT-symmetry implies that a system's Hamiltonian commutes with the PT operator, where the PT operator combines parity reflection with time reversal [41, 42]. PT-symmetric systems meet the condition $(n(x) = n^*(-x))$ for their refractive index [43, 44, 45], creating EPDs at critical transition points that shift the spectrum from real to complex eigenvalues. When the time reversal operator is applied to physical systems, energy

transforms from damping to growing and vice versa [46]. In PT-symmetric systems with balanced gain and loss, such as symmetrically coupled waveguides, these transitions form EPDs, marking key points where eigenvalues transition between real and complex as system variables are tuned. This characteristic is instrumental in applications involving coupled waveguides and resonators, where PT symmetry enables phenomena like low-threshold lasing [47] and ultra-sensitive sensing [5]. EPDs are also linked to bifurcation theory [48, 49], where they are identified as points in configuration space where multiple spectral branches converge, effectively functioning as branch points in the space control variable [50]. Additionally, EPDs are recognized as important points in multilayer waveguide systems [51, 49].

In electromagnetic systems, EPDs emerge when eigenvectors converge due to parameter variations in space or time. Figure 1.1 distinguishes between EPDs in spatial (k) versus in time (ω) domains. The EPD condition allows eigenvectors to merge by altering parameters like frequency, resulting in the emergence of generalized eigenvectors in both space [1, 12] and time [4, 3]. Under EPD conditions, the system matrix becomes non-diagonalizable, marking a departure from traditional degeneracies where the system matrix is diagonalizable [52]. Moreover, EPD could be classified based on whether degeneracy arises in configurations with or without gain and loss [53].

Outside of PT-symmetric systems, EPDs also appear in periodic structures [38] and in time-varying systems that may operate independently of gain or loss [4]. For instance, second-order EPDs in uniform coupled transmission lines (CTLs) with loss and gain have been analyzed from a bifurcation theory perspective [49]. Also, in periodic guiding structures, EPDs arise at photonic band edges, where the wave group velocity approaches zero [38]. Examples include Regular Band Edge (RBE) and higher-order Degenerate Band Edge (DBE) cases, both of which enhance the efficiency and power of devices like high-performance microwave, radio frequency and optical systems [39, 13].

This dissertation explores how EPDs can substantially improve the performance of electro-

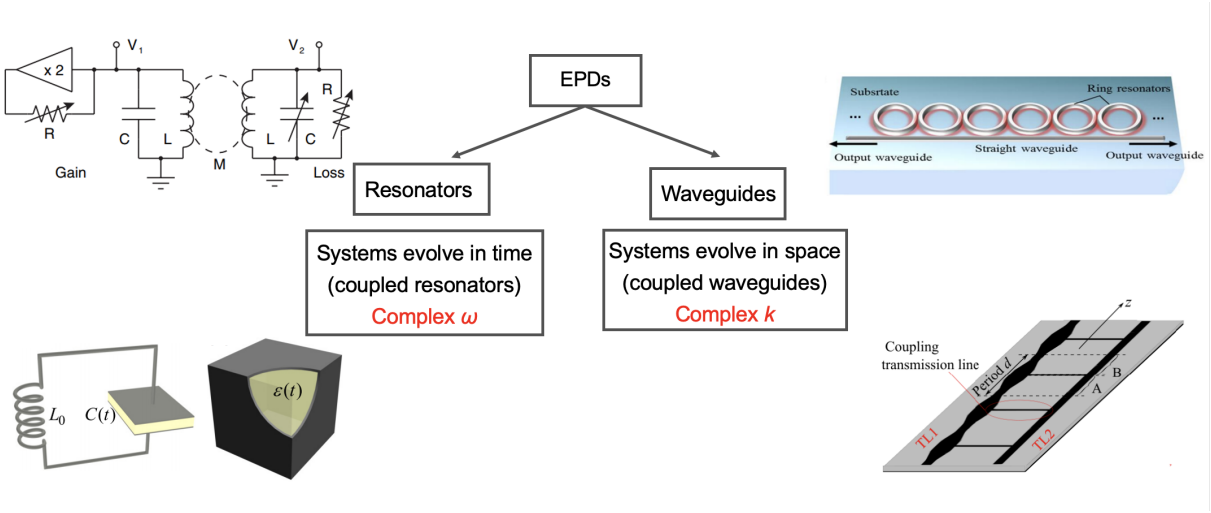

Figure 1.1: EPDs can be categorized based on system evolution: in waveguides, where systems evolve spatially (e.g., coupled waveguides), EPDs are associated with wave numbers k [1, 2]; in resonators, where systems evolve temporally (e.g., coupled resonators), EPDs correspond to frequencies ω [3, 4].

magnetic devices through sensitivity to parameter perturbations and leveraging nonlinearity in the system. By precisely engineering systems to achieve EPDs, this dissertation demonstrates how EPDs enable ultra-sensitive sensors, efficient oscillators, and numerous applications with potential impacts in high-speed communications, radar, and other advanced technology domains.

1.3 Applications of Exceptional Points of Degeneracy (EPDs)

EPDs demonstrate significant potential across various applications by enhancing system performance through precise parameter design. Systems that incorporate EPDs—such as sensors, oscillators, and amplifiers—exhibit remarkable features, including ultra-sensitivity and high efficiency. This section explores the broad range of EPD applications and highlights how EPDs improve functionality. We categorize EPD applications into three branches, where

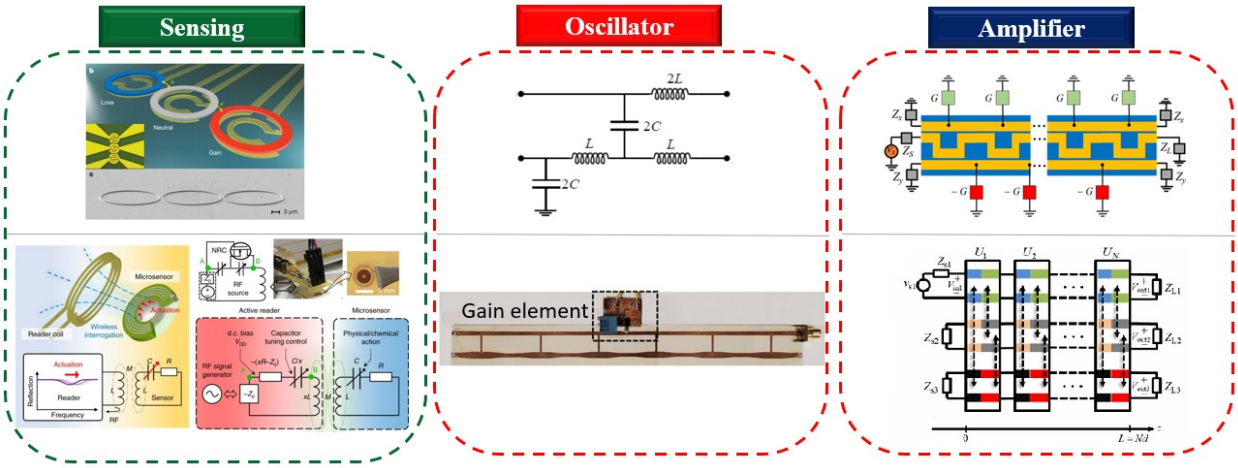

Figure 1.2: Applications of EPDs in sensing [5, 6], oscillators [7, 8], and amplifiers [9, 10].

degeneracy may occur either in space (k) or in time (ω), each enabling distinct applications as shown in Fig. 1.2.

1.3.1 Sensors

EPDs enable the development of sensors with ultra-high sensitivity to small perturbations. In optical microcavity systems, for example, traditional sensing methods rely on shifts in linewidth, frequency, or resonance splitting, scaling proportionally with perturbation strength. By operating at EPDs, however, sensors achieve enhanced sensitivity [5, 16].

In PT-symmetric systems, EPDs arise from carefully balanced gain and loss parameters, resulting in real eigenfrequencies that yield sharp resonances and improved sensitivity compared to passive systems. This improvement directly benefits the sensor's ability to detect slight environmental changes [3, 5, 16].

For instance, [5] demonstrates EPDs in a coupled-cavity photonic laser, where a precisely engineered gain-loss distribution enables EPD operation. Here, the frequency response follows a cube-root relationship with refractive index perturbations, indicating high sensitivity to structural changes. Similarly, [16] presents a sensor based on an optical microcavity with

nanoscale scatterers, where EPDs improve sensitivity through frequency splitting, making it far more responsive than traditional sensors. The sensitivity of resonance to perturbations in electronic circuits is examined in [3, 6], whereas the degeneracy condition was previously discussed in [17].

1.3.2 Oscillators

Oscillators based on EPDs offer significant advantages, particularly in RF and microwave applications, due to their ability to exploit modal degeneracy. This unique characteristic allows lower oscillation thresholds, frequency stability independent of load variations [54, 12], and elimination of active output buffering [28]. By achieving these benefits, EPD oscillators may deliver higher efficiency and improved overall performance.

Moreover, spatial periodicity in coupled transmission lines (TLs) enables degeneracy conditions that combine multiple Bloch eigenmodes at the band edge, resulting in high-Q resonances [55]. Designs based on EPDs include the double-ladder circuit DBE oscillator [7], which demonstrates lower oscillation thresholds and enhanced robustness against output loading. Another application of DBE-based structures is in cavity designs using periodic waveguides, where the DBE concept enables strong synchronization of a discrete set of oscillators, resulting in a stable, single mode of oscillation [12].

Additionally, the DBE-based oscillator model employs a periodically-loaded circular waveguide within a slow-wave system, where mode coalescence of four degenerate modes significantly reduces the beam current required for oscillation [56, 29]. Lastly, EPD conditions are discussed in the context of spatial periodicity in coupled microstrip lines [2]. Introducing a nonlinear gain element at the center of the structure induces oscillations, resulting in a robust oscillator [8] and enabling opportunities for pulse generation design [57].

1.3.3 Amplifiers

EPD-based amplifiers offer a promising approach to exceed the limitations of conventional amplification, providing enhanced gain, bandwidth, and efficiency. These amplifiers leverage electromagnetic eigenmode degeneracies, particularly in periodic slow-wave structures (SWS), where third-order degeneracies—known as stationary inflection points (SIPs)—enable the coalescence of three Floquet-Bloch eigenmodes, resulting in significantly improved performance. When synchronized with an electron beam (e-beam), an amplifier operating at an SIP achieves advantages such as gain enhancement, increased gain-bandwidth products, and higher power efficiency [10, 58]. Additionally, a three-way coupled waveguide structure has been developed to achieve a third-order EPD through glide-time (GT) symmetry [9], which holds potential for high-power array applications.

1.4 Organization of the Dissertation and Contents

The dissertation is organized into Chapters that involve the theory and applications of dispersion engineering in microwave, RF, and electron beam devices. We explore the conditions for various orders of EPDs to exist in different structures ranging from microwave to RF.

Chapter 2: We propose a scheme for highly sensitive oscillators based on a coupled-resonator system with an exceptional point of degeneracy. The oscillator with EPD is realized by coupling two resonators with nearly balanced small-signal gain and loss and leveraging nonlinear saturation effects in the active component. This design results in an oscillation frequency that is highly sensitive to circuit perturbations. We investigate two configurations: parallel LC resonators coupled wirelessly by mutual inductance or wired by a capacitor. This chapter demonstrates the conditions for a second-order EPD oscillator and its high sensitivity to component perturbations, including those breaking PT-symmetry. The scheme improves

sensitivity to both positive and negative changes in circuit components and has potential applications in ultrasensitive sensors, tunable oscillators, and modulators.

Chapter 3: We propose a scheme for generating oscillations using an EPD in two coupled resonators made of transmission lines with balanced gain and loss. An EPD occurs when eigenmodes coalesce in both eigenvalues and eigenvectors. Unlike a single transmission line, second-order EPDs are possible in two coupled lines terminated with balanced gain and loss. We demonstrate conditions for EPDs in three termination configurations and show eigenfrequency bifurcation at the EPD. We explore the oscillatory regime with nonlinear gain and highlight the extreme sensitivity of the self-oscillation frequency to perturbations. This highly sensitive EPD-based oscillator can be used as a sensor to detect small system variations. The material in the first four sections was initially led by a previous student, Dr. Hamidreza Kazemi from the same lab.

Chapter 4: We propose a high-sensitivity oscillator scheme based on an EPD using two LC resonators coupled with a gyrator. The oscillation frequency is highly sensitive to perturbations, such as changes in a capacitor's value. We analyze the conditions leading to EPD, including the use of negative inductance and capacitance. Through fabrication, we demonstrate that the circuit's instability leads to stable self-oscillations, with high sensitivity to small perturbations. The sensitivity of a gyrator-based oscillator to perturbations is higher than the one of a comparable simple LC linear resonator and is comparable to, or better than, other EPD circuits. This scheme can be used for high-precision sensors in various applications. Please note that Mr. Kasra Rouhi contributed to the theoretical section of this chapter.

Chapter 5: This chapter investigates the emergence of EPDs in three circuit configurations: gyrator-based coupled resonators, PT-symmetric coupled resonators, and a single resonator with a time-varying component. Each circuit displays high sensitivity to component perturbations, which can be used for sensing applications. Gyrator-based circuits exhibit real-

valued eigenfrequencies under perturbation but require active components and can operate in oscillatory regimes due to inherent instabilities. PT-symmetric circuits, with balanced gain and loss, also achieve high sensitivity, though they need precise tuning to maintain stability. The linear time-varying (LTV) circuit provides a simpler alternative, achieving EPDs by adjusting modulation frequency alone. Together, these EPD-based circuits show promise for designing highly sensitive, efficient sensors suitable for detecting minor variations in various physical, chemical, or biological conditions.

Chapter 6: We investigate how a single resonator with a time-modulated component extracts power from an external ambient source. The power collected depends significantly on the precise modulation signal frequency. Focusing on mechanical resonators, we show that time modulation of the damper can enhance power harvesting by over 10 times compared to systems without modulation. A narrow band pair of peak and dip in the absorbed power spectrum occurs due to an EPD. In this narrow frequency range, the delay between the damper modulation and external vibration significantly affects power collection. This high frequency-selectivity could be useful for sensing and spectrometer applications. Please note that this chapter was completed with an equal contribution from Dr. Kasra Rouhi.

Chapter 7: In this chapter, we show that an oscillator array tends to operate at an EPD in a waveguide with discrete nonlinear gain and radiating elements. The EPD concept achieves an exceptional synchronization regime, enhancing radiating power efficiency. The system maintains a steady-state degenerate oscillation mode at 3 GHz, even with nonuniform small-signal nonlinear gain. Contrarily to the original expectation of zero phase shift of the signal from a unit cell to the next one, after reaching saturation, the time-domain signal in consecutive unit cells displays a π phase shift. Therefore, we prove that the system converges to a distinct EPD. Unlike ordinary oscillating systems, the oscillation frequency remains independent of the array length. These findings are significant for high-power radiating arrays with distributed active elements.

Chapter 8: This chapter presents a novel periodic array of nonlinear gain and radiating elements that achieves stable oscillation at an EPD. Unlike conventional systems, the array's oscillation frequency is independent of its length, and the saturated gain across the array is uniformly distributed, even when the initial small-signal gain is non-uniform. Experimental and simulation results confirm that the array stabilizes at an EPD, producing low phase noise and uniform radiating power. The design is robust to variations in gain, loss, and element failure, making it highly suitable for high-power radiation applications requiring a stable low-noise frequency. This work overcomes previous limitations in Chapter 7 by demonstrating a system with non-zero saturated gain and consistent power distribution.

Chapter 2

Highly Sensitive Coupled Oscillator Based on an Exceptional Point of Degeneracy and Nonlinearity

We propose a scheme to obtain highly-sensitive oscillators in a coupled-resonator system with an exceptional point of degeneracy (EPD) and a small instability. The oscillator with the exceptional degeneracy is realized by using two coupled resonators with an almost balanced small-signal gain and loss, that saturates due to nonlinear effects of the active component, resulting in an oscillation frequency that is very sensitive to a perturbation of the circuit. Two cases are investigated, with two parallel LC resonators with balanced small-signal gain and loss that are either coupled wirelessly by mutual inductance or coupled-wired by a capacitor. This chapter demonstrates theoretically and experimentally the conditions to obtain a second-order EPD oscillator and analyzes the ultrasensitivity of the oscillation frequency to components' perturbation, including the case of asymmetric perturbation that breaks PT-symmetry. We discuss the effects of nonlinearity on the performance of the oscillator and how the proposed scheme improves the sensing's sensitivity of perturbations. In contrast to

previous methods, our proposed degenerate oscillator can sense either positive or negative changes of a circuit component. The degenerate oscillator circuit may find applications in various areas such as ultrasensitive sensors, tunable oscillators and modulators.

2.1 Motivation and State of the Art

Oscillators are fundamental components of radio frequency (RF) electronics. Traditionally, an oscillator is viewed as a positive feedback mechanism utilizing a gain device with a selective reactive circuit. An oscillator generates a continuous, periodic single-frequency output when the Barkhausen's criteria are satisfiedred [18]. The oscillator circuit should have a self-sustaining mechanism such that noise gets filtered, quickly grows and becomes a periodic signal. Most RF oscillators are implemented by only one active device for noise and cost considerations, such as Van der Pol and voltage-controlled oscillators [19]. Oscillators can be realized by a simple LC resonator with positive feedback using a negative resistance. Pierce, Colpitts, and tunnel diode oscillators play a role of negative resistance in a circuit, as well as a cross-coupled transistor pair [18, 20, 21]. All these oscillators are based on a single-pole operation, i.e., a single pole of the system matrix that describes the circuit [18] is rendered unstable when the system is brought above the threshold. Oscillators based on an LC resonator are the most common type of oscillator, other designs may feature distributed [22, 23, 8], ring [24, 59], coupled [60], or multi-mode [61] oscillators, which come with their own challenges and advantages.

In this chapter, we discuss the concept of a double-pole oscillator, i.e., an oscillator designed to utilize an exceptional point of degeneracy (EPD) in two coupled resonators, where the degenerate (double) pole is rendered unstable. A system reaches an EPD when at least two eigenmodes coalesce into a single degenerate one, in their eigenfrequencies (eigenvalues) and polarization states (eigenvectors) [34, 31, 35, 32, 33, 62, 63, 64, 65]. The letter "D" in

EPD refers to the key concept of "degeneracy" where the relevant eigenmodes, including the associated eigenvectors are fully degenerate [66]. The degeneracy order refers to the number of coalescing eigenmodes. The concept of EPD has been implemented traditionally in systems made of coupled resonators [17, 3, 67, 68, 69, 70, 71], periodic and uniform multimode waveguides [39, 72, 73, 2, 74], and also in waveguides using Parity-Time (PT) symmetry [75, 2, 76, 77]. EPDs have been recently demonstrated also in a temporally-periodic single resonator without a gain element [4, 78, 79, 69], inspired by the finding that EPD exists in spatially periodic lossless waveguides [1, 13, 38], resorting to a non-diagonalizability property of the transfer matrix associated to a periodic system.

A very significant feature of a system with EPD is the ultra-sensitivity of its eigenvectors and eigenvalues to a perturbation of a system's parameter. This property paves the way to measure a small change in either physical, chemical, or biological parameter that causes a perturbation in the system. Typically, a sensor's sensitivity is related to the amount of spectral shift of a resonance mechanism in response to a perturbation in environmental parameters, for example, a glucose concentration or other physical variations like changing pressure, etc. Sensors with EPD can be wired or wirelessly connected to the measuring part of the sensor [80, 81, 82]. In principle, higher sensitivity would be enabled with higher orders of degeneracy, such as the more complicated circuit in [83]. In Refs. [80, 81, 82, 83], sensitivity was discussed in the case of symmetric gain and loss. In this chapter, we show very high sensitivity of the oscillation frequency to external perturbations of a double-pole oscillator operating at a second-order EPD, focusing on the nonlinear aspects of the implementation.

Based on the general PT-symmetry concept [40], PT-symmetry circuits have been conceived as two coupled resonators [17, 3]. In demonstrating the sensitivity of these circuits's response when the circuit is perturbed away from its EPD, PT-symmetry has been maintained in order to obtain two real-valued frequencies: for example, in Ref. [6], when one side's capacitance is perturbed, the authors tuned the other side's capacitance using a varactor to keep the

PT-symmetry in the circuit, so they can still, observe two real-valued shifted frequencies perturbed away from the degenerate EPD frequency. Thus, in previously published schemes (implementing the demonstration of sensitive measurement of a perturbation) the exact value of such perturbation should be precisely known to tune the other side of the system in order to keep the circuit PT-symmetric. This seems to contradict the idea that the circuit is used as a sensor of an unknown measurable quantity. That scheme could be saved if combined with an iterative method performing an automatic scan to reconstruct the PT-symmetry. Anyway, this rebalancing procedure (to keep the system PT-symmetric) is a further complication for using such a scheme to design a sensor.

A limitation of PT-symmetry schemes is that they can detect only perturbations that lead to the same-sign change in a system's component, such as a capacitor's value. This is because a PT-symmetric system provides two real-valued frequencies only when the system is perturbed away from its EPD in one direction (for example for G values smaller than the G_e related to the EPD, when looking at the eigenfrequencies in Fig. 2.1). If the perturbation makes the system move in the other direction, the shift of the frequencies is in the imaginary parts [84, 3, 6, 17], leading to two complex-valued frequencies and hence to instability. One must also consider that any mismatch between the sensor side (typically the part with losses) and the reader side (typically the part with gain), even involuntary, leads to an asymmetric system. Thus, a PT-symmetric system in practice always shows two complex-valued eigenfrequencies and increases the risks of self-sustained oscillations (unless an EPD is designed with a large enough damping factor, larger than the eigenfrequency perturbation due to circuit tolerances). Noise and nonlinearities play a critical role in the robustness of these kinds of applications and affect the possibility of instability [85]. Some error-correction techniques are studied in [86] to overcome some of these drawbacks using a nonlinear PT-symmetry scheme to enhance the robustness of sensing. A closely related highly sensitivity approach has also been proposed using the concept of white light cavities that has been then demonstrated to be related to the concept of EPD in PT-symmetric systems [87, 88].

In this chapter, we provide a scheme that starts by using a quasi PT-symmetric condition, working near an EPD, that makes the double-pole system slightly unstable even before having any perturbation. In other words, we turn the above-mentioned practical problems that occur in PT-symmetric systems to our advantage when the circuit has to be used in a highly sensitive sensor. We set the gain value slightly higher than the loss counterpart to make the system slightly unstable. As a result of instability and nonlinear gain, the signal grows until the active gain component reaches saturation, and the working operation will be close to the EPD.

2.2 Oscillator Based on Coupled Resonators with EPD

We first show the behavior of wirelessly coupled LC resonators through the dispersion relation of the resonance frequency versus perturbation and we discuss the occurrence of EPDs in such a system. In section 2.3, we use the nonlinear model for the gain to achieve the oscillator's characteristics. We show that the oscillation frequency is very close to the EPD frequency. The EPD-based oscillator has an oscillation frequency that is very sensitive to perturbation, exhibiting the typical square root-like behavior of EPD systems, where the change in frequency of the oscillator is proportional to the square root of the perturbation. In section 2.4, we demonstrate the highly sensitive behavior of the circuit by breaking PT-symmetry, i.e., by perturbing the capacitance on the lossy side (the sensing capacitance). In this case, the circuit oscillates at a shifted frequency compared to the EPD one. Notably, both positive and negative perturbations in the capacitance are shown to lead to opposite shifted frequencies, i.e., the proposed scheme detects either positive or negative changes in the capacitance, in contrast to conventional PT-symmetry systems [3, 6, 67] that generate frequency shifts associated to only one sign of the perturbation. The EPD is demonstrated also by analyzing the bifurcation of the dispersion diagram at the EPD frequency by using the

Puiseux fractional power series expansion [89, 33]. In section 2.5, we show the condition to have an EPD in two resonators coupled by a capacitor and demonstrate the occurrence of the EPD by using the Puiseux series and experimentally, by using a nonlinear active element. Also, we discuss how noise contributes to the system by showing the power spectrum of the system and the phase noise. The theoretical results are in a good agreement with the experimental results, pointing out that small perturbations in the system can be detected by easily measurable resonance frequency shifts, even in the presence of thermal noise and electronic noise. The advantages of using the proposed circuit as an ultra-sensitive sensor and how the experimental results show that the oscillator is sensitive to both positive and negative capacitance changes are discussed in Section 2.5. Very sensitive sensors based on the oscillator scheme discussed here can be a crucial part of various medical, industrial, automotive and aerospace applications that require sensing physical, chemical or biological variations.

We investigate the coupled resonators shown in Fig. 2.1(a), where one parallel LC resonator includes gain (left side, or $n = 1$) and the other includes loss (right side, or $n = 2$). In this ideal circuit, the negative conductance $-G_1$ (gain) has the same magnitude as the loss G_2 to exactly satisfy PT-symmetry. When a system satisfies PT-symmetry, it means that the system is invariant to the application of the two operators of parity P transformation (making a spatial reflection (e.g., $x \rightarrow -x$)), and time-reversal T transformation ($t \rightarrow -t$), where x is the coordinate and t is the time.

By writing Kirchhoff's current laws, we obtain the equations

$$\begin{cases} \frac{d^2Q_1}{dt^2} = -\frac{1}{LC_1(1-k^2)}Q_1 + \frac{k}{LC_2(1-k^2)}Q_2 + \frac{G_1}{C_1}\frac{dQ_1}{dt} \\ \frac{d^2Q_2}{dt^2} = +\frac{k}{LC_1(1-k^2)}Q_1 - \frac{1}{LC_2(1-k^2)}Q_2 - \frac{G_2}{C_2}\frac{dQ_2}{dt} \end{cases} \tag{2.1}$$

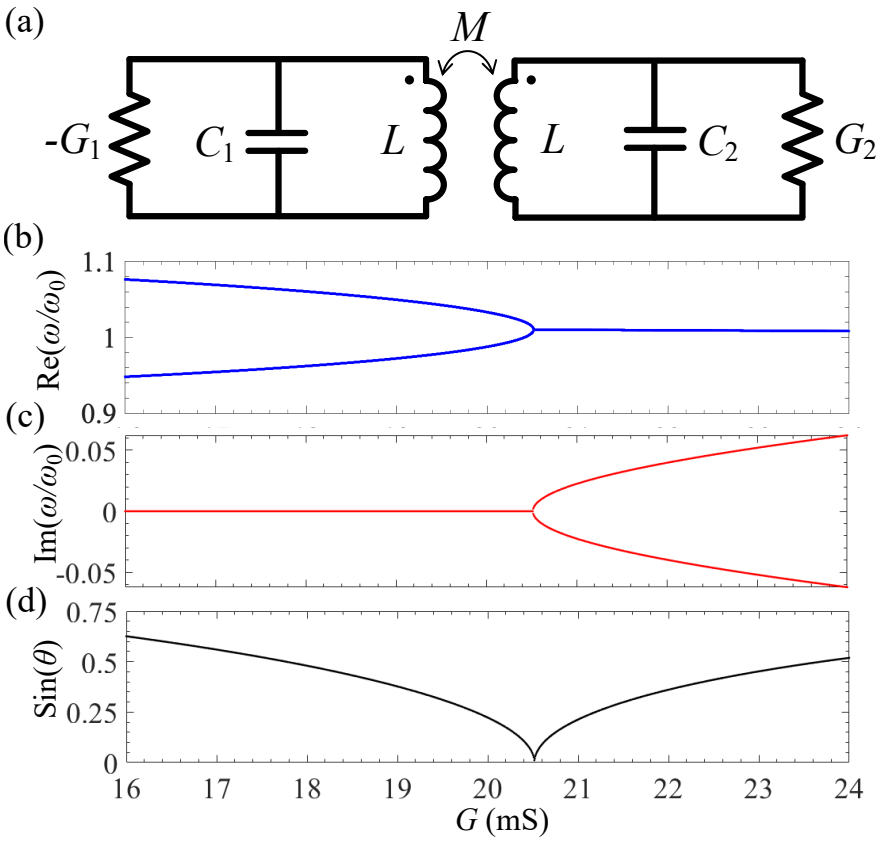

Figure 2.1: (a) Coupled resonators terminated with linear $-G_1$ on the gain side ($n = 1$) and G_2 on the loss side ($n = 2$), with $G_1 = G_2 = G$, and inductances $L = 0.1\,\mu$H, mutual coupling $k = M/L = 0.2$, capacitances of $C_n = C_0 = 1\,$nF ($n = 1, 2$). The natural frequency of each (uncoupled) LC resonator is $\omega_0 = 1/\sqrt{LC_0} = 10^8\,\text{s}^{-1}$. Normalized eigenfrequencies of the coupled circuit are calculated by using Eqs. (2.4) and (2.5). (b) Positive real, and (c) imaginary parts of the resonance angular frequencies normalized by ω_0 varying G on both sides of the EPD value. (d) At the EPD point ($G = G_e = 20.52\,\text{mS}$, $\omega_e = 1.01 \times 10^8\,\text{s}^{-1}$), two state eigenvectors coalesce demonstrated by the vanishing of $\sin(\theta)$.

where Q_n is the capacitor charge on the gain side ($n = 1$) and on the lossy side ($n = 2$), and $\dot{Q}_n \equiv dQ_n/dt$ is the current flowing into the capacitor. We define the system's state vector as $\mathbf{\Psi}(t) \equiv [Q_1, Q_2, \dot{Q}_1, \dot{Q}_2]^{\text{T}}$, consisting of a combination of stored charges and currents on both sides, and the superscript T denotes the transpose operation. Thus, we describe the system in a Liouvillian formalism as

$$\frac{d\mathbf{\Psi}}{dt} = \underline{\mathbf{M}}\mathbf{\Psi},$$

$$\underline{\mathbf{M}} = \begin{pmatrix} 0 & 0 & 1 & 0 \\ 0 & 0 & 0 & 1 \\ -\frac{1}{LC_1(1-k^2)} & \frac{k}{LC_2(1-k^2)} & \frac{G_1}{C_1} & 0 \\ \frac{k}{LC_1(1-k^2)} & -\frac{1}{LC_2(1-k^2)} & 0 & -\frac{G_2}{C_2} \end{pmatrix}. \tag{2.2}$$

We are interested in finding the eigenfrequencies and eigenvectors of the system matrix $\underline{\mathbf{M}}$. Assuming signals of the form $Q_n \propto e^{j\omega t}$, we write the eigenvalues problem associated with the circuit equations, $(\underline{\mathbf{M}} - j\omega\underline{\mathbf{I}})\mathbf{\Psi} = 0$, where $\underline{\mathbf{I}}$ is a 4 by 4 identity matrix. Then, by solving $P(\omega) \triangleq \det(\underline{\mathbf{M}} - j\omega\underline{\mathbf{I}}) = 0$, the four eigenfrequencies are found. By assuming $C_1 = C_2 = C_0$ and linear $G_1 = G_2 = G$, a symmetry condition that has been described as PT symmetric [17], the characteristic the equation takes the simplified form

$$\begin{aligned} P(\omega) &= (1-k^2)\left(\frac{\omega}{\omega_0}\right)^4 \\ &+ \left(G^2Z^2(1-k^2) - 2\right)\left(\frac{\omega}{\omega_0}\right)^2 + 1 = 0, \end{aligned} \tag{2.3}$$

where $Z = \sqrt{L/C_0}$ is a convenient normalizing impedance, and $\omega_0^2 = 1/(LC_0)$. The characteristic equation is quadratic in ω^2; therefore, ω and $-\omega$ are both solutions. Moreover, the ω's coefficients in the characteristic equation are real, hence ω and ω^* are both solutions, where * represents the complex conjugate operation. The 4 by 4 matrix $\underline{\mathbf{M}}$ results in 4 angular eigenfrequencies which are found analytically as,

$$\omega_{1,3} = \pm\omega_0\sqrt{\frac{1}{1-k^2} - \frac{G^2Z^2}{2} - \sqrt{b}}, \tag{2.4}$$

$$\omega_{2,4} = \pm\omega_0\sqrt{\frac{1}{1-k^2} - \frac{G^2Z^2}{2} + \sqrt{b}}, \tag{2.5}$$

$$b = -\frac{1}{1-k^2} + \left(\frac{G^2Z^2}{2} - \frac{1}{1-k^2}\right)^2. \tag{2.6}$$

Because of the mentioned symmetries of the eigenfrequencies in a realistic system with purely-real time domain signals (e.g., voltages and currents), in the follwoing we will focus mainly on the two solutions with positive real part, namely ω_1 and ω_2. The EPD frequency is found when the component values obey the condition

$$b = 0. \tag{2.7}$$

So far $b = 0$ is a necessary condition, but in a simple system like this, the eigenvectors can be represented as a function of the eigenvalues so this condition is also sufficient to show the convergence of the eigenvectors, hence for an EPD to occur. Under this condition, we calculate the EPD angular frequency based on Eqs. 2.4 and 2.7 as $\omega_1 = \omega_2 = \omega_e$ where

$$\omega_e = \frac{\omega_0}{\sqrt[4]{1-k^2}}. \tag{2.8}$$

Only the two eigenfrequencies with positive-real part, namely ω_1 and ω_2, are shown in Fig. 2.1(b) and (c) varying G. It is seen from this plot that the system's eigenfrequencies are coalescing at a specific balanced linear gain/loss value $G = G_e$, where $b = 0$. Note that in this scenario, the EPD-enabling value G_e is derived from Eq. (2.7) as

$$G_e = \frac{1}{Z}\left(\frac{1}{\sqrt{1-k}} - \frac{1}{\sqrt{1+k}}\right). \tag{2.9}$$

For clarification, when $G = 0$ (lossless and gainless circuit), we have two pairs of resonance frequencies $\omega_{1,3} = \pm\omega_0/\sqrt{1+k}$ and $\omega_{2,4} = \pm\omega_0/\sqrt{1-k}$, and $\omega_1 \neq \omega_2$ always, except for the trivial case with $k = 0$, when these eigenfrequencies are equal to those of the isolated circuits, but since the two circuits are isolated this is not an important degeneracy. With the given values of L and C in the caption of Fig. 2.1, a second-order EPD occurs when $G = G_e = 20.52\,\text{mS}$. In this case, the circuit's currents and charges grow linearly with increasing time as $Q_n \propto te^{j\omega_e t}$), and they oscillate at the degenerate frequency ω_e. Also, when perturbing G near the EPD point, the eigenfrequencies have a square root-like behavior as $|\omega - \omega_e| \propto \pm\sqrt{(GZ)^2 - (G_eZ)^2}$[3]. A second coalescence (i.e., degeneracy) happens for larger values of G, i.e., at $G_e' = \frac{1}{Z}\left(\frac{1}{\sqrt{1-k}} + \frac{1}{\sqrt{1+k}}\right)$. However, when $G > G_e'$ all eigenfrequencies are purely imaginary, so we only study cases with $G < G_e'$, discussed next. In the strong coupling regime, $0 < G < G_e$, the eigenfrequencies are purely real, and the oscillation wave has two fundamental frequencies. In the weak coupling regime, $G_e < G < G_e'$, the frequencies are complex conjugate and the imaginary part of the angular eigenfrequencies is non-zero, and it causes two system solutions (Q_1 and Q_2) with damping and exponentially growing signals in the system. Since the solution of the circuit is $Q_n \propto e^{j\omega t}$, the eigenfrequency with a negative imaginary part is associated to an exponentially growing signal and the oscillation frequency is associated to the real part of the eigenfrequency.

At each positive (real part) angular eigenfrequency ω_1 and ω_2, calculated by Eqs. (2.4) and (2.5), we find the two associated eigenvectors $\mathbf{\Psi_1}$ and $\mathbf{\Psi_2}$ by using Eq. (2.2). A sufficient condition for an EPD to occur is that at least two eigenvectors coalesce, and that is what we check in the following. Various choices could be made to measure the state vectors' coalescence at an EPD, and here, the "Hermitian angle" between the state amplitude vectors

$\mathbf{\Psi_1}$ and $\mathbf{\Psi_2}$ is defined as [90]

$$\theta = \arccos\left(\frac{|<\mathbf{\Psi_1}, \mathbf{\Psi_2}>|}{||\mathbf{\Psi_1}||\,||\mathbf{\Psi_2}||}\right). \tag{2.10}$$

Here, the inner product is defined as $<\mathbf{\Psi_1}, \mathbf{\Psi_2}>= \mathbf{\Psi_1^\dagger \Psi_2}$, where the dagger symbol $\dagger$ denotes the complex conjugate transpose operation, $||$ represents the absolute value, and $||\,||$ represents the norm of a vector. According to this definition, the state vectors $\mathbf{\Psi_1}$ and $\mathbf{\Psi_2}$ correspond to resonance frequencies ω_1 and ω_2, respectively. When some system's parameter is varied, eigenfrequencies and associated eigenvectors are calculated using Eq. (2.2). In the case when G varies, Fig. 2.1(d) shows that the sine of the angle θ between the two eigenvectors vanishes when the eigenfrequencies coalesce, which indicates the coalescence of the two eigenmodes in their eigenvalues and eigenvectors and hence the occurrence of a second-order EPD.

2.3 Oscillator Characteristics

This section describes the important features of a double-pole (degenerate) oscillator made of two coupled resonators with discrete (lumped) elements with balanced gain and loss, coupled wirelessly by a mutual inductance as in Fig. 2.1. The transient time-domain, frequency spectrum, and double pole (or zero, depending on what we look at) features are discussed. A cubic model (nonlinear) of the active component providing gain is considered. The parameters used here are the same as those used in the previous section, where $G_e = 20.52\,\text{mS}$ leads to an EPD of order two at a frequency of 16.1 MHz, except that red here $-G_1$ accounts also for the nonlinear part responsible for the saturation effect.

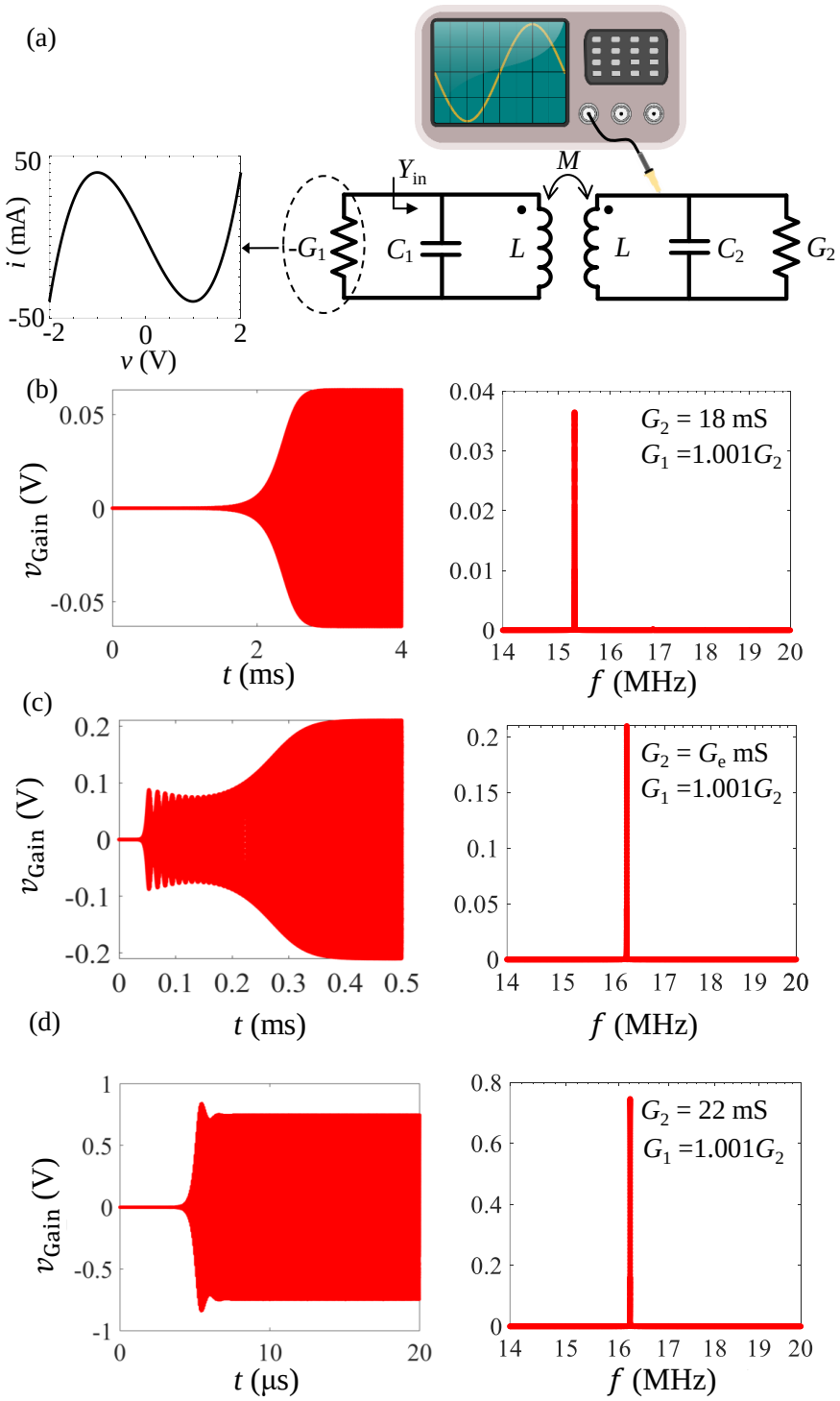

Figure 2.2: (a) Cubic gain $i - v$ curve with parameters $G_1 = G_e = 20.52\,\text{mS}$ and $\alpha = 6.84\,\text{mS/V}^2$ (it corresponds to $V_\text{b} = 1\,\text{V}$). Time-domain response and frequency spectrum of the oscillatory signal with a cubic model where the gain is always 0.1% more than the loss (i.e., $G_1 = 1.001G_2$) with: (b) $G_2 \lesssim G_1 < G_e$, (c) $G_1 = 1.001G_e$ and $G_2 = G_e$, and (d) $G_1 \gtrsim G_2 > G_e$, where $G_e = 20.52\,\text{mS}$.

A. Transient and Frequency Behavior

Time and frequency-domain responses of the coupled resonators circuit are obtained by using the Keysight Advanced Design System (ADS) circuit time-domain simulator, as shown in Fig. 2.2(b)-(d). The cubic model for gain, in Fig. 2.2(a), represented as

$$i = -G_1 v + \alpha v^3 \tag{2.11}$$

is a simplified description of the gain obtained from a cross-coupled transistor pair or an operational amplifier (opamp) based circuit. Here, $-G_1$ is the small-signal gain provided by the negative slope of the $i - v$ curve, i.e., is the negative conductance in the small-signal region, and $\alpha = G_1/\left(3V_{\mathrm{b}}^2\right)$ is a third-order nonlinearity that describes saturation, where V_{b} is the turning point voltage determined by the biasing direct current (DC) voltage. We assume $V_{\mathrm{b}} = 1\,\mathrm{V}$, and to start self-sustained oscillation, we assume that gain $-G_1$ is not a perfect balance of the loss G_2. Indeed, we assume that G_1 is 0.1% larger than G_2. Therefore, the system is slightly perturbed away from the PT-symmetry condition to start with. We also assume white noise (at the temperature of 298 K) is present in the loss resistor and it is indeed the initial condition for starting oscillations. The slightly broken small-signal gain and loss symmetry causes an eigenfrequency to have a slightly negative imaginary part. The signals in the system are in the form of $e^{j\omega t}$ and even a small negative imaginary part of an eigenfrequency makes the system unstable because the system's signal grows. Therefore, the system starts oscillating at a frequency associated to the eigenfrequency with a negative imaginary part; then, such frequency is slightly perturbed because of the nonlinear saturation effect.

Therefore, because $G_1 = G_2(1 + 0.001)$ the circuit is slightly unstable and starts oscillations; after a transient, the circuit saturates, yielding a stable oscillation, as shown in Fig. 2.2(b)-(d). As it was shown in Figs. 2.1(b) and (c) assuming linear gain, for values of $G_1 = G_2 < G_e$,

the system has two distinct eigenfrequencies ω_1 and ω_2 with zero imaginary part. However, when using the cubic nonlinear model with G_1=1.001G_2, with $G_2 \lesssim G_1 < G_e$, the imaginary part is not zero anymore because of the slightly broken PT-symmetry. Thus, when using the cubic model, after an initial transient, the oscillation signal associated to the eigenfrequency with a negative imaginary part dominates and makes the system saturates. Considering again the initial result in Figs. 2.1(b) and (c) assuming linear gain, it is noted that when $G_1 = G_2 > G_e$, we have two complex conjugate eigenfrequencies, and the one associated to the negative imaginary part makes the circuit oscillate. However, when using the cubic gain model with G_1=1.001G_2, with $G_1 \gtrsim G_2 > G_e$, eigenfrequencies approximately follow the linear gain eigenfrequency trend. It means that for the values $G_1 \gtrsim G_2 > G_e$, we have a larger negative imaginary part of the eigenfrequency than when $G_2 \lesssim G_1 \leq G_e$. The rising time is related to the magnitude of the negative imaginary part of the eigenfrequency; indeed, as shown in Fig. 2.2(b)-(d), the rising time is different in the three cases. By going further from the EPD point, the signal saturates in a shorter time. In all cases, the frequency spectrum of the time-domain signal is found by taking the Fourier transform of the voltage on the gain side after reaching saturation, for a time window of 10^3 periods.

B. Root Locus of Zeros of the Total Admittance

This subsection discusses the frequency (phasor) approach to better understand the degenerate resonance frequencies of the coupled resonators circuit. We use the admittance resonance method and we demonstrate the occurrence of double zeros at the EPD. The resonance condition based on the vanishing of the total admittance implies that

$$Y_{\text{in}}(\omega) - G_1 = \frac{P(\omega)}{j\frac{L}{\omega_0^2}\left(1-k^2\right)\omega^3 + L^2 G_1\left(1-k^2\right)\omega^2 - jL\omega} = 0, \tag{2.12}$$

where the Y_{in} is the input admittance of the linear circuit, including the capacitor C_1, looking

right as shown in Fig. 2.2(a). Here, we assume linear gain with $G_1 = G_2 = G$, i.e., satisfying PT symmetry.

The polynomial P(ω) is given in Eq. (2.3). We calculate the eigenfrequencies by finding the zeros of $Y_{\text{in}}(\omega) - G$, and this leads to the same ω-zeros of $P(\omega) = \det(\underline{\mathbf{M}} - j\omega\underline{\mathbf{I}}) = 0$. Note that both $\omega(G)$ and $-\omega(G)$ are both solutions of Eq. (2.12), as well as both $\omega(G)$ and $\omega^*(G)$. The trajectories of the zeros of this equation, i.e., the resonance frequencies $\omega(G)$, are shown in Fig. 2.3 by varying linear G from 18 mS to $G = 22$ mS (we recall that in this case $G = G_1 = G_2$), in the complex frequency plane. We show only the roots with $\text{Re}(\omega) > 0$ for simplicity. At the EPD occurring when $G = G_e = 20.52$ mS, the two ω-solutions coincide, and the above equation reduces to $Y_{\text{in}}(\omega) - G_e \propto (\omega - \omega_e)^2$, i.e., the admittance exhibits a double zero at the EPD angular frequency ω_e. This unique property is also responsible for the square root-like behavior of resonance frequency variation due to the perturbation in a system, as discussed next, which is the key to high sensitivity. Moreover, for values $G < G_e$, the two resonance frequencies are purely real, and for $G > G_e$, the two resonance frequencies are a complex conjugate pair.

2.4 Sensor Point of View

A. High Sensitivity and the Puiseux Fractional Power Expansion

As mentioned in the Introduction, when the system operates at an EPD, the eigenfrequencies are extremely sensitive to the system perturbations. This property is intrinsically related to the Puiseux series [89] that provides a fractional power series expansion of the eigenvalues in the vicinity of the EPD point. We consider a small relative perturbation

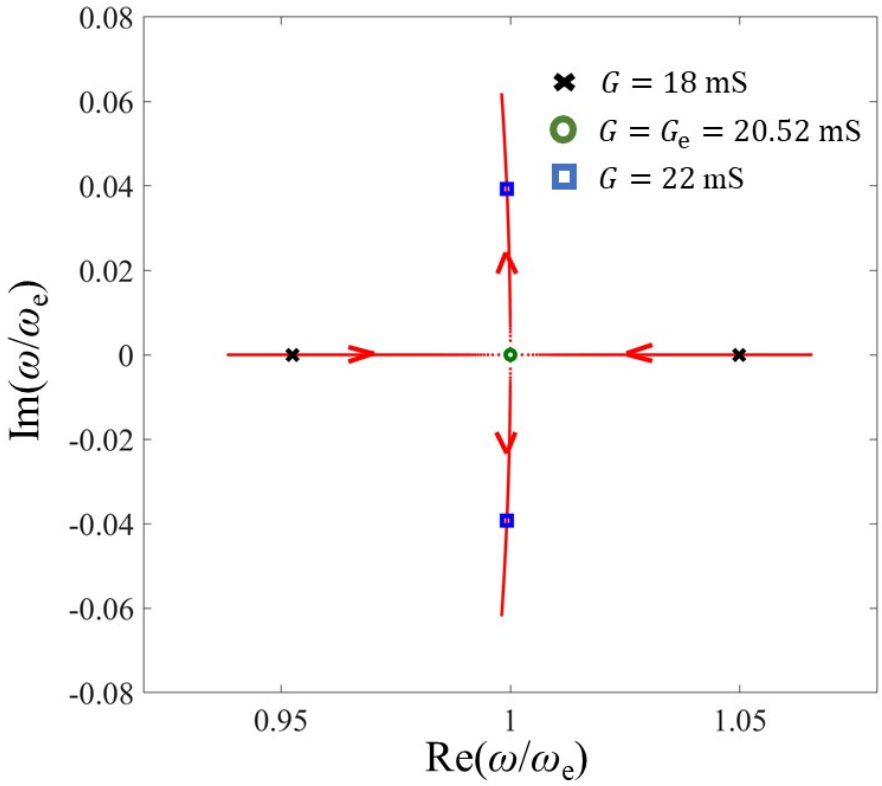

Figure 2.3: The trajectories of the zeros of $Y_{in}(\omega) - G = 0$ show the two resonance frequencies when varying G from 15 mS to 25 mS (we assume linear gain with $G_1 = G_2 = G$). When $G = G_e$, the two branches meet at ω_e. Therefore, at the EPD, the frequency ω_e is a double zero of $Y_{in}(\omega) - G_e = 0$. We plot only the trajectories of the two eigenfrequencies with positive real part.

$$\Delta_{\mathrm{X}} = \frac{X - X_e}{X_e}, \tag{2.13}$$

where X is the perturbated value of a system's element, and X_e is the unperturbed value that provides the EPD of second order. A perturbation Δ_{X} leads to a perturbed matrix $\underline{\mathbf{M}}(\Delta_{\mathrm{X}})$ and, as a consequence, it leads to two distinct perturbed eigenfrequencies $\omega_p(\Delta_{\mathrm{X}})$, with $p = 1, 2$, near the EPD eigenfrequency ω_e as predicted by the Puiseux series containing power terms of $\Delta_{\mathrm{X}}^{\frac{1}{2}}$. Accordingly, a good approximation of the two $\omega_p(\Delta_{\mathrm{X}})$, with $p = 1, 2$, is

given by the first order expansion

$$\omega_p(\Delta_{\mathrm{X}}) \simeq \omega_e + (-1)^p \alpha_1 \sqrt{\Delta_{\mathrm{X}}}. \tag{2.14}$$

Following [89, 33], we calculate α_1 as

$$\alpha_1 = \sqrt{-\frac{\frac{\partial H(\Delta_{\mathrm{X}},\omega)}{\partial \Delta_{\mathrm{X}}}}{\frac{1}{2!}\frac{\partial^2 H(\Delta_{\mathrm{X}},\omega)}{\partial \omega^2}}}, \tag{2.15}$$

where $H(\Delta,\omega) = \det[\underline{\mathbf{M}}(\Delta) - j\omega\underline{\mathbf{I}}]$ and its derivatives are evaluated at the EPD, i.e., at $\Delta_{\mathrm{X}} = 0$ and $\omega = \omega_e$.

Consider a coupled LC resonator, as described in Fig. 2.2(a), assume the capacitor C_2 on the lossy side is perturbed from the initial value as $(1+\Delta_{\mathrm{C_2}})C_e$, where C_e is the unperturbed value for both C_1 and C_2: the coefficient α_1 is found analytically as

$$\alpha_1 = \sqrt{\frac{L^2\omega_e^2 G_e^2 \left(1 + \frac{C_e\omega_e}{G_e}\right)(1-k^2) + (1 - C_e L\omega_e^2)}{L^2\left(6C_e^2\omega_e^2 + G_e^2\right)(1-k^2) - 2C_e L}}. \tag{2.16}$$

The Puiseux fractional power series expansion Eq. (2.14) indicates that for a small perturbation such that $|\Delta_{\mathrm{X}}| \ll 1$, the eigenfrequencies change dramatically from their original degenerate value due to the square root function. The Puiseux series first-order coefficient is evaluated by Eq. (2.16) as $\alpha_1 = 10^7(1.693 + j1.530)\,\mathrm{rad/s}$. The coefficient α_1 is a complex number implying that the system always has two complex eigenfrequencies, for any C_2 value. In Fig. 2.4 (a) and (b), the estimate of ω_p, with $p = 1, 2$, using the Puiseux series is shown by a dashed black line. The calculated eigenfrequencies by directly solving the characteristic equation of Eq. (2.3) are shown by solid blue and red lines, representing unstable and stable solutions, respectively.

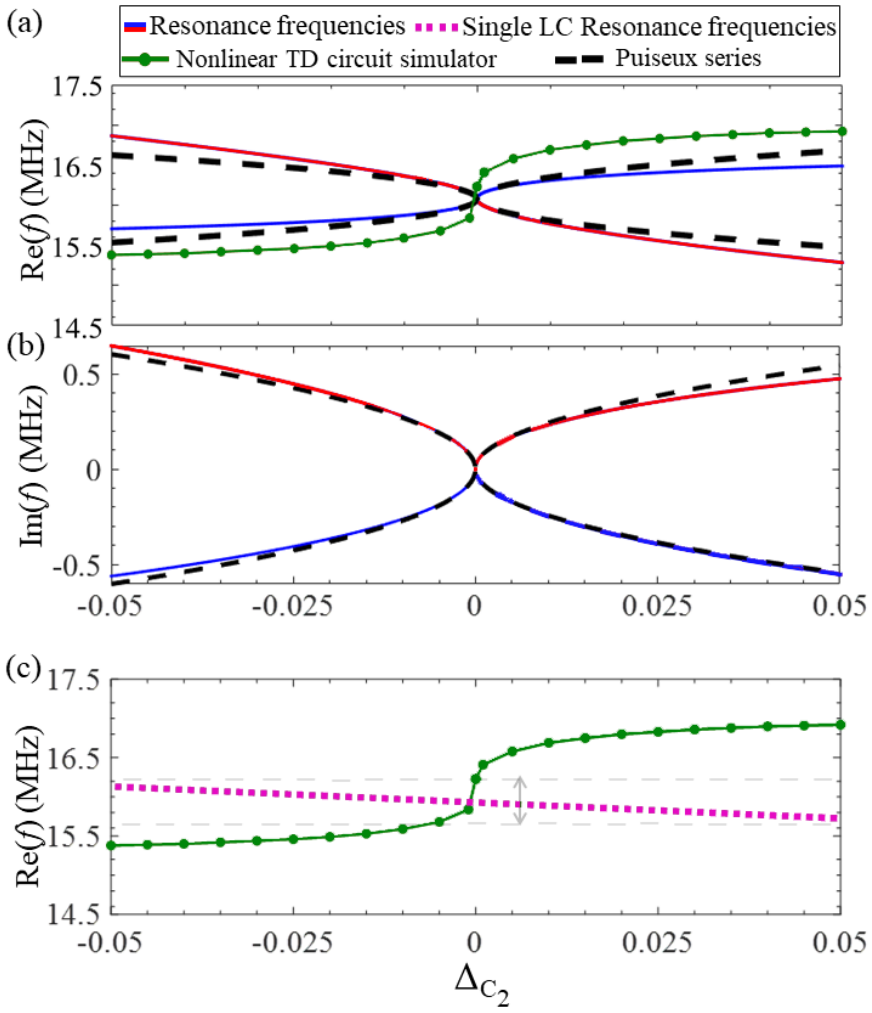

Figure 2.4: High sensitivity of the circuit to a variation of capacitance C_2 . We show the (a) positive-real and (b) imaginary parts of the resonance frequencies (using linear gain) when varying C_2, compared to the frequency of oscillation after saturation when using nonlinear gain. Solid blue and red lines show the resonance frequencies obtained by solving the characteristic equation of Eq. (2.3); dashed lines show the estimate obtained by using the Puiseux fractional power series expansion truncated to its first order. In both cases, gain is a linear negative conductance with $G_1 = G_2 = G_e$. Green dots in (a) show the oscillation frequencies using nonlinear gain; results are obtained by using the time-domain circuit simulator Keysight ADS using the small-signal negative conductance $-G_1$ with $G_1 = 1.001G_e$, i.e., it has been increased by 0.1% from its loss balanced value G_e (we recall that $G_2 = G_e$). The frequencies of oscillation are obtained by applying a Fourier transform of the capacitor C_1 voltage after the system reaches saturation, for each considered value of C_2. (c) Sensitivity comparison with single linear LC resonator, when varying Δ_{C_2}. The much higher sensitivity of the EPD oscillator with double pole is clear. Note that the whole frequency variation relative to the full perturbation range of capacitance ($-5\% < \Delta_{C_2} < 5\%$) for the single LC resonator could be achieved by only 1/10 of the perturbation ($-0.5\% < \Delta_{C_2} < 0.5\%$) when the EPD based circuit is used. The highest sensitivity of the EPD circuit is shown for very small perturbations Δ_{C_2}.

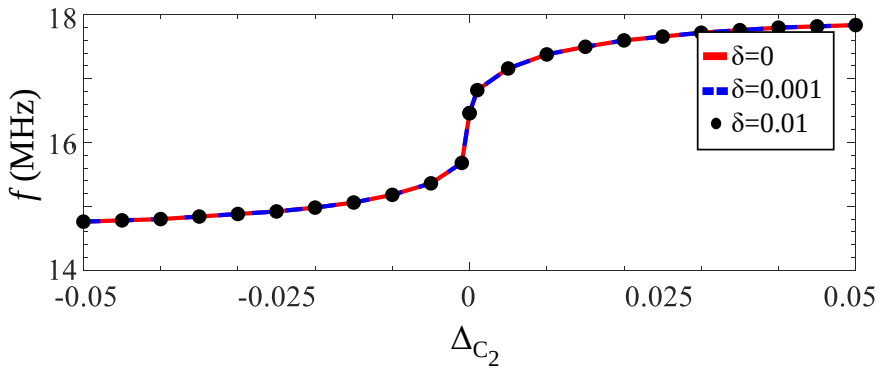

Figure 2.5: Robustness of the high sensitivity of the circuit to a variation of capacitance C_2 .The oscillator's fundamental frequencies of the circuit after each 0.5% perturbation on C_2 by using nonlinear gain are shown here, considering three values of gain $G_1 = G_e(1+\delta)$, where $G_2 = G_e$, for three different values of $\delta = 0,\ 0.001$, and 0.01. These three plots are on top of each other, meaning that even with a 1% mismatch between gain and loss, the oscillator's fundamental frequencies are the same as those for smaller unbalanced situations. It is important to note that both positive and negative perturbations of C_2 are detected.

In this example, C_2 is the sensing capacitance to detect possible variations in chemical or physical parameters, transformed into electrical parameters, like the frequency of oscillation in the circuit. For a small value of Δ_{C_2}, around the EPD value $\Delta_{C_2} = 0$, the imaginary and real parts of the eigenfrequencies experience a sharp change, resulting in a very large shift in the oscillation frequency. Note that this rapid change in the oscillation frequency is valid for both positive and negative changes of Δ_{C_2}, which can be useful for various sensing applications. Note also that a perturbation of PT symmetry led to instability.

To show how the telemetric sensor with nonlinearity works, we now consider that the gain element is nonlinear, following the cubic model in Eq. (2.11), where the small-signal negative conductance is $-G_1$, with value $G_1 = 1.001G_e$, i.e., increased by 0.1% from its loss balanced value G_e, as discussed earlier, to make the circuit slightly unstable and start self oscillations. The capacitor C_2 on the lossy side is perturbed by $\pm 0.5\%$ steps and we perform time-domain simulations using the circuit simulator implemented in the Keysight ADS circuit simulator. Noise is assumed in the lossy element G_2 to start oscillations. The time-domain voltage signal at the capacitor C_1 on the gain side is read, and then, we take the Fourier transform of such

signal, after reaching saturation, for a time window of 10^3 periods. The oscillation frequency evolution by changing Δ_{C_2} is shown in Fig. 2.4 by green dots. There is no imaginary part of the frequency associated to such a signal since it is saturated and steady, and the time-domain signal has the shape of an almost pure sinusoid after reaching saturation (phase noise is discussed later on in this chapter). The oscillation frequency curve dispersion (green dots) still has a square root-like shape of the perturbation.

To show how the sensitivity is improved when using the second-order EPD (double-pole) oscillator, we compare its sensitivity to an analogous scheme made of one single LC resonator, with an inductance of $L = 0.1\ \mu$H and capacitance of $C_2 = 1$ nF (same values as in the case of coupled LC circuits) without adding gain or loss. The resonance frequency of the LC resonator is $f_0 = 1/(2\pi\sqrt{LC_2})$ and by perturbing the capacitance C_2, the resonance frequency changes as $f \approx f_0(1-\Delta_{C_2}/2)$. Figure (2.4) (c) shows the comparison between two cases: (i) oscillation frequency of the EPD based oscillator with nonlinear gain (green dots) using the time-domain circuit simulator Keysight ADS, and (ii) the resonance frequency of the single LC resonator (dashed pink). The results demonstrate that the EPD-based circuit with nonlinearity has higher sensitivity (square root-like behavior due to the perturbation) than a single-LC resonator without EPD (linear behavior). The whole frequency variation, relative to the full perturbation range of capacitance ($-5\% < \Delta_{C_2} < 5\%$) for the single LC resonator, could be achieved by only 1/10 of the perturbation ($-0.5\% < \Delta_{C_2} < 0.5\%$) when the EPD based circuit is used. The highest sensitivity of the EPD circuit is shown for very small perturbations Δ_{C_2},e.g., $|\Delta_{C_2}| \approx 1\%$. For larger Δ_{C_2} variations, i.e., around $|\Delta_{C_2}| \approx 5\%$, the slope of the flattened square root-like curve is similar to the slope of the curve relative to the perturbed LC resonator.

Figure 2.5 shows another important aspect, the flexibility in choosing the gain value in the nonlinear circuit, i.e., different levels of mismatch between gain and loss, using different values for the small-signal negative conductance $G_1 = G_e(1+\delta)$ where $\delta = 0,\ 0.001$ and 0.01,

represents the mismatch between the loss and gain side (we recall that $G_2 = G_e$). As shown in Fig. 2.5, even with 1% mismatch between gain and loss, the nonlinear circuit shows the same behavior in the perturbation of the oscillation frequency, that is even matched to the case with $\delta = 0$. Thus, working in the unstable oscillation configuration using nonlinearity in the coupled circuit gives us the freedom to losely tune the gain component's value and it works well even with some mismatch between gain and loss.

The oscillation frequency is highly sensitive to the capacitance perturbation on either side of the circuit, either on the loss or gain side. Though not shown explicitly, we have observed this feature theoretically, by calculating the eigenfrequencies from $\det(\underline{\mathbf{M}} - j\omega\underline{\mathbf{I}}) = 0$ when varying C_1, and also verified the shifted resonance frequencies using the prediction provided by the Puiseux series. Also, we have observed in time-domain analyses with Keysight ADS circuit simulators using nonlinear gain, that the shift of the oscillation frequency is more sensitive to perturbation of C_1 than C_2. In this chapter, however, we only show the result from perturbing C_2 because we want to investigate how a telemetric sensor works (i.e., the sensing capacitance is on the passive part of the coupled resonators circuit).

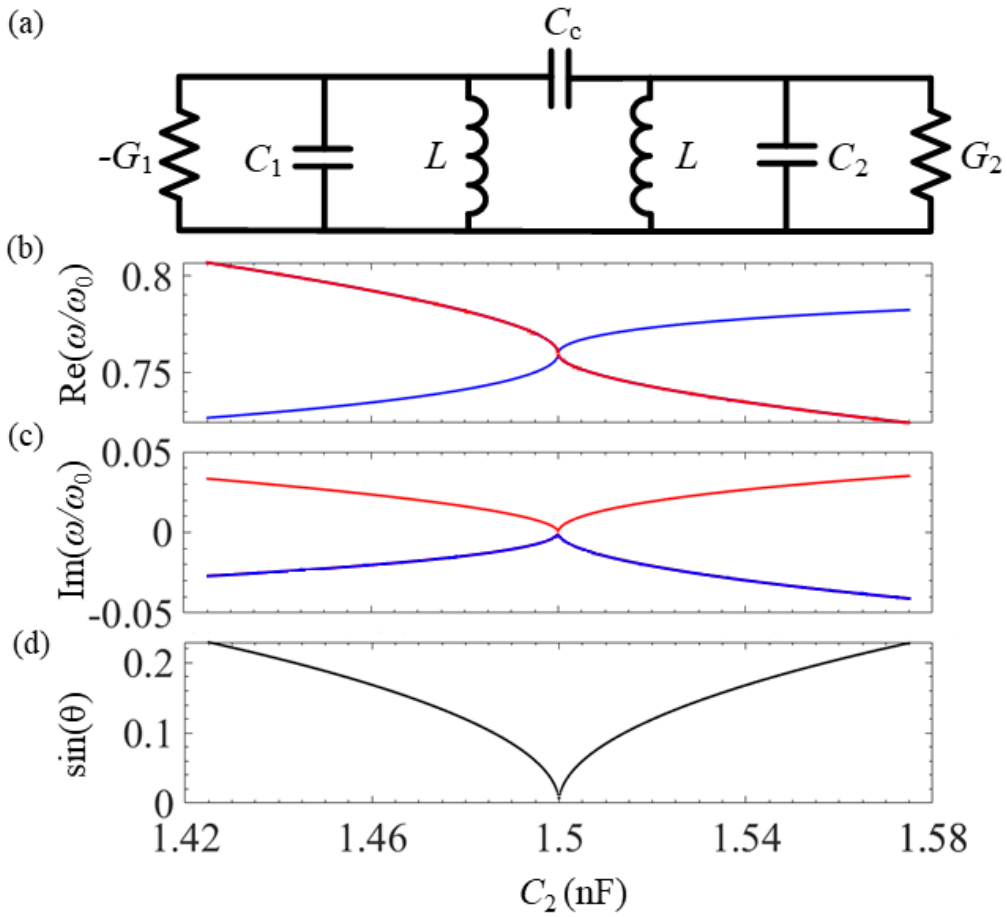

Figure 2.6: (a) Coupled resonators terminated with gain $-G_1$ and loss G_2, with $G_1 = G_2 = G_e = 9\,\mathrm{mS}$, and $L = 10\,\mu\mathrm{H}$, coupling capacitance $C_c = 1.5\,\mathrm{nF}$, capacitances $C_1 = C_2 = C_e = 1.5\,\mathrm{nF}$. These parameters lead to an EPD. The isolated (i.e., without coupling) resonance frequency of each LC resonator is $\omega_0 = 1/\sqrt{LC_e} = 25.8 \times 10^6\ \mathrm{s}^{-1}$. The eigenfrequencies of the coupled circuit are calculated by solving $\det(\underline{\mathbf{M}} - j\omega\underline{\mathbf{I}}) = 0$. (b) Positive-real and (c) imaginary parts of the angular eigenfrequencies normalized by ω_0, varying C_2 around the EPD value C_e. Blue and red solid lines represent the unstable and stable eigenfrequency solutions, respectively. (d) At the EPD, the coalescence parameter $\sin(\theta)$ vanishes, indicating that the two state vectors coalesce.

2.5 Experimental Demonstration of High Sensitivity: Case with Coupling Capacitance

An analogous system with the properties highlighted in the previous sections is made by the two resonators with balanced gain and loss (PT-symmetry) coupled by a capacitor C_c as shown in Fig. 2.6. Note that in this case the sensing part is capacitor-wired to the active part, whereas in the previous circuit the sensing part was connected without wires; both circuits are relevant in applications. In the following, we discuss the condition to have an EPD in this configuration with coupling capacitance and demonstrate the high sensitivity theoretically and experimentally.

First, we find the EPD condition by writing down Kirchhoff's laws and using the Liouvillian formalism using the system vector $\mathbf{\Psi} = [Q_1, Q_2, \dot{Q}_1, \dot{Q}_2]^{\mathrm{T}}$, where Q_n is the capacitor charge on the gain side ($n = 1$) and the lossy side ($n = 2$), and $\dot{Q}_n = dQ_n/dt$, leading to

$$\tfrac{d\mathbf{\Psi}}{dt} = \underline{\mathbf{M}}\mathbf{\Psi}$$

$$\underline{\mathbf{M}} = \tfrac{1}{A}\begin{pmatrix} 0 & 0 & A & 0 \\ 0 & 0 & 0 & A \\ -\frac{B_2}{LC_1} & -\frac{C_c}{LC_2^2} & \frac{GB_2}{C_1} & -\frac{GC_c}{C_2^2} \\ -\frac{C_c}{LC_1^2} & -\frac{B_1}{LC_2} & \frac{GC_c}{C_1^2} & -\frac{GB_1}{C_2} \end{pmatrix} \tag{2.17}$$

$$A = 1 + \tfrac{C_c}{C_1} + \tfrac{C_c}{C_2},\ B_1 = 1 + \tfrac{C_c}{C_1},\ B_2 = 1 + \tfrac{C_c}{C_2}.$$

In this configuration, EPD occurs at $C_1 = C_2 = C_c = C_e = 1.5$ nF, linear gain and loss $G_1 = G_2 = G_e = 9$ mS, $L = 10\ \mu$H. Figures 2.6(b) and (c) show the positive-real and imaginary parts of the eigenfrequencies when perturbing C_2, calculated by solving for ω

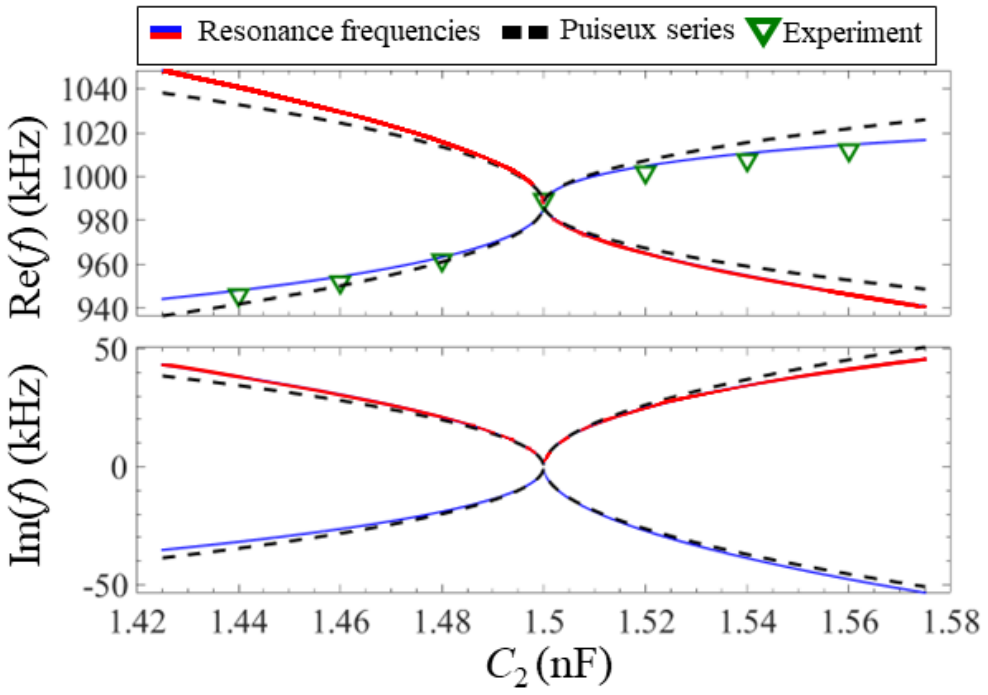

Figure 2.7: Experimental proof of exceptional sensitivity. (a) Experimental and theoretical changes in the real part of the resonance frequencies f due to a positive and negative relative perturbation Δ_{C_2} applied to the capacitance C_2 as $(1+\Delta_{C_2})C_e$. Solid blue and red lines represent the unstable and stable eigenfrequency solutions, respectively. Eigenfrequencies are calculated by finding the zeros of the dispersion equation $\det(\underline{\mathbf{M}} - j\omega\underline{\mathbf{I}}) = 0$ using linear gain $G_1 = G_2 = G_e = 9$ mS. Dashed-black: an estimate using the Puiseux fractional power expansion truncated to its first order, using linear gain. Green triangles: oscillation frequency measured experimentally (using nonlinear gain) after reaching saturation for different values of C_2. The measured oscillation frequency significantly departs from the EPD frequency $f_e = 988.6$ kHz even for a very small variation of the capacitance, approximately following the fractional power expansion $f(\Delta_{C_2}) - f_e \propto \mathrm{Sgn}(\Delta_{C_2})\sqrt{|\Delta_{C_2}|}$. Note that both positive and negative capacitance perturbations are measured.

the dispersion equation $\det(\underline{\mathbf{M}} - j\omega\underline{\mathbf{I}}) = 0$, and Fig. 2.6(d) demonstrates the convergence of eigenvectors at $C_2 = C_e$, hence demonstrating the EPD existence. The eigenfrequency shown with a solid blue line, with a negative imaginary part, represents the unstable solution that determines the oscillation frequency. The coalescence of two eigenvectors is observed by defining the angle between them as in Eq. (2.10), and this indicates the coalescence of the two eigenmodes in their eigenvalues and eigenvectors, and hence the occurrence of a second-order EPD. It is seen from this plot that the system eigenfrequencies are coalescing at a specific capacitance $C_2 = C_e$. The system is unstable for any $C_2 \neq C_e$ because of

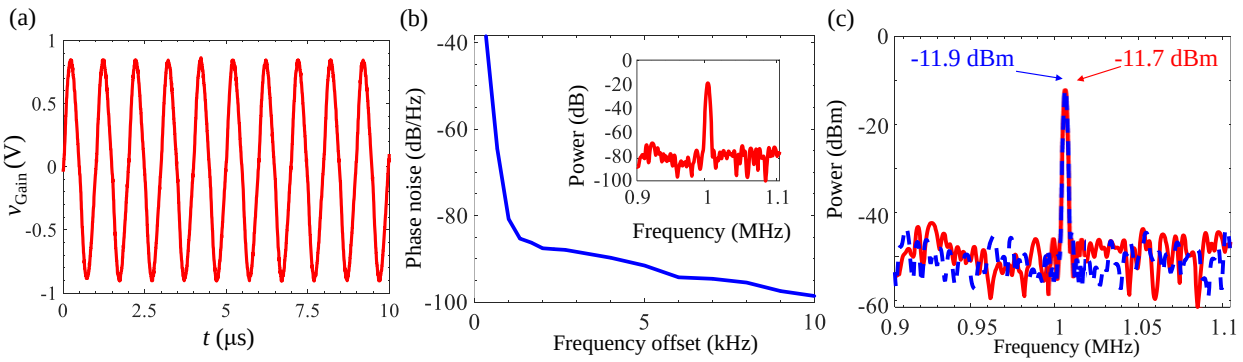

Figure 2.8: (a) Measured time-domain voltage signal at the capacitor C_1 using an oscilloscope, when the system is perturbed from EPD by $C_2 - C_e = 20$ pF, corresponding to a $\Delta_{C_2} = 0.013$. (b) Measured wideband spectrum by Spectrum Analyzer (Rigol DSA832E) signal analyzer as an inset with a fundamental frequency of oscillation of 1.002 MHz (theoretical expectation based on $\det(\underline{\mathbf{M}} - j\omega\underline{\mathbf{I}}) = 0$ is at 1.004 MHz). Phase noise of the power spectrum is measured by the Spectrum Analyzer at frequency offsets from a few Hz to 10 kHz. The resolution bandwidth is set to 300 Hz, while video bandwidth is set to 30 Hz to fully capture the spectrum. (c) Measured power spectrum corresponding to a perturbation $\Delta_{C_2} = 0.013$ applied to C_2, using two different gain values: the red curve is based on gain of the EPD, and the blue curve is based on a gain that is around 1% larger than the EPD value.

broken PT symmetry, since there is always an eigenfrequency with Im(ω)¡0 (blue curve). Moreover, the bifurcation of the dispersion diagram at the EPD is in agreement with the one provided by the Puiseux fractional power series expansion truncated to its first order, represented by a dashed black line in Fig. 2.7. The Puiseux series coefficient is calculated as $\alpha_1 = 1.084 \times 10^6 + j1.43 \times 10^6$ rad/s by using Eq. (2.15), assuming negative *linear* gain. The coefficient α_1 is a complex number that implies that the system always has two complex eigenfrequencies, for any C_2 value; that results in an unstable circuit, since one eigenfrequency has Im(ω) < 0, for any C_2 value.

In order to confirm *experimentally* the high sensitivity to a perturbation in the proposed oscillator scheme based on nonlinear negative conductance (nonlinear gain), the gain is now realized using an opamp (Analog Devices Inc., model ADA4817) whose gain is tuned with a resistance trimmer (Bourns Inc., model 3252W-1-501LF) to reach the proper small-signal gain value of $-G_1 = -9$ mS. Note that we assume that the nonlinear gain is a bit larger

(around 0.1 %) than the loss on the other side of the circuit to make the system slightly unstable. In the experiment, all the other parameters are as in the previous simulation example: a linear conductance of $G_2 = 9$ mS, capacitors of $C_1 = C_2 = C_c = 1.5$ nF, and inductors of $L = 10\ \mu$H (Coilcraft, model MSS7348-103MEC). This nonlinear circuit oscillates at the EPD frequency. The actual experimental circuit differs from the ideal simulations using nonlinear gain only in a couple of points: First, extra losses are present in the reactive components associated with their quality factor. The inductor has the lowest quality factor in this circuit with an internal d.c. resistance of 45 mΩ, from its datasheet, which is however small. Second, electronic components have tolerances. To overcome some of the imperfections in the experiment process, we use a capacitance trimmer (Sprague-Goodman, model GMC40300) and a resistance trimmer in our printed circuit board (PCB) to tune the circuit to operate at the EPD. Also, to have more tunability, a series of pin headers are connected in parallel to the lossy side, where extra capacitors and resistors could be connected in parallel, as mentioned in Appendix 2.8. The circuit is designed to work at the EPD frequency of $f_e = 988.6$ kHz, and indeed after tuning the circuit, we experimentally obtain an experimental EPD frequency at $f = 989.6$ kHz as shown in Fig. 2.7 with a green triangle at $C_2 = C_e$, very close to the designed one. The oscillation frequency is obtained by taking the FFT of the experimentally obtained time-domain voltage signal of the capacitor C_1 using an oscilloscope (Agilent Technologies DSO-X 2024A) after the signal reaches saturation for a time window of 10^2 periods with 10^6 points. The obtained oscillation frequency is in agreement with the result read directly on the spectrum analyzer (Rigol, model DSA832E).

We then perturb C_2 as $(1 + \Delta_{C_2})C_e$ where C_e satisfies the EPD condition, with small steps Δ_{C_2} as explained in Appendix 2.8. As shown in Fig. 2.7, the measured oscillation frequency dramatically shifts away from the EPD frequency, following the trend of square root of Δ_{C_2} as theoretically predicted by Eq. (2.14) for the linear-gain case. The experimental results (green triangles) in Fig. 2.7 demonstrate that even for a small positive and negative perturbation $C_2 - C_e = \pm 20$ pF, corresponding to a $\Delta_{C_2} = \pm 0.013$, the oscillation frequency

significantly changes, which can be easily detected even in practical noisy electronic systems. Figure 2.8(a) shows the experimental time-domain voltage signal of the capacitor C_1 with respect to the ground, when a relative perturbation $\Delta_{C_2} = 0.013$ is applied to C_2, measured by an oscilloscope. The spectrum's frequency is now measured with a spectrum analyzer, and shown in 2.8(b) as an inset. The frequency of the spectrum matches the perturbed ($\Delta_{C_2} = 0.013$) oscillation frequency, green triangle in Fig. 2.7, obtained from the Fourier transform of the time domain experimental data. These results confirm that the structure is oscillating at the predicted perturbed resonance condition after saturation.

An essential feature of any oscillator is its ability to produce a near-perfect periodic time-domain signal (pure sinusoidal wave), and this feature is quantified in terms of phase noise, determined here based on the measured power spectrum up to 10 kHz frequency offset. The phase noise and power spectrum in Fig. 2.8(b) demonstrate that electronic noise (which is significant in opamp) and thermal noise in the proposed highly sensitive oscillator scheme does not discredit the potential of this circuit to exhibit measurable high sensitivity to perturbations. Indeed, the low phase noise of -80.8dB/Hz at 1kHz offset from the oscillation frequency shows that the frequency shifts observed in Fig. 2.7 are well measurable. Note that this result is intrinsic in the nonlinear saturation regime proper of an oscillator. The resonance oscillation peaks have a very narrow bandwidth (linewidth), which makes the oscillation frequency shifts very distinguishable and easily readable.

In the experiment, a relative perturbation $\Delta_{C_2} = 0.013$ (i.e., 1.3%) applied to C_2 led to a frequency shift $\Delta f_{\Delta_{C_2}} = 1002\,\text{kHz} - 989.6\,\text{kHz} = 12.4\,\text{kHz}$,that is much larger than the 1 kHz offset associated to -80.8 dB/Hz noise. The measured -3dB (half power) spectral linewidth in the inset of 2.8(b) is equal to 0.8 kHz (using a resolution bandwidth of 300 Hz, and a video bandwidth of 30 Hz) that is much narrower than the measured frequency shift $\Delta f_{\Delta_{C_2}} = 12.4\,\text{kHz}$.

In this oscillator-sensor system, we also have some freedom in choosing the small-signal gain

value because the dynamics are also determined by the saturation arising from the nonlinear gain behavior. For example, in the experiment, we have verified that circuit has the same oscillation frequency when using an unbalanced small-signal gain 1% larger than the balanced loss value. Figure 2.8(c) shows two measured frequency spectra corresponding to a relative perturbation $\Delta_{C_2} = 0.013$ applied to C_2, using two different gain values. The spectrum has been measured using a resolution bandwidth of 300 Hz, while the video bandwidth is set to 30 Hz to fully capture the spectrum. The red curve is for the case with gain around 1% larger than the balanced loss whereas the blue curve is for the case where gain and loss are balanced. These two frequency responses show the same oscillation frequency, with a very small difference in the power spectrum peak, which is 0.2 dBm higher for the case with 1% larger gain, as shown in Fig.2.8(c). This important feature helps us design the circuit without a very accurate balance between gain and loss, i.e., oscillator-sensors can be realized without satisfying exactly PT symmetry (assuming the sensing perturbation is not applied yet). As mentioned earlier, the nonlinear oscillator with broken PT symmetry exhibits the very important feature that the oscillation frequency shifts are both positive and negative, depending on the sign of the perturbations Δ_{C_2}, hence *allowing for sensing both positive and negative* values of Δ_{C_2}. Note that the oscillator-sensing scheme is achieved without tuning the capacitance in the active part to keep the symmetry (to avoid instability), as it was instead done in a previous scheme using a PT-symmetric circuit [6].

2.6 Conclusions

We demonstrated that two coupled LC resonators terminated with nonlinear gain, with almost balanced loss and small-signal gain, working near an EPD, make an oscillator whose oscillation frequency is very sensitive to perturbations. The nonlinear behavior of the active component is essential for the three important features observed by simulations and

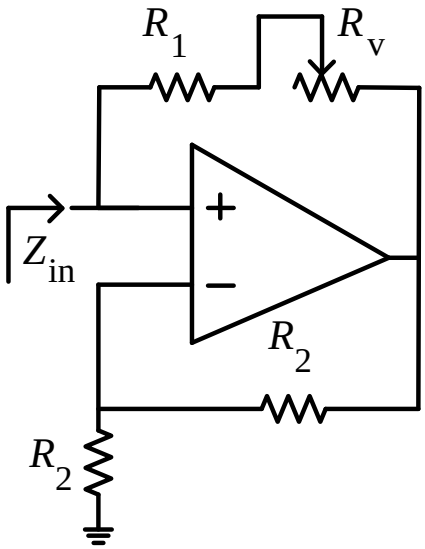

Figure 2.9: Negative resistance converter circuit implementation by using an opamp.

experimentally: (i) the oscillation frequency is very sensitive to perturbations, and both positive and negative perturbations of a capacitor are measured leading to very high sensitivity based on shifted oscillation frequency that approximately follows the square-root law, proper of EPD systems; (ii) the measured spectrum has very low phase noise allowing clean measurements of the shifted oscillation frequencies. (iii) It is not necessary to have a perfect gain/loss balance, i.e., we have shown that slightly broken gain/loss balance leads to the same results as in the case of a perfectly balanced gain and loss.

Note that none of the features above are available in current PT-symmetry circuits in the literature [3, 6]: Indeed, only one sign of the perturbation is measurable with the PT-symmetry circuits published so far, since the other sign leads to the circuit instability. Furthermore, to make a single sign perturbation measurement, in the literature, e.g., [6], the capacitor C_1 on the gain side has been tuned using a varactor to reach the value of the perturbed capacitor (C_2) on the reading side in order to rebuild the PT symmetry (but in a sensor operation it is not possible to know a priori the value that has to be measured); furthermore, to work at or very close to an EPD, using linear gain, the gain has to be set equal to the loss (balanced gain/loss condition).

The oscillation frequency shift follows the square root-like behavior predicted by the Puiseux series expansion, as expected for EPD-based systems. We show the performance of the oscillator-sensor scheme based on two configurations: wireless coupling with a mutual inductor, and wired coupling by a capacitor. The latter oscillator scheme has been fabricated and tested. We have analyzed how the nonlinearity in the gain element makes the circuit unstable and oscillate after reaching saturation. The oscillator's characteristics have been determined in terms of transient behavior and sensitivity to perturbations due to either capacitance or resistance change in the system. The experimental verification provided results in very good agreement with theoretical expectations. The measured high sensitivity of the oscillator sensor to perturbations can be used as a practical solution for enhancing sensitivity, also because the measured shifted frequencies are well visible with respect to underlying noise. The proposed EPD-based oscillator-sensor can be used in many automotive, medical, and industrial applications where detections of small variations of physical, chemical, or biological variations need to be detected.

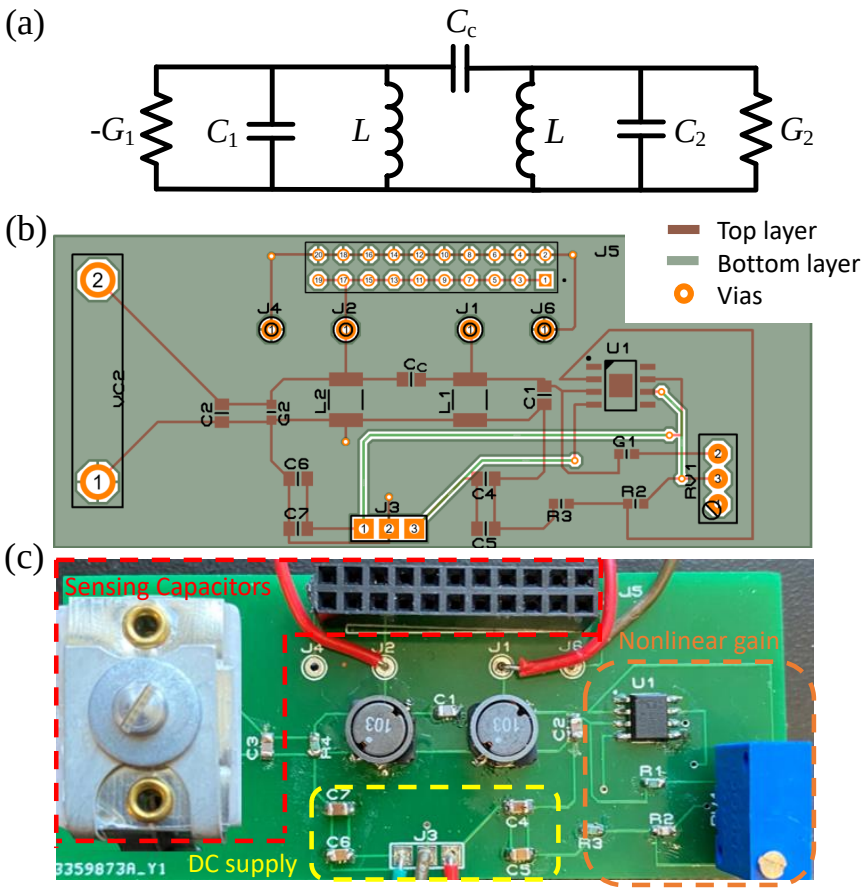

Figure 2.10: (a) Schematic of the two LC resonators coupled by $C_c = 1.5\,\text{nF}$ with inductor $L_1 = L_2 = L = 10\,\mu\text{H}$, the opamp U_1 (Analog Devices Inc., model ADA4817), the variable resistance RV_1 (Bourns Inc., model 3252W-1-501LF) and variable capacitance V_{C2} (Sprague-Goodman, model GMC40300), biasing capacitors $C_4 = C_6 = 0.1\,\mu\text{F}$ $C_5 = C_6 = 10\,\mu\text{F}$ as datasheet suggested. (b) PCB layout of the assembled circuit where the top layer traces are red, the ground plane and bottom traces are green, and the connecting vias are orange. In this design, Via J1 is a probe point for the capacitor voltage, whereas Vias J6 and J4 are test points connected to the ground plane and are used to connect the ground of the measurement equipment to the ground of the circuit. All the ground nodes are connected to the bottom green layer.

Acknowlegment

The text of Chapter 2 of this dissertation is a reprint of the material as it appears in Alireza Nikzamir, and Filippo Capolino. Highly Sensitive Coupled Oscillator Based on an

Exceptional Point of Degeneracy and Nonlinearity. Phys. Rev. Appl., 18, 054059, Nov 2022. The coauthor listed in this publication is Filippo Capolino. Filippo Capolino, who directed and supervised research which forms the basis for the dissertation. This material is based upon work supported by the USA National Science Foundation under Award NSF ECCS1711975.

2.7 Appendix A: Negative Resistance

Several different approaches provide negative nonlinear conductance needed for proposed circuits. In this subsection, we show the circuit in Fig. 2.9 that utilizes opamp to achieve negative impedance. The converter circuit converts the impedance as $Z_{in} = -R_1$ while we design the circuit to work at the EPD point by choosing $R_1 = 1/G_e$. In the experiment, we used $R_1 = 100\,\Omega$, and $R_2 = 2\,\mathrm{k}\Omega$ to achieve the EPD value. We tuned the negative resistance with resistor trimmer R_v to reach the EPD value $G_e = 9\,\mathrm{ms}$.

2.8 Appendix B: Implementation of the Nonlinear Coupled Oscillator

We investigate resonances and their degeneracy in the two LC resonators coupled by a capacitor as in Fig. 2.10(a), whereas Figs. 2.10(b) and (c) illustrate the PCB layout and assembled circuit. In the fabricated circuit, the sensing capacitance is shown in the red dashed box, the nonlinear gain is in the orange dashed box, and the DC supply is in the yellow dashed box. Inductors have values $L_1 = L_2 = 10\ \mu\mathrm{H}$, the loss value is set to $G_2 = 9\,\mathrm{mS}$ with a linear resistor, the capacitor on the gain side and the coupling capacitor are $C_1 = C_c = 1.5\,\mathrm{nF}$. The gain element is designed with an opamp (Analog Devices Inc.,

model ADA4817), where the desired value of gain is achieved with a variable resistor RV1. In the experiment, we setup the nonlinear gain to be a bit larger (around 0.1%) than the balanced gain by tuning the RV1 to make the system slightly unstable.To tune and find the exact value of the capacitance that leads to an EPD ($C_2 = C_e$), a variable capacitor (Sprague-Goodman, model GMC40300) and a series of pin headers, where extra capacitors could be connected in parallel to C_2, are provided. By adding small and known capacitors values on the load side, we tuned the capacitance C_2 to bring the circuit very close to the EPD and observe the EPD oscillation frequency $f = f_e$.

To show the square root-like behavior of the oscillator's frequency due to perturbations in Fig. 2.7 and 2.6, we perturbed the capacitor C_2 with pairs of extra 10 pF capacitors to make 20 pF steps, connected in parallel to C_2, using the pin headers shown in Fig. 2.10. After each perturbation, the oscillation frequency is measured with an oscilloscope and also with a spectrum analyzer (for comparison and verification purposes), as discussed in Section 2.8, and shown in Fig. 2.7 with green triangles. Moreover, for the perturbed circuit, considering $\Delta_{C_2} = 0.013$ applied to C_2 (any perturbed point can be chosen), we changed the variable resistor RV1 to study oscillation frequency variation for different unbalanced nonlinear gains. The goal was to show that the circuit using a bit unbalancednonlinear gain still has the same oscillation frequency. Indeed, by trimming the RV1, we verified the same oscillation frequency for roughly 1% unbalanced gain and loss, as shown in Fig. 2.8(c). Note that on the PCB, the ground plane (on the bottom layer) is designed to connect all the ground of the measurement equipments and DC supply to the circuit's ground.

Chapter 3

High-Sensitive Parity-Time Symmetric Oscillator in Coupled Transmission Lines with Nonlinear Gain

A scheme for generating oscillations based on an exceptional point of degeneracy (EPD) is proposed in two-coupled resonators made of two coupled transmission lines terminated on balanced gain and loss, exhibiting a double pole. The EPD is a point in the parameter space of the system at which two or more eigenmodes coalesce in both their eigenvalues (here, resonance frequencies) and eigenvectors. We show that a finite-length single transmission line terminated with gain and loss possesses no degeneracy point, whereas second-order EPDs are enabled in two finite-length coupled transmission lines (CTLs) terminated with balanced gain and loss. We demonstrate the conditions for EPDs to exist for three different termination configurations with balanced gain and loss, and show the eigenfrequency bifurcation at the EPD following the fractional power expansion series related to the Puiseux series. We study

the oscillatory regime of operation assuming the gain element is nonlinear, and the extreme sensitivity of the degenerate self-oscillation frequency to perturbations and how it compares with the sensitivity of the linear-gain case. Finally, we show that the sensitivity of the EPD-CTL resonator is much higher than the one of a single-TL resonator. The very sensitive EPD based oscillator can be used as sensors when very small variations in a system shall be detected.

3.1 Motivation and State of the Art

In this chapter, we present two interesting concepts: the double pole oscillator where the instability is related to a double pole instead of the usual one, and also an application of this concept as a very sensitive sensor. In particular, we study a system made of two distributed resonators, i.e., made of two coupled waveguides terminated on balanced gain and loss elements. It is important to distinguish between EPDs in systems made of coupled resonator (as in this chapter) where the eigenvalues are the natural frequencies, and EPDs in waveguides where the eigenvalues are the wavenumbers. This chapter deals with two coupled resonators made of two coupled waveguides of finite length, therefore the coalescing eigenvalues are two eigenfrequencies.

In the following, we first discuss the eigenfrequency of a "single pole" resonator made of finite-length transmission lines (TL) terminated on a gain and loss balance condition. Then, we investigate two CTLs terminated with balanced gain and loss following the PT-symmetry scheme and we show the existence of EPDs in such structures under different gain and loss configurations. Moreover, we characterize the performance of the CTL "double pole" oscillators operating at an EPD and show the transient behavior and their frequency response. We discuss the location of the double "poles" or "zeros" of the system and how they are sensitive to perturbations. Finally, we show the large resonance frequency shift due to sys-

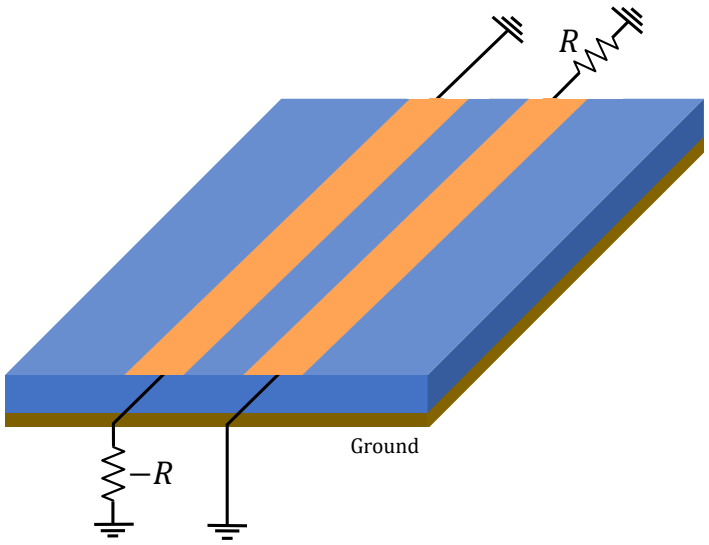

Figure 3.1: Two parallel coupled microstrip lines on a grounded dielectric substrate with terminations on a ground plane. This configuration exhibits the strong degeneracy condition called EPD.

tem's perturbations and discuss how such shift is predicted by the Puiseux fractional power expansion related to the Puiseux series. Such large frequency shift is also observed from time-domain simulation results obtained by Keysight ADS circuit simulator using nonlinear gain [7, 8] representing active semiconductor components based on CMOS transistors or operational amplifiers. The proposed circuit and method can be used in ultra high-sensitive sensing applications. The EPD-based circuit has a double pole, which makes the oscillation frequency highly sensitive to any perturbation to the system, like changes in permittivity, load resistance, etc. Indeed, the high sensitivity could be a drawback when implementing an oscillator using the proposed concept because the oscillation frequency would be highly sensitive to any imperfection, however, because of this sensitivity feature can also be used to our advantage, the proposed circuit is a good candidate for being used in sensing applications. The concepts explained here can be generalized to even higher operating frequencies.

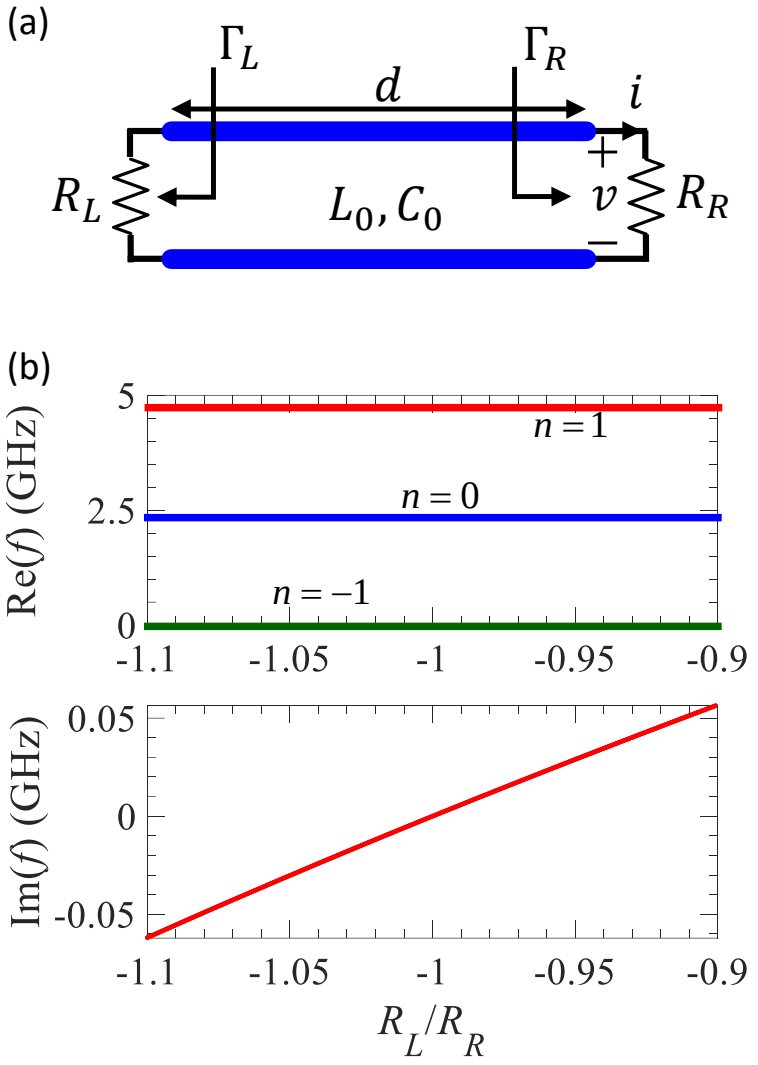

Figure 3.2: (a) Single finite-length TL terminated with R_L and R_R at its left and right ports, respectively. (b) Real and imaginary parts of the resonance frequency for different harmonics, calculated using Eq. (3.2). The complex resonance frequencies are calculated with the parameters of the structure set as $L_0 = 480\,\text{nH}$, $C_0 = 57.9\,\text{pF}$, $d = 40.1\,\text{mm}$, $R_R = 50\,\Omega$ and varying R_L. There is no EPD.

3.2 Single TL Oscillator

We consider a single finite-length TL terminated with a gain element (i.e., negative resistance) at one end and with a resistive load at the other end as shown in Fig. 3.2(a) where $Z_0 = \sqrt{L_0/C_0}$ is the characteristic impedance of the TL and d is its length. The resonance condition is

$$1 - \Gamma_L \Gamma_R e^{-j2\beta d} = 0, \tag{3.1}$$

where $\beta = \omega\sqrt{L_0 C_0}$ is the propagation constant, $\Gamma_L = (R_L - Z_0)/(R_L + Z_0)$ and $\Gamma_R = (R_R - Z_0)/(R_R + Z_0)$ are the reflection coefficients at the left and right ports, respectively (R_L is assumed negative), and we implicitly adopt the $\exp(j\omega t)$ time convention. The complex-valued resonance frequency of such a structure is derived from Eq. (3.1) as

$$f_n = \frac{1}{4\pi d\sqrt{L_0 C_0}} \left(\angle\Gamma_L + \angle\Gamma_R + 2n\pi - j \ln |\Gamma_L \Gamma_R| \right). \tag{3.2}$$

In general, for arbitrary values of R_L and R_R, the resonance frequency of such a structure is complex with a positive imaginary part when $|\Gamma_L \Gamma_R| < 1$, corresponding to decaying voltage and current; it has a negative imaginary part for $|\Gamma_L \Gamma_R| > 1$ corresponding to growing voltage and current in a lossless transmission line. In other words, for a nonzero imaginary part of the resonance frequency, an initial energy in the system will fully dissipate or will grow indefinitely. However, assuming $|\Gamma_L \Gamma_R| = 1$, the resonance frequency is purely real and such a condition corresponds to $R_L + R_R = 0$. Under this condition, we have a single TL where its left and right ports are terminated with balanced gain and loss loads, i.e., the two loads have the same magnitude with opposite signs (in other words, the resonator satisfies PT-symmetry). PT-symmetry is based on the combination of two operators: the

"P" parity transformation to make spatial reflections ($x \to -x$) and the "T" time-reversal transformation ($t \to -t$) , where x is the transverse coordinate and t is the time. In the phasor domain, the time-reversal operator "T" makes the imaginary unit $j \to -j$, hence loss goes into gain and vice versa. Therefore, since $\Gamma_L \Gamma_R = 1$, the structure has purely real resonance frequencies regardless of balanced gain and loss values. One may note that there exists no coalescence of the modes in such a single TL with balanced gain and loss; thus, we do not observe any exceptional point. Figure 3.2(b) shows the three lowest resonance frequencies of the single TL terminated with gain R_L and loss R_R for different values of R_L/R_R. The parameters are set as $L_0 = 480\,\text{nH}$, $C_0 = 57.9\,\text{pF}$, $d = 40.15\,\text{mm}$, and $R_R = 49.88\,\Omega$. This plot shows that the single TL has a purely real oscillation frequency when gain and loss are balanced. In summary, this system supports independent resonance modes and cannot achieve exceptional degeneracy of modes required for the occurrence of exceptional points.

3.3 Coupled TLs Oscillator

Two coupled, lossless, and identical TLs with finite length are shown in Fig. 3.3, terminated with resistive loads R_{l1} and R_{l2} at their left ports, and resistive loads R_{r1} and R_{r2} at their right ports. This is a model of the coupled microstrip circuit in Fig. 3.1, as well as many others. The distributed (per-unit-length) inductance and capacitance of the lines when they are isolated are L_0 and C_0, hence, the per unit length inductance and capacitance matrices of the coupled lines reads as [91, 92]

$$\underline{\mathbf{L}} = \begin{bmatrix} L_0 & L_m \\ L_m & L_0 \end{bmatrix}, \quad \underline{\mathbf{C}} = \begin{bmatrix} C_0 + C_m & -C_m \\ -C_m & C_0 + C_m \end{bmatrix}, \tag{3.3}$$

when the coupling between the lines is modeled by introducing a mutual per unit length inductance and capacitance L_m and C_m. Such a structure supports four different propagating

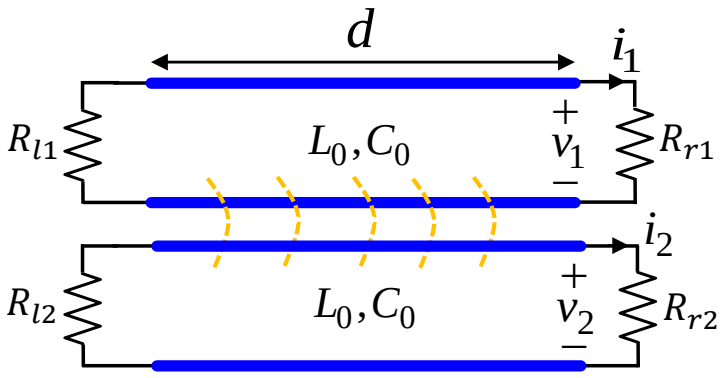

Figure 3.3: Two finite-length CTLs with terminations. The CTLs are both electrically and magnetically coupled. This configuration exhibits EPDs.

modes with propagation constants $\pm k_e$ and $\pm k_o$ where

$$k_e = \omega/u_e, \quad k_o = \omega/u_o, \tag{3.4}$$

and $u_e = 1/\sqrt{(L_0 + L_m)C_0}$ and $u_o = 1/\sqrt{(L_0 - L_m)(C_0 + 2C_m)}$ are the phase velocities of the even and odd modes.

Using the even and odd mode wavenumbers of the modes in the infinitely long CTL given in Eq. (3.4), we write the state vector $\mathbf{\Psi} = [\ V_1,\ \ V_2,\ \ I_1,\ \ I_2\ ]^{\mathrm{T}}$ that describes the voltages and currents at any point z as the summation of four modes

$$\begin{aligned} \mathbf{\Psi}(z) \ &= \ \mathbf{\Psi}_e^+ e^{-jk_e z} + \mathbf{\Psi}_e^- e^{jk_e z} \\ &\quad + \mathbf{\Psi}_o^+ e^{-jk_o z} + \mathbf{\Psi}_o^- e^{jk_o z}, \end{aligned} \tag{3.5}$$

where the corresponding eigenvectors are

$$
\begin{aligned}
\boldsymbol{\Psi}_e^+ &= V_e^+ \left[\begin{array}{cccc} 1, & 1, & Y_e, & Y_e \end{array} \right]^{\mathrm{T}}, \\
\boldsymbol{\Psi}_e^- &= V_e^- \left[\begin{array}{cccc} 1, & 1, & -Y_e, & -Y_e \end{array} \right]^{\mathrm{T}}, \\
\boldsymbol{\Psi}_o^+ &= V_o^+ \left[\begin{array}{cccc} 1, & -1, & Y_o, & -Y_o \end{array} \right]^{\mathrm{T}}, \\
\boldsymbol{\Psi}_o^- &= V_o^- \left[\begin{array}{cccc} 1, & -1, & -Y_o, & Y_o \end{array} \right]^{\mathrm{T}}.
\end{aligned} \tag{3.6}
$$

Here, $Y_e = u_e C_0$ and $Y_o = u_o(C_0 + 2C_m)$ represent the characteristic admittances of the even and odd modes, respectively, and the superscript T denotes the transpose operation. Using the state vector in Eq. (3.5), in order to derive the resonance frequencies for the two finite-length CTLs shown in Fig. 3.3, we enforce the boundary conditions at the four ports of the structure. We obtain a homogeneous system of four linear equations as

$$
\underline{\mathbf{A}}(\omega)\mathbf{V} = \mathbf{0}, \tag{3.7}
$$

where $\mathbf{V} = [V_e^+,\, V_e^-,\, V_o^+,\, V_o^-]^T$ represents the voltage amplitude vector, and

$$
\underline{\mathbf{A}}(\omega) = \left[\begin{array}{cccc}
1 + Y_e R_{l1} & 1 - Y_e R_{l1} & 1 + Y_o R_{l1} & 1 - Y_o R_{l1} \\
1 + Y_e R_{l2} & 1 - Y_e R_{l2} & -1 - Y_o R_{l2} & -1 + Y_o R_{l2} \\
(1 - Y_e R_{r1}) e^{-j\omega d/u_e} & (1 + Y_e R_{r1}) e^{j\omega d/u_e} & (1 - Y_o R_{r1}) e^{-j\omega d/u_o} & (1 + Y_o R_{r1}) e^{j\omega d/u_o} \\
(1 - Y_e R_{r2}) e^{-j\omega d/u_e} & (1 + Y_e R_{r2}) e^{j\omega d/u_e} & -(1 - Y_o R_{r2}) e^{-j\omega d/u_o} & -(1 + Y_o R_{r2}) e^{j\omega d/u_o}
\end{array} \right]. \tag{3.8}
$$

Free oscillation in such a structure occurs when there is a non-trivial solution of Eq. (3.7); therefore, oscillation frequencies are calculated as the roots of the vanishing determinant of

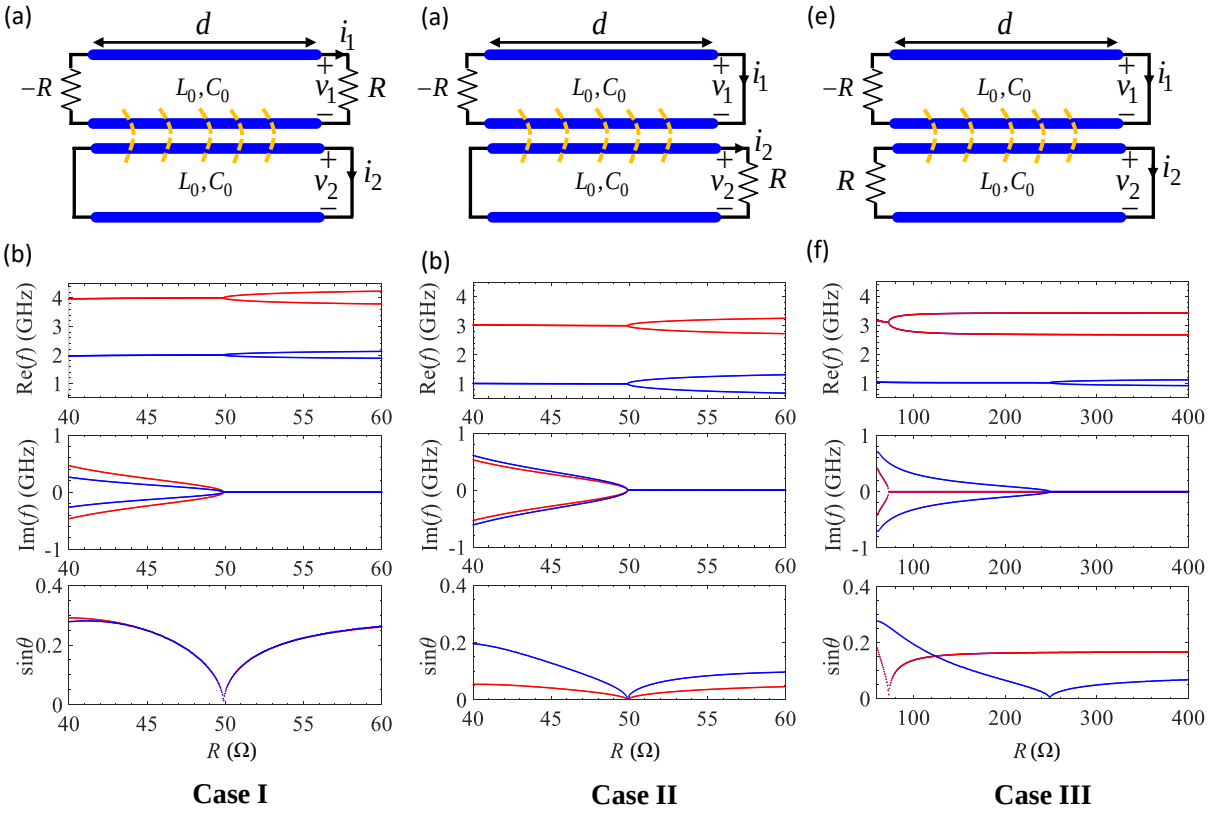

Figure 3.4: Three distinct cases of two coupled TLs termination and complex dispersion of the resonance frequencies. Blue lines show the two fundamental resonances and red lines represent the next two higher resonances. (a) Case I, showing the two coupled TLs where upper TL is terminated with linear gain $-R$ and load R; and lower TL is shorted at both ports. (b) Plots of real and imaginary parts of resonance frequencies varying R for Case I depicted in (a). (c) Case II, two coupled TLs where upper TL is terminated with linear gain $-R$ at the left port and it is shorted at the right port; and lower TL is shorted at the left port and it is terminated with load R at its right port. (d) Plots of real and imaginary parts of the resonance frequencies varying gain/load value R for Case II shown in (c). (e) Case III, two coupled TLs where upper TL is terminated with linear gain $-R$ at the left port and it is shorted at the right port; lower TL is terminated with load R at the left port and it is shorted at its right port. (f) Plots of real and imaginary parts of the resonance frequencies varying gain/load value R for Case III shown in (e).

$\underline{\mathbf{A}}$ as

$$\det(\underline{\mathbf{A}}(\omega)) = 0. \tag{3.9}$$

At each resonance frequency ω_i, with $i = 1, 2$, derived from Eq. (3.9) (we only show frequencies with positive real part here), we find the vector kernel $\mathbf{V}_i \quad i = 1, 2$ of the matrix $\underline{\mathbf{A}}(\omega_i)$ using the Gaussian elimination method. In other words, vectors $\mathbf{V}_1$ and $\mathbf{V}_2$ are the voltage amplitude vectors at the resonance frequencies ω_1 and ω_2, respectively. Various choices could be made to measure the coalescence of the voltage amplitude vectors at the resonance frequencies, and here the Hermitian angle between the voltage amplitude vectors $\mathbf{V}_1$ and $\mathbf{V}_2$ is adopted and defined as [90, 93, 2]

$$\cos\theta = \frac{|\langle \mathbf{V}_1, \mathbf{V}_2 \rangle|}{\|\mathbf{V}_1\| \, \|\mathbf{V}_2\|}.$$

The $\cos\theta$ is defined via the inner product $\langle \mathbf{V}_1, \mathbf{V}_2 \rangle = \mathbf{V}_1^{\dagger}\mathbf{V}_2$, where the dagger symbol $\dagger$ denotes the complex conjugate transpose operation, $||$ represents the absolute value and $\|\mathbf{V}\| = \sqrt{\langle \mathbf{V}, \mathbf{V} \rangle}$ represents the norm of a complex vector. According to this definition, when $\sin\theta = 0$ the voltage amplitude vectors $\mathbf{V}_1$ and $\mathbf{V}_2$ coalesce, corresponding also to the coalescence of the two resonance frequencies ω_1 and ω_2.

In this chapter, we are interested in CTLs terminated on symmetrically balanced gain and loss, hence, in the following we consider three different values of R, $-R$, and 0 as loads in such a structure. Note that, different arrangement of these three load values at four distinct ports of the structure results in twelve sets of boundary conditions. However, since the structure is symmetric with respect to its ports, these twelve arrangements of loads shrink to only three distinct ones; shown in Fig. 3.4(a), (c) and (e). In the following, we analyze each

particular structure separately and find the resonance frequency in two CTLs with balanced gain and loss varying the gain/loss value R in the absence of voltage generators. Moreover, we show the existence of EPD resonances, where resonance frequencies coalesce as well as the corresponding voltage vectors $\mathbf{V}_1$ and $\mathbf{V}_2$.

In the following examples, the CTL is made of two TLs with parameters $L_0 = 480\,\text{nH}$, $C_0 = 57.9\,\text{pF}$, $d = 40.15\,\text{mm}$, they are same as those we used for the single TL, but we now consider the coupling inductance $L_m = 367.4\,\text{nH}$ and capacitance $C_m = 102.7\,\text{pF}$ between the two TLs. As shown later on, a gain-resistance value of $R = 49.88\,\Omega$ will lead to an EPD of order two.

3.4 CTLs Oscillator Characteristics

We show some important features of an oscillator based on the CTLs of Case II, namely, the transient time-domain behavior, frequency spectrum, and sensitivity to perturbations. The oscillator is studied using a cubic model (nonlinear) of the active component providing gain. The CTL parameters used here are the same as those used in the previous section. A value $R = 49.88\,\Omega$ leads to an EPD of order two at a frequency of 1 GHz.

3.4.1 Transient Behavior and Frequency Spectrum

The time-domain (TD) response of the proposed CTLs oscillator as well as its frequency spectrum are depicted in Fig. 3.5 where the structure is terminated with balanced gain and loss satisfying the resonance condition. The TD simulation result is obtained using the TD method implemented in the circuit simulator of Keysight ADS. The gain element is realized using a cubic model with an $i - v$ curve described as

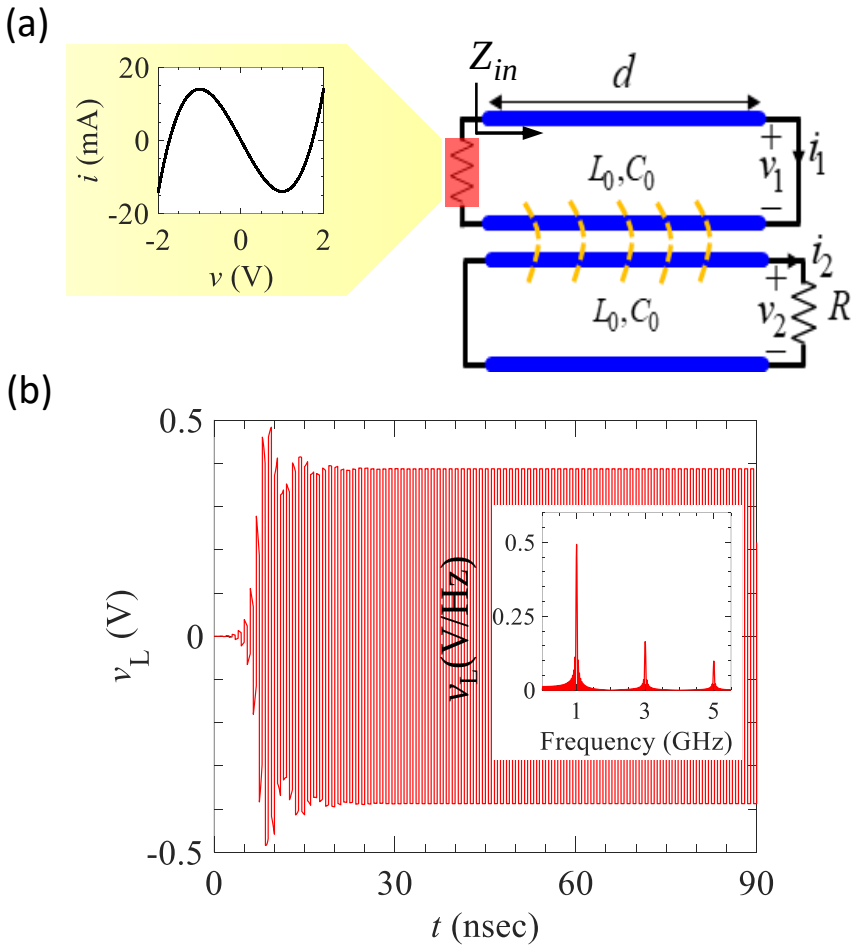

Figure 3.5: (a) The cubic model used as a realistic gain element where its $i - v$ curve is shown in the inset. Parameters of the cubic model are set as gain $g_m = 20.1\,\text{mS}$, $\alpha = 6.7\,\text{mS}$ and saturation voltage $V_b = 1\,\text{V}$. (b) Time-domain simulation result of the PT-symmetric oscillator shown in (a) and the frequency spectrum of the load voltage as the inset.

$$i = -g_m v + \alpha v^3, \tag{3.10}$$

shown in Fig. 3.5(a), where $-g_m$ is the negative slope of the $i-v$ curve in the active resistance region and α is the third-order nonlinearity constant that models the saturation characteristic of the device. To realize a constant DC voltage-biased active device, we choose the turning point V_b of the $i - v$ characteristics to be constant (when varying g_m) and equal to $V_b = 1\,\text{V}$ under different biasing levels. The value of the saturation characteristic α determines the steady-state oscillation amplitude and in particular, we set $\alpha = g_m/(3V_b^2)$. Moreover, for

simplicity we assume that the parasitic capacitance associated with the negative resistance device is negligible. In the shown TD results, the resistor is chosen to be $R = 49.88\Omega$, the g_m has been increased by 0.1% from its EPD gain-loss balanced value (in other words, the PT-symmetry is slightly perturbed), hence $g_m = 1.001/R$, in order to make the system unstable, hence to start and reach a stable oscillation. We use a voltage pulse at the right port of the first transmission line as the initial condition to start oscillations (alternatively, the simulation may have assumed the presence of noise to start oscillations). The frequency spectrum of the voltage at the load location is shown as an inset in Fig. 3.5(b), and it shows the fundamental frequency and harmonics of the oscillating voltage. The harmonics of the fundamental frequency are generated by the nonlinear nature of the gain element. An important observation is that the oscillation frequency mainly coincides with the fundamental EPD frequency of 1 GHz.

3.5 Double Pole Behavior and High Sensitivity to Perturbations

In this subsection, we study the system in the frequency (phasor) domain to offer a different perspective of the special degeneracy discussed in this chapter. The resonance frequencies of the system are here determined by using the impedance resonance method, and we show the relation between the EPD and the occurrence of double solutions (double zeros). With reference to the Case II structure in Fig. 3.6(a), the resonance condition imposed by the vanishing of the total series impedance implies that

$$Z_{in}(\omega) - R = \frac{\det\left[\underline{\mathbf{A}}(\omega)\right]}{P(\omega)} = 0, \tag{3.11}$$

where $P(\omega)$ is

$$
\begin{aligned}
P(\omega) = R\left(Y_0^2 + Y_e^2\right)\sin\left(\tfrac{\omega d}{u_e}\right)\sin\left(\tfrac{\omega d}{u_0}\right) \\
-2RY_eY_o\left(1+\cos\left(\tfrac{\omega d}{u_e}\right)\cos\left(\tfrac{\omega d}{u_0}\right)\right) \\
-2j\left(Y_e\cos\left(\tfrac{\omega d}{u_e}\right)\sin\left(\tfrac{\omega d}{u_0}\right) + Y_o\cos\left(\tfrac{\omega d}{u_0}\right)\sin\left(\tfrac{\omega d}{u_e}\right)\right),
\end{aligned}
\tag{3.12}
$$

and $-R$ is the gain element, assumed linear in this subsection. Here, $Z_{in}(\omega)$ is the input impedance of the CTLs seen from the upper left port when a load resistor R is connected to the bottom right port, shown in Fig. 3.5(a). The input impedance is obtained using the transfer matrix $\underline{\mathbf{T}} = \exp(-j\omega\underline{\mathbf{M}}d)$ of a CTL of length d, where is the waveguide system matrix $\underline{\mathbf{M}}$ is defined in Appendix A, and assuming the upper CTL is shorted at the right port, and the lower CTL is shorted at the left port. The series total impedance $Z_{in}(\omega) - R$ has the same ω-zeros as $\det[\underline{\mathbf{A}}(\omega)]$. Note that $\omega(R)$ and $-\omega^*(R)$ are both solutions of Eq. (3.11). In Fig. 3.6(a), we plot the zeros with $\mathrm{Re}(\omega) > 0$ of $Z_{in}(\omega) - R$ for varying R, in the complex frequency plane (there are other zeros, but we plot only those relative to the fundamental pair of frequencies). The trajectory of the resonance frequencies ω for the two modes with $\mathrm{Re}(\omega) > 0$ are plotted with increasing resistance R from $40\,\Omega$ to $60\,\Omega$. The double zero at ω_{EPD} occurs at $R_{EPD} = 49.88\,\Omega$, where the two curves meet. Therefore, when $R = R_{EPD} = 49.88\,\Omega$, for frequencies close to the EPD one can write $Z_{in}(\omega) - R \propto (\omega - \omega_{EPD})^2$ and the resonance condition becomes $(\omega - \omega_{EPD})^2 = 0$, which shows the double (degenerate) resonance. From this interesting property one can infer that if a perturbation is applied to the circuit so it is not anymore at its EPD, the variation of the resonance frequency follows a square root behavior, which is the key to high sensitivity. For resistances such that $R > R_{EPD}$, the two resonance frequencies are purely real, despite the presence of balanced losses and gain. Instead, for $R < R_{EPD}$, the two resonance frequencies are complex conjugate, as shown in Fig. 3.6.

3.5.1 Oscillation Frequency Highly Sensitive to Perturbations

It is known that in systems operating at EPDs some quantities (like eigenvalues and eigenvectors) are extremely sensitive to perturbation of system parameters. In particular, a small perturbation Δ_{X} of a system parameter X results in a tremendous change in the state of the system [94, 6, 78]. By applying a perturbation Δ_{X} as

$$\Delta_{\mathrm{X}} = \frac{X - X_{EPD}}{X_{EPD}}, \tag{3.13}$$

where X is the perturbed component's value, and X_{EPD} is the unperturbed value that provides the EPD condition, the matrix $\underline{\mathbf{A}}\left(\Delta_{\mathrm{X}}\right)$ is perturbed. In the CTLs structure with balanced gain and loss, the two degenerate resonance frequencies (they are the eigenvalues) change due to a small perturbation Δ_{X}, resulting in two distinct resonance frequencies, following the behavior predicted by the fractional power expansion series. The two perturbed angular eigenfrequencies $\omega_i\left(\Delta_{\mathrm{X}}\right)$, with $i = 1, 2$, are estimated by using the fractional power expansion series around a second-order EPD given by

$$\omega_i\left(\Delta_{\mathrm{X}}\right) \simeq \omega_{EPD} + \left(-1\right)^i \alpha_1 \sqrt{\Delta_{\mathrm{X}}} + \alpha_2 \Delta_{\mathrm{X}}. \tag{3.14}$$

Following the steps in Appendix A and [95, 89], we calculate the coefficients as

$$\alpha_1 = \sqrt{-\frac{\frac{\partial H(\Delta_{\mathrm{X}},\omega)}{\partial \Delta_{\mathrm{X}}}}{\frac{1}{2!}\frac{\partial^2 H(\Delta_{\mathrm{X}},\omega)}{\partial \omega^2}}}, \tag{3.15}$$

$$\alpha_2 = -\frac{\alpha_1^3 \frac{1}{3!}\frac{\partial^3 H(\Delta_{\mathrm{X}},\omega)}{\partial \omega^3} + \alpha_1 \frac{\partial^2 H(\Delta_{\mathrm{X}},\omega)}{\partial \omega \partial \Delta_{\mathrm{X}}}}{\alpha_1 \frac{\partial^2 H(\Delta_{\mathrm{X}},\omega)}{\partial \omega^2}}, \tag{3.16}$$

where $H\left(\Delta_{\mathrm{X}}, \omega\right) = \det\left[\underline{\mathbf{A}}\left(\Delta_{\mathrm{X}}, \omega\right)\right]$ and its derivatives are evaluated at the EPD, i.e., at

$\Delta_{\mathrm{X}} = 0$ and $\omega = \omega_{EPD}$. This fractional power expansion provides a good approximation of the perturbed eigenfrequencies as demonstrated in the following.

We consider the CTLs in Case II shown in Fig. 3.4(c), with an EPD resonance when $R = R_{EPD}$, and we assume the same parameter values given in Sec. 3.3. We apply a small perturbation in both linear gain and resistance as $R = R_{EPD}\,(1 + \Delta_{\mathrm{R}})$. The calculated coefficient $\alpha_1 = 5.56 \times 10^9$ rad/s is purely real and Fig. 3.6(b) illustrates the separation between the two resonance frequencies varying the perturbation Δ_{R}.

The result in Fig. 3.6(b) demonstrates that for a small perturbation $-0.1 < \Delta_{\mathrm{R}} < 0.1$ of both the positive and negative resistive terminations, the resonance frequency f is significantly changed for positive resistive changes $\Delta_{\mathrm{R}} > 0$, where the real part of the resonance frequency follows the square root behavior. The square root behavior shows the exceptional sensitivity of the proposed system operating at an EPD, which can be used to conceive a new class of very sensitive sensors. For positive values Δ_{R}, the structure shows two real resonance frequencies. Fig. 3.6(b) exhibits also the structure's sensitivity due to the fractional power expansion series limited to its first order, displayed by a dashed line. Moreover, green dots show results using the nonlinear cubic model for gain: the frequencies are calculated from the Fourier transform of the time-domain circuit simulator implemented in Keysight ADS after reaching saturation, using the nonlinear cubic model for the gain in Eq. (3.10) where $g_m = 1.001/R$, i.e., has been increased by 0.1% from its loss balanced value. We use a voltage pulse at the right port of the first transmission line as the initial condition to start oscillations. For both resistance-gain perturbations with $R > R_{EPD}$, the circuit oscillates at two distinct resonance frequencies (green dots). This latter result demonstrates the ultra sensitive frequency of oscillation (green dots) of the oscillator when used in a sensor scheme. The fast Fourier transform is calculated from 500 MHz to 1.5 GHz using 10^6 signal samples in the time window from 200 ns to 1 μs.

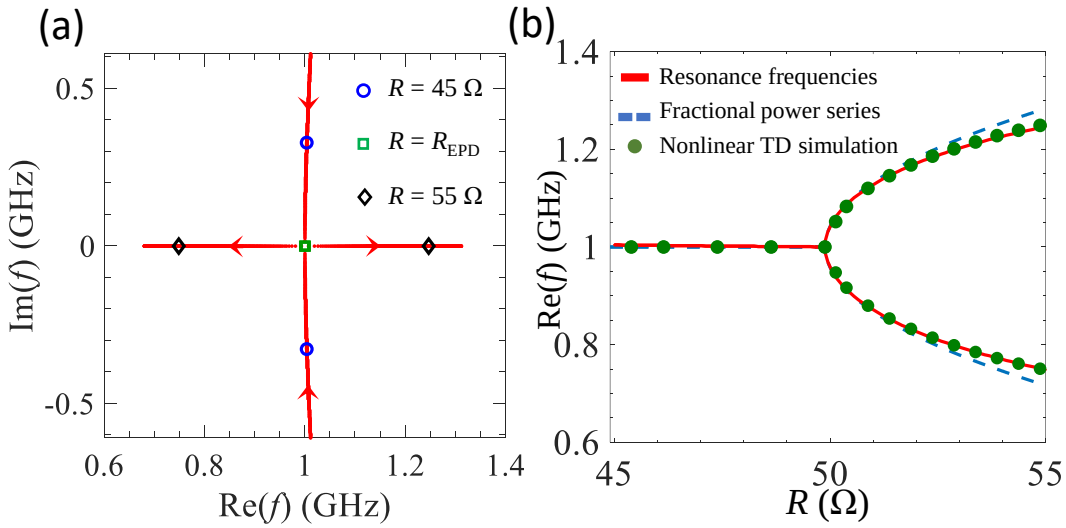

Figure 3.6: (a) Root locus of two frequency zeros of $Z_{in}(2\pi f) - R$ showing the fundamental pairs of resonance frequencies of the CTLs in Case II, varying both the linear negative and positive values of R. (b) Resonance frequencies obtained from solving Eq. (3.9) (red line), and from the first-order fractional power expansion series expansion (dashed blue line), when varying both the linear gain and resistance R. Results accounting for the nonlinear cubic model of the gain elements Eq. (3.10) using the time-domain circuit simulator by ADS Keysight are shown by green dots, where $g_m = 1.001/R$ has been increased by 0.1% from its loss balanced value.

3.5.2 Sensitivity to Variations of the Load Resistance R Only

This section discusses how sensitive the circuit is to the perturbation of only the passive resistance (i.e., the one on the lossy side). This perturbation could be the one happening in a sensor based on resistivity changes. By breaking PT-symmetry and perturbing just the lossy side resistance as $R = R_{EPD}(1+\Delta_{\mathrm{R}})$ from its EPD value R_{EPD}, while the (linear) gain component is kept fixed to $-R_{EPD}$, the circuit shows a large shift of the resonance frequencies for positive resistive changes $\Delta_{\mathrm{R}} > 0$, where the real part of the resonance frequency follows the square root behavior as shown in Fig. 3.7(a). This perturbation brings the system away from the PT–symmetry condition and the system becomes unstable demonstrated by the fact that shifted frequencies have an imaginary part with a negative sign, for either sign of Δ_{R} as shown in Fig. 3.7(b). The solid-red line shows the resonance frequency evaluation by solving Eq. (3.9), the dashed-blue line represents the two eigenfrequencies estimated

by the fractional power expansion series truncated to its second order. The coefficients in Eqs. (3.15) and (3.16) are calculated as $\alpha_1 = 3.95 \times 10^9 + j3.91 \times 10^8$ rad/s and $\alpha_2 = -9.40 \times 10^7 - j2.61 \times 10^9$ rad/s, they are complex, which means that for all values of small loss resistance changes, the two eigenfrequencies are complex valued and the system is unstable, for either $\Delta_{\mathrm{R}} < 0$,(i.e., $R < R_{EPD}$) or $\Delta_{\mathrm{R}} > 0$ (i.e., $R > R_{EPD}$). For $\Delta_{\mathrm{R}} > 0$, the bifurcation of $\mathrm{Re}(\omega)$ is more significant than for $\Delta_{\mathrm{R}} < 0$, thus, the circuit is more sensitive to positive changes of Δ_{R}, corresponding to a larger value of $\mathrm{Re}(\omega)$ than $\mathrm{Im}(\omega)$. To have approximately the same frequency shift for either positive or negative relative perturbations Δ_{R}, one should design an EPD where the real and imaginary parts of α_1 are approximately equal. Moreover, the green dots show the frequencies calculated when using the nonlinear gain in Eq. (3.10), where g_m has been increased by 0.1% than the EPD value, hence $g_m = 1.001/R_{EPD}$. The result is obtained by applying the Fourier transform to the TD signal after reaching saturation evaluated using the circuit simulator implemented in Keysight ADS, using the same initial condition as in the last section. For different loss resistance perturbations, the circuit oscillates at two resonance frequencies, shown in green dots. This latter result demonstrates the high sensitivity of the frequencies of oscillation (green dots) when used in a sensor scheme. This configuration where the loss resistance is changing is useful for sensors like a moister detector, strain gauge, thermistor, etc. The frequency domain spectrum is calculated from 500 MHz to 1.5 GHz using 10^6 signal samples in the time window from 200 ns to 1 μs.

3.5.3 Sensitivity to the Per-Unit-Length Capacitance C_0

The oscillator scheme described in this chapter can be used as a distributed capacitance sensor, i.e., for sensing perturbations of the per-unit-length capacitance C_0 of both the CTLs as shown in Fig. 3.8. In this setup, the system is very sensitive to a change in permittivity in the materials (above or below) surrounding the CTLs. Assuming that the perturbation

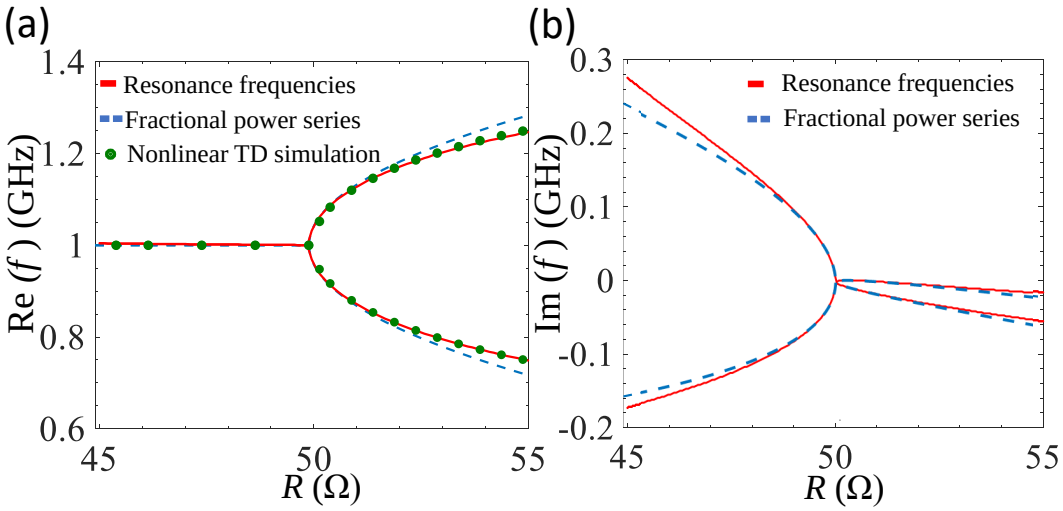

Figure 3.7: (a) Real part and (b) imaginary part of the eigenfrequencies, when varying only the load resistance and the gain is $-R_{EPD}$. The red-solid line represents the resonance frequencies obtained by solving Eq. (3.9), using linear model of the gain. The dashed-blue line represents the eigenfrequencies estimated using the fractional power expansion series up to the second order, using linear model of the gain. The green dots represent the frequencies obtained by applying the Fourier transform to the TD results using the nonlinear cubic model of the gain elements Eq. (3.10) where $g_m = 1.001/R$.

Δ_{C_0} is applied to the per unit length self capacitance of the CTLs C_0, the perturbed C is expressed as $C = (1 + \Delta_{C_0})C_0$. In this scheme, the oscillation frequency is sensitive to negative changes of the per-unit-length capacitance $\Delta_{C_0} < 0$ where the real part of the resonance frequency follows the square root behavior. The active gain element is assumed to be the nonlinear cubic model in Eq. (3.10), where $g_m = 1.001/R_{EPD}$ has been increased by 0.1% from its EPD gain-loss balanced value $1/R_{EPD}$. Using a voltage pulse at the right port of the first transmission line as the initial condition the circuit starts to oscillate.

Fig. 3.8(a) shows the TD simulation result using Keysight ADS by using the cubic model for the gain in Eq. (3.10) of the perturbed circuit with $\Delta_{C_0} = -5\%$ (green color) and $\Delta_{C_0} = -1\%$ (blue color). By perturbing C_0, the circuit oscillates at two resonance frequencies as seen in the frequency spectrum of the load voltage in the inset, calculated from 500 MHz to 1.5 GHz using 10^6 signal samples in the time window of 200 ns to 1 μs. The two oscillation frequencies shift further away from each other when more perturbation is applied to C_0. The

difference between the two frequencies Δf is shown in Fig. 3.8(b) for negative values of Δ_{C_0}, obtained from TD simulations using nonlinear gain, and the square root-like behavior shows the high sensitivity to perturbations of C_0. For instance, when C_0 is perturbed by $-1\,\%$ from its EPD value, the CTL shows the two real resonance frequencies at 959 MHz and 1.04 GHz, associated to a $\Delta f/f_{EPD} = 8.3\,\%$. Also, when C_0 is perturbed by $-5\,\%$ from its EPD value, the CTL shows the two real resonance frequencies at 906 MHz and 1.09 GHz, associated to a $\Delta f/f_{EPD} = 19\,\%$. In conclusion, when there is a small perturbation in the per-unit-length capacitance, the oscillation frequencies shift dramatically so the proposed circuit has a promising use as a scheme for high-sensitive sensors. To better understand how the EPD-based sensor improves the sensitivity compared to a conventional resonator, we compare its sensitivity to the one of single TL terminated with a short circuit on both sides without adding gain or loss. The lowest resonance condition for such single TL is $\beta d = \pi$, which corresponds to the resonance frequency $f = 1/\left(2d\sqrt{L_0C_0}\right)$. By perturbing the per-unit length capacitance of the TL, C_0, the resonance frequency is shifted by $\Delta f = -\Delta_{C_0}/(4d\sqrt{L_0C_0})$. In Fig. 3.8(b), we show a comparison between the shift of resonance frequency due to perturbations in C_0 for two cases: (i) the EPD-CTL (solid red line) and (ii) the single TL (solid black line). This figure shows that the sensitivity of the EPD-CTL structure with nonlinear gain (solid red line) is much higher (it follows a square–root-like behavior) than the one of the conventional TL without EPD (solid black line).

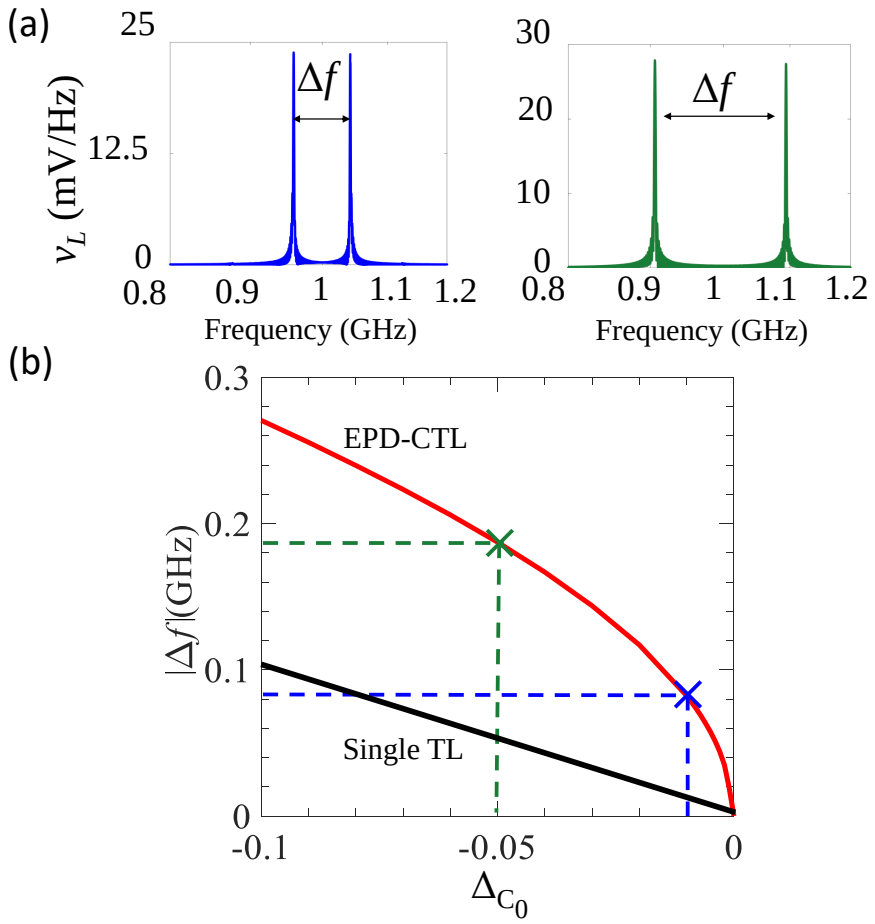

Figure 3.8: (a) Frequency spectrum of the load voltage obtained from the Fourier transform of the time-domain simulation result using the nonlinear cubic model of the gain elements Eq. (3.10) where $g_m = 1.001/R_{EP.D}$. We perturb the per-unit-length capacitance as $\Delta_{C_0} = -1\,\%$ (blue line) and $\Delta_{C_0} = -5\,\%$ (green line). The system shows two oscillation frequencies and the separation depends on the perturbation. (b) Separation between the two oscillation frequencies varying Δ_{C_0} based on the EPD-CTL structure with nonlinear gain (red line). For comparison we also show the shift of the eigenfrequency of the resonator made of a single TL varying Δ_{C_0}(black line). The EPD-CTL shows much higher sensitiviy to a perturbation.

3.6 Conclusions

We have shown the existence of a second-order EPD in two coupled resonators made of a pair of finite-length CTLs, terminated with balanced gain and loss satisfying different configurations of PT-symmetry. The degenerate eigenfrequencies are highly sensitive to

perturbations of the system. We have also provided an alternative view of second-order EPD of the system observing the occurrence of a "double pole" and that the CTL oscillator oscillates at that double-pole frequency also when gain is nonlinear. We have analyzed three different scenarios to perturb the system. First, by perturbing both gain and loss together (PT-symmetry is slightly broken by putting gain 0.1% higher than the balanced loss value, to start oscillations), then by perturbing the loss resistance while the gain is kept constant and equal to the EPD value, and finally by perturbing the per-unit-length capacitance of both the TLs: all the three cases lead to large values of resonance frequency shifts and consequently to shifts of the self-oscillation frequencies. . We have shown that the circuit's eigenfrequencies are exceedingly sensitive to a perturbation of the circuit components, and this may have significant implications in sensing technology and RF sensors. Note that however the system needs to work at, or very close to, the EPD to obtain the square root sensitivity. While any imperfection in manufacturing leads to a shift from the EPD, a fine-tuning process is required to configure the system at the EPD to be ready to exhibit the square root sensitivity to perturbations. Finally, we have demonstrated that the sensitivity of the EPD-based CTL oscillator is much higher than the one of a conventional resonator made of a single TL not working at an EPD.

Acknowlegment

The text of Chapter 3 of this dissertation is a reprint of the material as it appears in Hamidreza Kazemi, Alireza Nikzamir, Tarek Mealy, Ahmed Abdelshafy, and Filippo Capolino. High-Sensitive Parity-Time Symmetric Oscillator in Coupled Transmission Lines with Nonlinear Gain. IEEE Journal of Microwaves, vol. 2, no. 3, pp. 389-400, July 2022. The coauthors listed in this publication are Hamidreza Kazemi, Tarek Mealy, Ahmed Abdelshafy, and Filippo Capolino. Filippo Capolino directed and supervised research which

forms the basis for the dissertation. This work was supported in part by the National Science Foundation under Award NSF ECCS-1711975 and in part by Northrop Grumman.

3.7 Appendix A: Using Puiseux Series To Calculate The Sensitivity To System's Perturbations

In this Appendix, the z-axis origin is assumed to be at the center of the CTL for convenience, and by applying the boundary conditions at $z = -d/2$ and $z = d/2$ shown in Fig. 3.9, the $\underline{\mathbf{A}}$ matrix reads

$$\underline{\mathbf{A}}(\omega) = \begin{bmatrix} (1+Y_eR_{l1})\,e^{+j\omega d/(2u_e)} & (1-Y_eR_{l1})\,e^{-j\omega d/(2u_e)} & (1+Y_oR_{l1})\,e^{j\omega d/(2u_o)} & (1-Y_oR_{l1})\,e^{-j\omega d/(2u_o)} \\ (1+Y_eR_{l2})\,e^{+j\omega d/(2u_e)} & (1-Y_eR_{l2})\,e^{-j\omega d/(2u_e)} & (-1-Y_oR_{l2})\,e^{j\omega d/(2u_o)} & (-1+Y_oR_{l2})\,e^{-j\omega d/(2u_o)} \\ (1-Y_eR_{r1})\,e^{-j\omega d/(2u_e)} & (1+Y_eR_{r1})\,e^{j\omega d/(2u_e)} & (1-Y_oR_{r1})\,e^{-j\omega d/(2u_o)} & (1+Y_oR_{r1})\,e^{j\omega d/(2u_o)} \\ (1-Y_eR_{r2})\,e^{-j\omega d/(2u_e)} & (1+Y_eR_{r2})\,e^{j\omega d/(2u_e)} & -(1-Y_oR_{r2})\,e^{-j\omega d/(2u_o)} & -(1+Y_oR_{r2})\,e^{j\omega d/(2u_o)} \end{bmatrix}. \tag{3.17}$$

The goal is to provide an analytical expression for the perturbed eigenfrequencies of the system when a small perturbation Δ_{X} is applied to one of its parameters or components without starting from an eigenvalue problem. The eigenfrequencies are given by solving $H(\Delta_{\mathrm{X}}, \omega) \triangleq \det[\underline{\mathbf{A}}(\Delta_{\mathrm{X}}, \omega)] = 0$ for ω. Close to the EPD angular frequency ω_{EPD}, the matrix $\underline{\mathbf{A}}(\Delta_{\mathrm{X}}, \omega)$ is expanded as

$$\underline{\mathbf{A}}(\Delta_{\mathrm{X}}, \omega) = \underline{\mathbf{A}}(\Delta_{\mathrm{X}}, \omega_{EPD}) + \frac{d\underline{\mathbf{A}}(\Delta_{\mathrm{X}}, \omega)}{d\omega}|_{\omega_{EPD}}(\omega - \omega_{EPD}) + \underline{\mathbf{O}}, \tag{3.18}$$

where $\underline{\mathbf{O}}(\Delta_{\mathrm{X}}, \omega)$ defines higher order terms, i.e., terms that vanish at least as $(\omega - \omega_{EPD})^2$,

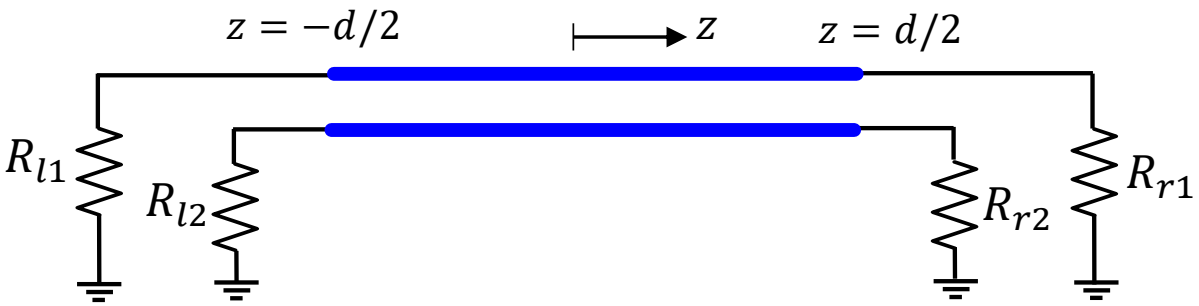

Figure 3.9: Shifting the z-axis to the middle of the transmission line to find the new $\underline{\mathbf{A}}$.

where ω_{EPD} is the solution of $\det\left[\underline{\mathbf{A}}\left(\Delta_{\mathrm{X}}=0,\omega\right)\right]=0$. In order to apply the Puiseux series to find the perturbation of the eigenfrequencies for a small Δ_{X}, we rewrite the system equation $\underline{\mathbf{A}}\left(\Delta_{\mathrm{X}},\omega\right)\mathbf{V}=0$ in an eigenvalue problem form, e.g., as $\left(\underline{\mathbf{B}}-\omega\underline{\mathbf{I}}\right)\mathbf{V}=0$, assuming that $\omega\approx\omega_{EPD}$, where $\underline{\mathbf{I}}$ is the 4×4 identity matrix. This can be achieved by left multiplying Eq. (3.18) by $\underline{\mathbf{D}}\left(\Delta_{\mathrm{X}}\right)\equiv-\left(\frac{d\underline{\mathbf{A}}(\Delta_{\mathrm{X}},\omega)}{d\omega}|_{\omega_{EPD}}\right)^{-1}$. It is convenient to define

$$\underline{\mathbf{B}}\left(\Delta_{\mathrm{X}}\right)=\omega_{EPD}\underline{\mathbf{I}}+\underline{\mathbf{D}}\left(\Delta_{\mathrm{X}}\right)\underline{\mathbf{A}}\left(\Delta_{\mathrm{X}},\omega_{\mathrm{EPD}}\right), \tag{3.19}$$

where $\underline{\boldsymbol{B}}$ depends only on the perturbation Δ_{X}, and not on ω. This procedure leads to

$$\underline{\mathbf{B}}\left(\Delta_{\mathrm{X}}\right)-\omega\underline{\mathbf{I}}=\underline{\mathbf{D}}\left(\Delta_{\mathrm{X}}\right)\underline{\mathbf{A}}\left(\Delta_{\mathrm{X}},\omega\right)+\underline{\mathbf{O}}_{B}, \tag{3.20}$$

where $\underline{\mathbf{O}}_{B}=-\underline{\mathbf{DO}}$ is a term that vanishes at least as $\left(\omega-\omega_{EPD}\right)^{2}$. Since from Eq. (3.7) we know that at each eigenfrequency one has $\underline{\mathbf{A}}\left(\Delta_{\mathrm{X}},\omega_{i}\right)\mathbf{V}=0$, at those eigenfrequencies we have

$$\left(\underline{\mathbf{B}}-\omega_{i}\underline{\mathbf{I}}\right)\mathbf{V}=\underline{\mathbf{DA}}\mathbf{V}+\underline{\mathbf{O}}_{B}\mathbf{V}=\underline{\mathbf{O}}_{B}\mathbf{V}\approx0. \tag{3.21}$$

Therefore, the terms of this equation tend to zero as $\omega_i \to \omega_{EPD}$, which means that the angular frequencies that satisfy $(\underline{\mathbf{B}} - \omega\underline{\mathbf{I}})\,\mathbf{V} = 0$ and $\underline{\mathbf{A}}\mathbf{V} = 0$ are approximately the same, for any Δ_{X}, when they are very close to ω_{EPD}. Furthermore, when $\Delta_{\mathrm{X}} = 0$, the eigenvalue of $(\underline{\mathbf{B}} - \omega\underline{\mathbf{I}})\,\mathbf{V} = 0$, coincides with the ω-solution of $\underline{\mathbf{A}}\mathbf{V} = 0$. A more precise procedure should show also the higher order terms when discussing the approximation. We now use the Puiseux series expansion [89] to estimate the perturbed eigenvalues of $(\underline{\mathbf{B}} - \omega\underline{\mathbf{I}})\,\mathbf{V} = 0$ when a perturbation Δ_{X} is applied to the system. The first-order Puiseux series expansion yields

$$\omega_i\left(\Delta_{\mathrm{X}}\right) \simeq \omega_{EPD} + (-1)^i\,\alpha_1\sqrt{\Delta_{\mathrm{X}}}, \tag{3.22}$$

which describes the perturbation of the two eigenvalues ($i = 1, 2$) when a small relative perturbation Δ_{X} of a system's parameter near its EPD value $\Delta_{\mathrm{X}} = 0$ occurs. The series coefficients are calculated using the explicit recursive formulas given in [89] pertaining to the eigenvalue problem $(\underline{\mathbf{B}} - \omega\underline{\mathbf{I}})\,\mathbf{V} = 0$. Thus, to find α_1 we have to find the derivatives of $H_B\left(\Delta_{\mathrm{X}}, \omega\right) \triangleq \det\left(\underline{\mathbf{B}} - \omega\underline{\mathbf{I}}\right)$ with respect to Δ_{X} and ω at the EPD point as

$$\alpha_1 = \sqrt{-\frac{\frac{dH_B(\Delta_{\mathrm{X}},\omega)}{d\Delta_{\mathrm{X}}}}{\frac{1}{2!}\frac{d^2H_B(\Delta_{\mathrm{X}},\omega)}{d\omega^2}}\Big|_{\omega_{EPD},\,X_{EPD}}}. \tag{3.23}$$

Using Eq. (3.20), the relation between H_B and $H\left(\Delta_{\mathrm{X}}, \omega\right) \triangleq \det\underline{\mathbf{A}}\left(\Delta_{\mathrm{X}}, \omega\right)$ is found to be

$$H_B(\Delta_{\mathrm{X}}, \omega) \approx \det\underline{\mathbf{D}}\left(\Delta_{\mathrm{X}}\right) H\left(\Delta_{\mathrm{X}}, \omega\right). \tag{3.24}$$

Using this relation between H_B and H, the numerator in the square root of α_1 is rewritten as

$$\frac{dH_B}{d\Delta_{\mathrm{X}}} \approx \det\underline{\mathbf{D}}\frac{dH}{d\Delta_{\mathrm{X}}} + H\frac{d\det\underline{\mathbf{D}}}{d\Delta_{\mathrm{X}}}. \tag{3.25}$$

Note that α_1 has to be calculated at the EPD point and $H\left(\Delta_{\mathrm{X}},\omega\right)|_{\omega_{EPD},\,X_{EPD}} = \det\underline{\mathbf{A}}\left(\Delta_{\mathrm{X}},\omega\right)|_{\omega_{EPD},\,X_{EPD}} = 0$, so we simplify the above relation as

$$\frac{dH_B}{d\Delta_{\mathrm{X}}}|_{\omega_{EPD},\,X_{EPD}} \approx \det\underline{\mathbf{D}}|_{X_{EPD}} \frac{dH}{d\Delta_{\mathrm{X}}}|_{\omega_{EPD},\,X_{EPD}}. \tag{3.26}$$

Analogously, the denominator in the square root of α_1 at the EPD point is found to be

$$\frac{d^2H_B}{d\omega^2}|_{\omega_{EPD},\,X_{EPD}} \approx \det\underline{\mathbf{D}}|_{X_{EPD}} \frac{d^2H}{d\omega^2}|_{\omega_{EPD},\,X_{EPD}}. \tag{3.27}$$

Therefore, we calculate the $d^2H_B/d\omega^2$ and $dH_B/d\Delta_{\mathrm{X}}$ at the EPD point (ω_{EPD}, X_{EPD}), leading to the approximation for α_1 as

$$\alpha_1 = \sqrt{-\frac{\frac{dH_B}{d\Delta_{\mathrm{X}}}|_{\omega_{EPD},\,X_{EPD}}}{\frac{1}{2!}\frac{d^2H_B}{d\omega^2}|_{\omega_{EPD},\,X_{EPD}}}} \approx \sqrt{-\frac{\frac{dH}{d\Delta_{\mathrm{X}}}|_{\omega_{EPD},\,X_{EPD}}}{\frac{1}{2!}\frac{d^2H}{d\omega^2}|_{\omega_{EPD},\,X_{EPD}}}}. \tag{3.28}$$

We conclude that α_1 found for the Puiseux series expansion of the ω-eigenvalues of $\underline{\mathbf{B}}\left(\Delta_{\mathrm{X}}\right)$ is approximately the same as the coefficient used in the fractional power series expansion of the ω solutions of $\det\underline{\mathbf{A}}\left(\Delta_{\mathrm{X}},\omega\right) = 0$, demonstrating Eq. (3.15).

Chapter 4

Exceptional Points in Gyrator-Based Circuit and Nonlinear High-Sensitivity Oscillator

We present a scheme for high-sensitive oscillators based on an exceptional point of degeneracy (EPD) in a circuit made of two LC resonators coupled by a gyrator. The frequency of oscillation is very sensitive to perturbations of a circuit element, like a capacitor. We show conditions that lead to an EPD, assuming one of the two resonators is composed of an inductor and a capacitor of negative values. The EPD occurrence and sensitivity to perturbations in the linear case are demonstrated by showing that the eigenfrequency bifurcation around the EPD is described by the relevant Puiseux (fractional power) series expansion. We also investigate the effect of small losses in the system and show that they lead to instability. We fabricate the circuit, and exploit its instability and nonlinearity, observing experimentally stable self-oscillations under the saturated regime. We measure the circuit's sensitivity to a small capacitor perturbation. A shift in frequency of oscillation after saturation is well detectable with very distinct spectral peaks with 10 Hz linewidth, clean until -70 dB from

the peak value. The sensitivity is (i) higher than the one of a comparable simple LC linear resonator, (ii) comparable or better than other published EPD circuits, and (iii) applicable to both negative and positive values of the capacitance perturbation, contrary to what happens in PT-symmetric circuits. The proposed scheme can pave the way for a new generation of high-sensitive sensors to measure slight variations in physical, chemical or biological quantities.

4.1 Motivation and State of the Art

Recent advancements associated with the concept of exceptional points of degeneracy (EPDs) have attracted a surge of interest due to their potential for various applications. An EPD is a point in the parameter space of a system for which the eigenvalues and the eigenvectors of the relevant matrix coalesce [31, 32, 33, 34, 35, 62, 84, 65, 63]. The EPD concept has been investigated in temporally periodic electric and mechanical systems [78, 96], in coupled-resonator systems with loss and/or gain under parity-time symmetry [40, 84, 3, 70]. The EPD concept using saturable nonlinear gain has been exploited in conceiving oscillators based on two coupled transmission line [70, 97] and two resonator circuits [98]. Since the characterizing feature of an exceptional point is the full degeneracy of at least two eigenmodes, as mentioned in [66], the significance of referring to it as "degeneracy" is here emphasized, hence including the D in EPD. In essence, an EPD is obtained when the system matrix associated to a linear system is similar to a matrix that comprises a non-trivial Jordan block. In recent years, frequency splitting phenomena at EPDs have been proposed for sensing applications [99, 100, 101]. Frequency splitting occurs at degenerate resonance frequencies where system eigenmodes coalesce. Such a degenerate resonance frequency is extremely sensitive to a small perturbation in system parameters. This perturbation leads to a shift in the system resonance frequency that can be detected and measured. This concept has been exploited

in new sensing schemes such as optical microcavities [16], optical gyroscopes [102, 103] and mass sensor [104]. Recently, EPD in nonlinear systems has gained interest by showing its potential in advancing sensing technologies and stability analysis. These studies [105, 106] illustrate how nonlinear dynamics at EPDs enhance sensor sensitivity and signal-to-noise ratio and pave the way for innovative electronic system designs, underlining EPDs' critical role in sensing applications.

It has been recently shown that negative capacitors and inductors are useful to realize EPDs in a system made of two resonators coupled via a gyrator [107, 108, 68, 109]. These non-passive negative reactive components are synthesized with negative impedance converters (NICs) or negative impedance inverters (NIIs), which produce a negative capacitor or a negative inductor with feedback circuits [110]. Negative capacitances and inductances are largely used in electronics where negative capacitors are obtained with op amps [111, 112] or with other semiconductor devices [113]. Negative inductances were obtained as early as 1965 using a grounded NII [111], and various circuits have been proposed for floating negative inductance using different types of op amps for operation below 1 MHz. An ideal gyrator is a two-port network that transforms a current into a voltage and vice versa and causes 180 degrees phase shift difference in the signal transmission from one side to the other [114]. Gyrators have been designed using operational amplifiers (op amps) [115] or microwave circuits [116].

In this paper, we explore for the first time the saturation regime due to the nonlinearity in active negative inductance and negative capacitance, in an EPD resonator topology based on a gyrator, and explore the measured high sensitivity. We describe several EPD features in gyrator-based coupled resonant circuits, where two LC resonators (series-series and parallel-parallel configurations) are coupled to each other through a gyrator. We illustrate the necessary conditions to obtain the EPD in both parallel and series resonant circuit configurations and show the signal behavior using time domain simulations. We also provide

a frequency domain analysis in terms of phasors and show that the EPD corresponds to a double zero of the total impedance defining the resonance. Importantly, we discuss the effect of additional losses in the system and show how they make the circuit unstable. The effect of the circuit's nonlinearities is observed experimentally after saturation is achieved, leading to a stable oscillatory regime. When the system is perturbed away from its EPD, the self-oscillation frequency is shifted, and such a shift is measured to determine the circuit's sensitivity. Compared to our previous studies in [107, 108, 68, 109], we focus on the analysis of the series-series configuration including losses that we did not explore before; we also analyze a parallel-parallel configuration, and fabricate a gyrator-based circuit for the first time. We then observe experimentally the self oscillatory regime under saturation and perturb a capacitance value to measure the oscillation frequency shifts. In addition, we compare the sensitivity of our proposed circuit to previous linear and nonlinear circuits supporting EPD [3, 98, 78, 97], highlighting how its sensitivity is comparable and emphasizing the capability of detecting small perturbations. The proposed circuit and method have promising applications in ultrasensitive sensors at various operating frequencies.

4.2 EPD in Parallel Configuration

We show a configuration in which we get an EPD by using a gyrator-based circuit. Two parallel resonators are utilized in two different lossy/lossless configurations. We briefly introduce the gyrator element and later on, we write the required circuit equations in the Liouvillian formalism. Then, we solve the eigenvalue problem to calculate the resonant frequencies (i.e., the eigenfrequencies) and determine the conditions for obtaining EPD at a desired frequency in a lossy circuit. We discuss the conditions for real-valued EPD frequency and stability in the system. In order to provide a comprehensive analysis of the presented circuit and its stability, in Section 4.2.2, we study the eigenfrequencies in the lossless resonators, and

we verify our theoretical calculations by using a time-domain circuit simulator (Keysight Advanced Design System (ADS)). Then, we provide an example and the eigenfrequency dispersion with respect to changes in parameters and we show the perturbation effects on the circuit's eigenfrequencies.

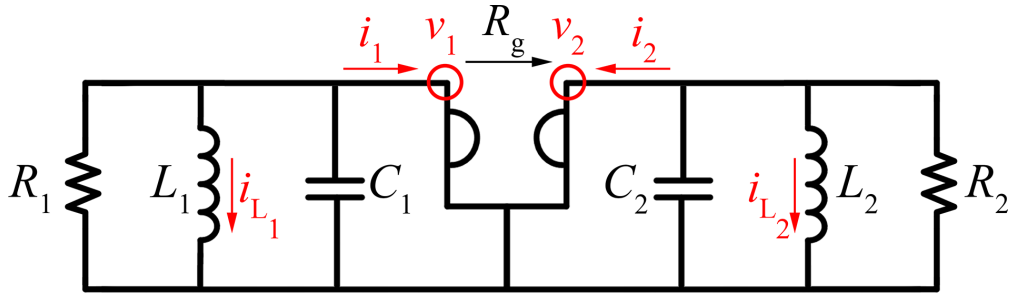

Figure 4.1: Schematic view of the lossy parallel-parallel configuration including losses in each resonator. Inductance and capacitance are negative in the right resonator.

4.2.1 EPD in Lossy Parallel Circuit

The gyrator is a passive, linear, lossless, nonreciprocal, two-port electrical element. It allows network realizations of devices that cannot be realized with the conventional four components (i.e., resistors, inductors, capacitors, and transformers) [114, 117]. An important property of a gyrator is that it inverts the current-voltage characteristic; therefore, an impedance load is also inverted across the gyrator. In other words, a gyrator can make a capacitive circuit behave inductively, and a series LC circuit behaves like a parallel LC circuit. The instantaneous voltages and currents on the gyrator ports are related by [114]

$$\begin{cases} v_2 = R_g i_1 \\ v_1 = -R_g i_2 \end{cases} \tag{4.1}$$

where the gyration resistance R_g is the important parameter in the ideal gyrator. In the parallel-parallel configuration, two parallel RLC resonators are coupled by a gyrator as dis-

played in Fig. 4.1. We find the EPD condition in this circuit by writing the Kirchhoff current law equations and finding the associated Liouvillian matrix. Hence, we assume that all components are ideal, and inductors and capacitors contain no additional resistance. We write the two Kirchhoff current law equations and by using the state vector as, $\mathbf{\Psi} \equiv \left[Q_1, Q_2, \dot{Q}_1, \dot{Q}_2\right]^{\mathrm{T}}$, where Q_n is the stored charge in the capacitor C_n ($n = 1$ for the left resonator and $n = 2$ for the right resonator), and the superscript T denotes the transpose operation. The circuit dynamics are described based on the Liouvillian formalism as

$$\frac{\mathrm{d}\mathbf{\Psi}}{\mathrm{dt}} = \underline{\mathbf{M}}\mathbf{\Psi},\ \underline{\mathbf{M}} = \begin{pmatrix} 0 & 0 & 1 & 0 \\ 0 & 0 & 0 & 1 \\ -\omega_{01}^2 & 0 & -\gamma_1 & \frac{1}{R_{\mathrm{g}}C_2} \\ 0 & -\omega_{02}^2 & -\frac{1}{R_{\mathrm{g}}C_1} & -\gamma_2 \end{pmatrix}, \tag{4.2}$$

where $\underline{\mathbf{M}}$ is the 4×4 circuit matrix, and $\gamma_1 = 1/(R_1C_1)$ and $\gamma_2 = 1/(R_2C_2)$ represent the resonators loss parameter (losses on the right resonator are represented by a negative γ_2 since C_2 is negative). Furthermore, $\omega_{01} = 1/\sqrt{C_1L_1}$, and $\omega_{02} = 1/\sqrt{C_2L_2}$ are resonance angular frequencies of two isolated left and right resonators, assumed to be both real (the case where they are imaginary is shown in Ref. [68]. Assuming signals of the form $Q_n \propto e^{j\omega t}$, we write the associated eigenvalue problem, and the characteristic equation is obtained from $\det(\underline{\mathbf{M}} - j\omega\underline{\mathbf{I}}) = 0$, where $\underline{\mathbf{I}}$ is the identity matrix, leading to

$$\begin{aligned} \omega^4 - j\omega^3(\gamma_1 - \gamma_2) - \omega^2\left(\omega_{01}^2 + \omega_{02}^2 + \gamma_1\gamma_2 + \tfrac{1}{R_{\mathrm{g}}C_1C_2}\right) \\ +j\omega(\gamma_1\omega_{02}^2 + \gamma_2\omega_{01}^2) + \omega_{01}^2\omega_{02}^2 = 0. \end{aligned} \tag{4.3}$$

The coefficients of the odd-power terms of the angular eigenfrequency (ω and ω^3) in the characteristic equation of Eq. (4.3) are imaginary. Eigenfrequencies ω and $-\omega^*$ are both roots. In order to have a stable circuit with real-valued eigenfrequencies, the odd-power terms of the angular eigenfrequency $-j\omega^3(\gamma_1 - \gamma_2)$ and $j\omega(\gamma_1\omega_{02}^2 + \gamma_2\omega_{01}^2)$ in the characteristic

equation of Eq. (4.3) should be zero. The coefficient of the ω^3 term is zero when $\gamma_1 = \gamma_2$. We recall that γ_2 is negative, so the condition $\gamma_1 = \gamma_2$ happens either in absence of losses or when one resonator has gain. However, under this latter gain condition enabling $\gamma_1 = \gamma_2$, the coefficient of the ω term $\gamma_1 \left(\omega_{02}^2 + \omega_{01}^2\right)$ is non-zero because ω_{01}^2 and ω_{02}^2 are both positive, and also in this case it would not be possible to have purely real eigenfreqiencies. On the other hand, the coefficient of the ω term vanishes when $\gamma_1/\gamma_2 = -\omega_{01}^2/\omega_{02}^2$, and under this condition, the coefficient of the ω^3 term $\gamma_1 \left(1 + \omega_{02}^2/\omega_{01}^2\right)$ cannot vanish. In summary, it is not possible to have all real-valued coefficients in the characteristic polynomials, unless $\gamma_1 = \gamma_2 = 0$, which corresponds to a lossless circuit. In other words, under any amount of small loss, there is no condition to make both ω and ω^3 coefficients equal to zero, hence the eigenfrequencies are complex, leading to instabilities that cause oscillations. In the following subsection, we analyze the eigenfrequency in a lossless structure to further understand the stability of the lossless structure.

4.2.2 EPD in Lossless Parallel Circuit

To meet the EPD condition for real valued eigenfrequency, we assume $\gamma_1 = \gamma_2 = 0$. Accordingly, the circuit consists of two lossless parallel LC resonators coupled by a gyrator. The eigenfrequencies for this case are found by solving

$$\omega^4 - \omega^2 \left(\omega_{01}^2 + \omega_{02}^2 + \frac{1}{C_1 C_2 R_{\mathrm{g}}}\right) + \omega_{01}^2 \omega_{02}^2 = 0. \tag{4.4}$$

All the ω's coefficients are real hence ω and ω^* are both roots of the characteristic equation. Moreover, it is a quadratic equation in ω^2, therefore ω and $-\omega$ are both solutions. The system's angular eigenfrequencies are

$$\omega_{1,3} = \pm\sqrt{a+b},\ \omega_{2,4} = \pm\sqrt{a-b}, \tag{4.5}$$

$$a = \frac{1}{2}\left(\omega_{01}^2 + \omega_{02}^2 + \frac{1}{C_1 C_2 R_\mathrm{g}}\right), \tag{4.6}$$

$$b^2 = a^2 - \omega_{01}^2 \omega_{02}^2. \tag{4.7}$$

The EPD is obtained when the resonance frequencies of the circuit coalesce, i.e., when

$$b = 0, \tag{4.8}$$

which happens when $a^2 = \omega_{01}^2 \omega_{02}^2$. The positive EPD angular frequency is then given by $\omega_\mathrm{e} = \sqrt{a}$, where we assume $a > 0$. The condition to obtain real value for EPD frequency is rewritten as

$$\omega_{01}^2 + \omega_{02}^2 - \omega_\mathrm{gp}^2 > 0, \tag{4.9}$$

where it has been convenient to define $\omega_\mathrm{gp}^2 = -1/\left(C_1 C_2 R_\mathrm{g}\right)$ for the parallel-parallel configuration (note that $\omega_\mathrm{gp}^2 > 0$ because one capacitor is negative). When both Eq. (4.8) and inequality in Eq. (4.9) are satisfied, two eigenfrequencies coalesce at a real EPD angular frequency,

$$\omega_\mathrm{e} = \sqrt{\tfrac{1}{2}\left(\omega_{01}^2 + \omega_{02}^2 - \omega_\mathrm{gp}^2\right)} = \sqrt{\omega_{01}\omega_{02}}. \tag{4.10}$$

4.2.3 Dispersion Relation of Lossless and Lossy Parallel-parallel Configurations

As an example, we use the following values: $L_1 = 47\,\mu$H, $L_2 = -47\,\mu$H, $C_2 = -47\,$nF, and $R_\mathrm{g} = 50\,\Omega$. We then obtain two values of capacitance $C_{1,\mathrm{e}} = 6.34\,$nF and $C_{1,\mathrm{e}} = 125.25\,$nF by imposing Eq. (4.8) to be satisfied. Here, both capacitors lead to $a > 0$, enabling the EPD angular frequency to be real valued. Indeed, the $C_{1,\mathrm{e}} = 6.34$nF leads to $\omega_\mathrm{e} = 1.11\times10^6\,$rad/s, whereas $C_{1,\mathrm{e}} = 125.25$nF leads to $\omega_\mathrm{e} = 5.26\times10^5\,$rad/s. In the following we use $C_{1,\mathrm{e}} = 6.34$nF. The results in Figs. 4.2(a) and (b) show the branches of the real and imaginary parts of perturbed eigenfrequencies obtained from the eigenvalue problem when varying the gyrator resistance near $R_{\mathrm{g,e}} = 50\Omega$. The bifurcation of the real part in this case happens for $R_\mathrm{g} > R_{\mathrm{g,e}}$. Perturbing other components like C_1 or L_1 leads to analogous results.

The time domain simulation result for the node voltage v_1 in Fig. 4.2(c) is obtained using the Keysight ADS circuit simulator by employing the ideal model for the gyrator, using the above circuit values that lead to the EPD. We assume the capacitor has an initial voltage on C_1 equal to 1 mV. The voltage grows linearly with increasing time, demonstrating two eigenvalues of the circuit are coalescing, and the system exhibits a double pole, as shown later on. This is peculiar of a second-order EPD. The spectrum of the voltage v_1 in Fig. 4.2(d) is calculated after performing the FFT. The oscillation frequency is $f_\mathrm{o} = 176.66\,$kHz, which is the EPD frequency calculated above.

By perturbing the gyration resistance, the circuit no longer operates at EPD. For a higher gyration resistance value, $R_\mathrm{g} = 52.5\,\Omega > R_{\mathrm{g,e}} = 50\,\Omega$ as a 5% increase, we obtain two distinct real-valued eigenfrequencies in the system. Thus, we could estimate the amount of perturbation in R_g by measuring the frequency of these two resonances. On the other hand, by reducing the amount of perturbed parameter by 5%, leading to $R_\mathrm{g} = 47.5\Omega < R_{\mathrm{g,e}} = 50\Omega$, the system has two complex eigenfrequencies with non-zero imaginary parts. The circuit

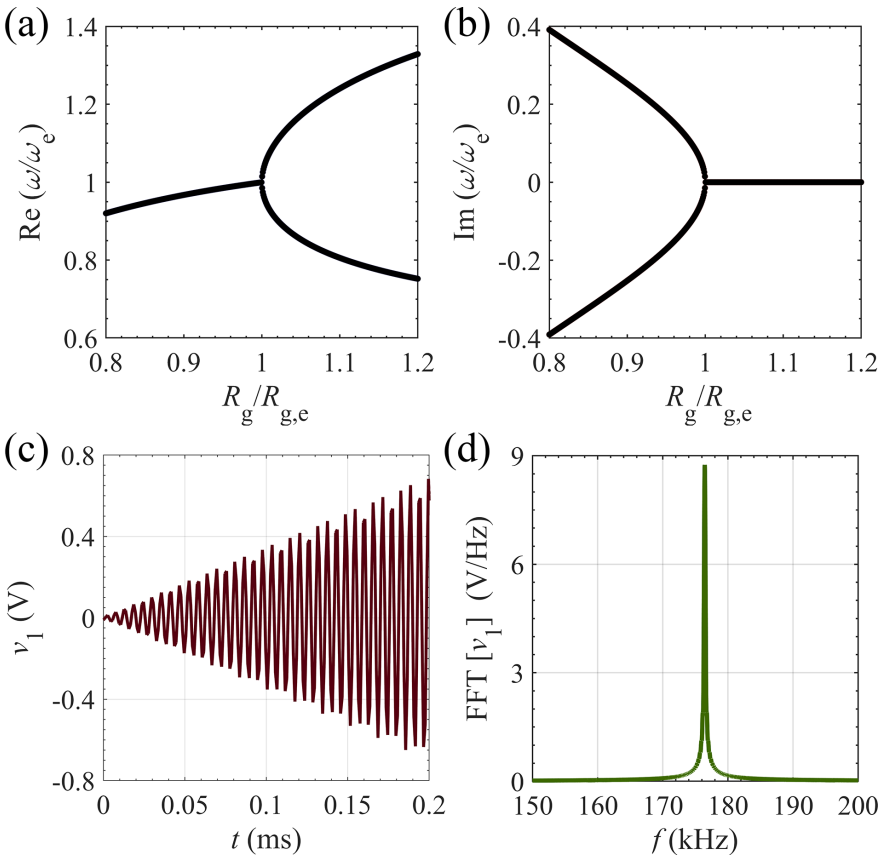

Figure 4.2: Variation of the (a) real and (b) imaginary parts of the two eigenfrequencies to a gyration resistance perturbation in the lossless parallel-parallel configuration. The bifurcation in the real part is observed for $R_g > R_{g,e}$. Voltage v_1 under the EPD condition in the (c) time domain, and (d) frequency domain. The frequency domain result is calculated from 150 kHz to 200 kHz performing an FFT with 10^6 samples in the time window between 0 ms to 0.2 ms.

contains signals that are damping or growing exponentially.

In the lossy circuit, we use the same values of lossless parallel-parallel configuration for the resonators and gyration resistance plus the two resistances. In Figs. 4.3(a) and (b), we vary γ_1 and assume $\gamma_2 = 0$, whereas in Figs. 4.3(c) and (d), we perturb $-\gamma_2$ and assume $\gamma_1 = 0$. In fact, when we vary γ_1 or γ_2, we actually vary R_1 or R_2, while keeping constant C_1 and C_2. When $\gamma_1 = \gamma_2 = 0$, the EPD frequency is the same as the one found earlier for the lossless configuration in Section 4.2.2. Figures 4.3(a)-(d) show the bifurcation of the real and imaginary parts of eigenfrequencies on both sides of the EPD. It means that the

circuit is very sensitive to both positive and negative variations in the resistance value. The angular eigenfrequencies are complex-valued for any amount of loss and the circuit is in the self-oscillation regime. The circuit's signal oscillates with the frequency associated with the real part of the unstable eigenfrequency, and the signal grows exponentially based on the unstable imaginary part of the eigenfrequency. The calculated results show that we achieve higher sensitivity when perturbing γ_2.

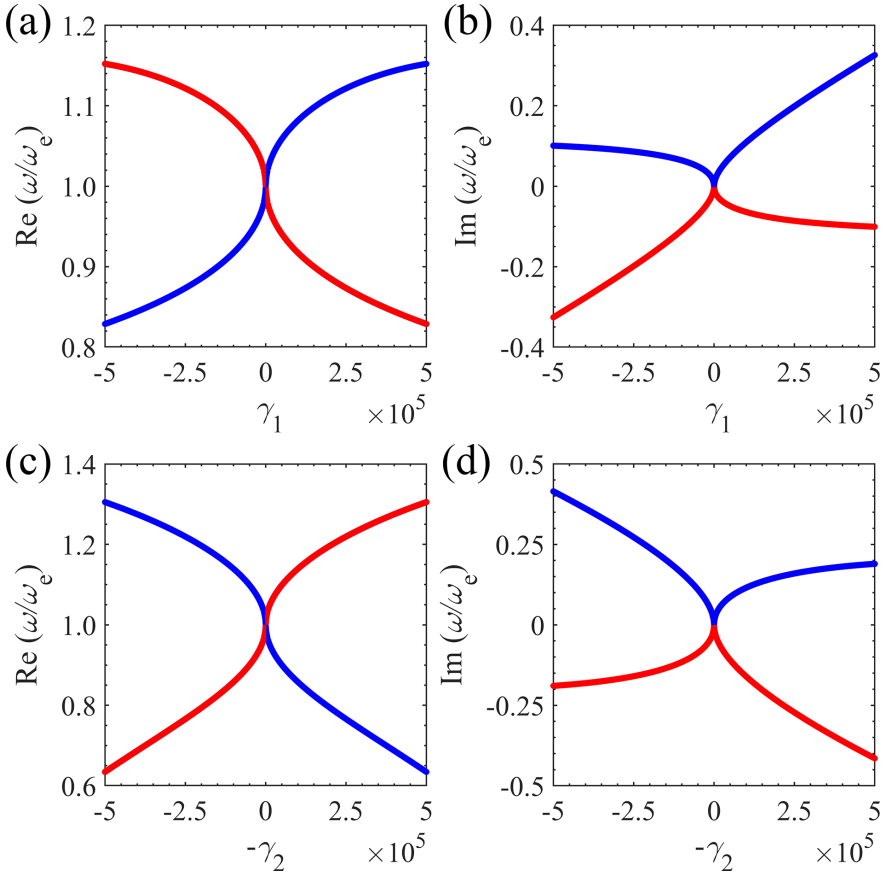

Figure 4.3: Variation of (a) real and (b) imaginary parts of the angular eigenfrequencies to a resistor perturbation on the left resonator. In these plots, γ_1 is varied whereas we assume $\gamma_2 = 0$. Variation of (c) real and (d) imaginary parts of the angular eigenfrequencies to a resistor perturbation on the right resonator. In these plots, $-\gamma_2$ is varied whereas we assume $\gamma_1 = 0$. In these plots, blue curves show stable branches with positive imaginary parts and red curves show unstable branches with negative imaginary parts. In addition, the right half of each plot demonstrates the variation in eigenfrequencies due to varying positive resistance, whereas the left half demonstrates the variation in eigenfrequencies due to varying negative resistance.

4.2.4 Parallel Lossless Circuit Sensitivity

The degenerate eigenvalue (resonance frequency) at an EPD is exceedingly sensitive to perturbations of system parameters. Here, we show that the sensitivity of a system's observable to a specific variation of a component's value is large because of EPD. Let us consider the parallel-parallel configuration in the EPD regime, with the values of the components given in Section 4.2.2. We select the parallel case because all elements are grounded and this sometimes represents a simplification when using realistic active components that require biasing (for more information on dispersion relation for series-series configuration you can refer to the Appendix 4.5-A). For simplicity, we discuss the case without resistances and we define the relative circuit perturbation Δ_{X} as

$$\Delta_{\mathrm{X}} = \frac{X - X_{\mathrm{e}}}{X_{\mathrm{e}}}, \tag{4.11}$$

where X is the perturbed value of a component and X_{e} is the unperturbed value that provides the EPD. The subscript "X" denotes the perturbed parameter. In this section, we consider variations of C_1 and L_1, one at a time, in the lossless configuration. The calculated diagrams for the real and imaginary parts of the eigenfrequencies near the EPD are shown in Fig. 4.4. We conclude that the individual variation of the parameters of C_1 or L_1 show similar sensitivity behavior, i.e., the real part of the eigenfrequencies splits for $\Delta_{\mathrm{X}} < 0$. Note that the L_1 perturbation shows higher sensitivity because of the wider bifurcation in the dispersion diagram.

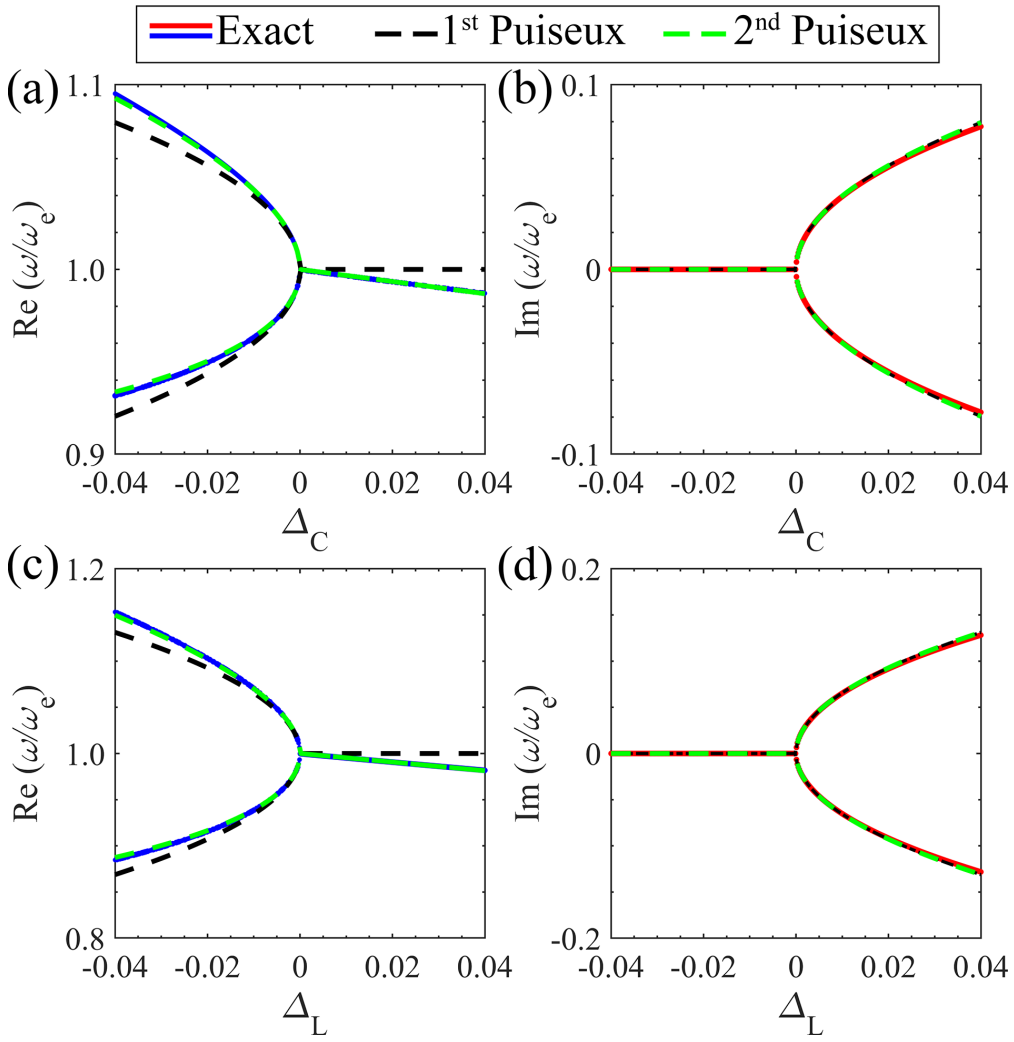

Figure 4.4: High sensitivity of the (a) real and (b) imaginary parts of the eigenfrequencies to relative capacitance perturbation $\Delta_{\mathrm{C}} = (C_1 - C_{1,\mathrm{e}})/C_{1,\mathrm{e}}$. The two perturbed frequencies are real for $\Delta_{\mathrm{C}} < 0$. High sensitivity of the (c) real and (d) imaginary parts of the eigenfrequencies to relative inductance perturbation $\Delta_{\mathrm{L}} = (L_1 - L_{1,\mathrm{e}})/L_{1,\mathrm{e}}$. The two perturbed frequencies are real for $\Delta_{\mathrm{L}} < 0$.

We explain the extreme sensitivity by resorting to the general theory of EPDs. Note that after applying a perturbation in Δ_{X} value, we will have a perturbed matrix $\underline{\mathbf{M}}(\Delta_{\mathrm{X}})$. Consequently, the two degenerate eigenvalues at the EPD change considerably due to the small perturbation in Δ_{X}, resulting in two distinct eigenfrequencies $\omega_p(\Delta_{\mathrm{X}})$, with $p = 1, 2$. A single convergent Puiseux series is used to represent the two perturbed eigenvalues near an EPD, where the coefficients are calculated using the explicit recursive formulas presented in

[89]. An approximation of $\omega_p(\Delta_X)$ around a second-order EPD is given by

$$\omega_p(\Delta_X) \approx \omega_e + (-1)^p \alpha_1 \sqrt{\Delta_X} + \alpha_2 \Delta_X. \tag{4.12}$$

Following [89], we calculate the coefficients as

$$\alpha_1 = \sqrt{-\frac{\frac{\partial H(\Delta_X,\omega)}{\partial \Delta_X}}{\frac{1}{2!}\frac{\partial^2 H(\Delta_X,\omega)}{\partial \omega^2}}}, \tag{4.13}$$

$$\alpha_2 = -\frac{\alpha_1^3 \frac{1}{3!}\frac{\partial^3 H(\Delta_X,\omega)}{\partial \omega^3} + \alpha_1 \frac{\partial^2 H(\Delta_X,\omega)}{\partial \omega \partial \Delta_X}}{\alpha_1 \frac{\partial^2 H(\Delta_X,\omega)}{\partial \omega^2}}, \tag{4.14}$$

evaluated at the EPD, i.e., at $\Delta_X = 0$ and $\omega = \omega_e$, where $H(\Delta_X, \omega) = \det[\underline{\mathbf{M}}(\Delta_X) - j\omega\underline{\mathbf{I}}]$. Eq. (4.12) indicates that for a small perturbation $\Delta_X \ll 1$, the eigenvalues change dramatically from their original degenerate value due to the square root function. In the first example, the perturbed parameter is the positive capacitance on the left resonator, $\Delta_C = (C_1 - C_{1,e})/C_{1,e}$, and the Puiseux series first-order coefficient is calculated by Eq. (4.30) as $\alpha_1 = j4.4138 \times 10^5$ rad/s and the second-order coefficient is calculated as $\alpha_2 = -3.6503 \times 10^5$ rad/s. The result in Figs. 4.4(a) and (b) shows the two branches of the perturbed eigenfrequencies ω obtained directly from the eigenvalue problem (or characteristic equation) when the perturbation Δ_C is applied. This example uses C_1 as a sensing component to detect variation in physical or chemical parameters converted into electrical parameters. However, variation in other components' values can also be used in various realistic scenarios. Figures 4.4(a) and (b) demonstrate that the perturbed eigenvalues can be estimated with great accuracy by using the Puiseux series truncated at its second order (green dashed lines). We have also shown the first-order approximation in Figs. 4.4(a) and (b) for better comparison (black dashed lines), which is also in good agreement with the

eigenfrequencies obtained by the characteristic equation. For a small positive value of Δ_{C}, the imaginary parts of the eigenfrequencies experience a sharp change, while their real parts remain more or less constant. A small negative value of Δ_{C} causes a rapid variation in the real part of the eigenfrequencies.

In the second example, the perturbed parameter is the positive inductance on the left resonator, $\Delta_{\mathrm{L}} = \left(L_1 - L_{1,\mathrm{e}}\right)/L_{1,\mathrm{e}}$, and the Puiseux series first-order coefficient is calculated by Eq. (4.31) as $\alpha_1 = j7.2792 \times 10^5$ rad/s and the second-order coefficient is calculated as $\alpha_2 = -5.1598 \times 10^5$ rad/s. The calculated results in Fig. 4.4(c) and (d) show the two branches of the perturbed eigenfrequencies obtained from the eigenvalue problem when the perturbation in inductance is applied. By applying the Puiseux series truncated at its second order, it is possible to estimate the perturbed eigenfrequencies with high accuracy. However, the first order also provides relatively accurate results. The imaginary parts of the eigenfrequencies undergo a sharp change for very small positive perturbations, while their real parts remain relatively unchanged. A small negative perturbation in the inductor value causes rapid variation in the eigenfrequencies' real part. This feature is one of the most extraordinary physical properties associated with the EPD and it can be exploited for designing ultra-sensitive sensors [5].

4.2.5 Frequency Domain Analysis of The Degenerate Resonance

We show how the EPD regime is associated to a special kind of circuit's resonance, directly observed in a frequency domain analysis of the circuit. We calculate the total input admittance, $Y_{\mathrm{total}}(\omega)$ (see Fig. 4.5(a)), for the parallel-parallel circuit by finding the transferred impedance $Y_{\mathrm{trans}}(\omega)$ on the left side of the circuit. We define the two admittances of the resonators as $Y_1 = j\omega C_1 + 1/(j\omega L_1)$, $Y_2 = j\omega C_2 + 1/(j\omega L_2)$, and calculate the transferred admittance on the left side as

$$Y_{\text{trans}}(\omega) = \frac{1}{R_{\text{g}}^2 Y_2}. \tag{4.15}$$

The total admittance $Y_{\text{total}}(\omega)$ is calculated as

$$Y_{\text{total}}(\omega) \triangleq Y_1(\omega) + Y_{\text{trans}}(\omega) = Y_1 + \frac{1}{R_{\text{g}}^2 Y_2}. \tag{4.16}$$

The resonant angular frequencies are obtained imposing $Y_{\text{total}}(\omega) = 0$. A few steps lead to the same ω-zeros given by Eq. (4.5). We calculate the resonance frequencies for various gyration resistance values in Fig. 4.5(b). When considering the EPD gyrator resistance $R_{\text{g}} = R_{\text{g,e}} = 50\,\Omega$, one has $Y_{\text{total}}(\omega) \propto (\omega - \omega_{\text{e}})^2$, i.e., the two zeros coincide, represented by the point where the two curves meet exactly at EPD angular frequency. For $R_{\text{g}} < R_{\text{g,e}}$, resonance angular frequencies are complex conjugate pairs and for $R_{\text{g}} > R_{\text{g,e}}$, the resonance angular frequencies are purely real, consistent with the results in Fig. 4.2(a) and (b).

4.3 Experimental Sensitivity in the Saturated Regime

We explore experimentally what happens in the proposed second-order EPD circuit due to unavoidable instabilities, and we actually exploit them by making an oscillator. The key experimental observations are that we have stable oscillations after reaching saturation and the oscillation frequency exhibits high sensitivity to perturbations. We also show that such sensitivity is higher than that of a perturbed single LC resonator. We begin with the linear case, detailing the design of the different components in the circuit. Furthermore, we test the proposed circuit for each part, such as the gyrator implementation with op amps.

Next, we study the gyrator-based circuit in the saturation regime, where the oscillation occurs due to the nonlinearity induced by op amps and losses/gains in each resonator. Finally, we analyze the circuit's sensitivity to capacitance changes. The values for the experiment are set as $C_1 = 400\,\text{nF}$, $L_1 = 47\,\mu\text{H}$, $L_2 = -10\,\mu\text{H}$ and $C_2 = -470\,\text{nF}$ where these values ideally lead to an EPD at $f = 51.9\,\text{kHz}$.

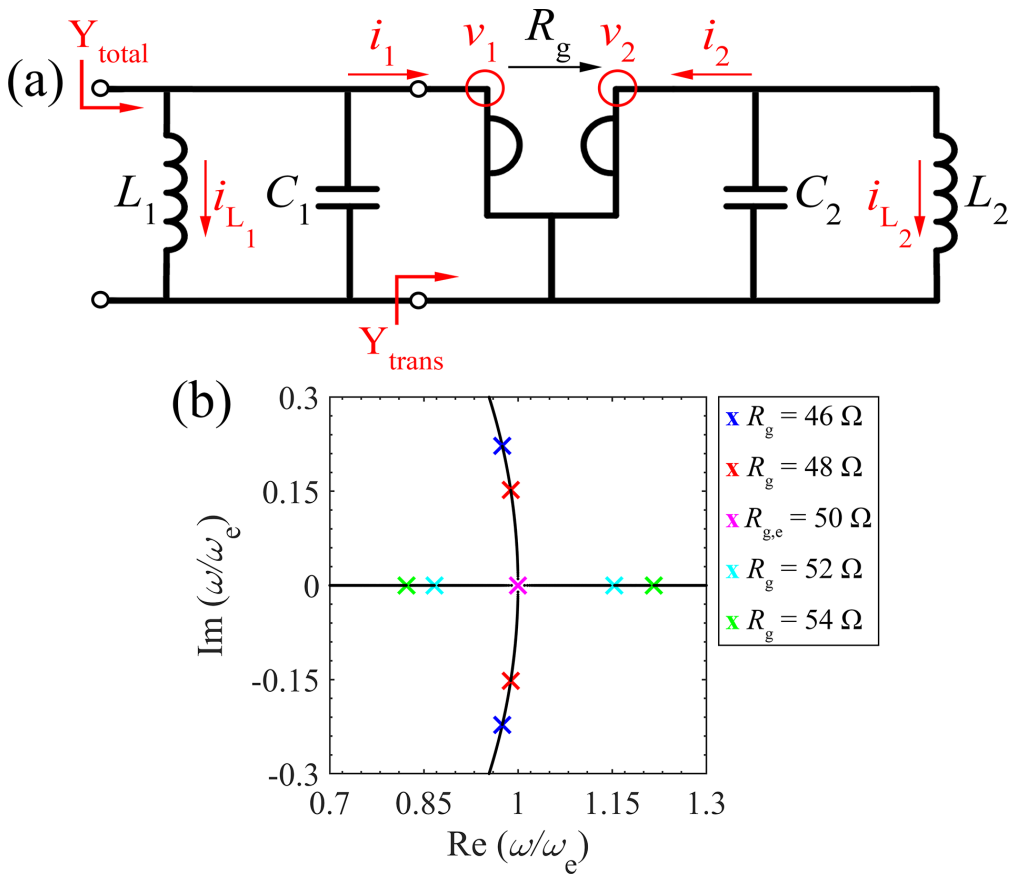

Figure 4.5: (a) Schematic view of the lossless parallel-parallel configuration. (b) Root locus of zeros of Y_{total} shows the real and imaginary parts of resonance frequencies of the parallel configuration when varying gyration resistance. The EPD frequency corresponds to a double zero of the admittance Y_{total}.

4.3.1 Observation of Instability in The Circuit

The gyration resistance has an associated direction indicated by an arrow in the schematic illustrated in Fig. 4.6(a). Consider the gyrator circuit shown in Fig. 4.6(b) implemented

using two op amps of the same model (Texas Instruments, model TLE2071ACP) and seven resistors. By selecting the proper value for the resistors (i.e., R_g in Fig. 4.6(b)), we control the gyration parameter R_g. The gyrator asymmetric impedance matrix $\underline{\mathbf{Z}}_g$ is given by Eq. (4.1). To achieve a gyration $R_g = 10\,\Omega$, all the resistances in the circuit shown in Fig. 4.6(b) are set to the same value of $10\,\Omega$. We tested the gyrator circuit shown in Fig. 4.6(b) with different loads to ensure that it works properly. We put a load of $Z_L = 33\,\Omega$ on the right port of gyrator and measure the transferred impedance on the left port as $Z_{trans} = 3.56\,\Omega$ and $Z_{trans} = 3.42\,\Omega$, at frequency of 10 and 100 kHz, respectively, showing an experimental gyration of approximately $9.3\,\Omega$ and $9.65\,\Omega$, respectively. The impedances are measured with an LCR meter (Keysight, model U1733C).

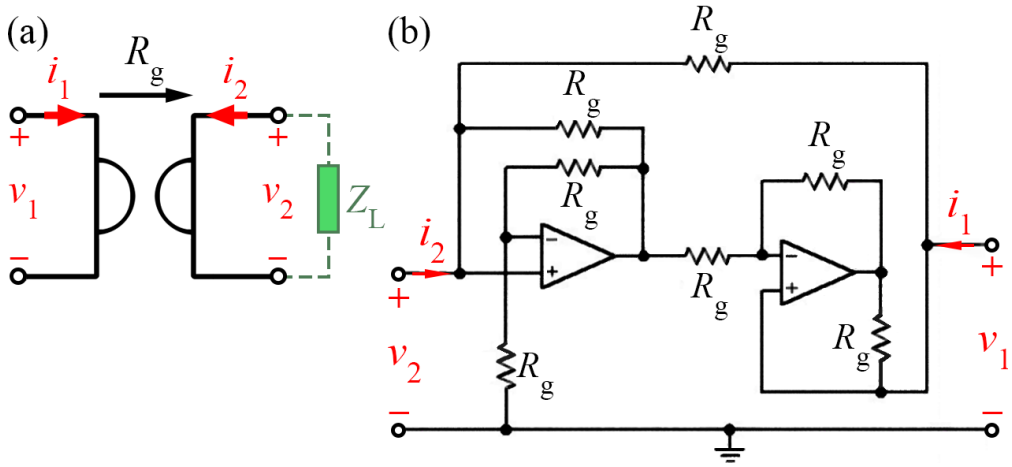

Figure 4.6: (a) Gyrator schematic and corresponding voltages, currents, and gyration resistance direction. (b) A possible circuit for a gyrator implementation by using two op amps and seven resistors.

To satisfy the EPD condition based on the theory discussed in Subsection 4.2.2, the positive capacitance in the experiment C_1 is built by paralleling fixed capacitors with values 220 nF, 150 nF, 22 nF and a trimmer (FTVOGUE , model Variable Capacitance Kit) to reach the value of 400nF. The inductance L_1 is built by using a commercial inductor of 47μH (Coilcraft, model MSS7348-473) with a series DC loss of $0.15\,\Omega$ and $\pm 20\%$ tolerances. However, due to tolerances, our chosen inductor had a smaller value than the nominal one. We then tuned

the inductance by a series inductor with a value of 1 μH (Bourns, model 78F1R0K-TR-RC), reaching the measured value of 46.8 μH at 100 kHz.

The negative capacitance and inductance are implemented based on the circuits shown in Appendix 4.8-D using the same op amp model of the gyrator. In particular, the negative inductance L_2 is built by using a commercial inductor of 10 μH (Coilcraft, model MSS7348-103MEC) with a series DC loss 0.045 Ω and $\pm$20% tolerances followed by an inverter in Appendix 4.8-D. However, due to tolerances, our chosen inductor had a smaller value than the nominal one. Then, we tuned the inductance by adding a series inductor with a value of 1 μH (Bourns, model 78F1R0K-TR-RC) and a 0.47 μH (Bourns, model 542-78FR47K-RC) reaching a measured value of 10.1 μH at 100 kHz.

The value of $C_2 = -470$ nF comes from the inverter described in Appendix 4.8-D, where we ignored the gain associated to inversion because of the capacitance's high quality factor. We use a capacitance trimmer (FTVOGUE , model Variable Capacitance Kit) in parallel to a commercial fixed capacitor with a value of 470 nF to achieve a value close to the desired capacitance of 470 nF. All capacitances and inductances are measured with an LCR meter (Keysight, model U1733C) at 100 kHz to ensure the tuning process leads to the desired capacitances and inductances design values. The dispersion diagram of the complex eigenfrequencies by varying the capacitance C_1 is shown in Fig. 4.7. The system is unstable for any shown value of the perturbed capacitor because of the non-zero imaginary part of eigenfrequencies.

Due to the presence of loss in the prototype, which is caused mainly by the two inductors, we do not have the perfect degeneration of the eigenfrequencies, as shown in Fig. 4.7(b) where we do not have any more $\mathrm{Im}\,(f) = 0$ near the bifurcation (plot obtained via simulation in the linear regime). In addition, in the nonlinear regime, the negative inductance and capacitance are responsible of the saturation regime because they act as gain when transferred by the negative impedance converter shown in Appendix 4.8-D. Nevertheless, we can still get in the

vicinity of the original EPD frequency.

Since the stored charge in the capacitors is $Q_n \propto e^{j\omega t}$, even a small negative imaginary part of an eigenfrequency leads to an instability and the establishment of self substained oscillations, while the charge associated with the other eigenfrequency with positive imaginary part decays. In conclusion, the small gain generated by the inverters leads to non-zero $\mathrm{Im}\,(f)$, which induces the system state vectors to grow exponentially and it results in an unstable system. We use the instability of the system to our advantage by letting the system oscillate at the EPD frequency, and we investigate the sensitivity of the system in the saturation regime close to the original EPD frequency.

4.3.2 Measurements in The Saturation Regime

In the experimental setup, the system saturates exhibiting a steady oscillation at $f_{\mathrm{osc},0} = 50.7\mathrm{kHz}$, measured using a spectrum analyzer (Rigol, model DSA832E), which is close to the frequency shown in Fig. 4.7 where the bifurcation is imperfect. We observe that the gyration value is close to the designed value of $10\,\Omega$ even after reaching saturation by measuring the voltages v_1 and v_2 in the circuit shown in Fig. 4.6(a). Also, we considered the transformed admittance of the positive LCR tank after the gyrator ($1/Y_{\mathrm{trans}} = R_g^2(C_1 j\omega \parallel 1/(L_1 j\omega + R_1))$ at the frequency of oscillation to find $i_2 = v_2 Y_{\mathrm{trans}}$. As a result, the gyration parameter in the saturated regime at the oscillation frequency of $f_{\mathrm{osc}} = 50.7\mathrm{kHz}$ was calculated as $R_{\mathrm{g}} = 10.8\Omega$, which is close to the theoretical design value of $R_{\mathrm{g}} = 10\,\Omega$ and from those measured in the linear regime.

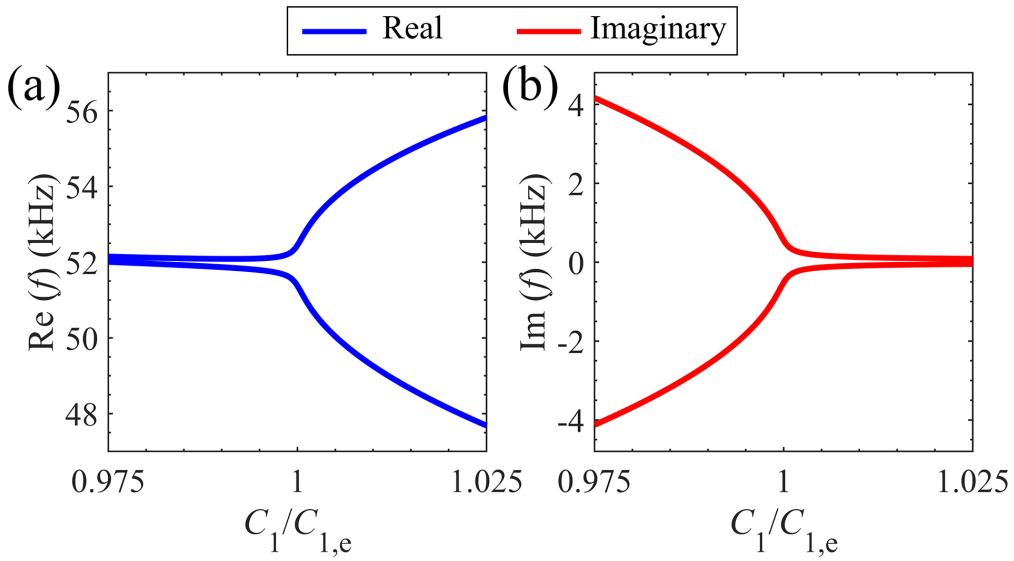

Figure 4.7: Variation of (a) real (blue) and (b) imaginary (red) parts of the eigenfrequencies to a capacitance perturbation on the left resonator.

The goal here is to measure the sensitivity of the self oscillation frequency (after reaching saturation) to the perturbation of the capacitance C_1. Indeed, the measured oscillation frequency dramatically shifts away significantly from the unperturbed frequency $f_{\mathrm{osc},0} = 50.7\,\mathrm{kHz}$ even when small perturbations are applied. Figure 4.8(a) shows the experimental time-domain voltage signal v_1 of the capacitor C_1 with respect to the ground, when a relative perturbation $\Delta_\mathrm{C} = 2.5\,\%$ ($\Delta_\mathrm{C} = \Delta C/C_{1,0}$, where subscript 0 refers to the unperturbed value of $C_{1,0} = 400\,\mathrm{nF}$) is applied to C_1, measured by an oscilloscope. The voltage frequency is measured with a spectrum analyzer (Rigol DSA832E), and shown in Fig. 4.8(b), for various C_1 values. A fundamental frequency of oscillation of $f_{\mathrm{osc},0} = 50.7\,\mathrm{kHz}$ was observed for no perturbation (blue); 49.96 kHz for perturbation $\Delta_\mathrm{C} = 0.625\,\%$ (gray); 49.8 kHz for perturbation $\Delta_\mathrm{C} = 1.25\,\%$ (green); 49.43 kHz for perturbation $\Delta_\mathrm{C} = 1.875\,\%$ (purple); and 48.9 kHz for perturbation $\Delta_\mathrm{C} = 2.5\,\%$ (red). We used a resolution bandwidth of 10 Hz, and a video bandwidth of 10 Hz. In all cases, the measured spectrum is clean approximately down -70 dB from the peak values. The linewidths, calculated at -3 dB from the peak, are approximately 10 Hz which are significantly smaller than the measured frequency shifts.

The measured oscillation frequencies versus C_1 are captured in Fig. 4.8(c) with circles, with the corresponding colors used in Fig. 4.8(b). In the experiment, a relative perturbation $\Delta_{\mathrm{C}} = 2.5\,\%$ applied to C_1 in the gyrator-based circuit led to a frequency shift $|\Delta f| = |48.9\,\mathrm{kHz} - 50.7\,\mathrm{kHz}| = 1.8\,\mathrm{kHz}$, where $f_{\mathrm{osc},0} = 50.7\,\mathrm{kHz}$ is the oscillation frequency with no perturbation and $f_{\mathrm{osc}} = 48.9\,\mathrm{kHz}$ is perturbed oscillation frequency. The measured -3-dB (half power) spectral linewidth of 10 Hz (using a resolution bandwidth of 10 Hz, and a video bandwidth of 10 Hz) is 180 times narrower than the measured frequency shift $|\Delta f| = 1.8\,\mathrm{kHz}$. For the smallest perturbation of $\Delta_{\mathrm{C}} = 0.625\,\%$, the associated frequency shift $|\Delta f| = 0.74\,\mathrm{kHz}$ is 74 times larger than the linewidth of 10 Hz, indicating that the perturbed frequency spectrum is clearly detectable (consider also that the noise floor is 70 dB lower than the peak).

4.3.3 Discussion on Sensitivity and Capability to Detect Small Perturbation

We now elaborate on the sensitivity of the gyrator-based oscillator in the saturation regime to circuit perturbations and discuss how the obtained experimental results are comparable to those of (i) a single LC resonator in the linear regime, and (ii) other circuits based on EPDs from the literature [3, 78, 98, 97]. In particular, we compare the sensitivity $S = |\Delta_{\mathrm{f}}| \,/\, |\Delta_{\mathrm{X}}|$ in the various cases, where $\Delta_{\mathrm{f}} = |\Delta f| \,/ f_0$ and $\Delta_{\mathrm{X}} = |\Delta X| \,/ X_0$ are the normalized changes in the perturbed frequency and a generic parameter X in the circuit (subscript 0 refers to the unperturbed value). The change in the generic parameter X represents changes in capacitance or resistance, as will be discussed next.

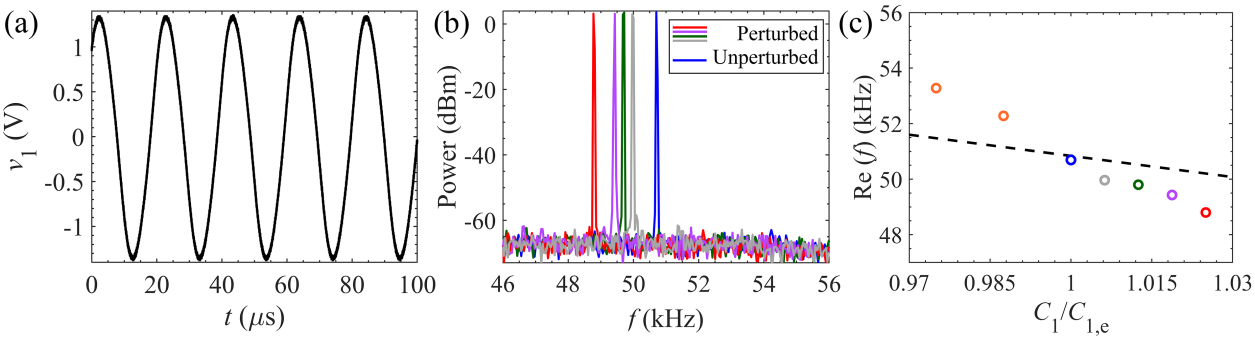

Figure 4.8: (a) Measured time-domain voltage signal at the capacitor C_1 when the system is perturbed from the EPD by $C_1 - C_{1,0} = 2.5\,\text{nF}$. (b) Measured capacitor voltage spectrum with the unperturbed frequency of oscillation of 50.7 kHz (blue); 49.96 kHz for perturbation $\Delta_C = 0.625\,\%$ (gray); 49.8kHz for $\Delta_C = 1.25\,\%$ (green); 49.43kHz for $\Delta_C = 1.875\,\%$ (purple); and 48.9 kHz for $\Delta_C = 2.5\,\%$ (red). (c) Comparison of the measured oscillation frequencies of the proposed nonlinear circuit (color dots) and those of the perturbed single LC linear circuit (dashed black line), when perturbing the positive capacitance.

We first look at the comparison with a single LC resonator in linear regime, shown in Fig. 4.8(c), where the variation of the experimental oscillation frequency by perturbing the positive capacitor C_1 (colored circles) of the gyrator-based circuit is compared to the resonant frequency shift of a *linear single* LC resonator (dashed black line). The single LC resonator has an inductance $L_s = 24.5\,\mu\text{H}$ and capacitance $C_s = C_1 = 400\,\text{nF}$ (same as $C_{1,0}$ value at EPD), with resonance frequency $f_0 = 1/\left(2\pi\sqrt{L_s C_s}\right) = 50.8\,\text{kHz}$. Perturbing the capacitance C_s leads to a changed frequency of approximately $f \approx f_0\,(1 - \Delta_{C_s}/2)$, where $\Delta_{C_s} = (C - C_s)/C_s$. The results clearly showcase that the gyrator-based circuit in the saturation regime exhibits higher sensitivity compared to that of the linear single LC resonator. Notably, the resonance frequency variation due to the perturbation of capacitance of $\Delta_{C_s} = 10\%$ for the single LC resonator is comparable of the oscillation frequency shift of only 1/8 of the perturbation ($\Delta_C = 1.25\%$) when using the saturation regime of the gyrator-based oscillator. This result shows that the sensitivity of our proposed gyrator-based oscillator is 8 times larger than the one of a single LC resonator.

We now compare the sensitivity of the presented oscillator with those obtained using the

four circuits in Refs. [3, 78, 98, 97]. In our developed gyrator-based circuit, we measured a first perturbed frequency $|\Delta_{\mathrm{f}}| = 1.46\,\%$ for the smallest capacitance perturbation $\Delta_{\mathrm{C}} = 0.625\,\%$. Hence, the gyrator-based EPD oscillator exhibits a sensitivity of $S = 2.34$, (for $\Delta_{\mathrm{C}} = 0.625\,\%$.) which is comparable to or higher than the counterpart circuits as shown next. In the linear single LC resonator, the sensitivity shown in Fig. 4.8(c) is $S = 0.5$, hence it is lower than that of the proposed circuit oscillator.

In Ref. [78], they used a linear regime in a single time-varying resonator, and they measured a sensitivity of $|\Delta_{\mathrm{f}}| = 0.66\,\%$, calculated based on the separation of the two perturbed resonance frequencies, for their smallest perturbation considered $\Delta_{\mathrm{C}} = 0.3\,\%$, as shown in Fig. 6(a) of their paper. Thus, in [78], they achieved an approximate sensitivity of $S = 2.2$ for the first perturbation.

Sensitivity in the PT-symmetric two-coupled resonators in Ref. [3] was measured approximately as $S = 0.75$ in Fig. 2 of that paper with $|\Delta_{\mathrm{f}}| = 5\,\%$, calculated based on the separation of the two resonance frequencies after perturbation, for their smallest applied perturbation of $\Delta_{\gamma} = 6.7\,\%$ where in this case $X = \gamma = R^{-1}\sqrt{L/C}$. Therefore, the highest sensitivity measured in [3] was just slightly higher than that of a single linear LC resonator. Since experimental data at the EPD were not available, the sensitivity was calculated based on the frequency shift corresponding to perturbation of normalized γ approximately from 1.042 to 0.975. These two points correspond to the first perturbations occurring just before and after the EPD.

In Ref. [98], the authors used an oscillator scheme using a nonlinear saturated regime (analogous to what considered in this paper) in two-coupled resonators, and measured a frequency change of $|\Delta_{\mathrm{f}}| = 1.29\,\%$ for their smallest perturbation of $\Delta_{\mathrm{C}} = 1.3\%$. Therefore, in [98], the sensitivity was measured to be $S = 0.99$.

In [97], the EPD concept using saturable nonlinear gain was exploited to design oscillators

based on two coupled transmission lines as in [70]. They observe oscillation frequency changes in response to perturbations in the load resistance, so in this case we have $X = R$, and $\Delta_X = \Delta_R$. In their measurement (Fig. 16 in [97]), they observed a $|\Delta_f| = 20\%$ for a resistance perturbation of $\Delta_R = 9.8\%$, resulting in a sensitivity of $S = 2.04$. Since experimental data at the EPD were not available, the sensitivity was calculated based on the frequency shift obtained by perturbing the load resistance from 51 Ω to 56 Ω, relative to a fundamental frequency of 1 GHz.

Note that besides aiming at high sensitivity, another very important parameter is the *capability to detect small perturbations*. The measured capacitance variation $\Delta_C = 0.625\%$ in the gyrator-based circuit in this paper is higher only than the case in Ref. [78] where $\Delta_C = 0.3\%$. Hence, the smallest perturbation in the gyrator-based oscillator is smaller than the one in [98] where $\Delta_C = 1.3\%$, and it is much smaller than the smallest variation in [3], $\Delta_\gamma = 6.7\,\%$ (note that the low sensitivity measured in [3] probably depends on the large variation they considered, since the EPD-based sensitivity decreases when moving away from the EPD). Furthermore, the perturbation measured in [97] was $\Delta_R = 9.8\%$.

The capability to detect small variations Δ_X depends on both the *sensitivity* and the *linewidth* of the oscillator spectrum. The linewidth of the experimental oscillation frequency was measured to be only 10 Hz. However, such a linewidth could be even smaller than that measured value because we did not have the capability to use a narrower intermediate frequency bandwidth of the spectrum analyzer to test it.

Nonlinear effects such as gain saturation and Kerr nonlinearity in systems with EPD play an important role in sensitivity and stability [118]. The analysis of the nonlinear modes of the system can be carried over by resorting to nonlinear dynamics tools [119], where the modes of the system are identified as fixed points of the system equations. At the same time, the stability of such fixed points (ultimately determining whether the system will operate in those modes) is obtained from the Lyapunov exponents associated to the Jacobian matrix of

the system equations linearized around the fixed point. Some dynamics related to EPDs in nonlinear systems are discussed in [120, 121], or more recently in the framework of electronic circuits, in [105] where a singularity is found in the nonlinear framework. In [105], they discussed the sensitivity of the system supporting the EPD and how nonlinearity helps the signal-noise ratio (how much noise contributes to the system). In this work, we do not focus on describing the system's nonlinearity but we observe the saturated regime using an implementation with electronic components. Based on the experimental results shown in Fig. 4.8(b) , which shows a clear and sharp spectrum, for each perturbed case, we conclude that our nonlinear system works effectively in the saturation regime, for each value of the perturbed capacitor.

4.4 Conclusions

We have shown that two resonators connected via a gyrator support an EPD when one resonator is made of a negative inductance and a negative capacitance. We have provided the theoretical conditions for such EPD to exist at a purely real frequency and verified our theoretical calculations by using a time domain circuit simulator (Keysight ADS). We have demonstrated that the eigenfrequencies are exceptionally sensitive to a perturbation of the system and this may have significant implications for ultra-sensitive sensing technology and RF sensors. In addition, we show that the system has two complex eigenfrequencies, one of which is always associated to the circuit instability. We have fabricated the circuit and using the saturated regime, we have measured the sensitivity of the self-oscillation frequency to small capacitance perturbations. We have measured both the *sensitivity* and the *linewidth* of the oscillator's spectrum, because these two parameters are important for detecting small circuit perturbations. The spectrum exhibited a very narrow linewidth (i.e., 10 Hz), and the measured signal had a noise floor at -70 dB from the spectrum peak, and the circuit's

sensitivity was measured to be comparable or better than cases previously published. We believe that the demonstrated concept of an oscillator in the saturated regime that is very sensitive to perturbations could pave the way for the development of new operation schemes to boost the performance of highly sensitive sensors.

Acknowlegment

This material is based upon work supported by the National Science Foundation (NSF) under Grant No. ECCS-1711975 and by Air Force Office of Scientific Research (AFOSR) under Grant No. FA9550-19-1-0103.

4.5 Appendix A: Circuits Duality

The concept of duality applies to many fundamental physics/engineering concepts. For instance, this concept has been utilized many times in electromagnetic and electric circuits. Two circuits are dual if the mesh equations that describe one of them have the same mathematical form as the nodal equations that characterize another circuit [122]. We consider the mesh equations in the parallel-parallel configuration using the Kirchhoff's voltage law. According to the duality theorem, if we substitute voltage by current, current by voltage, capacitance by inductance, and inductance by capacitance, we can obtain mesh equations for series-series configuration. Thus, we present a dual circuit of the parallel configuration, achieving an EPD by utilizing gyrator-based circuits with two series-series resonators.

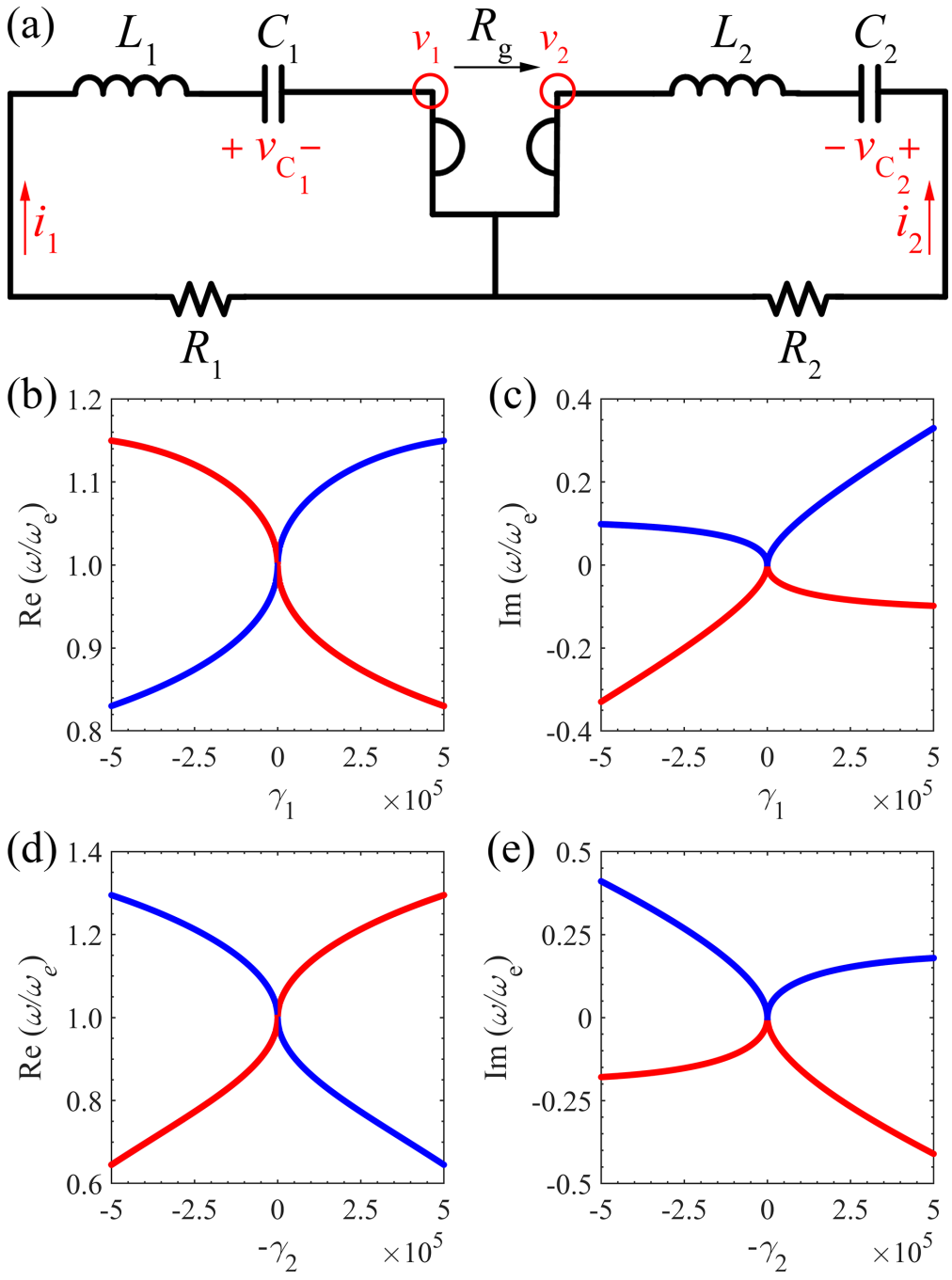

Figure 4.9: (a) Schematic view of the lossy series-series configuration including a resistor in each resonator. The right resonator is made of negative inductance and capacitance. Variation of (b) real and (c) imaginary parts of the angular eigenfrequencies to a resistor perturbation in the left resonator. In these plots, γ_1 is varied whereas we assume $\gamma_2 = 0$. Variation of (d) real and (e) imaginary parts of the angular eigenfrequencies to a resistor perturbation on the right resonator. In these plots, $-\gamma_2$ is varied whereas we assume $\gamma_1 = 0$. In these plots, blue curves show stable branches with positive imaginary parts and red curves show unstable branches with negative imaginary parts. The right half of each plot demonstrates the variation in eigenfrequencies due to varying positive resistance, whereas the left half demonstrates the variation in eigenfrequencies due to varying negative resistance.

4.5.1 EPD in Lossy Series Circuit

We analyze the EPD condition in the series-series configuration by accounting for series resistors R_1 and R_2 in both resonators. Using the Liouvillian formalism, the Kirchhoff voltage law equations for the two loops of the circuit in Fig. 4.9(a), and the state vector of $\mathbf{\Psi} \equiv \left[Q_1, Q_2, \dot{Q}_1, \dot{Q}_2\right]^{\mathrm{T}}$, we obtain

$$\frac{\mathrm{d}\mathbf{\Psi}}{\mathrm{dt}} = \underline{\mathbf{M}}\mathbf{\Psi},\ \underline{\mathbf{M}} = \begin{pmatrix} 0 & 0 & 1 & 0 \\ 0 & 0 & 0 & 1 \\ -\omega_{01}^2 & 0 & -\gamma_1 & \frac{R_\mathrm{g}}{L_1} \\ 0 & -\omega_{02}^2 & -\frac{R_\mathrm{g}}{L_2} & -\gamma_2 \end{pmatrix}, \tag{4.17}$$

where, $\gamma_1 = R_1/L_1$ and $\gamma_2 = R_2/L_2$ describe losses (losses on the right resonator are represented by a negative γ_2 since L_2 is negative). These eigenfrequencies are solutions to the following characteristic equation

$$\begin{aligned} \omega^4 - j\omega^3\left(\gamma_1 - \gamma_2\right) - \omega^2\left(\omega_{01}^2 + \omega_{02}^2 + \gamma_1\gamma_2 + \tfrac{R_\mathrm{g}}{L_1 L_2}\right) \\ + j\omega\left(\gamma_1\omega_{02}^2 + \gamma_2\omega_{01}^2\right) + \omega_{01}^2\omega_{02}^2 = 0. \end{aligned} \tag{4.18}$$

An eigenfrequency with a negative imaginary part is associated with an exponentially growing signal. The coefficients of the odd-power terms of the angular eigenfrequency (ω and ω^3) in the characteristic equation of Eq. (4.18) are imaginary. In the characteristic equation, eigenfrequencies ω and $-\omega^*$ are both roots. In order to have a stable circuit with real-valued eigenfrequencies the odd-power terms of the angular eigenfrequency $-j\omega^3\left(\gamma_1 - \gamma_2\right)$ and $j\omega\left(\gamma_1\omega_{02}^2 + \gamma_2\omega_{01}^2\right)$ in the characteristic equation of Eq. (4.18) should be zero, otherwise a complex eigenfrequency needed to satisfy the characteristic equation of Eq. (4.18). The coefficient of the ω^3 term is zero when $\gamma_1 = \gamma_2$, and under this condition the coefficient of

the ω term $\gamma_1\left(\omega_{02}^2+\omega_{01}^2\right)$ is non-zero value because ω_{01}^2 and ω_{02}^2 are both positive. Moreover, the coefficient of the ω term vanishes when $\gamma_1/\gamma_2 = -\omega_{01}^2/\omega_{02}^2$, and under this condition, the coefficient of the ω^3 term $\gamma_1\left(1+\omega_{02}^2/\omega_{01}^2\right)$ cannot vanish. Thus, it is not possible to have all real-valued coefficients in the characteristic polynomials, unless $\gamma_1 = \gamma_2 = 0$ which corresponds to a lossless circuit. In the following subsection, we examine the eigenfrequency in a lossless structure to understand its stability conditions.

4.5.2 EPD in Lossless Series Circuit

To have a real-valued EPD frequency and fulfill the EPD conditions, we suppose $\gamma_1 = \gamma_2 = 0$. In this configuration, two series LC resonators are connected by a gyrator, as illustrated in Fig. 4.10(a). We assume that all components are ideal, and the circuit does not contain any resistance. By writing down the Kirchhoff voltage law equations in two loops, we write the eigenvalue problem associated to the circuit equations, and the characteristic equation is obtained from $\det\left(\underline{\mathbf{M}} - j\omega\underline{\mathbf{I}}\right) = 0$, leading to

$$\omega^4 - \omega^2\left(\omega_{01}^2+\omega_{02}^2+\frac{R_\mathrm{g}}{L_1L_2}\right)+\omega_{01}^2\omega_{02}^2 = 0. \tag{4.19}$$

In this characteristic equation, ω is the angular eigenfrequency of the system. All the ω's coefficients are real hence ω and ω^* are both roots of the characteristic equation, where * represents the complex conjugate operation. Moreover, it is a quadratic equation in ω^2; therefore, ω and $-\omega$ are both solutions. For $R_\mathrm{g} = 0$, the two resonators are uncoupled, and the two circuits have two angular eigenfrequency pairs of $\omega_{1,3} = \pm\omega_{01}$, and $\omega_{2,4} = \pm\omega_{02}$.

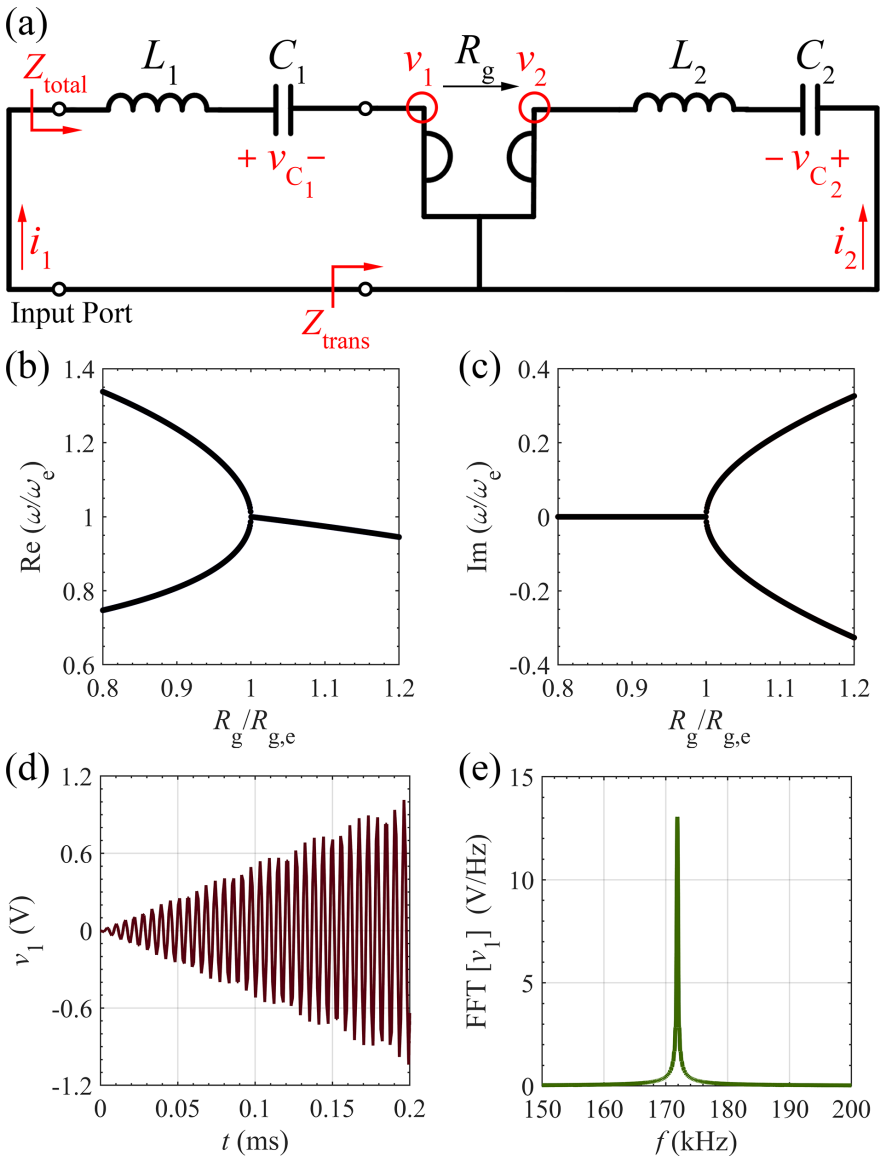

Figure 4.10: (a) Series-series configuration: two different LC resonators in series configuration connected via an ideal gyrator. The right resonator is made of negative inductance and capacitance. Variation of the (b) real and (c) imaginary parts of the two eigenfrequencies to a gyration resistance perturbation. The bifurcation in the real part is observed for $R_g < R_{g,e}$. Voltage v_1 under the EPD condition in the (d) time domain, and (e) frequency domain. The frequency domain result is calculated from 150 kHz to 200 kHz with 10^6 samples in the time window between 0 ms to 0.2 ms.

We assume that the resonance frequency of each single LC resonator is real-valued; this happens when inductance and capacitance in the same resonator have both the same sign. In this case, the component values on the left side are positive, whereas they are negative

on the right side. We explain the reason for this issue in Appendix 4.6-B1. The angular eigenfrequencies (resonance frequencies) in the coupled circuit are calculated as

$$\omega_{1,3} = \pm\sqrt{a+b},\ \omega_{2,4} = \pm\sqrt{a-b}, \tag{4.20}$$

where

$$a = \frac{1}{2}\left(\omega_{01}^2 + \omega_{02}^2 + \frac{R_\mathrm{g}}{L_1 L_2}\right), \tag{4.21}$$

$$b^2 = a^2 - \omega_{01}^2\omega_{02}^2. \tag{4.22}$$

According to Eq. (4.20), the EPD condition requires

$$b = 0, \tag{4.23}$$

and the EPD angular frequency is $\omega_\mathrm{e} = \pm\sqrt{a}$. Here, we assume positive values for a in order to have a real EPD angular frequency and we will only refer to positive values of ω_e in the following. From Eq. (4.22), the EPD condition is rewritten as $a^2 = \omega_{01}^2\omega_{02}^2$. Since we look for real-valued EPD frequencies, $a > 0$, and from Eq. (4.21) one has

$$\omega_{01}^2 + \omega_{02}^2 - \omega_\mathrm{gs}^2 > 0, \tag{4.24}$$

where it has been convenient to define the equivalent gyrator frequency $\omega_\mathrm{gs}^2 = -R_\mathrm{g}/(L_1 L_2)$ for the series-series configuration (note that $\omega_\mathrm{gs}^2 > 0$ because one inductor is negative). The EPD frequency is calculated by using Eqs. (4.21), (4.22), and (4.23) as

$$\omega_{\mathrm{e}} = \sqrt{\tfrac{1}{2}\left(\omega_{01}^2 + \omega_{02}^2 - \omega_{gs}^2\right)} = \sqrt{\omega_{01}\omega_{02}}. \tag{4.25}$$

4.5.3 Dispersion Relation of Lossless and Lossy Series-Series Configurations

As an example, we explain the required procedure to obtain an EPD in this configuration by presenting a specific example. Many different combinations of values for the circuit's components will satisfy the EPD condition, and here as an example, we assume this set of values for components: $L_1 = 47\,\mu\mathrm{H}$, $L_2 = -47\,\mu\mathrm{H}$, $C_2 = -47\,\mathrm{nF}$, and $R_{\mathrm{g}} = 50\,\Omega$. As mentioned before, the desired value for the gyration resistance is achieved by determining the appropriate values for the resistors in the circuit for the gyrator illustrated in Fig. 4.6(b). Also, the capacitance C_1 is determined by solving the quadratic equation from the EPD condition in Eq. (4.23). There are two different values of the capacitance C_1 in the first resonator that satisfy Eq. (4.23), namely $C_{1,\mathrm{e}} = 7.05\,\mathrm{nF}$ and $C_{1,\mathrm{e}} = 139.16\,\mathrm{nF}$. For the smaller value ($C_{1,\mathrm{e}} = 7.05\,\mathrm{nF}$), we obtain a positive value for a in Eq. (4.24), so the EPD frequency is real. On the contrary, the second value ($C_{1,\mathrm{e}} = 139.16\,\mathrm{nF}$) gives us a negative value for a, so the EPD frequency would be imaginary and we discard it since we investigate a gyrator-based circuit with real-valued EPD frequency in this paper. In the following, we select the smaller value for the left resonator capacitance, $C_1 = 7.05\,\mathrm{nF}$. The results in Figs. 4.10(b) and (c) exhibit the two branches of the real and imaginary parts of perturbed eigenfrequencies obtained from the eigenvalue problem, varying the gyration resistance R_{g} in the neighborhood of $R_{\mathrm{g,e}} = 50\,\Omega$. Here, only the two solutions with $\mathrm{Re}\,(\omega) > 0$ are shown in Figs. 4.10(b) and (c). In this example, we obtain $\omega_{\mathrm{e}} = 1.08 \times 10^6\,\mathrm{rad/s}$ and the coalesced eigenvalues at EPD are exceedingly sensitive to perturbations in system parameters.

The time domain simulation results obtained using the Keysight ADS circuit simulator are

illustrated in Figs. 4.10(d) and (e). These two plots show the voltage $v_1(t)$ in the left resonator, and its spectrum, where we put 1 mV as an initial voltage on C_1. In the circuit simulator, an ideal gyrator has been utilized. According to Fig. 4.10(d), the voltage grows linearly with increasing time. This important aspect is peculiar of an EPD, and it is the result of coalescing system eigenvalues and eigenvectors that also corresponds to a double pole in the system. A linear growth indicates a second-order EPD in the system. We take a fast Fourier transform (FFT) of the voltage $v_1(t)$ to show the frequency spectrum, and the calculated result is illustrated in Fig. 4.10(e). The observed oscillation frequency is $f_o = 172.05\,\text{kHz}$, which is in good agreement with the theoretical value $\omega_e/(2\pi)$ calculated above.

By perturbing the gyration resistance, the operation point moves away from the EPD. By selecting a lower value for the gyration resistance, the system has two different real-valued eigenfrequencies. For instance, we reduce the amount of perturbed parameter by 5% equal to $R_g = 47.5\,\Omega < R_{g,e} = 50\,\Omega$. In the perturbed condition, we do not observe any signal growth in the system with increasing time. If we consider an additive 5% of perturbation in the gyration resistance, i.e., $R_g = 52.5\,\Omega$ ¿$R_{g,e} = 50\,\Omega$, the imaginary part of the angular eigenfrequencies is non-zero, and it causes eigensolutions with damping and growing signals in the system. Since the signal is in the form of $Q_n \propto e^{j\omega t}$, the eigenfrequency with negative imaginary part is associated to an exponentially growing signal.

In lossy circuit, we use the same values as lossless series-series configuration for the resonators and gyration resistance. In Figs. 4.9(b) and (c), γ_1 is varied while we assume $\gamma_2 = 0$. In Figs. 4.9(d) and (e), $-\gamma_2$ is perturbed while $\gamma_1 = 0$. These two figures show the real and imaginary parts of eigenfrequencies when perturbing each resistor individually. The EPD angular frequency is obtained when $\gamma_1 = \gamma_2 = 0$, which is the same EPD frequency as the lossless configuration shown in Section 4.5.2. In Figs. 4.9(b)-(e), we observe the bifurcations of the real and imaginary parts of the eigenfrequencies, so the circuit is very sensitive to

variations in both resistance values. Angular eigenfrequencies here are complex-valued; it means that by perturbing γ_1 or γ_2 away from $\gamma_1 = \gamma_2 = 0$, the circuit gets unstable; hence it starts to oscillate with the fundamental frequency associated with the real part of the unstable angular eigenfrequency. When γ_1 or γ_2 is perturbed from the EPD value, the oscillation frequency is shifted from the EPD frequency, and it could be measured for sensing applications. In Figs. 4.9(b)-(e), both conditions $\gamma_1 > 0$ and $-\gamma_2 > 0$ represent losses, whereas the conditions $\gamma_1 < 0$ and $-\gamma_2 < 0$ represent gains in the circuit through a negative resistance. In both cases, by adding either losses or gains, the system is unstable. We observe more sensitivity when perturbing R_2, because a small perturbation in R_2 results in a larger variation of the eigenfrequencies than when varying R_1. Indeed, a wider bifurcation indicates higher sensitivity.

4.5.4 Frequency Domain Analysis of The Degenerate Resonance

We calculate the total input impedance, $Z_{\text{total}}(\omega)$ (see Fig. 4.10), for the series-series circuit with the same approach discussed in the Section 4.2.5. We calculate the transferred impedance on the left side of the circuit in Fig. 4.10, that is

$$Z_{\text{trans}}(\omega) = \frac{R_{\text{g}}^2}{Z_2}. \tag{4.26}$$

where $Z_2(\omega) = j\omega L_2 + 1/(j\omega C_2)$ is the series impedance on the right side of the circuit. Thus, the total impedance observed from the input port in this circuit is calculated by

$$Z_{\text{total}}(\omega) \triangleq Z_1(\omega) + Z_{\text{trans}}(\omega) = Z_1 + \frac{R_{\text{g}}^2}{Z_2}, \tag{4.27}$$

as shown in Fig. 4.10, where $Z_1(\omega) = j\omega L_1 + 1/(j\omega C_1)$. The complex-valued resonant frequencies are obtained by imposing $Z_{\text{total}}(\omega) = 0$. A few steps lead to the ω-zeros given

by Eq. (4.20). Figure 4.11 shows the zeros of such total impedance $Z_{\text{total}}(\omega)$ for various gyration resistance values. When considering the EPD gyration resistance $R_{\text{g}} = R_{\text{g,e}} = 50\,\Omega$, one has $Z_{\text{total}}(\omega) \propto (\omega - \omega_{\text{e}})^2$, i.e., the two zeros coincide with the EPD angular frequency ω_{e}, that is also the point where the two curves in Fig. 4.11 meet. For gyrator resistances such that $R_{\text{g}} < R_{\text{g,e}}$, the two resonance angular frequencies are purely real. Instead, for $R_{\text{g}} > R_{\text{g,e}}$, the two resonance angular frequencies are complex conjugate, consistent with the result in Fig. 4.11. In other words, the EPD frequency coincides with double zeros or double poles of the frequency spectrum, depending on the way the circuit is described.

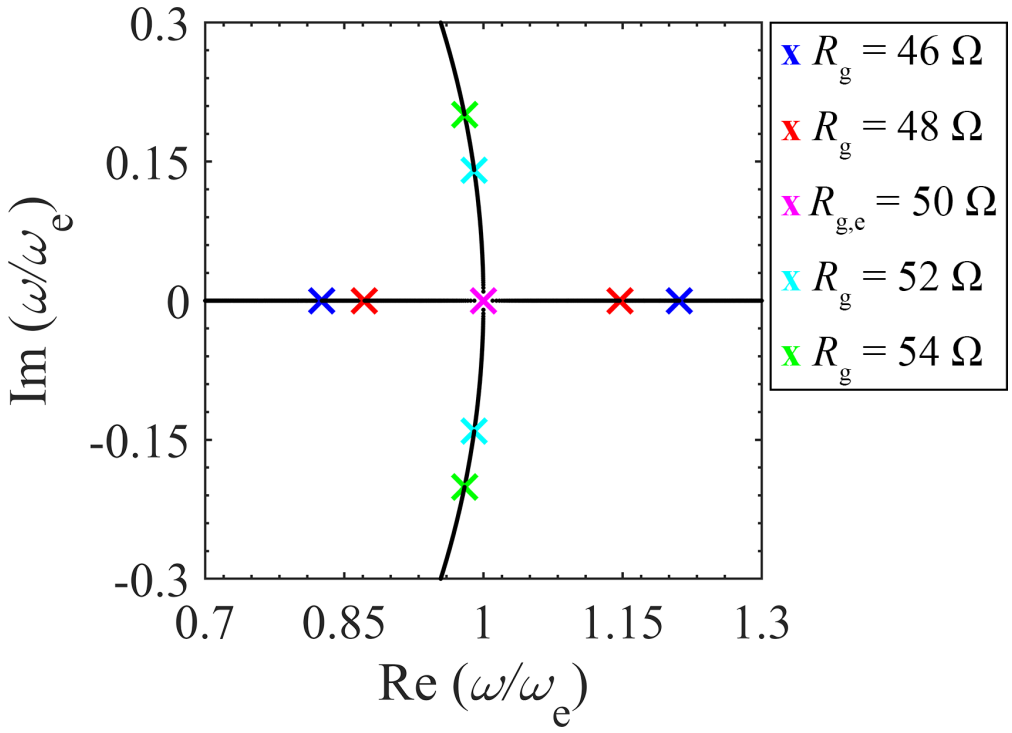

Figure 4.11: Root locus of zeros of $Z_{\text{total}}(\omega)$ of the series-series configuration when varying the gyration resistance. The EPD frequency corresponds to a double zero of the impedance $Z_{\text{total}}(\omega)$.

4.6 Appendix B: Components Sign and Simplification of EPD Condition

1) Series-Series Configuration

In order to obtain an EPD in the series-series configuration using Eqs. (4.21), (4.22) and (4.23) the following equation must be satisfied:

$$(\omega_{01} - \omega_{02})^2 = \omega_{\mathrm{gs}}^2. \tag{4.28}$$

We investigate three possible scenarios to satisfy Eq. (4.28). First, if ω_{01} and ω_{02} are pure real, the values of L_1 or L_2 should be negative to have the same sign on both sides of Eq. (4.28). Thus, one of the resonators should have a negative inductance to have a pure real ω_{01} or ω_{02}. Second, if both ω_{01} and ω_{02} have imaginary values, the considered values for L_1 and L_2 should have the same sign, either positive or negative. When L_1 and L_2 are positive, C_1 and C_2 should be negative or vice versa. Finally, if just one of the ω_{01} or ω_{02} is imaginary and the other one has a real value, there are no conditions to obtain an EPD.

To have a real EPD frequency $\omega_{\mathrm{e}} = \pm\sqrt{a}$, a should be positive and this happens when Eq. (4.24) is satisfied. The region leading to $a > 0$ is represented by the white area in Fig. 4.12(a), whereas the gray area represents the region with $a < 0$. The red curves show different combinations of ω_{01} and ω_{02} which satisfy the EPD condition of Eq. (4.28), assuming ω_{gs} constant. In this figure, $C_1 = 1/\left(\omega_{01}^2 L_1\right)$ and $C_2 = 1/\left(\omega_{02}^2 L_2\right)$ are varied, while R_{g}, L_1 and L_2 are constant. We have shown only results for positive real values of ω_{01} and ω_{02}. The green cross marks the values used for the example provided in Section 4.5.2.

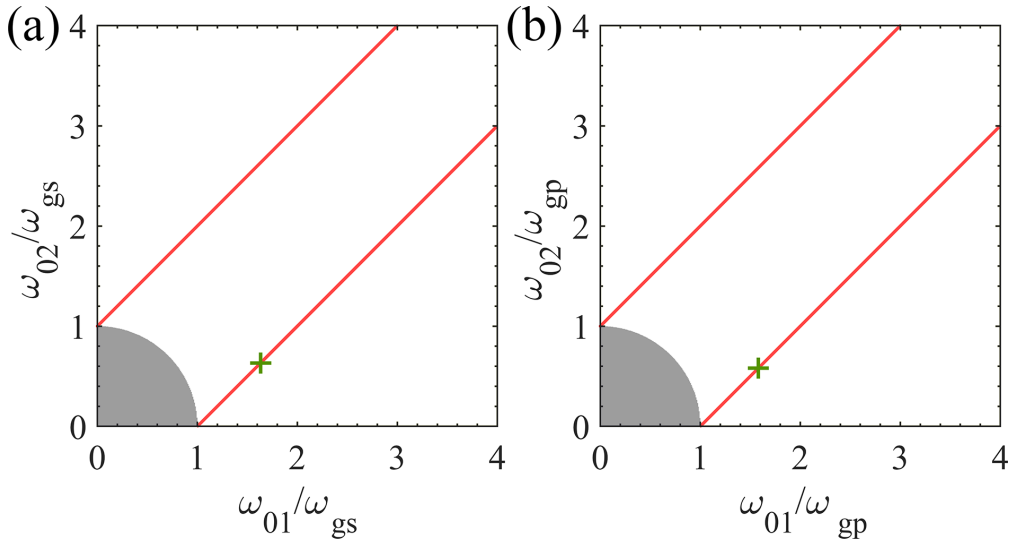

Figure 4.12: Possible combinations of ω_{01} and ω_{02} to have a real eigenfrequency in the (a) series-series and (b) parallel-parallel configurations are shown by the white area, and the gray area represents complex eigenfrequencies based on (a) Eq. (4.24) for series-series configuration and (b) Eq. (4.9) for parallel-parallel configuration. Red curves satisfy (a) Eq. (4.28) for series-series configuration and (b) Eq. (4.29) for parallel-parallel configuration and show possible combinations of ω_{01} and ω_{02} that lead to a real EPD frequency. In the results presented in plot (a), we keep R_g, L_1 and L_2 fixed as in Section 4.5.2, and C_1 and C_2 are varied. In the results presented in plot (b), we keep R_g, C_1 and C_2 fixed as in Section 4.2.2, and L_1 and L_2 are varied.

2) Parallel-Parallel Configuration

In order to get an EPD in the parallel-parallel configuration by using Eqs. (4.6), (4.7) and (4.8) the following condition must be satisfied:

$$(\omega_{01} - \omega_{02})^2 = \omega_{gp}^2. \tag{4.29}$$

We consider three different cases for the parallel-parallel configuration to choose the components' values. First, if ω_{01} and ω_{02} are pure real, the values of C_1 or C_2 should be negative to have the same sign on both sides of Eq. (4.29). Hence, to have a real ω_{01} and ω_{02} one resonator should be made of both negative C and L. Second, if both ω_{01} and ω_{02} have

imaginary values, then C_1 and C_2 should have the same sign. Finally, if just one of the ω_{01} or ω_{02} is imaginary and the other is real, there is no condition that leads to an EPD. In this paper, we consider the first scenario, where both ω_{01} and ω_{02} are real.

To have a real EPD frequency $\omega_e = \pm\sqrt{a}$, a should be positive and this occurs when Eq. (4.9) is satisfied. The region leading to $a > 0$ is represented by the white area in Fig. 4.12(b), whereas the gray area represents the region with $a < 0$. The red curves show different combinations of ω_{01} and ω_{02} which satisfy the EPD condition of Eq. (4.29), assuming ω_{gp} constant. In this figure, $L_1 = 1/(\omega_{01}^2 C_1)$ and $L_2 = 1/(\omega_{02}^2 C_2)$ are varied, while R_g, C_1 and C_2 are constants. We show only results for the positive and real values of ω_{01} and ω_{02}. The points on the red curves, which are located in the white area, can be selected to have an EPD with real and positive EPD frequency. The location marked by the green cross shows the values used for the example in Subsection 4.2.2.

4.7 Appendix C: The Coefficient of The Leading Term of The Puiseux Series

Using Eq. (4.13), we obtain the following expression for the coefficient of the leading term of the Puiseux series,

$$\alpha_1 = \sqrt{\frac{\omega_{01}^2 R_g(\omega_e - \omega_{02}^2) + \frac{\omega_e}{C_1 C_2}}{\frac{1}{C_1 C_2} + R_g(\omega_{01}^2 + \omega_{02}^2 - 6\omega_e)}}, \tag{4.30}$$

when we perturb the capacitance. Instead, when we perturb the inductance, the coefficient is

$$\alpha_1 = \sqrt{\frac{\omega_{01}^2 R_{\mathrm{g}} \left(\omega_{\mathrm{e}} - \omega_{02}^2\right)}{\frac{1}{C_1 C_2} + R_{\mathrm{g}} \left(\omega_{01}^2 + \omega_{02}^2 - 6\omega_{\mathrm{e}}\right)}}. \tag{4.31}$$

4.8 Appendix D: The Impedance Inverter

There are several circuits that can provide for negative capacitances and inductances needed for the gyrator-based EPD circuits. Two circuits to obtain negative impedances by using op amps are shown in Fig. 4.13. The circuit in Fig. 4.13(a) converts the impedance $Z_{\mathrm{Load}}(\omega)$ to $Z_{\mathrm{in}}(\omega) = -Z_{\mathrm{Load}}(\omega)$. Therefore, when $Z_{\mathrm{Load}}(\omega)$ in the circuit in Fig. 4.13(a) is a capacitor in parallel to an inductor, i.e., $Z_{\mathrm{Load}}(\omega) = 1/(j\omega C) \parallel (j\omega L)$, we obtain $Z_{\mathrm{in}}(\omega) = -\left(1/(j\omega C) \parallel (j\omega L)\right)$ at the input port, that corresponds to a negative capacitor in parallel to a negative inductor. In Sec. 4.3, we used this method to realize negative capacitance and inductance in the measurement. Figure 4.13(b) shows an alternative way to achieve negative inductance without an inductor. By using a single capacitor in the mentioned inverter $Z_{\mathrm{Load}}(\omega) = 1/(j\omega C)$ resulting in $Z_{\mathrm{in}}(\omega) = -j\omega R^2 C$, hence, desired negative inductance values are achieved with proper sets of values for R and C. Therefore, it is possible to generate a negative capacitance and a negative inductance by only using capacitive loads.

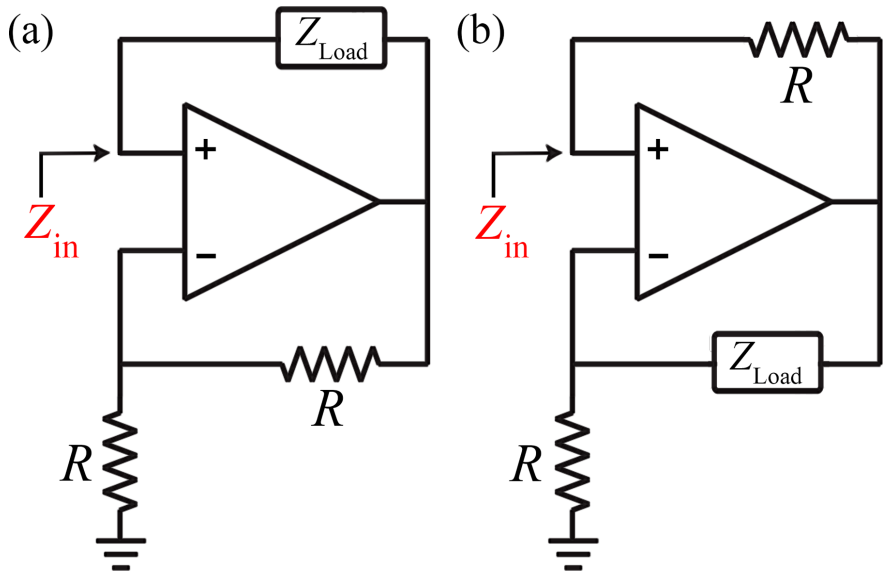

Figure 4.13: Negative impedance converter circuit implementations by using an op amp. (a) Circuit used in the experimental setup where the load is the parallel between a positive capacitor and a positive inductor. (b) A negative inductance can be generated using a positive capacitor (not used in the experimental setup).

4.9 Appendix E: Implementation of The Gyrator-based Circuit

Assembled gyrator-based circuit with different blocks highlighted is shown in Fig. 4.14. The green dashed square shows the designed gyrator using two op amps, and the red dashed square shows the inverter circuit to provide a negative inductor in parallel to a negative capacitor. The circuit also consists of a sensing capacitor C_1, where a variable capacitor (FTVOGUE, model Variable Capacitance Kit) and a series of extra capacitors could be connected in parallel, as shown in the blue box. To demonstrate the sensitivity of the oscillator's frequency to perturbations, we perturb the capacitor C_1 by connecting pairs of extra 2.5 nF capacitors in parallel to C_1. After each perturbation, the oscillation frequency is measured using an oscilloscope and a spectrum analyzer for comparison and verification purposes. Note that on the board, all elements and the DC supply share a common ground

and the VSS (−5 V) and VCC (+5 V) are connected to op amps as shown in Fig. 4.14.

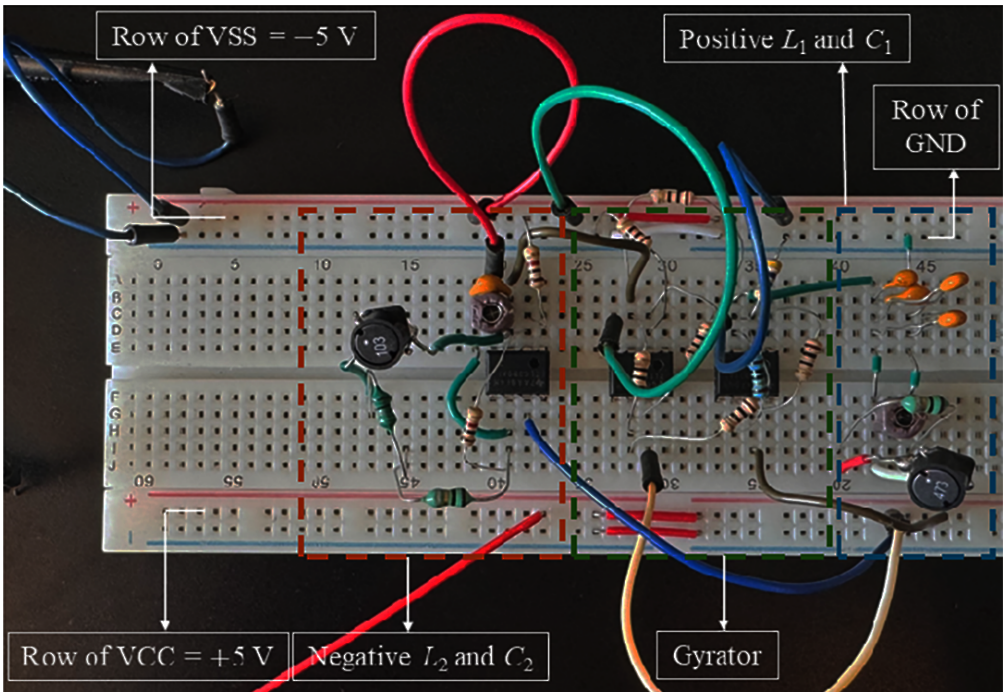

Figure 4.14: Assembled gyrator-based oscillator circuit prototype with different blocks highlighted.

Chapter 5

How to achieve exceptional points in coupled resonators using a gyrator or PT-symmetry, and in a time-modulated single resonator: high sensitivity to perturbations

We study the rise of exceptional points of degeneracy (EPD) in various distinct circuit configurations such as gyrator-based coupled resonators, coupled resonators with PT-symmetry, and in a single resonator with a time-varying component. In particular, we analyze their high sensitivity to changes in resistance, capacitance, and inductance and show the high sensitivity of the resonance frequency to perturbations. We also investigate stability and instability conditions for these configurations; for example, the effect of losses in the gyrator-based circuit leads to instability, and it may break the symmetry in the PT-symmetry-based circuit, also resulting in instabilities. Instability in the PT-symmetry circuit is also generated by

breaking PT-symmetry when one element (e.g., a capacitor) is perturbed due to sensing. We have turned this instability "inconvenience" to an advantage, and we investigate the effect of nonlinear gain in the PT-symmetry coupled-resonator circuit and how this leads to an oscillator with oscillation frequency very sensitive to perturbation. The circuits studied in this chapter have the potential to lead the way for a more efficient generation of high-sensitivity sensors that can detect very small changes in chemical, biological, or physical quantities.

5.1 Motivation and State of the Art

In order to improve the detection limit for small perturbation sensors, an operation based on the exceptional point of degeneracy concept (EPD) can be a valuable option. EPD is a point at which two or more eigenvalues and the corresponding eigenvectors of the system coalesce (i.e., they are degenerate) [31, 123, 33, 34, 124, 35, 40, 125, 62, 38, 39, 36, 37, 64, 52, 126]. The main feature of an exceptional point is the strong full degeneracy of the relevant eigenmodes (including their eigenvectors), justifying the presence of "D" in EPD that stands for "degeneracy" [66]. Exceptional points have been observed in various circuits as in coupled resonators [6, 67, 3, 71, 17, 68, 127], temporally-periodic systems [78, 4, 79], and spatially periodic structures [38, 1, 128].

Sensors are used widely and extensively in many industrial, automotive, and medical applications. In recent years, numerous approaches have been used to sense variations of physical, biological, or chemical changes, e.g., to sense pressure [6, 129, 130], temperature [131], humidity [132], electron beam velocity [100], and chemical or biological quantities [133, 134, 135, 136]. Since sensitivity is an essential feature of measurement systems, various types of sensors are needed to sense. Thus, low-cost, simple, and highlysensitive sensors are desirable to measure different quantities. In conventional sensors, the perturbation by a small value Δ results in shifting the system's eigenfrequency by an amount in the same order

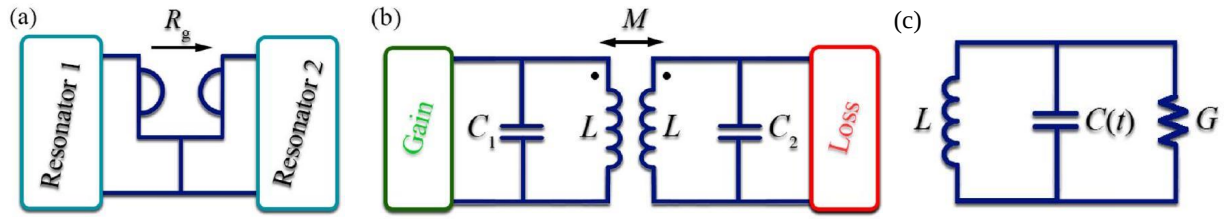

Figure 5.1: Three different configurations where support EPD. (a) Two resonators coupled through gyrator. (b) Two mutually coupledresonator terminated with balanced gain and loss (PT-symmetry circuit). (c) Time-varying circuit which just one component in the circuit needed to change over time periodically. The time-varying component here could be capacitor or inductor or loss.

of Δ (linear behavior), like perturbing a simple LC resonator (or tank). It means that in conventional sensing applications, the perturbation and the measurable changes, like frequency, follow the same trend. To increase the sensitivity, EPDs have offered a new method. Rather than typical detecting systems, where the eigenfrequency changes are of the same order of the perturbation Δ, the change of an eigenfrequency $\Delta\omega$ in a system working at an EPD of order two follows the behavior $\Delta\omega\alpha\Delta^{1/2}$ as shown in [137, 99, 94, 138]. EPDs are found in many physical settings under PT-symmetry properties [40, 6, 67, 3, 17, 76]. However, EPDs are also found in more general forms, which do not require a system to satisfy PT-symmetry [78, 4, 79, 137, 139]. Breaking the symmetry due to the external perturbance eigenvalues split from the degenerated value can be used as a detecting system.

This chapter treats EPDs using four methods: First, by using the circuit's characteristic equation and showing the degeneracy of the eigenmodes. Second, the coalescence of eigenvectors, which is observed analytically. Third, timedomain results obtained from simulations show the linear growth revealing the second-order EPD. The related frequency response is also studied, and it is shown how it is associated with the EPD. Fourth, the approximate fractional power expansion series using the Puiseux series shows the bifurcation and square root-like behavior of the eigenvalues with respect to perturbations.

To address the effectiveness of the discussed EPD circuits, we consider the systems' sensi-

tivity to perturbations of capacitance, inductance, and resistance, which are used as sensing elements, depending on the application. In Section 5.2, we provide an overview of the three circuit configurations leading to second-order EPDs. In Section 5.3, we describe the second-order EPD in the gyrator-based circuit with parallel configuration in lossless and lossy cases. Also, we study the stability of the circuit, manifested in its eigenfrequencies. Details and analysis of the series configuration, not shown here, are discussed in [68, 127, 108, 107]. In Section 5.4, we study the second-order EPD in two coupled resonators with balanced gain and loss satisfying PT-symmetry. In this circuit, we consider nonlinear gain, and by perturbing only one side of the coupled resonator, we break PT-symmetry making the system unstable and causing oscillation. In [6], when a perturbation occurs on one side of the coupled resonator circuit, the other side is tuned accordingly to keep PT-symmetry. This procedure made the operational regime difficult to implement since the exact value of the changes should be known a priori. Moreover, the sign of the perturbation was consistent with the bifurcation direction, which means that only either positive or negative changes in the circuit's quantities could be sensed, not both. Instead, working as in the oscillator regime enables sensing of perturbations with both positive and negative signs. Also, when using nonlinear gain and the oscillatory regime, there is no need to tune a circuit's side to keep symmetry, as we show in Section 5.4. Nonlinearity plays a critical role in this circuit operational regime and helps us find the EPD more easily. While the circuit with EPD and nonlinearity is sensitive to any perturbation sign, the nonlinearity keeps the circuit at an EPD even with a 1% miss-match between the gain and loss. Finally, in Section 5.5, we study a single LC resonator with a time-varying element and show how this simple configuration leads to an EPD by just tuning the modulation frequency. In order to find the EPD, we assume a time-varying capacitor connected to a fixed inductance. Then, the loss effect is taken into account in the analysis. We study the eigenfrequency dispersion by varying modulation frequency, where the LC tank is connected to loss or gain. Also, EPD is found in the time-modulated circuit when the LC tank is terminated with time-varying gain or loss.

5.2 Second-order EPD in Three Distinct Possible Configurations

We discuss here three different methods to obtain a secondorder EPD. First, the degeneracy of the eigenvalues (i.e., eigenfrequencies) occurs in a gyrator-based circuit where two LC tanks are coupled with a gyrator, as shown in Fig. 5.1(a). Second, we study two mutually coupled LC circuits with balanced gain and loss, satisfying PT-symmetry, shown in Fig. 5.1(b).

In Figs. 5.1(a) and (b), both circuits support square root sensitive behavior to perturbations of the resistance, capacitance, and inductance. However, some differences must be observed: for example, the conventional PT-symmetry circuit in Fig. 5.1(b) needs the tuning on both sides to keep the PT-symmetry and avoid self oscillations (arising from non-zero Im(ω)). In other words, it is not possible to change one side only and observe two purely real eigenfrequencies. Instead, the gyrator-based circuit shows that the perturbation on only one side leads to two purely real eigenfrequencies. Thus, there is no need to tune the other side after a perturbation in the gyrator-based circuit. However, any gain or loss in the gyrator-based circuit will cause oscillation and instability, as we will discuss later in more detail.

We show how to turn the instability of a circuit (e.g., the one in Fig. 5.1(b)) to our advantage. Using nonlinear gain, we make the circuit oscillate and saturate, and by perturbing the capacitance on one side, a square root-like change in oscillation frequency is detected. Working in an oscillator regime has certain advantages compared to the conventional PT-symmetry regime of operations in the previous literature [18]. For instance, there is no need to tune the circuit to reach PT-symmetry again after the perturbed values (of a capacitor, for example) are measured in this circuit. Also, nonlinearity helps to fine-tune the circuit to the EPD in an easier way. We discuss these concepts in more detail later on in Section 5.4.

The third circuit we discuss here, shown in Fig. 5.1(c), is a linear time-varying (LTV) system in which an inductor is connected to the time-varying capacitor. This configuration does not need any negative components to realize the EPD, like a negative capacitance and inductance in the gyrator-based circuit or an active gain element in the PT-symmetric coupled-resonator circuit. In addition, we need only one time-varying resonator in this third scheme rather than two fixed resonators. Similarly, an EPD is found in the LTV circuit when an inductor and capacitor are connected in parallel to the time-varying loss or gain.

5.3 EPD in Gyrator-Based Circuit

In this section, we study the first scheme to obtain EPD by using two coupled LC tanks connected through a gyrator. An ideal gyrator is a nonreciprocal linear two-port device whose current on one port is related to the voltage on the other port. More details about the gyrator and various realization methods are discussed in references [114, 140, 141, 142]. The instantaneous relations between voltages and currents on the gyrator are described by

$$\begin{cases} v_2(t) = R_g i_1(t) \\ v_1(t) = -R_g i_2(t), \end{cases} \tag{5.1}$$

where the gyration resistance R_g has a unit of Ohm with the direction indicated by an arrow in the circuit.

We find the eigenvalues (i.e., the eigenfrequencies) and demonstrate the condition for obtaining an EPD at the desired frequency. Finally, we show the sensing potentials by applying a perturbation, and we study the effects of losses on the stability of eigenfrequencies. In addition, by using a time-domain circuit simulator, we verify the circuit behavior predicted by the theoretical calculations and also show that the eigenfrequencies can be predicted by

using the Puiseux fractional power series expansion.

5.3.1 Lossless Configuration

Two parallel LC tanks are coupled by a gyrator, as shown in Fig. 5.2(a). By writing the circuit equations and defining the state vector as $\mathbf{\Psi} \equiv \left[Q_1, Q_2, \dot{Q}_1, \dot{Q}_2\right]^{\mathrm{T}}$, leads to

$$\frac{\mathrm{d}\mathbf{\Psi}}{\mathrm{d}t} = \underline{\mathbf{M}}\mathbf{\Psi}, \tag{5.2}$$

where

$$\underline{\mathbf{M}} = \begin{bmatrix} 0 & 0 & 1 & 0 \\ 0 & 0 & 0 & 1 \\ -\omega_{01}^2 & 0 & 0 & \frac{1}{R_g C_2} \\ 0 & -\omega_{02}^2 & -\frac{1}{R_g C_1} & 0 \end{bmatrix}, \tag{5.3}$$

and $\underline{\mathbf{M}}$ is the circuit matrix. The eigenfrequencies of this circuit are calculated by solving the characteristic equation [127, 143],

$$\omega^4 - \omega^2 \left(\omega_{01}^2 + \omega_{02}^2 + \frac{1}{C_1 C_2 R_g^2}\right) + \omega_{01}^2 \omega_{02}^2 = 0. \tag{5.4}$$

The characteristic equation is quadratic in ω^2 and all the coefficients are real, so both ω and $-\omega$ and ω and ω^* are solutions. The angular eigenfrequencies are determined as

$$\omega_{1,3} = \pm\sqrt{a+b}, \omega_{2,4} = \pm\sqrt{a-b}, \tag{5.5}$$

$$a = \frac{1}{2}\left(\omega_{01}^2 + \omega_{02}^2 + \frac{1}{C_1 C_2 R_g^2}\right), \tag{5.6}$$

$$b^2 = a^2 - \omega_{01}^2 \omega_{02}^2. \tag{5.7}$$

According to Eq. (5.5), a necessary condition for an EPD to occur is $b = 0$, which results in an EPD angular frequency of $\omega_e = \sqrt{a} = \sqrt{\omega_{01}\omega_{02}}$. So, we rewrite Eq. (5.7) as

$$(\omega_{01} - \omega_{02})^2 = -\frac{1}{C_1 C_2 R_g^2} \tag{5.8}$$

In order to obtain an EPD with real angular frequency, we consider the case with purely real value for ω_{01} and ω_{02}, so the value of either C_1 or C_2 should be negative. As a result, to have a real value for ω_{01} and ω_{02}, one resonator needs to be composed of both negative C and L, and more details are discussed in [108, 107]. Another scenario with an unstable uncoupled resonator is conceivable, which was studied for a series configuration in [68]. As an example, here we use the following values for the components shown in Fig. 5.2(a): $L_1 = 100\,\mu\text{H}, L_2 = -100\,\mu\text{H}, C_2 = -100\,\text{nF}$, and $R_g = 50\,\Omega$. Then, the positive capacitance C_1 is found by solving the quadratic equation obtained from the EPD condition. Since the equation of the EPD condition is quadratic, it would yield two answers for C_1. In this chapter, we select the value that leads to real EPD frequency, which is $C_1 = 13.51\text{nF}$. Then the corresponding value for EPD angular frequency is calculated as $\omega_e = 5.22 \times 10^5$ rad/s. In this circuit, an opamp-based invertor could realize the negative components. The designed circuit to obtain negative impedance is shown in Fig. 5.2(b), which converts the impedance $Z_l(\omega)$ to $Z_{\text{invert}}(\omega) = -Z_l(\omega)$. Thus, we can provide the required negative capacitance and inductance by employing that configuration.

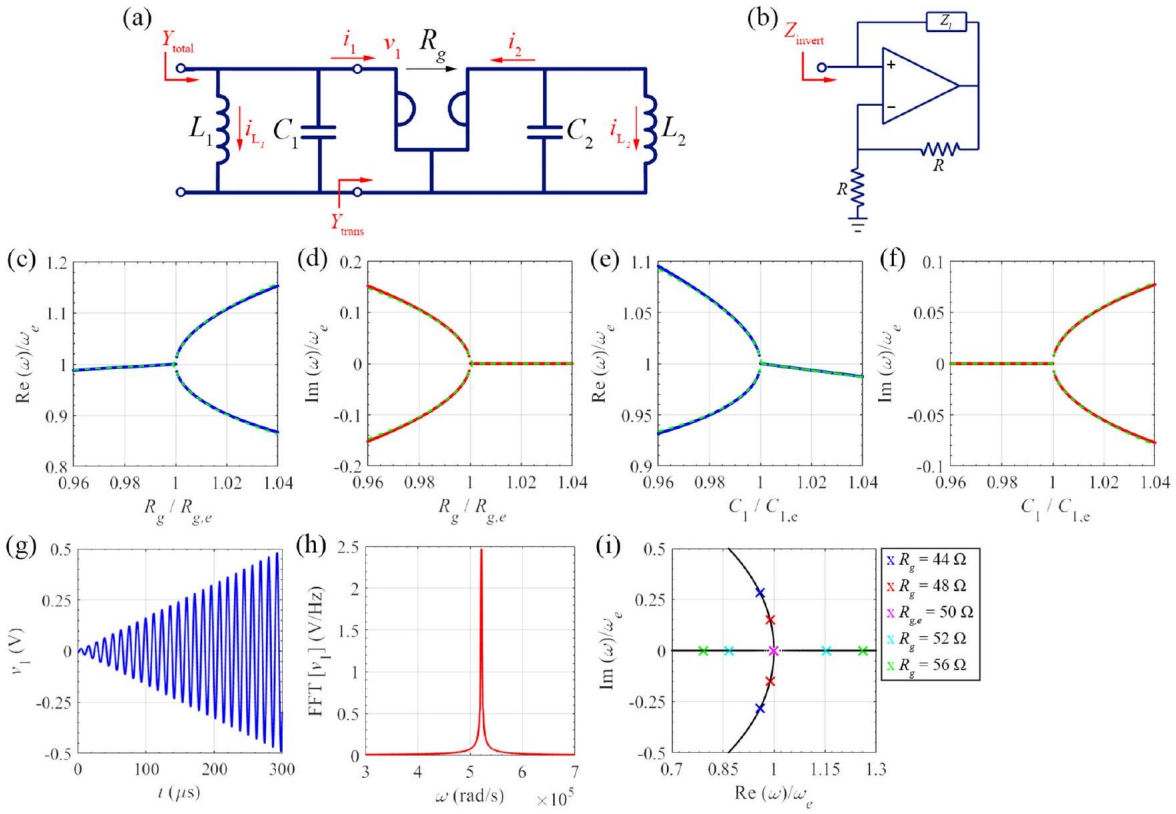

Figure 5.2: (a) The gyrator-based circuit with the ideal gyrator connected two parallel LC tanks. (b) Opamp-based circuit configuration to obtain negative inductance and capacitance. The sensitivity of the (c), (e), real and (d), (f), imaginary parts of the eigenfrequencies to (c), (d) gyration resistance, (e), (f) positive capacitance C_1. Solid lines: solution of eigenvalue problem of Eq. (5.2); green-dashed lines: Puiseux series approximation truncated to its second term. Voltage of positive capacitance $v_1(t)$ at EPD (g) time-domain, and (h) frequency-domain. The frequency-domain result is calculated by applying an FFT with 10^6 samples in the time window of 0 to 3 ms. (i) Root locus of zeros of $Y_{\text{total}}(\omega) = 0$ showing the real versus imaginary parts of resonance frequencies by perturbing gyration resistance. At the EPD, two zero collide at ω_e and the system's total admittance has the form of $Y_{\text{total}}(\omega) \propto (\omega - \omega_e)^2$.

The real and imaginary parts of perturbed eigenfrequencies normalized to the EPD angular frequency by varying R_g are shown in Figs. 5.2(c) and (d), and analogous results by perturbing the positive capacitance C_1 are shown in Figs. 5.2(e) and (f). In addition, the eigenfrequencies are well approximated by using the Puiseux fractional power series expansion (green dashed lines). Appendix 5.7 provides the concept and formulas for this method. The approximated results obtained by the Puiseux series show an excellent

agreement with the "exact" values calculated directly from the eigenvalue problem. The coefficients of the Puiseux series up to second-order for the mentioned example are calculated as, $\alpha_1 = 3.85 \times 10^5$ rad/s, and $\alpha_2 = 1.42 \times 10^5$ rad/s when perturbing R_g, and $\alpha_1 = j2.07 \times 10^5$ rad/s, and $\alpha_2 = -1.72 \times 10^5$ rad/s when perturbing C_1. The bifurcation of the real part of the eigenfrequencies, which indicate the stable sensing region, is observed when $R_g > R_{g,e}$, and $C_1 < C_{1,e}$.

Time-domain simulation result for the voltage $v_1(t)$ is obtained using the Keysight Advanced Design System (ADS) time-domain circuit simulator, and the result is plotted in Fig. 5.2(g). The frequency spectrum corresponding to the simulated time-domain voltage is found by taking the Fast Fourier Transform (FFT), as shown in Fig. 5.2(h). The results are obtained using the initial voltage of 1 mV on the left capacitor C_1. We observe that the voltage increases linearly with time. As well known in circuit theory, this linear growth indicates that two system eigenvalues collided, and a double pole describes the system response. This is a specific property of a second-order EPD. The oscillation frequency is $\omega_o = 5.22 \times 10^5$ rad/s, which is exactly equal to EPD angular frequency ω_e.

We now observe the EPD in a frequency-domain analysis by calculating the circuit's total input admittance $Y_{\text{total}}(\omega)$, as shown in Fig. 5.2(a). We define the two admittances of two LC tanks as $Y_1 = j\omega C_1 + 1/(j\omega L_1)$ and $Y_2 = j\omega C_2 + 1/(j\omega L_2)$. Then the transferred admittance of the Y_2 to the left side is $Y_{\text{trans}}(\omega) = 1/\left(R_g^2 Y_2\right)$. The total admittance observed from the circuit input port is calculated by

$$Y_{\text{total}}(\omega) = Y_1(\omega) + Y_{\text{trans}}(\omega) \tag{5.9}$$

The resonant angular frequencies are achieved by imposing $Y_{\text{total}}(\omega) = 0$; the normalized resonance frequencies to the EPD angular frequency by varying the gyration resistance are

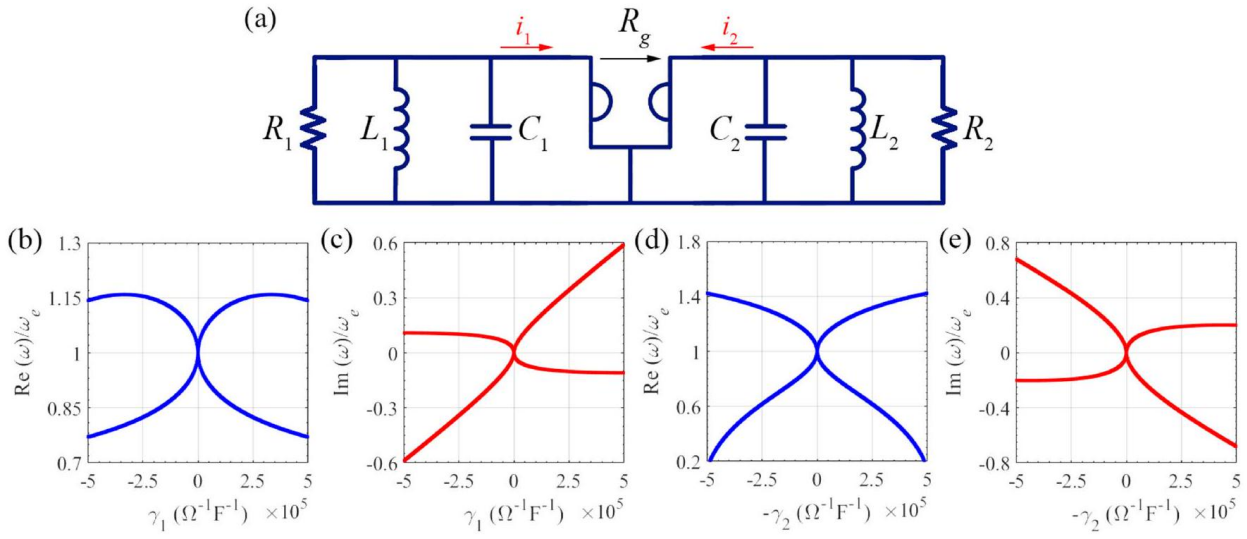

Figure 5.3: (a) Schematic view of the lossy gyrator-based circuit, with a resistor in each resonator. Variation of (b) real and (c) imaginary parts of the angular eigenfrequencies to a resistor perturbation on the left resonator, i.e., when γ_1 changes and $\gamma_2 = 0$. Variation of (d) real and (e) imaginary parts of the angular eigenfrequencies to a resistor perturbation on the right resonator, i.e., when $-\gamma_2$ changes and $\gamma_1 = 0$.

shown in Fig. 5.2(i). Two zeros of total admittance coincide exactly at EPD.

5.3.2 Lossy configuration and stability

In this section, we study the loss effects on the eigenfrequencies of the gyrator-based circuit. Two parallel resistors R_1 and R_2 are connected to both resonators, as shown in Fig. 5.3(a). By writing down the circuit equations and assuming the same state vector as introduced in the lossless case, the associated Liouvillian formalism reads as

$$\frac{\mathrm{d}\mathbf{\Psi}}{\mathrm{d}t} = \underline{\mathbf{M}}\mathbf{\Psi}, \tag{5.10}$$

$$\underline{\mathbf{M}} = \begin{bmatrix} 0 & 0 & 1 & 0 \\ 0 & 0 & 0 & 1 \\ -\omega_{01}^2 & 0 & -\gamma_1 & \frac{1}{R_g C_2} \\ 0 & -\omega_{02}^2 & -\frac{1}{R_g C_1} & -\gamma_2 \end{bmatrix}, \tag{5.11}$$

where $\gamma_1 = 1/(R_1 C_1)$ and $\gamma_2 = 1/(R_2 C_2)$ represent the losses made by resistors. The eigenfrequencies are found by solving the characteristic equation,

$$\omega^4 - j\omega^3(\gamma_1 - \gamma_2) - \omega^2\left(\omega_{01}^2 + \omega_{02}^2 + \gamma_1\gamma_2 + \frac{1}{C_1 C_2 R_g^2}\right) + j\omega\left(\gamma_1\omega_{02}^2 + \gamma_2\omega_{01}^2\right) + \omega_{01}^2\omega_{02}^2 = 0. \tag{5.12}$$

Here, eigenfrequencies ω and $-\omega^*$ are both roots of the characteristic equation. In order to have a stable circuit, eigenfrequencies should be purely real, but the characteristic equation in Eq. (5.12) has some imaginary coefficients. Here, to have purely real eigenfrequencies in the lossy circuit, the odd-power terms of the angular eigenfrequency in the characteristic equation should vanish. Otherwise, a complex eigenfrequency is needed to satisfy the characteristic equation. There is no condition to make both ω and ω^3 coefficients equal to zero [68]. Hence, eigenfrequencies are always complex, leading to instabilities that cause oscillations in the circuit.

By considering the same value for components as already used in the lossless case, the evolution of eigenfrequencies is shown in Figs. 5.3(b) and (c). In these plots, loss on the first resonator is changed, and loss on the second resonator is eliminated. Moreover, in Figs. 5.3(d) and (e), we perturb the loss on the second resonator while the loss on the first resonator is removed. When both losses are zero, the system has the same EPD frequency of a lossless configuration, but perturbed eigenfrequencies are complexvalued for any amount of losses. So, the lossy circuit oscillates at the frequency associated with the real part of the

unstable eigenfrequency. Also, the eigenfrequency is extremely sensitive to either positive or negative variations in the parallel resistances (square root behavior due to the perturbation). A working option is based on preventing the circuit from reaching saturation by switching off the circuit and operating on the circuit's transient response, as was done in [78] for an EPD based on a time modulated circuit.

5.4 EPD in PT-Symmetric Coupled Resonators and Nonlinearity Effects

This section discusses the EPD in two mutually coupled resonators based on PT-symmetry. This is the circuits studied so far by most of the researchers in the last decade [40, 6, 67, 3, 17]. We show the occurrence of an EPD by using the concept of the eigenvector coalescence parameter. Moreover, we study the resonance condition when the total admittance of the circuit is equal to zero (i.e., the double zero condition). The negative conductance in the analyzed circuit could be achieved via cross-coupled or opamp-based circuits. The negative conductance obtained from these transistor-based circuits has nonlinearity effects due to the saturation. Thus, the nonlinearity in negative conductance would alter the circuit operation, as discussed later on. We model the nonlinearity with a cubic $i - v$ characteristic and show the time-domain analysis and frequency responses by using time-domain simulations that are the right tool when nonlinearity is present.

Moreover, we stress the EPD sensitivity characteristic and provide an example where the sensing scheme involves the perturbation of a capacitance. It means that the PT-symmetry is broken. We demonstrate the high sensitivity behavior of the eigenfrequencies for either positive or negative changes in capacitance and show that the system becomes unstable. In [6], the authors discussed sensitivity using two PT-symmetric coupled resonators. They

demonstrated the sensitivity of the eigenfrequencies of the circuit due to the capacitance perturbation while they kept the PT-symmetry configuration. Thus, they needed to tune the other (nonsensing) side of the circuit to have balanced capacitance on both sides to keep the PT-symmetry even after each sensing operation. It means that the exact value of the changes in the sensing capacitance should be somehow known to tune the other side, which is not possible in practical sensing scenarios. Also, they could only measure the perturbation in the bifurcation direction (i.e., only the negative (or positive) capacitance changes, based on the design). Both positive and negative capacitance perturbation sensing ranges should be desirable, and the tuning process should be made easier since there is no priori knowledge of the sensing capacitance variation. Hence, it is not possible to keep the system PT-symmetric while sensing unless possible iterative schemes are researched that guess the unknown capacitance value. Finally, we confirm the eigenfrequency's sensitivity and square root behavior to the perturbation by using the Puiseux fractional power series expansion.

5.4.1 EPD in Mutual Coupled Resonators with PT-Symmetry

Two coupled LC tanks terminated on the left side with a gain given by the negative conductance $-G_1$ and terminated on the right side with loss G_2 are illustrated in Fig. 5.4(a). By writing Kirchhoff's current law, we obtain the two equations for the circuit

$$\begin{cases} \ddot{Q}_1 = -\frac{Q_1}{LC_1(1-k^2)} + \frac{kQ_2}{LC_2(1-k^2)} + \frac{G_1}{C_1}\dot{Q}_1 \\ \ddot{Q}_2 = \frac{kQ_1}{LC_1(1-k^2)} - \frac{Q_2}{LC_2(1-k^2)} - \frac{G_2}{C_2}\dot{Q}_2 \end{cases}, \tag{5.13}$$

where Q_1 is the capacitor charge on the gain side (left resonator), Q_2 is the capacitor charge on the loss side (right resonator), and $k = M/L$ is the transformer coupling coefficient. In addition, $\dot{Q}_1, \ddot{Q}_1, \dot{Q}_2$, and $\ddot{Q}_2$ are the first and the second time derivatives of the capacitors'

charge. We define the state vector as $\mathbf{\Psi} \equiv \left[Q_1, Q_2, \dot{Q}_1, \dot{Q}_2\right]^{\mathrm{T}}$ where superscript T denotes the transpose operation. Therefore, the circuit evolution is described by

$$\frac{\mathrm{d}\mathbf{\Psi}}{\mathrm{d}t} = \underline{\mathbf{M}}\mathbf{\Psi}, \tag{5.14}$$

$$\underline{\mathbf{M}} = \begin{bmatrix} 0 & 0 & 1 & 0 \\ 0 & 0 & 0 & 1 \\ \frac{-1}{LC_1(1-k^2)} & \frac{k}{LC_2(1-k^2)} & \frac{G_1}{C_1} & 0 \\ \frac{k}{LC_1(1-k^2)} & \frac{-1}{LC_2(1-k^2)} & 0 & -\frac{G_2}{C_2} \end{bmatrix}. \tag{5.15}$$

Assuming signals in the form of $Q_n \propto e^{j\omega t}, C_1 = C_2 = C_0$ and $G_1 = G_2 = G$; we get the eigenfrequencies of the circuit by solving the characteristic equation, $\det(\underline{\mathbf{M}} - j\omega\underline{\mathbf{I}}) = 0$, leading to

$$\begin{cases} \omega_{1,3} = \pm\omega_0\sqrt{\frac{1}{1-k^2} - \frac{\gamma^2}{2} - \sqrt{b}} \\ \omega_{2,4} = \pm\omega_0\sqrt{\frac{1}{1-k^2} - \frac{\gamma^2}{2} + \sqrt{b}} \end{cases}, \tag{5.16}$$

where

$$b = -\frac{1}{1-k^2} + \left(\frac{\gamma^2}{2} - \frac{1}{1-k^2}\right)^2. \tag{5.17}$$

In the above equations, $\gamma = G\sqrt{L/C_0}$ and $\omega_0 = 1/\sqrt{LC_0}$. According to Eq. (5.17), the required condition to obtain an EPD is $b = 0$, which leads to an EPD angular frequency of

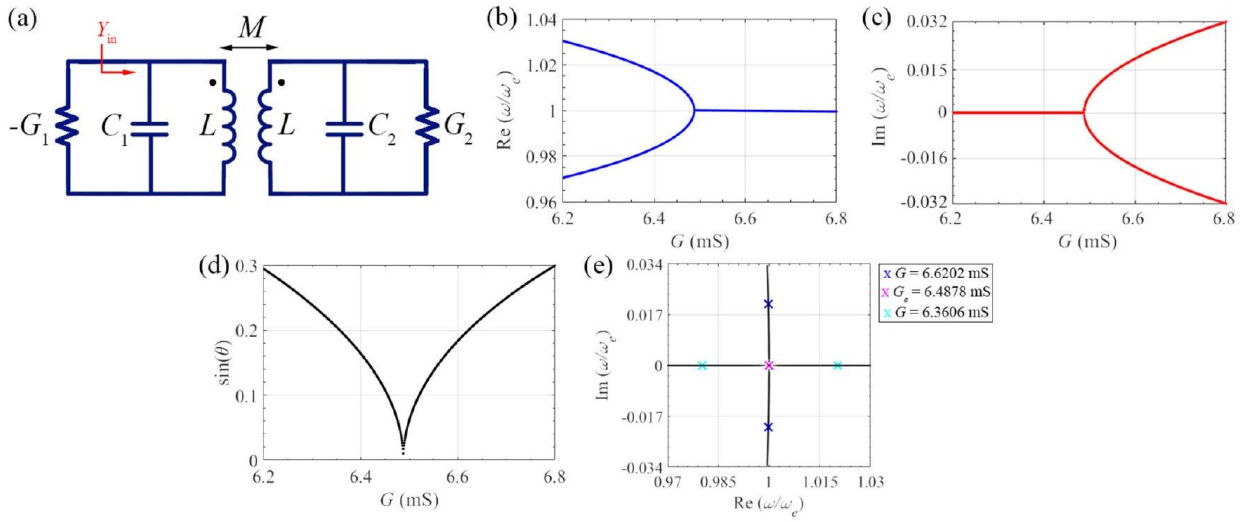

Figure 5.4: (a) Two mutually coupled LC tanks terminated with balanced gain on the left and loss on the right side $G_1 = G_2 = G$; (b) real and (c) imaginary parts of evaluated eigenfrequencies by perturbing G. In the illustrated plots, only eigenvalues with the positive real parts are drawn. (d) The coalescence factor corresponding to calculated eigenvectors which showing the degeneracy of two eigenvectors exactly at G_e(e) Root locus of zeros of $Y_{in}(\omega) - G = 0$ showing the real and imaginary parts of resonance frequencies of the circuit when perturbing both load resistance and gain G. At the EPD, the system's total admittance is $Y_{\text{in}}(\omega) - G_e \propto (\omega - \omega_e)^2$; hence it shows a double zero at ω_e.

$$\omega_e = \frac{\omega_0}{\sqrt[4]{1-k^2}}. \tag{5.18}$$

In the presented example, we use $L = 1\mu\,\text{H}$, $C_1 = C_2 = 1\,\text{nF}$, where inductors are mutually coupled via $k = 0.2$, and terminated with balanced gain and loss $G_1 = G_2 = G$. After solving the eigenvalue problem, the evolution of real and imaginary parts of the eigenfrequencies are shown in Figs. 5.4(b) and (c). The eigenfrequencies of the circuit coalesce at a specific balanced gain/loss value of $\gamma = \gamma_e = 0.205$, where γ_e that leads to an EPD is derived as

$$\gamma_e = \frac{1}{\sqrt{1-k}} - \frac{1}{\sqrt{1+k}}. \tag{5.19}$$

To validate the results, we assume $\gamma = 0$, which means there is no gain or loss in the sys-

tem and it results in two simple mutual LC tanks. The mentioned circuit has two pairs of eigenfrequencies $\omega_{1,3} = \pm\omega_0/\sqrt{1+k}$ and $\omega_{2,4} = \pm\omega_0/\sqrt{1-k}$. If we remove the coupling, i.e., $k = 0$, the eigenfrequencies are equal to the independent LC tank circuits $\pm\omega_0$. For the values, $0 < \gamma < \gamma_e$, the system's eigenfrequencies are purely real, and the system has two fundamentals real eigenfrequencies. For the values, $\gamma_e < \gamma$, the two eigenfrequencies are complex conjugate, and system solutions grow or damp depending on the sign of the imaginary part of the angular eigenfrequencies; the system exhibits self (unstable) oscillations at the frequency associated with the real part of the eigenfrequency. The eigenvector coalescence factor is defined to evaluate how the circuit's operation point is close to an EPD and measure the coalescence of two eigenvectors. It is defined as C.F. $= |\sin(\theta)|$, where $\cos(\theta)$ is

$$\cos(\theta) = \left(\frac{|\langle \mathbf{\Psi}_1, \mathbf{\Psi}_2 \rangle|}{\|\mathbf{\Psi}_1\| \, \|\mathbf{\Psi}_2\|} \right). \tag{5.20}$$

In the determined equation $\langle \ , \ \rangle$ is the inner product and $\|\|$ denotes the eigenvector norm. The coalescence factor for the presented example is shown in Fig. 5.4(d). As we observe in this plot, two eigenvectors have coalesced at the corresponding value for EPD.

5.4.2 Root locus of zeros of admittance

In this section, the resonance condition based on the vanishing of the total admittance is studied. We find the admittance Y_{in}, shown in Fig. 5.4(a), and demonstrate its double zero at the EPD. The resonance condition for this circuit is expressed as

$$Y_{in}(\omega) - G = 0. \tag{5.21}$$

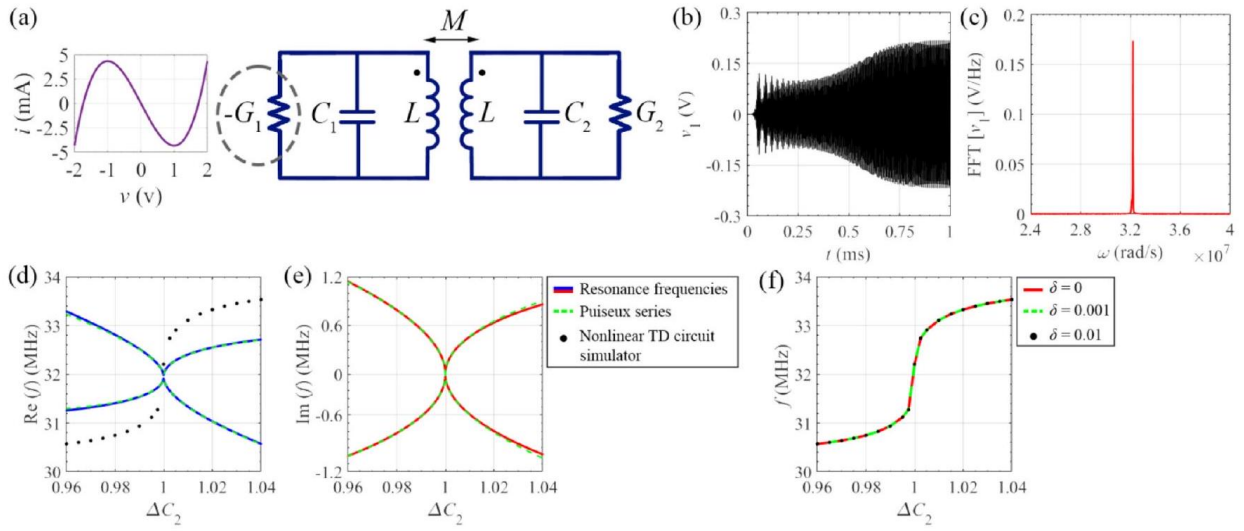

Figure 5.5: (a) Two mutually coupled LC tanks terminated with nonlinear gain on the left and linear loss resistance on the right side where always $G_1 = 1.001 \times G_2$. (b) Time domain response. (c) Frequency response of the gain-side capacitor voltage at the EPD point. (d) Real and (e) imaginary parts of the eigenfrequencies versus load capacitance perturbation ΔC_2; solid line: result from $\det(\underline{\mathbf{M}} - j\omega\underline{\mathbf{I}}) = 0$; green dashed line: Puiseux fractional power series expansion terminated to its second order; black dots are obtained from the nonlinear time domain simulation. (f) Oscillation frequency versus load capacitance perturbation for three different mismatches between gain and loss $\delta = 0$, 0.001, 0.01: the three different gains provide the same saturated oscillation frequencies.$v_c\,(0^-) = 50\,\text{mV}$, and $f_m = 63.95\,\text{kHz}$.

Here, the circuit is PT-symmetric, assuming linear gain and loss with $G_1 = G_2 = G$. We calculate the eigenfrequency by finding the zeros of the $Y_{in}(\omega) - G$, which results in the same eigenfrequencies obtained from $\det(\underline{\mathbf{M}} - j\omega\underline{\mathbf{I}}) = 0$. From the zeros trajectory, both ω and $-\omega$ and ω and ω^* are solutions of Eq. (5.21), and we only show the eigenfrequencies with positive real value in Fig. 5.4(e).

5.4.3 Nonlinear Gain and Oscillator Characteristics

In this section, we discuss the oscillator characteristics and nonlinear gain effects in two wireless coupled resonators, as in Fig. 5.5. The transient and frequency response of the system are discussed when using a cubic (nonlinear) negative conductance model of the gain element. The system's parameters are the same as in the previous section where $G_1 = G_2 =$

$G_e = 6.49$ mS, and the EPD angular frequency is $\omega_e = 3.19 \times 10^6$ rad/s. The relation between voltage and current of the nonlinear negative conductance is [8]

$$i = -G_1 v + \alpha v^3, \tag{5.22}$$

where $-G_1$ is the small-signal negative conductance and $\alpha = G_1/3$ is a third-order nonlinearity that is related to the active device's saturation. We now assume the small-signal nonlinear gain G_1 to be slightly bigger than the balanced loss, as $G_1 = 1.001G_2 = 1.001G_e$ to make the circuit slightly unstable (slightly breaking PT-symmetry). The timedomain response and frequency response obtained from Keysight ADS time-domain circuit simulator are shown in Figs. 5.5(b) and (c), where the circuit operates in the proximity of the EPD. To show the sensitivity of this oscillator, we perturb the capacitor C_2 on the lossy side by 0.5%. The oscillation frequency at each perturbation, shown with the black dots, is found by taking the FFT of the time-domain voltage signal at the capacitor C_1 (on the gain side) after reaching saturation. The FFT is calculated by using 10^6 samples in the time window of 1000 periods after saturation, for each perturbed case. The system shows a distinct saturated oscillation frequency at each perturbed capacitor value. The frequency shift from the case without perturbation could be easily measured. For the sake of comparison with the linear case, solid blue and red lines in Figs 5.5(d) and (e) show the eigenfrequency evolution versus load capacitance perturbation as $\Delta C_2 = (C_2 - C_{2,e})/C_{2,e}$ ($C_{2,e}$ is the capacitor's value at EPD) by assuming linear gain for $-G_1$. The green dashed lines show the Puiseux fractional power series expansion truncated to its second order, which exhibits the square-root-like sensitivity of the eigenvalues to a perturbation. Using both linear and nonlinear gain, the resonance frequency behavior shows the square root variation with capacitance perturbation. The difference in the frequency values between the nonlinear time-domain simulation and theoretical eigenvalue solutions arises from the nonlinearity and the subsequent saturation regime. The Puiseux series coefficients are calculated as, $\alpha_1 = 5.35 \times 10^6 - j4.84 \times 10^6$ rad/s,

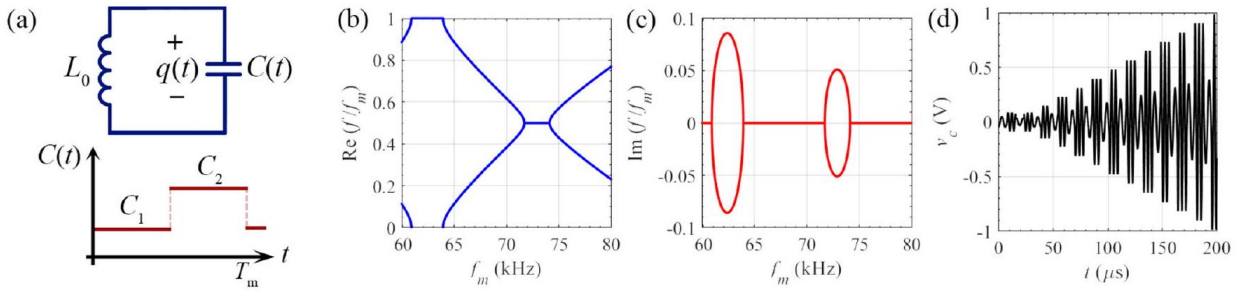

Figure 5.6: (a) Time periodic capacitor connected to the inductor in parallel. The capacitor varies between two values C_1 and C_2 with T_m period, as shown as an inset. (b) Real and (c) imaginary parts of resonanse frequency evolution varying modulation frequency f_m. (b) The time domain signal revealing the second order EPD due to the capacitor's voltage linear growth, with initial condition of $v_c\,(0^-) = 50\,\text{mV}$, and $f_m = 63.95\,\text{kHz}$.

and $\alpha_2 = -7.90 \times 10^6 - j1.62 \times 10^6$ rad/s.

The use of nonlinear gain in the circuit and the saturation effects make the EPD sensing regime robust. An error-correction method is discussed to enhance the robustness of sensing using nonlinearity in [86]. Also, the nonlinearity works as a self-correcting process in two coupled optical ring resonators in [144]. Nonlinearity in our proposed circuit helps maintain the oscillation frequency at the EPD frequency, within a range of small mismatches between gain and loss. The results obtained from the simulation shown in Fig. 5.5(f) demonstrate that even with a 1% mismatch between gain and loss, the circuit oscillates at the same frequency as the case with balanced loss and gain.

The red curve shows the oscillation frequency for the system with an exact match between the (nonlinear) smallsignal gain and loss (i.e., $G_1 = G_2$), the dashed green is related to the case with $G_1 = 1.001G_2$, and the black points denote the case with even larger small-signal gain, $G_1 = 1.01G_2$. They all show the same results in terms of shifted oscillation frequency versus C_2 perturbation.

5.5 EPD in a Time-Varying Single Resonator

We now discuss a completely different way to obtain an EPD in a single resonator containing a time-varying element. It can be used as a highly sensitive circuit. As in the PT-symmetry system with balanced gain and loss discussed in the previous section, the EPD's highly sensitive characteristics are also found in the time-varying single resonator, without the need for a gain component. For instance, we show an EPD in a periodic time-varying simple LC circuit in Fig. 5.6(a). We summarize the general formulation that can be applied to electronic and optical circuits. By assuming the state vector $\mathbf{\Psi}(t) = [\Psi_1(t),\ \Psi_2(t)]^{\mathrm{T}}$ where T is the transpose operator. The differential equation describing the state vector time evolution is

$$\frac{\mathrm{d}\mathbf{\Psi}(t)}{\mathrm{d}t} = \underline{\mathbf{M}}(t)\mathbf{\Psi}(t), \tag{5.23}$$

where $\underline{\mathbf{M}}(t)$ is the 2×2 time-variant system matrix. Here, the system matrix changes periodically in time, unlike the cases discussed in Sections 5.3 and 5.4. Thus, we do not have only one system matrix, and we employ time-periodic analysis to achieve eigenvalues using the transition matrix. For LTV systems with period T_m, the state vector evolution from the time instant t to $t + T_m$ is given by

$$\mathbf{\Psi}\left(t + T_m\right) = \underline{\mathbf{\Phi}}\left(t + T_m, t\right)\mathbf{\Psi}(t), \tag{5.24}$$

where $\underline{\Phi}\left(t_2, t_1\right)$ is the state transition matrix that transfers the state vector $\mathbf{\Psi}$ from t_1 to t_2 [145]. The eigenvalue problem is

$$(\underline{\mathbf{\Phi}} - \lambda\underline{\mathbf{I}})\mathbf{\Psi}(t) = 0, \tag{5.25}$$

where $\underline{\mathbf{I}}$ is a two-by-two identity matrix and λ represents an eigenvalue. The eigenvalues are found by solving the characteristic equation $\det(\underline{\mathbf{\Phi}} - \lambda\underline{\mathbf{I}}) = 0$, leading to

$$\begin{cases} \lambda_p = \frac{\mathrm{tr}(\mathbf{\Phi})}{2} \pm \sqrt{\left(\frac{\mathrm{tr}(\mathbf{\Phi})}{2}\right)^2 - \det(\underline{\mathbf{\Phi}})}, p = 1, 2 \\ \mathbf{\Psi}_p(t) = \left[\Phi_{12}, \lambda_p - \Phi_{11}\right]^{\mathrm{T}}, \end{cases} \tag{5.26}$$

where Φ_{12} and Φ_{11} are elements of the two-by-two matrix $\underline{\mathbf{\Phi}}$. For the illustrated circuit in Fig. 5.6(a), the eigenvalues are $\lambda_p = e^{j2\pi f_p T_m}$, with $p = 1, 2$, where f_p are the two resonance frequencies, with all $f_p \pm n f_m$ harmonics (n is the integer number with modulation frequency $f_m = 1/T_m$).

We now demonstrate the degeneracy in an LTV-LC tank shown in Fig. 5.6(a). The capacitance $C(t)$ varies between two values $C_1 = 1.5C_0$ and $C_2 = 0.5C_0$ with period T_m, where $C_0 = 20$ nF.

Defining the state vector $\mathbf{\Psi}(t) = [q(t), i(t)]^{\mathrm{T}}$ with capacitor's charge $q(t)$ and the inductance current $i(t)$, we find the system matrix as

$$\underline{\mathbf{M}}_p = \begin{bmatrix} 0 & -1 \\ 1/\left(L_0 C_p\right) & 0 \end{bmatrix}, p = 1, 2. \tag{5.27}$$

The resonant frequencies versus modulation frequency f_m are shown in Figs. 5.6(b) and (c). We restrict the plot to frequencies with positive real value, in the range of $0 < f/f_m < 1$, which could be identified as the fundamental Brillouin Zone (BZ) in a time-varying system. EPD happens at $f_{m,e} = 71.72$ kHz and $f_{m,e} = 63.95$ kHz, where the subscript e denotes the corresponding value at the EPD. At an EPD, two eigenvectors and eigenvalues collide, corresponding to a non-diagonalizable transition matrix $\mathbf{\Phi}$ with a degenerate eigenvalue λ_e which is related to the resonance frequency f_e. In this configuration, two scenarios may

happen to have the EPD (i.e., when the state transition matrix $\underline{\mathbf{\Phi}}$ is equivalent to a second-order Jordan-Block matrix). First, when the degenerate eigenvalue is $\lambda_e = -1$, which is related to a resonance frequency $f_e = f_m/2$, and due to the time periodicity, it also happens at harmonics ($f_e = f_m/2 \pm nf_m$). Second, when $\lambda_e = 1$, which is related to $f_e = 0$ and to the harmonics $f_e = \pm nf_m$. Note that here we assume a lossless LC tank (besides the energy injection due to time variation), and we consider the loss effects later on. For modulation values such that $63.95\,\text{kHz} < f_m < 71.72\,\text{kHz}$, the system has two real resonance frequencies, whereas for modulation frequency such that $71.72\text{kHz} < f_m < 74.13$ kHz, the system experiences complex resonance frequencies, which cause instability and oscillation (rising signal associated with the resonance frequency's negative imaginary part). Here, we tend to work on the stable part, which has two different real resonance frequencies. At the EPD frequency associated with a modulation frequency of $f_m = 63.95\,\text{kHz}$, the capacitor's voltage grows linearly, considering the initial condition of $v_c\,(0^-) = 50\,\text{mV}$, which indicates that two eigenfrequencies have coalesced.

5.5.1 Loss Effects on LTV Circuit

We shall consider and study loss effects. To validate the occurrence of the EPDs in temporally LC resonator with losses, we assume an LC tank where the constant conductance G is associated to the losses or gain is connected in parallel, as shown in Fig. 5.7(a). In this circuit, the capacitance C changes between two-level capacitance ($C_1 = 1.5C_0$ and $C_2 = 0.5C_0$) with period T_m, as in the previous lossless case. We consider two scenarios where we connect the system to a loss ($G > 0$) or gain ($G < 0$) element. Defining the state vector $\mathbf{\Psi}(t) = [q(t), i(t)]^{\mathrm{T}}$ with capacitor's charge $q(t)$ and the inductance current $i(t)$, we find the system matrix as

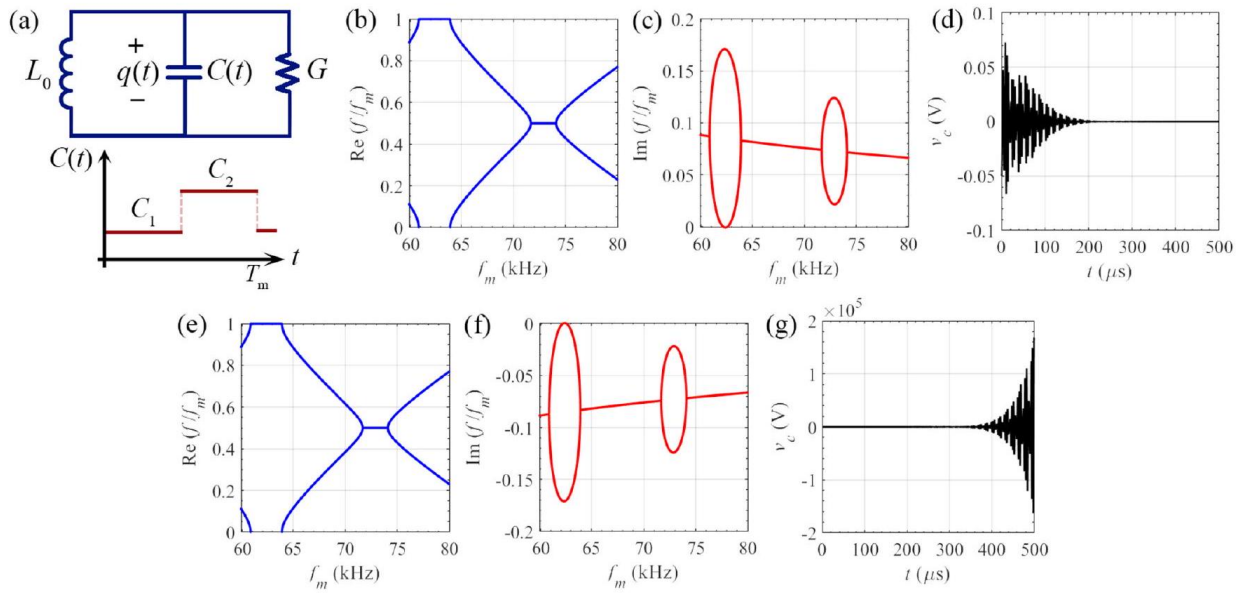

Figure 5.7: (a) Time periodic capacitor $C(t)$ connected to the inductor L_0 and associated loss/gain G in parallel. The capacitor varies between two values C_1 and C_2 with T_m period, as shown in the subset. (b) Real and (c) imaginary parts of resonance frequency evolution varying modulation frequency f_m where the LC tank is connected to the lossy conductance $G = 1$ mS. (d) The time domain signal of the second order EPD which is indicated the decaying signal associated to the positive imaginary part of eigenfrequencies. (e) Real and (f) imaginary parts of resonance frequency evolution varying modulation frequency f_m where the LC tank is connected to the negative conductance $G = -1$ mS. (g) Capacitor's voltage obtained from Keysight ADS circuit simulator, which shows the rising signal. In all time domain simulation, the capacitor has an initial condition of $v_c(0^-) = 50$ mV.

$$\underline{\mathbf{M}}_p = \begin{bmatrix} -G/C_p & -1 \\ 1/(L_0 C_p) & 0 \end{bmatrix}, p = 1, 2. \tag{5.28}$$

Time-Varying Capacitor: lossy case ($G > 0$)

The eigenfrequencies' dispersion diagram in Figs. 5.7(b) and (c) show real and imaginary parts of the eigenfrequencies versus modulation frequency shown. The system parameters are the same as those as in the previous section: $L_0 = 33\,\mu$H, $C_0 = 20$ nF, $G = 1$ mS. Figure 5.7(d) shows the capacitor's voltage at the EPD associated with $f_m = 63.95$ kHz due to

the initial condition of $v_c\,(0^-) = 50\,\text{mV}$ obtained from Keysight ADS time-domain circuit simulator.

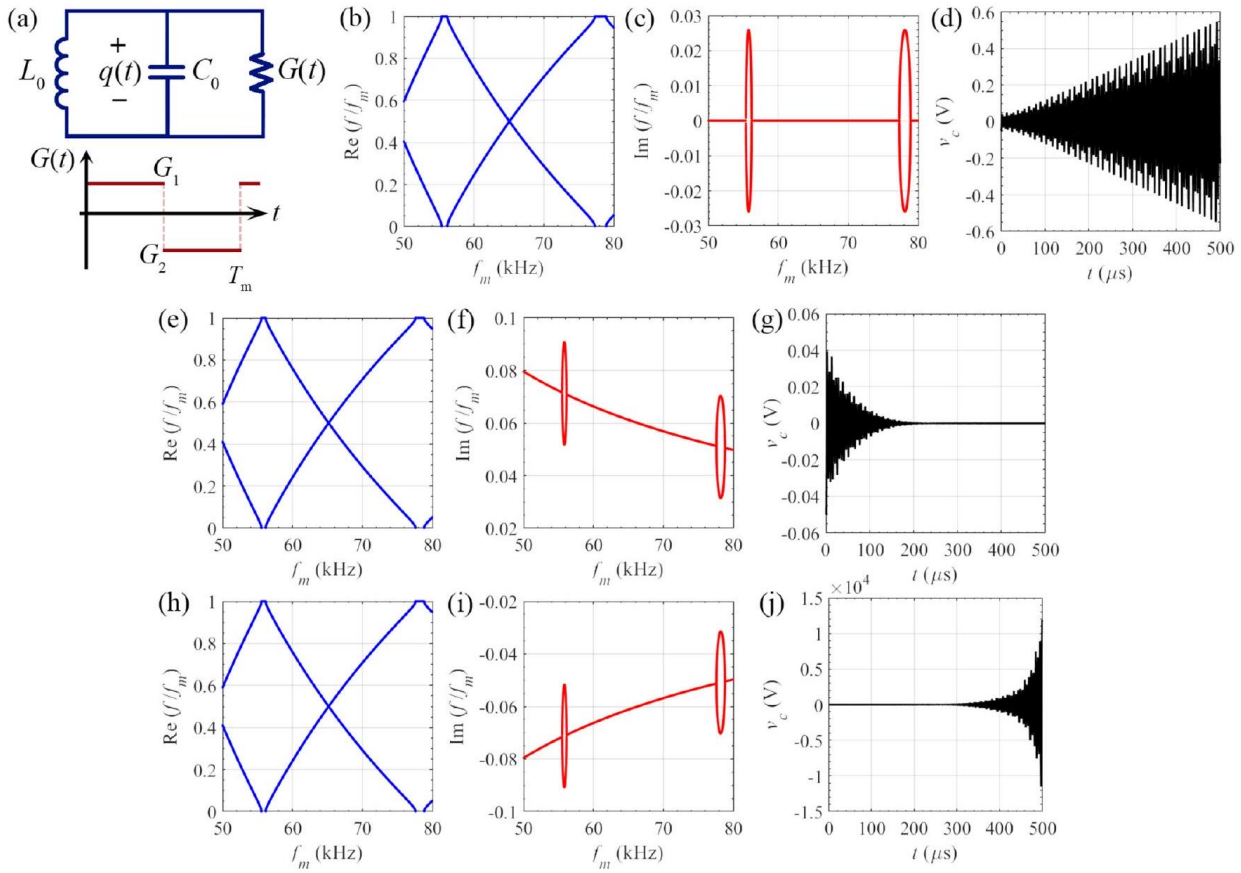

Figure 5.8: (a) Circuit scheme including LC tank connected to the time-varying loss. (b) Real and (c) imaginary parts of eigenfrequency versus modulation frequency f_m, where the loss average is zero. (d) Time-domain signal capacitance's voltage $v_c(t)$, which shows the linear growth at EPD. (e) real and (f) imaginary parts of eigenfrequency versus modulation frequency f_m, where the loss average is positive (G works as a lossy component in average). (g) Time-domain signal capacitance voltage $v_c(t)$ is decaying related to the positive imaginary part of eigenfrequency at EPD. (h) Real and (i) imaginary parts of eigenfrequency versus modulation frequency f_m, where the loss average is negative (G works as a gain component in average). (j) Time-domain signal capacitance voltage $v_1(t)$ is rising related to the negative imaginary part of eigenfrequency at EPD. In all time-domain simulation the capacitor has an initial condition of $v_c\,(0^-) = 50\,\text{mV}$.

In this configuration, the LTV circuit with loss shows that the imaginary part of the eigenfrequency at every EPD is positive. The state vector, which contains the capacitor's voltage and inductor current, is proportional to the $e^{j\omega t}$. An eigenfrequency with a positive imag-

inary part leads to a decaying signal (exponential decay in system state vector), as shown for the case in Fig. 5.7(d).

Time-Varying Capacitor: Gain Case ($G < 0$)

Figs 5.7(e) and (f) show the real and imaginary parts of the system's eigenfrequencies where the system's parameters are selected as $L_0 = 33\,\mu\text{H}, C_0 = 20\,\text{nF}, G = -1\,\text{mS}$. The negative conductance G here shows the gain which results in EPD frequencies with a negative imaginary part. Thus, the state vector is rising exponentially and making the system unstable. Fig. 5.7(g) shows the capacitor's voltage at an EPD associated to $f_m = 63.95\,\text{kHz}$ due to the initial condition of $v_c\left(0^-\right) = 50\,\text{mV}$ obtained from Keysight ADS circuit simulator. The signal shows a rising behavior, which makes the system unstable and oscillating.

5.5.2 Time-Varying Conductance

In this section, we consider the time-varying loss/gain element with the time periodicity of T_m in the LTV circuit in Fig. 5.8(a). We show the occurrence of EPDs. The parallel conductance is set to G_1 for half period, and to G_2 for the other half. Generally, G_1 and G_2 could be positive and negative values acting as loss or gain in this scheme. By defining the state vector $\mathbf{\Psi}(t) = [q(t),\, i(t)]^{\text{T}}$ with capacitor's charge $q(t)$ and the inductance current $i(t)$, we find the system matrix as

$$\underline{\mathbf{M}}_p = \begin{bmatrix} -G_p/C_0 & -1 \\ 1/\left(L_0 C_0\right) & 0 \end{bmatrix}, p = 1, 2. \tag{5.29}$$

We have three scenarios where the time average of the conductance,

$$\mathrm{Avg}(G) = G_1 \frac{T_m}{2} + G_2 \frac{T_m}{2}, \tag{5.30}$$

is positive (lossy), negative (gain), and zero. The average $\mathrm{Avg}(G) > 0$ means that loss is dominant, whereas $\mathrm{Avg}(G) < 0$ means that gain is dominant, and when $\mathrm{Avg}(G) = 0$ the system has balanced gain and loss. The solution for the system's state vector $\mathbf{\Psi}$ (contains the solution of the charge on the capacitor and current on the inductor) is proportional to the eigenfrequency as $\mathbf{\Psi} \propto e^{j\omega t}$. The signal at an EPD, i.e., when the system experiences the coalescence of the eigenvalues at a real ω_e, voltages and currents grow linearly as $te^{j\omega t}$. This is due to the double pole in the Laplace transform of a signal of a system at the EPD. Moreover, when the eigenfrequencies are complex, signals in the system (currents and voltages) experience exponential growth or decay. In this section, the value of components in the LC tank is set as $L_0 = 33\,\mu\mathrm{H}$ and $C_0 = 20\,\mathrm{nF}$.

Time-Varying Conductance: Zero Average $\mathrm{Avg}(G) = 0$

Figs. 5.8(b) and (c) show the complex dispersion diagram, eigenfrequencies versus frequency modulation, with a zero time-average conductance. The conductance for half a period $T_m/2$ is $G_1 = 4\,\mathrm{mS}$ while for the other $T_m/2$ is $G_2 = -4\,\mathrm{mS}$. The EPDs eigenfrequencies are real-valued here, and the dispersion diagram looks the same as the dispersion diagram of the lossless system. To validate it, we calculate the determinant of the transition matrix as

$$\det(\underline{\mathbf{\Phi}}) = e^{-\left(G_1 \frac{T_m}{2} + G_2 \frac{T_m}{2}\right)/(2C_0)} \tag{5.31}$$

Thus, for zero time-average conductance ($\mathrm{Avg}(G) = 0$) we have $\det(\underline{\Phi}) = 1$, which leads to $\lambda_e = \pm 1$. Thus, under the mentioned conditions, the system has a real-valued EPD

frequency f_e. Fig. 5.8(d) shows the time-domain signal obtained from Keysight ADS that indicates the secondorder EPD behavior associated to $f_m = 56.2\,\text{kHz}$, which exhibits a linear growth of the capacitor's voltage as $v_c \propto t\cos(\omega t + \theta)$.

Time-Varying Conductance: Positive Average $\text{Avg}(G) > 0$

The real and imaginary parts of the eigenfrequencies for positive time average conductance ($\text{Avg}(G) > 0$) are shown in Figs. 5.8(e) and (f). The system's parameters are, $G_1 = 4\text{mS}$ and $G_2 = -2\,\text{mS}$, hence the loss is dominant in the system. The EPDs are complex frequencies with a positive imaginary part, which is associated with a damping signal in the circuit, as exhibited in Figure 5.8(g), where modulation frequency is $f_m = 56.2\,\text{kHz}$.

Time-varying Conductance: Negative Average $\text{Avg}(G) < 0$

Figs. 5.8(h) and (i) show the real and imaginary parts of the eigenfrequencies for negative time average conductance ($\text{Avg}\,(G) < 0\,$). The conductances are $G_1 = 2\text{mS}$ and $G_2 = -4\text{mS}$, hence the gain is dominant in the system. The EPDs frequencies have a negative imaginary part corresponding to an exponential rise of the signal making the system unstable, as shown in Fig. 5.8(j), where modulation frequency is $f_m = 56.2\,\text{kHz}$.

5.6 Conclusions

We considered three different circuit configurations supporting an EPD of order two: gyrator-based, PT-symmetry based, and linear time-varying systems. All the configurations exhibit ultra-sensitive responses to perturbations, though their operational regimes differ. Each design has some advantages compared to the others. For example, in a gyrator-based circuit,

the system has purely real perturbed eigenfrequencies when perturbing one component (e.g., a capacitor), while negative capacitance and inductance are needed to realize such a circuit, which require active components. Small losses or gains in this circuit cause instability. Though it seems to be a complication at first sight and may require working in the transient regime before reaching saturation, instability offers the possibility to work in the unstable oscillatory regime. An EPD is also present in two coupled resonators with balanced gain and loss, i.e., satisfying PT symmetry. The presence of gain in one side of the circuit requires active electronic components to provide a precise gain value. To achieve the sensitive feature of the EPD, a component is varied in a standard sensing scheme (e.g., a capacitor), and the perturbed resonant frequency is detected. However, the sensing scheme proposed in the PT-symmetry regime required tuning the capacitance on the nonsensing part of the circuit to keep the circuit under PT-symmetry while the sensing component is varied [6]. This was done to keep the two shifted frequencies real-valued and avoid instabilities. (However, in a sensing scheme, the value of the varied component is usually the one to be measured; hence it is not known a priori). This complication is not needed in the circuit using the gyrator, and it is also not needed in the circuit based on the single LTV resonator.

Compared to the conventional PT-symmetric circuit where people observed shifted resonance frequencies [6, 3], here instead, we have shown that we can work in an oscillatory regime generated by the instability and the nonlinear behavior of the circuit. In other words, we have turned the instability due to broken PT-symmetry (due to a perturbation) to our advantage. The oscillation frequency after reaching saturation is very sensitive to perturbations. Still, it shows the square-root-like dependency with respect to perturbations and the possibility to measure both signs of an element perturbation (this is not possible with the other schemes in the linear regime discussed in this chapter). This nonlinear oscillator scheme is also robust in terms of bringing the system near the EPD, independent of the amount of (nonlinear) small gain used.

Finally, EPDs are found in linear time-varying single resonator circuits where a time-varying capacitor is connected to an inductor. There is no need for gain and lossy elements, though the time modulation requires active components. The effect of additional loss and gain has been discussed for this circuit. We have also shown that timevarying gain or loss connected to a stationary LC tank is another method that leads to EPDs. The simple tuning procedure is one important advantage of the LTV circuit compared to gyrator-based and PT-symmetric circuits. In PT-symmetric and gyrator-based circuits, a tuning process is needed to obtain an EPD, e.g., variable capacitors, gain, or resistors are deemed necessary. On the other hand, in the LTV circuit, the EPD is found by simply changing the modulation frequency, which is done easily in electronics. Note that to obtain the system's resonance frequency, we need a long enough time interval to measure the signal to derive its frequency response with good accuracy. Thus, the rise/fall time of the signal is important. In this chapter, we used the practical quantities as modulation frequency discussed in [78]. There are two work regimes for the system to study the resonance frequencies evolution. First, the circuit needs to be reset periodically, like the circuit in [68], and resonance frequencies are found by looking at the transient response. Second, let the system saturate and then study the system in an oscillatory regime. Note that the system must be designed properly to have a rational rise/fall time in signals. At the same time, fast rising or damping signals cause losing the frequency response resolution.

Acknowlegment

The text of Chapter 5 of this dissertation is a reprint of the material as it appears in Alireza Nikzamir, Kasra Rouhi, Alexander Figotin, and Filippo Capolino. How to achieve exceptional points in coupled resonators using a gyrator or PT-symmetry, and in a time-modulated single resonator: high sensitivity to perturbations. EPJ Applied Metamaterials, vol. 9, p.

14, 2022. The coauthors listed in this publication are Kasra Rouhi, Alexander Figotin, and Filippo Capolino. Alexander Figotin and Filippo Capolino directed and supervised research which forms the basis for the dissertation. This material is based upon work supported by the National Science Foundation (NSF) awards ECCS-1711975 and by the Air Force Office of Scientific Research Award No. FA9550-19-1-0103.

5.7 Appendix A: Puiseux Fractional Power Series Expansion

The sensitivity of a system due to the perturbation of a system's component is detected by measuring changes in the system's observables, like the system's resonance frequency. The Puiseux fractional power series expansion helps us find the eigenvalues ω_p related to the perturbations when working at an EPD of order p. We consider a small perturbation Δ_X of a system parameter X as

$$\Delta_X = \frac{X - X_e}{X_e}, \tag{5.32}$$

where X_e is the parameters' value at the EPD, and X is the parameter's value after applying perturbation.

Away from an EPD of order p, the system matrix $\underline{\mathbf{M}}$ is diagonalizable, and there are p independent eigenvectors. Whereas at an EPD, $\underline{\mathbf{M}}$ is non-diagonalizable, and the system has only one eigenvector and $p-1$ generalized eigenvectors, and p repeated eigenvalues (i.e., eigenfrequencies). Therefore, the system matrix is similar to a matrix that contains a $p \times p$ dimension Jordan block.

For a system with the characteristic equation of $\det\left(\underline{\mathbf{M}}\left(\Delta_X\right)-j\omega\underline{\mathbf{I}}\right)=0$, under the condition $\partial\left[\det\left(\underline{\mathbf{M}}\left(\Delta_X\right)-j\omega\underline{\mathbf{I}}\right)\right]/\partial\omega\neq 0$ at the EPD, the $\underline{\mathbf{M}}$ matrix is made of a $p\times p$ Jordan block. Thus, the perturbed eigenfrequencies could be expressed by the Puiseux fractional power series expansion, including powers of $\Delta_X^{1/p}$ such as

$$\omega_p=\omega_e+\alpha_1\zeta+\alpha_2(\zeta)^2+\alpha_3(\zeta)^3+\ldots \tag{5.33}$$

where $\zeta=\exp(2\pi j/p)\Delta_X^{1/p}$ and the series is a kind of convergent Taylor series of power of $\Delta_X^{1/p}$. Note that the eigenvalues follow the Puiseux fractional power series expansion at and very near the EPD frequency is a way to validate the existence of an EPD (bifurcation of the eigenvalues). Eq. (5.33) shows that the eigenfrequency shift from an EPD $\left|\omega\left(\Delta_X\right)-\omega_e\right|$ is proportional to $\Delta_X^{1/p}$ for small Δ_X. For second order EPDs, a perturbation Δ_X results in the perturbed eigenvalues $\omega_p\left(\Delta_X\right)$ with $p=1,2$, and the Puiseux fractional power series expansion of $\omega_p\left(\Delta_X\right)$ is given by [34, 89]

$$\omega_p\left(\Delta_X\right)\approx\omega_e+\alpha_1(-1)^p\sqrt{\Delta_X}+\alpha_2\Delta_X. \tag{5.34}$$

The first two coefficients are expressed

$$\alpha_1=\left(-\frac{\frac{\partial H(\Delta_X,\omega)}{\partial\Delta_X}}{\frac{1}{2!}\frac{\partial^2 H(\Delta_X,\omega)}{\partial\omega^2}}\right)^{\frac{1}{2}} \tag{5.35}$$

$$\alpha_2=-\frac{\frac{\alpha_1^3}{3!}\frac{\partial^3 H(\Delta_X,\omega)}{\partial\omega^3}+\alpha_1\frac{\partial^2 H(\Delta_X,\omega)}{\partial\omega\partial\Delta_X}}{\alpha_1\left(\frac{\partial^2 H(\Delta_X,\omega)}{\partial\omega^2}\right)}, \tag{5.36}$$

where $H\left(\Delta_X,\omega\right)=\det\left(\underline{\mathbf{M}}\left(\Delta_X\right)-j\omega\underline{\mathbf{I}}\right)$. The coefficients are calculated at the EPD, i.e., at $\Delta_X=0$ and $\omega=\omega_e$.

Chapter 6

Time Modulation to Manage and Increase the Power Harvested from External Vibrations

We investigate how a single resonator with a time-modulated component extracts power from an external ambient source. The collected power is largely dependent on the black precise modulation signal frequency choice. We focus on the power absorbed from external vibration using a mechanical resonator and how time modulation of the damper can make a significant difference in the amount of harvested power, leading to more than 10 times enhancement compared to an analogous system without time modulation. We also find that a narrow band pair of peak and dip in the spectrum of the absorbed power occurs because of the presence of an exceptional point of degeneracy (EPD). In this narrow frequency range, the delay between the damper modulating signal and the external vibrating signal largely affects the collected power. The high frequency-selectivity of EPD-induced power management could potentially be used in sensing and spectrometer applications.

6.1 Motivation and State of the Art

Energy harvesting has attracted considerable interest in electrical [146, 147] and mechanical [148, 149] systems. It offers a battery-less strategy by recovering energy from ambient sources such as vibrations, wind, etc., and transform it into another form, such as electrical power. Applications include micro-electromechanical systems (MEMS) vibration energy harvesters [150, 151], low-power wireless sensors [152] and fluid energy harvesting [153]. In some of these applications, only a small fraction of energy needs to be extracted to power isolated devices. Therefore, collected power from a nearby ambient source can be used to power the inside isolated circuits. A dynamic system has parametric excitation when the effect of force appears as a coefficient of a variable in the governing equations of motion [154, 155]. The parametric excitation leads to a class of time-varying equations, whose coefficients are explicit functions of time. Parametric excitation can enhance the maximum response attainable in different kind of systems [156]. Different vibration-based energy harvesting methods have been used recently [157, 158, 159, 160, 161, 162], though more work needs to be done on utilizing parametric excitation in time-varying systems. Analogous principles could be used to manage the absorption of vibration or filter out particular vibration frequencies in mechanical systems [163].

Low vibration amplitudes cannot be efficiently collected, hence various approaches are developed to increase energy harvesting efficiency [164, 165]. Vibration energy harvesters have been proposed with different nonlinear arrangements that increase their frequency range and dynamic range, most notably using nonlinear springs and dampers [166, 167]. Moreover, semi-active strategies and nonlinear damping in the form of cubic damping [160, 161] and nonlinear piezoelectric converters [168, 169] have been used to extend an energy harvester's dynamic range. In addition, some have analyzed systems where mass changes over time [170, 171, 172]. However, challenges remain about maximizing the amount of energy harvested, and the ideas should be further explored.

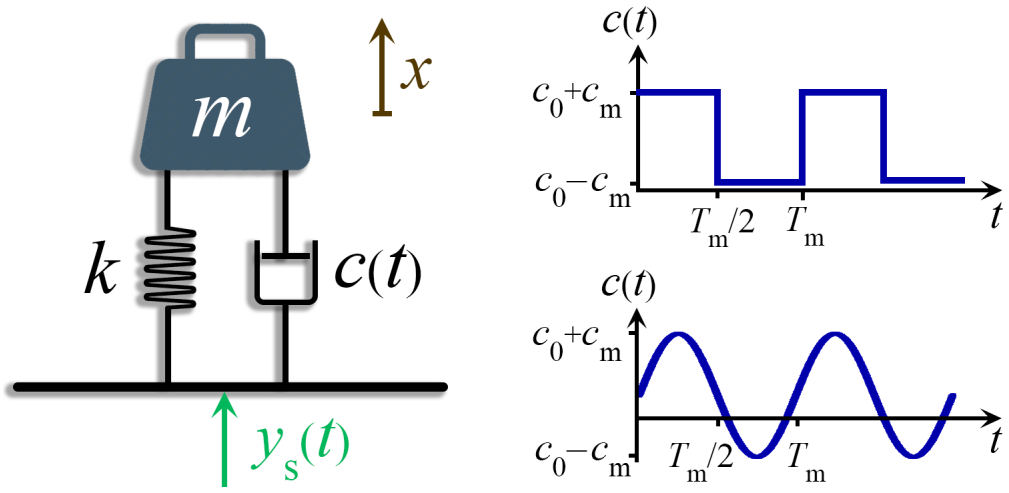

Figure 6.1: Time-modulated mechanical system for kinetic energy harvesting. The external vibrational displacement of the whole system is $y_s(t)$. Two examples of time modulation of the chapter).

In this letter, a resonator with a linear time-periodic (LTP) damper is considered for harvesting or managing energy from an outside source, focusing on a mechanical mass-spring-damper resonator subject to external vibration [148, 173], as shown in Fig. 6.1. However, the physical principle here discussed is general and can be applied to other systems as shown in the appendixes A and D. We demonstrate how parametric LTP modulation can boost motion amplitude, enabling a more efficient flow from the energy source to the harvesting system. By applying time variation to the system, power harvesting is improved (even 10 times) in a specific frequency range compared to the unmodulated system. We observe extremely narrow spectral features in the harvested energy spectrum and explain it by resorting to the concept of exceptional points of degeneracy (EPD). Such degeneracy is a point in the parameter space of a resonating system at which multiple eigenmodes coalesce in both their eigenvalues and eigenvectors [31, 35, 38, 84]. The concept of EPD has been investigated in circuits with loss and/or gain under parity-time symmetry [17, 3], and also in spatially [1, 2] and temporally [4, 174, 78] periodic structures. Moreover, the degenerate eigenvalues of the system are exceptionally sensitive to perturbations in system parameters [33] that can be used to achieve high sensitivity in various sensing scenarios [3, 5, 6, 100, 68, 98].

The kinetic energy harvesting mechanical scheme discussed here is shown in Fig. 6.1. The

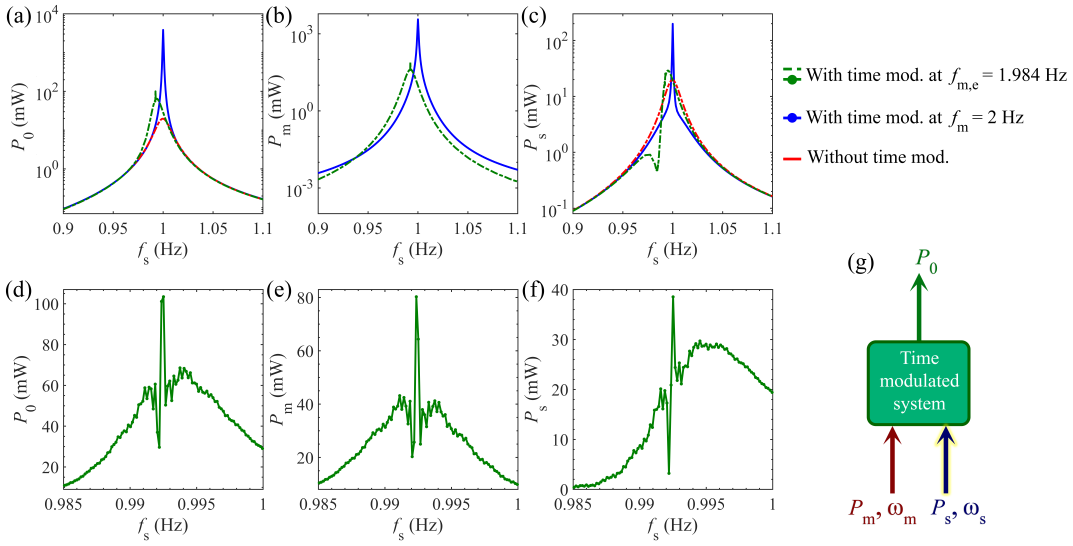

Figure 6.2: Time-averaged power levels after reaching steady state for: (a) P_0 delivered to the damper c_0; (b) P_m provided by the time-varying damper $c_\mathrm{m}(t)$; and (c) P_s extracted (harvested) from the external vibration, by varying the vibration frequency in a wide range around $f_0 = 1\,\mathrm{Hz}$. Two time-modulated cases are considered here: (i) modulation frequency $f_\mathrm{m} = 2\,\mathrm{Hz}$ at the center of the modulation gap (blue), and (ii) modulation frequency $f_\mathrm{m} = f_{\mathrm{m,e}} = 1.984\,\mathrm{Hz}$ (green). For comparison, powers are also shown for the case without time modulation (red). (d)-(f) Zoomed-in analysis for frequencies near the EPD frequency $f_\mathrm{e} = f_{\mathrm{m,e}}/2 = 0.992\,\mathrm{Hz}$ and with time modulation at $f_\mathrm{m} = f_{\mathrm{m,e}} = 1.984\,\mathrm{Hz}$. There is a remarkable highly varying power level around f_e. (g) Collected time-average power P_0 equals the sum of P_m and P_s.

system consists of a mass connected to a spring and a damper with an additional time-varying portion. It is excited by external monochromatic vibration represented by the imposed displacement $y_\mathrm{s}(t)$, caused by an external force that drives the mechanical resonator. Here, m is the mass, k is the spring stiffness constant, $c(t) = c_0 + c_\mathrm{m}(t)$ is the damping parameter that includes a constant part c_0 and a time-periodic one $c_\mathrm{m}(t)$ of period T_m and x represents the mass displacement. The electric counterpart circuit, the possible practical methods to realize time-modulated dampers and the realistic application of a spring-mass-damper model are discussed in Appendix A. The governing equation of the time-varying system is

$$m\ddot{x} + c(t)(\dot{x} - \dot{y}_\mathrm{s}) + k(x - y_\mathrm{s}) = 0. \tag{6.1}$$

The constant damping coefficient $c_0 = c_\mathrm{p} + c_\mathrm{t}$ represents the energy losses within the system due to parasitic loss mechanisms c_p (e.g., viscous friction with air), and by the intentional mechanism of damping c_t, i.e., the mechanical energy extracted by the transduction mechanism [175, 176, 177]. Hence, part of the mobile mass's kinetic energy is lost in mechanical parasitic damping and some other is turned into electricity thanks to an energy converter (e.g., magnet/coil, piezoelectric material, variable capacitor, etc.) [178, 179, 180]. Here, we presume that the damping force is proportional to the velocity, which can be described as an electromechanical transducer [181, Ch. 2]. However, our study is general in nature, and this method can be applied to any system described by the differential equation shown in Eq. (6.1). We define the relative mass displacement parameter $z = x - y_\mathrm{s}$, and the governing dynamic equation is rewritten as

$$\ddot{z} + 2\zeta\left(t\right)\omega_0\dot{z} + \omega_0^2 z = -\ddot{y}_\mathrm{s}, \tag{6.2}$$

where $\zeta\left(t\right) = \zeta_0 + \zeta_\mathrm{m}\left(t\right) = c_0/\left(2m\omega_0\right) + c_\mathrm{m}\left(t\right)/\left(2m\omega_0\right)$ is the time-modulated damping rate and $\omega_0 = \sqrt{k/m}$ is the natural angular frequency of the unmodulated and lossless system. Assuming a time harmonic dependence of the form $z \propto e^{j\omega t}$ for the *unmodulated* homogeneous system ($c_\mathrm{m} = 0$ and $y_\mathrm{s} = 0$), we obtain the complex eigenfrequencies $\omega = \omega_0\left(\pm\sqrt{1-\zeta_0^2} + j\zeta_0\right)$ associated to damped oscillations. We define the state vector as $\mathbf{\Psi}\left(t\right) \equiv \left[z, \dot{z}\right]^\mathrm{T}$, where the superscript T denotes the transpose operation, leading to

$$\begin{aligned} \mathrm{d}\mathbf{\Psi}\left(t\right)/\mathrm{d}t &= \underline{\mathbf{M}}\left(t\right)\mathbf{\Psi}\left(t\right) + \begin{pmatrix} 0 \\ -\ddot{y}_\mathrm{s} \end{pmatrix}, \\ \underline{\mathbf{M}}\left(t\right) &= \begin{pmatrix} 0 & 1 \\ -\omega_0^2 & -2\zeta\left(t\right)\omega_0 \end{pmatrix}, \end{aligned} \tag{6.3}$$

where $\underline{\mathbf{M}}(t)$ is the time-variant system matrix. We analyze the power transfer from an external vibration $y_{\mathrm{s}}(t) = y_0 \cos(2\pi f_{\mathrm{s}} t)$, where y_0 is its amplitude and f_{s} is its frequency, into the LTP spring-mass-damper system using a time-domain numerical simulator (see Supplementary Material S1). We determine the time-averaged power P_{s} delivered by the external vibration, the time-averaged power P_{m} delivered by the time modulation, and the time-averaged power P_0 delivered to (or harvested by) the constant damper c_0. Note that f_{m} is the modulation frequency of the time-varying damper. In realistic applications, particularly those on a small scale, mechanical systems are very small, and ambient vibrations are generally low in amplitude (0.1–5 $\mathrm{m/s^2}$) and frequency ($< 100\,\mathrm{Hz}$) [179]. Because of the low energy of some external sources in realistic applications, we investigate how we can maximize both the power P_{s} absorbed from the external source and the power P_0 harvested by the constant damper by using time modulation.

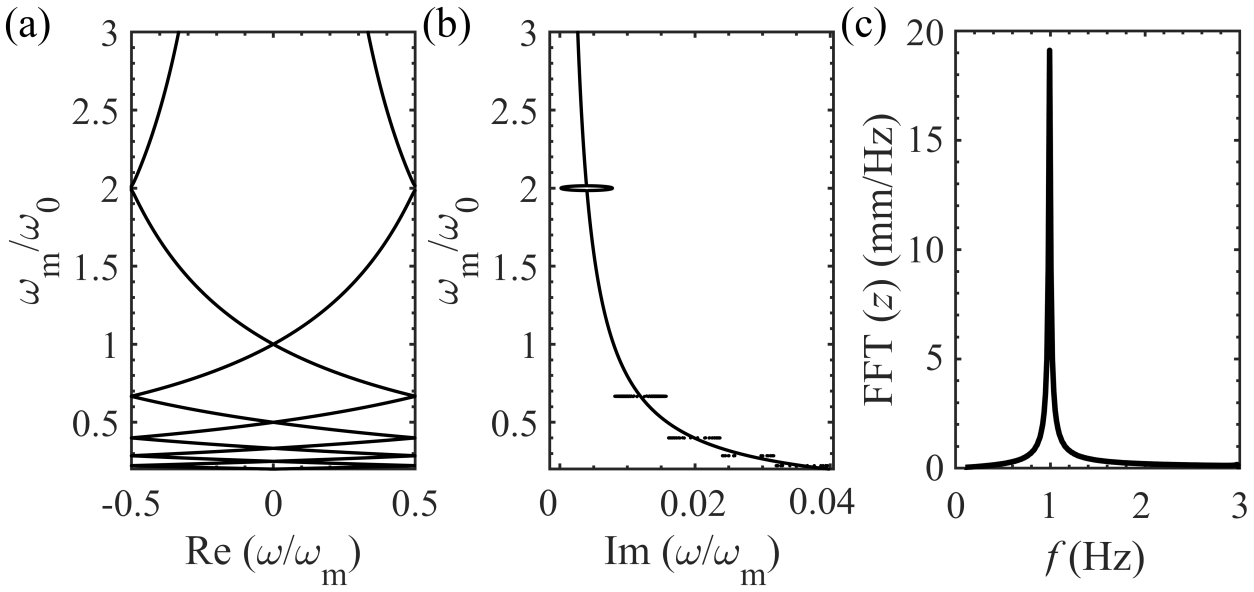

Figure 6.3: The (a) real and (b) imaginary parts of eigenfrequencies $\omega + q\omega_{\mathrm{m}}$, where q is an integer, of the system by varying ω_{m}. (c) Frequency spectrum of the relative mass displacement $z(t)$. The largest frequency spectral component of the displacement occurs at the fundamental harmonic $q = 0$, i.e., at the EPD frequency $f_{\mathrm{e}} = f_{\mathrm{m,e}}/2 = 0.992\,\mathrm{Hz}$.

An example is shown in Fig. 6.2, where $k = 4\pi^2\,\mathrm{N/m}$ and $m = 1\,\mathrm{kg}$ leading to $f_0 = 1\,\mathrm{Hz}$, and $y_0 = 1\,\mathrm{mm}$. We only consider for simplicity a two-level piece-wise constant time-periodic

damping $c(t)$, which is c_0+c_m in the time interval $0 \leqslant t < T_\mathrm{m}/2$ and c_0-c_m in $T_\mathrm{m}/2 \leqslant t < T_\mathrm{m}$. We assume $c_0 = 0.1\,\mathrm{Ns/m}$ and $c_\mathrm{m} = 0.15\,\mathrm{Ns/m}$. We also study the unmodulated system with constant damper $c(t) = c_0$, where maximum energy can be extracted when the excitation frequency f_s matches the natural frequency of the system f_0. In Fig. 6.2 we compare the LTP system with the unmodulated system to show that time modulation has a strong effect on the time-averaged powers P_s and P_0. For the considered modulation frequency of $f_\mathrm{m} = 2\,\mathrm{Hz}$ that is equal to $2f_0$, P_s and P_0 are largely enhanced when f_s is in the neighbor of f_0. The plot in Fig. 6.2(c) shows the maximum harvested power in the unmodulated system is $P_\mathrm{s} = 19.7\,\mathrm{mW}$, whereas the maximum power that the time modulated system absorbs from the source is $P_\mathrm{s} = 198.4\,\mathrm{mW}$(10 times higher).

The results in Figs. 6.2(a)-(c) show also another interesting feature, i.e., the very narrow frequency range around $f_\mathrm{s} = 0.992\,\mathrm{Hz}$ (which is half of $f_\mathrm{m,e}$) where the power exhibits a sharp maximum and a local minimum when $f_\mathrm{m} = f_\mathrm{m,e}$, where $f_\mathrm{m,e} = 1.984\,\mathrm{Hz}$ is a modulation frequency that leads to the EPD. This rapid power level variation is shown better in the zoomed-in frequency region in Figs. 6.2(d)-(f). To understand the reasons for this very sharp variations in the time averaged power values we look at the eigenvalues of the system and their degeneracy.

We look at the eigenstates of the time-varying system without external vibration. The evolution of the state vector in the LTP system with time periodicity T_m is given by $\mathbf{\Psi}(t+T_\mathrm{m}) = \underline{\mathbf{\Phi}}(t+T_\mathrm{m}, t)\,\mathbf{\Psi}(t)$, where $\underline{\mathbf{\Phi}}(t+T_\mathrm{m}, t) = e^{\underline{\mathbf{M}}_2 T_\mathrm{m}/2} e^{\underline{\mathbf{M}}_1 T_\mathrm{m}/2}$ is the state transition matrix, where $\underline{\mathbf{M}}_1$ and $\underline{\mathbf{M}}_2$ are the system matrices in the first and second time intervals [182, Ch. 2]. We look for eigensolutions of the system that satisfy

$$\mathbf{\Psi}(t+T_\mathrm{m}) = e^{j\omega T_\mathrm{m}}\mathbf{\Psi}(t)\,, \tag{6.4}$$

where ω (with all the harmonics $\omega + 2\pi q/T_\mathrm{m}$, where q is an integer) is the complex eigenfre-

quency. Therefore, the eigenvalue problem is

$$\underline{\mathbf{\Phi}}\mathbf{\Psi}\left(t\right)=\lambda\mathbf{\Psi}\left(t\right), \tag{6.5}$$

and the eigenvalues $\lambda_n = e^{j\omega_n T_\mathrm{m}}, n = 1, 2$, are obtained by solving the characteristic polynomial equation $\det\left(\underline{\mathbf{\Phi}} - \lambda\underline{\boldsymbol{I}}\right) = 0$. The eigensolutions $\mathbf{\Psi}\left(t\right)$ have Fourier harmonics with frequencies $\omega_n + q\omega_\mathrm{m}$, where $\omega_\mathrm{m} = 2\pi f_\mathrm{m}$ is the modulation angular frequency [4]. When a transition matrix made of real values elements describes the system, the characteristic polynomial has real coefficients, so the eigenvalues are either real or complex conjugate pairs. The transition matrix determinant is written as [182, Ch. 2]

$$\det\left(\underline{\mathbf{\Phi}}\right)=\lambda_1\lambda_2=e^{[\mathrm{tr}(\underline{\mathbf{M}}_1 T_\mathrm{m}/2)+\mathrm{tr}(\underline{\mathbf{M}}_2 T_\mathrm{m}/2)]}, \tag{6.6}$$

where tr is the trace of the matrix. The determinant can be either $\det\left(\underline{\mathbf{\Phi}}\right) = e^{2\mathrm{Im}(\omega_1)T_\mathrm{m}}$, when eigenvalues are complex conjugate pair, or $\det\left(\underline{\mathbf{\Phi}}\right) = e^{js\pi}e^{(\mathrm{Im}(\omega_1)+\mathrm{Im}(\omega_2))T_\mathrm{m}}$, when λ_1 and λ_2 are both real and s is an integer. The two eigenvalues are

$$\lambda_{1,2}=\frac{\mathrm{tr}\left(\underline{\mathbf{\Phi}}\right)}{2}\pm\sqrt{\left(\frac{\mathrm{tr}\left(\underline{\mathbf{\Phi}}\right)}{2}\right)^2-\det\left(\underline{\mathbf{\Phi}}\right)}, \tag{6.7}$$

and the two associated eigenvectors are

$$\mathbf{\Psi}_1=\begin{bmatrix}\varphi_{12}\\ \lambda_1-\varphi_{11}\end{bmatrix},\ \mathbf{\Psi}_2=\begin{bmatrix}\varphi_{12}\\ \lambda_2-\varphi_{11}\end{bmatrix}, \tag{6.8}$$

where φ_{11} and φ_{12} are elements of the matrix $\underline{\mathbf{\Phi}}$. The two eigenvalues are degenerate ($\lambda_1 = \lambda_2 = \mathrm{tr}\left(\underline{\mathbf{\Phi}}\right)/2$) when

$$\mathrm{tr}\,(\underline{\mathbf{\Phi}}) = \pm 2\sqrt{\det\,(\underline{\mathbf{\Phi}})}. \tag{6.9}$$

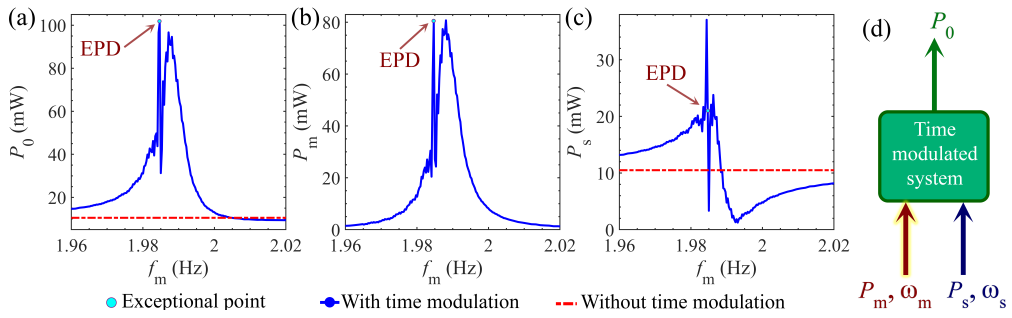

Figure 6.4: Time-averaged powers by varying the modulation frequency f_{m} (blue curves), for the case of $f_{\mathrm{s}} = f_{\mathrm{m,e}}/2$. (a) P_0; (b) P_{m}; and (c) P_{s}. The red dashed line is the time-averaged power level of the unmodulated system. (d) Collected time-average power P_0 equals the sum of P_{m} and P_{s}.

According to Eq. (6.8), degenerate eigenvalues result in degenerate eigenvectors. A transition matrix at an EPD is similar to a Jordan block with two degenerate eigenvalues associated with degenerate eigenvectors. As a matter of energy analysis, in a time-periodic system energy can be transferred into or out of the system via the time-variation mechanism.

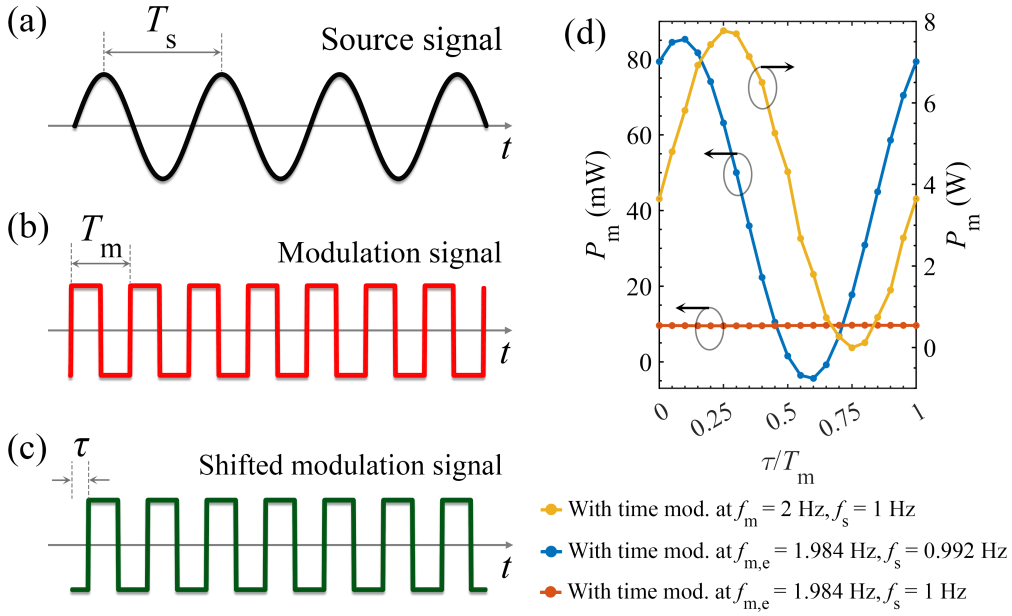

Figure 6.5: (a) Source sinusoidal signal with a period of $T_{\mathrm{s}} = 2T_{\mathrm{m}}$. (b) Piece-wise constant time modulated damper with a period of T_{m} and (c) shifted by a delay τ. (d) Time-averaged power P_{m} versus delay τ for three different scenarios.

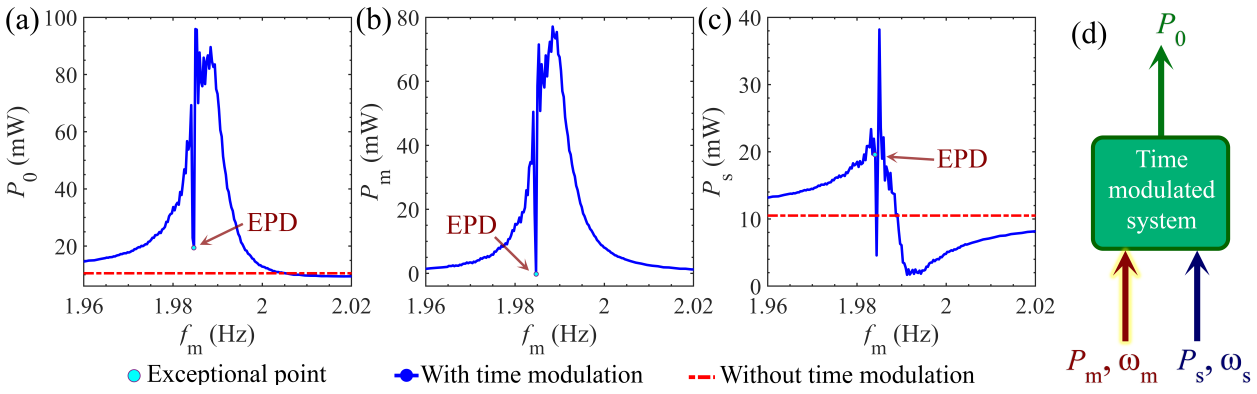

Figure 6.6: Time-averaged power levels, after reaching steady state, as in Fig. 6.4, but assuming a time delay $\tau = 0.51T_{\mathrm{m}}$ in the modulation of the damper, in the case of $f_{\mathrm{s}} = f_{\mathrm{m,e}}/2$.

The system's eigenfrequency dispersion diagram is shown in Figs. 6.3(a) and (b). EPDs happen at two modulated frequencies, $f_{\mathrm{m,e}} = 1.984$Hz and $f_{\mathrm{m,e}} = 2.015$Hz. The quality factor of a resonating system is $Q = \mathrm{Re}\,(\omega)\,/\,(2\mathrm{Im}\,(\omega))$, that is higher for smaller $\mathrm{Im}\,(\omega)$. In general, a higher quality factor implies a higher power harvested by the system. A modulation gap in the dispersion diagram of eigenfrequencies happens when the two eigenfrequencies have two non-vanishing imaginary parts, i.e., between two closeby EPDs. When the modulation frequency is selected in the middle of the modulation gap, i.e., $f_{\mathrm{m}} = 2$Hz, one eigenfrequency has the smaller $\mathrm{Im}\,(\omega)$, corresponding to a better quality factor compared to the two neighbor EPDs at slightly higher and lower frequencies. Thus, we expect the largest improvement in harvested power in the middle of the modulation gap. Also, by selecting $f_{\mathrm{m,e}} = 1.984$ Hz the system experiences harsh changes around $f_{\mathrm{s}} = f_{\mathrm{m,e}}/2 = 0.992$Hz due to the degeneracy of the eigenfrequencies. The spectrum of the relative displacement $z\,(t)$ when the source-free system is modulated at $f_{\mathrm{m}} = f_{\mathrm{m,e}} = 1.984$ Hz and it is excited by an initial condition (see Appendix A) is illustrated in Fig. 6.3(c). The spectrum peak is observed at $f_{\mathrm{e}} = f_{\mathrm{m,e}}/2 = 0.992$ Hz, that is same as the one obtained from solving the eigenvalue problem shown in Figs. 6.3(a) and (b).

When $f_{\mathrm{m}} = f_{\mathrm{m,e}} = 1.984$ Hz, the mechanical system operates at the EPD. The frequency spectrum in Fig. 6.3(c) shows that the first harmonic at $f = f_{\mathrm{e}} = f_{\mathrm{m,e}}/2 = 0.992$ Hz,

carries the maximum power. After setting $f_s = f_e = f_{m,e}/2 = 0.992\,\text{Hz}$, Fig. 6.4 shows the powers by varying the modulation frequency around its EPD value $f_{m,e} = 1.984\,\text{Hz}$. In this plot, time-modulated case is in blue curve, whereas the red dashed-line reminds the power values of the system without time-modulation. The numerical results show that the system operating close to EPD (cyan point) harvests more power from the external source ($P_s = 20.9\,\text{mW}$) compared to the system without time-modulation ($P_s = 10.5\,\text{mW}$). Thus, time modulation leads to harvest more power from external vibration, with an improvement of 99%. In addition, the time-modulated element delivers the power of $P_m = 80.3\,\text{mW}$ to the system and the constant part of the damper absorbs $P_0 = P_s + P_m = 101.2\,\text{mW}$ from the system, at the EPD frequency.

The eigenfrequencies near the EPD are very sensitive to a system's variation, like a small change in the modulation frequency, as discussed in Appendix C. When such a small relative perturbation $\delta_m = (f_m - f_{m,e})/f_{m,e}$ is applied, the resulting two distinct eigenfrequencies $f_{1,2}(\delta_m)$ are estimated using the Puiseux series power expansion $f_{1,2}(\delta_m) \approx f_e \mp j\,(f_m/2\pi)\,\alpha_1\sqrt{\delta_m}$ [78], where α_1 is the first-order expansion coefficient. The square root function demonstrates that the eigenfrequencies are highly sensitive to modulation frequency perturbations around the EPD, as shown in Fig. 6.3. This is reflected by the power levels that change dramatically when a small change in f_m is applied, as shown in Fig. 6.4. To harvest power, the modulation frequency must be chosen precisely, very close to the EPD frequency. It could be chosen exactly either at the EPD or between the two EPD frequencies as explained in the following.

To control the power provided by the time modulated portion of the circuit, Fig. 6.5(d) shows P_m delivered by $c_m(t)$ versus delay τ. Three combinations of modulation and source frequencies are considered. For the two cases shown with blue and yellow curves in Fig. 6.5(d), we assume that the frequency of the source is fixed to $f_s = f_m/2$, hence, the period of the modulation signal is half of the source's one when operating at the EPD ($T_{m,e} = T_s/2$).

In the third case (orange line), we assume that $f_{\mathrm{m}} = f_{\mathrm{m,e}}$, and source frequency at $f_{\mathrm{s}} = 1\,\mathrm{Hz}$. It is clear that the variation of the delay τ has a strong effect on P_{m} when the modulation frequency is selected as $f_{\mathrm{m}} = 2f_{\mathrm{s}}$ (both blue and yellow curves). However, in the case shown by the orange curve, which is a slight modification from the other two cases, P_{m} is more or less constant and the delay does not have much effect on it. When $f_{\mathrm{m}} = f_{\mathrm{m,e}}$, and $f_{\mathrm{s}} = f_{\mathrm{m}}/2$ (blue curve), and at a specific delay $\tau = 0.51T_{\mathrm{m}}$, the power delivered by the time-varying damper reaches the minimum and it is as small as $P_{\mathrm{m}} = 0.04\,\mathrm{mW}$. By assuming the latter particular condition with $f_{\mathrm{s}} = f_{\mathrm{m,e}}/2$ and $\tau = 0.51T_{\mathrm{m}}$, the numerical results in Fig. 6.6 show the source, modulation and constant damper powers by varying the modulation frequency (compared to the results in Fig. 6.4, where $\tau = 0$). Blue curves represent the power in the system with time modulation (note that the modulated power is near zero at the EPD), while red curves illustrate the power levels for the case without time modulation, as was done in Fig. 6.4. At the EPD modulation frequency $f_{\mathrm{m}} = f_{\mathrm{m,e}} = 1.984\,\mathrm{Hz}$ (cyan point), the power extracted from the source vibration is $P_{\mathrm{s}} = 19.38\,\mathrm{mW}$ and the power delivered to the constant part of the damper is $P_0 = 19.42\,\mathrm{mW}$. Thus, time modulation improves power harvesting by 85% compared to the case without time modulation. Note also that in this case the power delivered by the modulation is very small ($P_0 \approx P_{\mathrm{s}}$). However, the calculated powers around the EPD vary dramatically when changing the modulation frequency. That is one of the most peculiar properties associated with an EPD, as already depicted in Figs. 6.4, and 6.6. The reason is that the eigenstates at the EPD are extremely sensitive to any perturbation, as shown in Fig. 6.3, which causes large variation when interacting with forced excitation. The system could possibly harvest even more power with a precise choice of modulation frequency close to EPD and proper time delay. However, even without a precise modulation frequency choice, the system harvests more power on average, over f_{s} or f_{m} variation.

As a conclusion, we have shown that a mechanical resonator with time modulation harvests much higher power (even ten times higher) from ambient vibration than its counterpart

without time modulation. Moreover, using the concept of second-order EPDs, we also explain the existence of a very sharp spectral peak at some modulation frequencies. The power levels vary rapidly with only a very slight variation in a parameter (like modulation frequency). Indeed, using the Puiseux fractional series expansion, we have demonstrated that the degenerated system's eigenfrequency is highly sensitive to perturbations in the modulation frequency. It would be possible to use this effect for sensing applications or very precise spectrometers. The physics associated with an EPD in an LTP mechanical system is vital for getting a deeper insight into different ways to improve the narrow frequency features of the power transfer mechanism. We used a time-modulated damping factor that could be realized in a variety of ways including magneto-rheological or electro-rheological dampers where the damping factor can be tuned by changing fields. Specifically, the improvement in harvesting power is advantageous for applications with low energy requirements and low ambient source amplitude where direct access to the device is not possible and battery recharging or replacement is not feasible such as wireless sensors, bio-implantable devices, wireless body area networks, etc. Nevertheless, the capabilities of this method are not limited to low power applications and LTP energy harvesters can be beneficial for energy harvesting in building structures, roadways, railways, bridges, wind turbines, etc [183, 11].

Acknowlegment

The text of Chapter 6 of this dissertation is a reprint of the material as it appears in Alireza Nikzamir, Kasra Rouhi, Alexander Figotin, and Filippo Capolino. Time Modulation to Manage and Increase the Power Harvested from External Vibrations. Applied Physics Letters 123, no. 21, 2023. The coauthors listed in this publication are Kasra Rouhi, Alexander Figotin, and Filippo Capolino. Alexander Figotin and Filippo Capolino directed and supervised research which forms the basis for the dissertation. This material is based upon the

work supported by the Air Force Office of Scientific Research (AFOSR) under Grant No. FA9550-19-1-0103.

6.2 Appendix A: Dual Circuit with Time-Modulated Conductance

We show the analogous (dual) system made of a LC resonator and a linear time-periodic (LTP) conductance connected to the external source in series to the capacitor as shown in Fig. 6.7. In order to calculate the power in the dual LTP system, we consider piece-wise constant time-periodic conductance $G(t)$, i.e., $G(t) = G_0 + G_\mathrm{m}$ during the time interval $0 \leq t < T_\mathrm{m}/2$, and $G(t) = G_0 - G_\mathrm{m}$ during the time interval $T_\mathrm{m}/2 \leq t < T_\mathrm{m}$. Analogously to the mechanical LTP system, we define the system state vector as $\mathbf{\Psi}(t) = [v(t), \dot{v}(t)]^\mathrm{T}$, where $v(t)$ is the voltage on the inductor and $\dot{v}(t)$ is its time derivative. In general, $G(t)$ can be either lossy or gain (positive or negative respectively). Kirchhoff's circuit laws apply to time-varying circuits as follows:

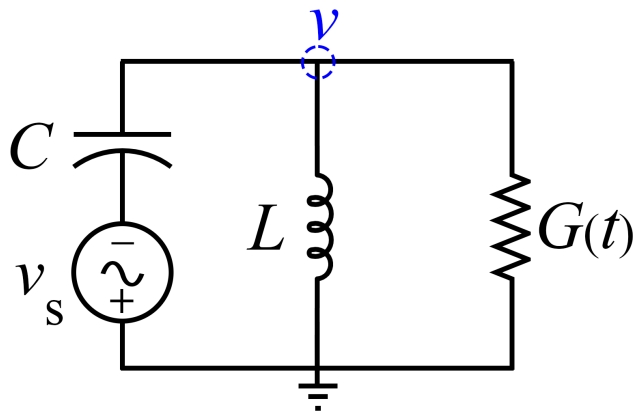

Figure 6.7: The dual time-varying circuit where an inductance is connected in parallel to a time-varying conductance, with an external source $v_\mathrm{s}(t)$ in series to the capacitor. The conductance is designed to have a two-level piece-wise constant time-periodic conductance, where $G(t) = G_0 + G_\mathrm{m}$ during the time interval $0 \leq t < T_\mathrm{m}/2$, and $G(t) = G_0 - G_\mathrm{m}$ during the time interval $T_\mathrm{m}/2 \leq t < T_\mathrm{m}$.

$$G(t)\,\dot{v} + \frac{v}{L} + C\,(\ddot{v} + \ddot{v}_{\mathrm{s}}) = 0. \tag{6.10}$$

The circuit equation is rewritten as

$$\ddot{v} + 2\alpha(t)\,\dot{v} + \omega_0^2 v = -\ddot{v}_{\mathrm{s}}. \tag{6.11}$$

where $\alpha(t) = \alpha_0 + \alpha_{\mathrm{m}}(t) = G_0/(2C) + G_{\mathrm{m}}(t)/(2C)$ is the time-modulated damping factor and $\omega_0 = 1/\sqrt{LC}$ is the natural frequency of the unmodulated and lossless circuit. Assuming time harmonic dependence of the form $v \propto e^{j\omega t}$ for the unmodulated homogeneous circuit, we obtain the eigenfrequencies as $\omega = j\alpha(1 \pm \sqrt{1-\omega_0^2/\alpha^2})$. By writing the differential equation in the eigenvalue problem format, the time evolution of the state vector $\mathbf{\Psi}(t)$ is given by

$$\begin{aligned} d\mathbf{\Psi}(t)/dt &= \underline{\mathbf{M}}_{\mathrm{c}}(t)\,\mathbf{\Psi}(t) + \begin{pmatrix} 0 \\ -\ddot{v}_s \end{pmatrix}, \\ \underline{\mathbf{M}}_{\mathrm{c}}(t) &= \begin{pmatrix} 0 & 1 \\ -\omega_0^2 & -2\alpha(t) \end{pmatrix}, \end{aligned} \tag{6.12}$$

where $\underline{\mathbf{M}}_{\mathrm{c}}(t)$ is the equivalent circuit matrix. The differential equation and the circuit matrix are dual to the time-varying mechanical system whose time-varying damper is connected to the spring and mass. The duality transformation is $k \to 1/L$, $m \to C$ and $c(t) \to G(t)$ and both systems have an external excitation $\ddot{y}(t) \to \ddot{v}_{\mathrm{s}}(t)$ as summarized in Table 6.1 [184]. Also, we show the duality of the characteristic equations in mechanical systems and their dual version in electric circuits in Table 6.2. By applying the conversion between force and current ($\mathscr{F} \longleftrightarrow i$) and velocity and voltage ($\dot{z} \longleftrightarrow v$), Newton's equations and

instantaneous mechanical power relate to the electric dual equations. We analyze the dual LTP circuit by using the Keysight Advanced Design System (ADS) time-domain simulator to calculate the power. We excite the circuit with a sinusoidal source at a frequency of f_{s} and the amplitude of 10 mV. Also, the capacitor has a 10 mV as an initial condition for the case where no external source excites the system. We numerically calculate the power using a built-in power block in the simulator and then report the time-averaged power based on 1000 time periods after the time domain signal saturates (i.e., for the time window from 3500 s to 4500 s).

Table 6.1: Component values in the mechanical system and their dual values in the dual electrical circuit.

Mechanical system	Dual electrical circuit	Duality
$k = 4\pi^2\,\mathrm{N/m}$	$L = 0.025\,\mathrm{H}$	$k \to 1/L$
$m = 1\,\mathrm{kg}$	$C = 1\,\mathrm{F}$	$m \to C$
$c_0 = 0.1\,\mathrm{Ns/m}$	$G_0 = 0.1\,\mathrm{S}$	$c_0 \to G_0$
$c_{\mathrm{m}} = 0.15\,\mathrm{Ns/m}$	$G_{\mathrm{m}} = 0.15\,\mathrm{S}$	$c_{\mathrm{m}} \to G_{\mathrm{m}}$
$c(t) = \begin{cases} c_0 + c_{\mathrm{m}}, & 0 \le t < T_{\mathrm{m}}/2 \\ c_0 - c_{\mathrm{m}}, & T_{\mathrm{m}}/2 \le t < T_{\mathrm{m}} \end{cases}$	$G(t) = \begin{cases} G_0 + G_{\mathrm{m}}, & 0 \le t < T_{\mathrm{m}}/2 \\ G_0 - G_{\mathrm{m}}, & T_{\mathrm{m}}/2 \le t < T_{\mathrm{m}} \end{cases}$	$c(t) \to G(t)$

6.3 Appendix B: Vibration Conversion

Table 6.2: Dual equations in the mechanical system and dual electrical circuit, where $\mathscr{F}$ is the force and i is the current.

Mechanical system		Dual electrical circuit	
Spring	$\mathscr{F} = kz$	$i = (1/L)\int v\,dt'$	Inductor
Mass	$\mathscr{F} = m\ddot{z}$	$i = C\dot{v}$	Capacitor
Damper	$\mathscr{F} = c\dot{z}$	$i = Gv$	Conductance
Mechanical Power	$p = \mathscr{F}\dot{z}$	$p = iv$	Electrical Power
Duality			
$\mathscr{F} \longleftrightarrow i$			
$\dot{z} \longleftrightarrow v$			

As already mentioned in the paper, $c_0 = c_{\mathrm{p}} + c_{\mathrm{t}}$ is responsible for the energy losses within the system due to parasitic loss mechanisms c_{p} (e.g., viscous friction with air), and by the

intentional mechanism of damping c_{t}, i.e., the mechanical energy extracted by the transduction mechanism. This model is based on the idea that converting energy from an oscillating mass to electricity (whatever the mechanism is) can be modeled as a linear damper in a mass-spring system. This model is quite accurate for certain types of electromechanical converters, such as those analyzed by Williams and Yates [185]. For other types of converter, such as electrostatic and piezoelectric, the model may be modified. However, the conversion will always result in a loss of mechanical kinetic energy, which can be referred to as damping [186]. Despite the fact that the current damper model does not accurately model all kinds converter types, the present analysis can be extended to electrostatic and piezoelectric systems [186]. The power extracted from the mechanical system via c_{t} is due to electrically induced damping and it is constitutes the whole time-averaged power P_0 if the parasitic damping vanishes. The instantaneous power in the constant part of the damper c_0, i.e., the combination of parasitic loss mechanisms c_{p} and transduction mechanism c_{t}, can be calculated as a product of induced force $c_0\dot{z}$ and velocity $\dot{z}$. Thus, the absorbed instantaneous power in the constant part of the damper is expressed by

$$p_0(t) = c_0\dot{z}^2. \tag{6.13}$$

The total time-averaged power P_0 is calculated by averaging the time domain expression. In a monochromatic regime, assuming no modulation, the total time-averaged power dissipated within the damper, i.e., the power extracted via the transduction mechanism and the power lost by parasitic damping mechanisms, is given by [176, 181, 187]

$$P_0 = \frac{m\zeta_0\omega_0\omega_{\mathrm{s}}^2\left(\frac{\omega_{\mathrm{s}}}{\omega_0}\right)^3 y_0^2}{\left(2\zeta_0\frac{\omega_{\mathrm{s}}}{\omega_0}\right)^2 + \left(1-\left(\frac{\omega_{\mathrm{s}}}{\omega_0}\right)^2\right)^2}, \tag{6.14}$$

where y_0 is the magnitude of the source vibration, $\zeta_0 = \zeta_t + \zeta_p = c_0/(2m\omega_0)$ is the constant damping ratio. Maximum power dissipation within the generator occurs when the device is operated at $\omega_s = \omega_0$, and in this case the total time-averaged power dissipated in the constant part of the damper is given by

$$P_0 = \frac{m\omega_0^3 y_0^2}{4\zeta_0}. \tag{6.15}$$

6.4 Appendix C: Sensitivity to Perturbation

Sensitivity of a system's observable to a particular parameter is a measure of how much a perturbation to that parameter affects the observable quantity of the system. The eigenvalues of the system at exceptional points of degeneracy (EPDs) are extremely sensitive to parameter changes, which is a significant feature. Applying a perturbation to a system parameter such as the modulation frequency $\delta_m = (f_m - f_{m,e})/f_{m,e}$, leads to a perturbed transition matrix $\underline{\mathbf{\Phi}}(\delta_m)$ and perturbed eigenvalues $\lambda_p(\delta_m)$, with $p = 1, 2$. Therefore, the degenerate resonance frequency occurring at the EPD f_e, splits into two distinct resonance frequencies $f_p(\delta_m)$, due to a small perturbation δ_m. We can calculate the perturbed eigenvalues near the EPD by using the convergent Puiseux fractional power series expansion, with coefficients calculated using the explicit recursive formulas in [89]. In the presented mechanical system with a second-order EPD, we utilize a first-order approximation of the perturbed eigenvalues as

$$\lambda_p(\delta_m) \approx \lambda_e + (-1)^p \alpha_1 \sqrt{\delta_m}, \tag{6.16}$$

where λ_e is the eigenvalue at EPD and the first order coefficient is expressed by

$$\alpha_1 = \left(-\frac{\partial H\left(\delta_{\mathrm{m}}, \lambda\right)/\partial \delta_{\mathrm{m}}}{\frac{1}{2!}\partial^2 H\left(\delta_{\mathrm{m}}, \lambda\right)/\partial \lambda^2} \right)^{\frac{1}{2}} \Bigg|_{\delta_{\mathrm{m}}=0,\, \lambda=\lambda_{\mathrm{e}}}, \tag{6.17}$$

where $H\left(\delta_{\mathrm{m}}, \lambda\right) = \det\left(\underline{\mathbf{\Phi}}\left(\delta_{\mathrm{m}}\right) - \lambda \underline{\mathbf{I}}\right)$ and $\underline{\mathbf{I}}$ is the 2×2 identity matrix. The perturbed resonance frequencies are approximately calculated as

$$f_p\left(\delta_{\mathrm{m}}\right) \approx f_{\mathrm{e}} \pm j \frac{f_{\mathrm{m}}}{2\pi} (-1)^p \alpha_1 \sqrt{\delta_{\mathrm{m}}}. \tag{6.18}$$

This formula proves that the time-modulated system supporting the EPD is very sensitive to variations in the modulation frequency f_{m}. Figures 2, 4 and 6 of the paper demonstrate that the harvested power is very sensitive to variations in the system's parameters when operating at or near an EPD.

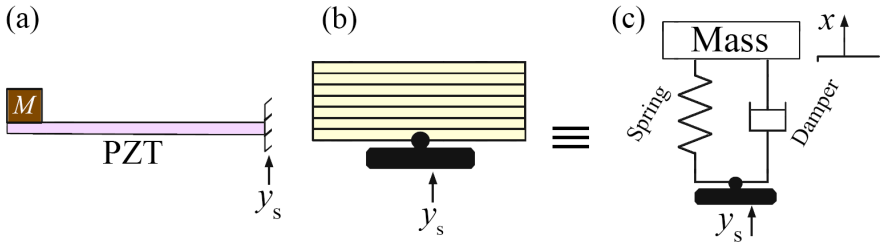

Figure 6.8: (a) The cantilever beam with tip mass, (b) multilayer PZT subjected to transverse external vibration excited at the base and (c) equivalent lumped spring-mass-damper system [11, Ch. 1].

6.5 Appendix D: Realistic Applications

In general, a mechanical model based on a spring–mass system gives a meaningful description of vibration behavior and can be used to model energy harvesting devices and inertial-based generators. For example, the cantilever can be represented by its equivalent model, which is composed of a mass, a spring and a damper. All these components are enclosed in a casing and mechanically connected to the vibration source. The most common examples of

cantilever design are cantilevered balconies, walkways, and overhangs, as well as some parts of bridge designs [188, Ch. 4], [189, Ch. 11]. In addition, our method can be extended to piezomagnetoelastic cantilevers [178, 190], a basic bimorph piezoelectric cantilever [188, Ch. 4], and a piezoelectric pendulum [191] in a realistic setup.

Fig. 6.8(a) shows a diagram of a cantilever beam with piezoelectric plates bonded on a substrate and a proof mass at the end; Fig. 6.8(b) shows multilayer piezoelectric plates and Fig. 6.8(c) provides the equivalent lumped spring-mass with external excitation. For piezoelectric energy harvesting devices, cantilever structures with tip masses are the most commonly used configurations. The vibration source is shown with an arrow at the base of the contact point. The configuration shown in Fig. 6.8(c) applies to both the energy harvesting mechanisms illustrated in Fig. 6.8(a) and (b).

6.6 Appendix E: Realization of Time-Modulated Damper

The time varying mechanisms can be implemented in realistic designs using tunable/controllable devices. For example, a controllable damper can be realized via variable orifice dampers with an external actuator modifying the orifice diameter, controllable fluid dampers and adjustable tuned liquid dampers [192, 193, 194, 160]. The variable orifice dampers have shown relatively low response speeds. However, in recent years, magneto-rheological (MR) dampers where the viscosity of the magnetic fluid is controlled via tuning of the field have received considerable attention due to their ability to rapidly alter their properties in response to the applied magnetic field [195]. In this configuration, variable damping control can be achieved by varying a small electric current to the MR dampers [196, 197, 198].

An alternative method of achieving semi-active damping is the use of electro-rheological (ER) fluids whose viscosity can be controlled by applying an electric field. This technology has been applied to the control of semi-active suspensions and flexible structures [199, 200, 201]. More investigation into the tunability methods and review of the recent works in this area can be found in [195].We can therefore realize the time-modulated damper needed for our proposed structure by varying the damping coefficient periodically via the described approaches.

6.7 Appendix F: Scale Parameter in the Mechanical System

In this paper, we adopted practical values for system parameters. However, according to the governing equation of the time-varying system in Eq. (1), parameters can be scaled by a factor S as shown in Table (6.3).

Table 6.3: Parameters in the mechanical system scalable by factor S.

Parameter	Scale
Mass	$m \to Sm$
Spring stiffness	$k \to Sk$
Damper damping	$c \to Sc$

As a result of applying this transformation, we obtain the same governing equation with the same eigenvalues.

6.8 Appendix G: Noise in the Energy Harvesting Systems

Ambient noise may strongly influence the energy harvesters performance, therefore it is important to study energy harvesting systems to improve the performance. For developing micropower generators applicable to noise environments, it has become important to harvest energy utilizing different mechanisms. Even though many configurations have been developed to harvest ambient vibration energy, crucial questions remain about how to optimize performance under different noise levels [202]. The efficiency of harvesting energy from noise has also been explored by some researchers [203, 204, 205, 206, 207, 208, 209, 210, 211]. Borowiec et al. [212] investigated the effect of noise on energy harvester performance.

In summary, noise in an energy harvesting system has been investigated from different perspectives. First, noise can affect the main resonator and the relevant circuit. Nevertheless, the resonator is isolated from the environment, which minimizes the noise effects. Secondly, noise in the ambient source can affect energy harvesting system performance. For instance, Liu et al. proposed a stochastic averaging method to study the response characteristics of an energy harvesting system in the case of colored noise [207]. Also, Su et al. analyzed the effect of Gaussian white noise intensity on the system [213]. Moreover, the influence of ambient sinusoidal excitation and additive noise on the energy harvesting performance of piecewise bistable energy harvesters were investigated in [214]. Considering the importance of this topic, many other studies have studied noise's effect on ambient sources in detail [215, 216, 217, 218, 219, 220, 221, 222]. Furthermore, noise may be a source of energy, and an energy harvester could be designed in such a way that it extracts the maximum power from the statistical external noise [223, 224, 225, 226]. Finally, noise may be affected by EPDs. Some papers have discussed the relation between noise and EPD and provided methods to analyze it [227, 82, 228, 229, 85, 230, 231, 232, 233, 58]. However, this subject is

beyond the scope of this paper and requires a separate in-depth study.

Chapter 7

Exceptional Point Degeneracy as Desirable Operation Point of Oscillator Array with Discrete Nonlinear Gain and Radiating Elements

In this chapter, We show that an oscillator array prefers to operate at an exceptional point of degeneracy (EPD) occurring in a waveguide periodically loaded with discrete nonlinear gain and radiating elements. The concept of the EPD is employed to conceptualize an exceptional synchronization regime, which leads to enhanced radiating power efficiency. The system maintains a steady-state degenerate mode of oscillation at a frequency of 3 GHz, even when the small-signal nonlinear gain values are nonuniform along the array. We designed the system using small-signal gain to work at the EPD of zero phase shift in consecutive unit cells. Contrarily to the original expectation of zero phase shift, after reaching saturation, the

time domain signal in consecutive unit cells displays a π phase shift. Hence, we demonstrate that the saturated system tends to oscillate at a distinct EPD, associated to a π phase shift between consecutive cells, than the one at which the system was originally designed using small-signal gain. This new EPD at which the nonlinear system is landing is associated to higher radiating power efficiency with respect to power provided by nonlinear gains. Finally, we demonstrate that the oscillation frequency is independent of the length of the array, contrarily to what happens ordinary oscillating systems based on one-dimensional cavity resonances. These findings may have a high impact on high-power radiating arrays with distributed active elements.

7.1 Motivation and State of the Art

Exceptional points of degeneracy (EPDs) in waveguides have become increasingly popular in the fields of electromagnetics, photonics, and radio frequency (RF) circuits [75, 36, 76, 234, 235, 2]. EPD is the condition at which two or more eigenmodes coalesce in their eigenvalues and eigenvectors [31, 33, 32, 35]. The term EP has been in use since [33]; as was also emphasized in [66], the key physics feature is the "degeneracy", and that is the reason for the "D" in EPD. Exceptional points have been the subject of study in different areas, including absorbers [236], reflectionless applications [237], sensing applications [99, 238], and low thresholds lasers [15]. At the EPD, the system matrix or transfer matrix representing the mode evolution in the system is similar to a matrix containing a non-trivial Jordan block [39, 239]. The order of the degeneracy is the number of coalescing eigenmodes at the EPD. Close to an EPD of order 2 in a waveguide, the dispersion relation between frequency and wavenumber is $(\omega - \omega_e) \propto (k - k_e)^2$, where the subscript e denotes EPD. When the system refractive index obeys $n(x) = n^*(-x)$, where x is a coordinate in the system orthogonal to the propagation direction z, and $*$ is the complex conjugate, the system is parity time

(PT) symmetric [40, 240, 44]. PT symmetry is a condition that enables the occurrence of EPDs with a degenerate real eigenvalue [36, 235, 241, 76], though it is not a necessary condition to get EPDs [30]. Moreover, the degeneracy of eigenvalues discussed in this chapter is in the wavenumber k, rather than the degeneracy of PT-symmetric structure that is often in the eigenfrequency domain ω as in [3, 71, 6]. EPDs in periodic structures can be classified into two categories: (i) those obtained without gain and loss [39, 242, 243, 2] (note that in some of these papers, the author did not use the term EP), and (ii) those obtained with gain and/or loss [44, 36, 76, 75, 9, 30, 232]. The occurrence of an EPD enables special and unique physical features that can be used in different applications from RF to optics. The EPD concept has been proposed to provide notable enhancements in the performance of oscillators and amplifiers: there are two main categories of these applications, classified according to the presence or absence of loss and gain. The first category involves EPD in waveguides without loss and gain, such as the degenerate band edge (DBE) or stationary inflection point (SIP) laser concepts [15] that exhibit a new threshold scaling law of quality factor and absorbance [244, 245], and in microstrip waveguides for arrayed antennas and providing a stable oscillation [12]. The second category involves waveguides where EPDs are obtained thanks to the presence of loss and gain (PT symmetry is an example) that leads to the concepts of arrays of radiators with high-output power, backward-wave oscillators with distributed power extraction, etc [9, 30, 246, 128] (these examples do not involve PT symmetry; one involves Glide-Time symmetry). In particular, accurate particle-in-cell simulations have shown that this kind of EPD in a waveguide with distributed gain and power extraction may enhance the performance of high-power electron beam devices [246]. In this chapter, we focus on the second category of EPDs, i.e., EPDs that exist in waveguides with loss and gain, aiming at applications where a large array radiates a highly coherent beam with high power.

Oscillators play a vital role in microwave, THz, and optics applications. At RF, there is interest in making oscillators that offer stable oscillation frequency [25, 247], high-quality

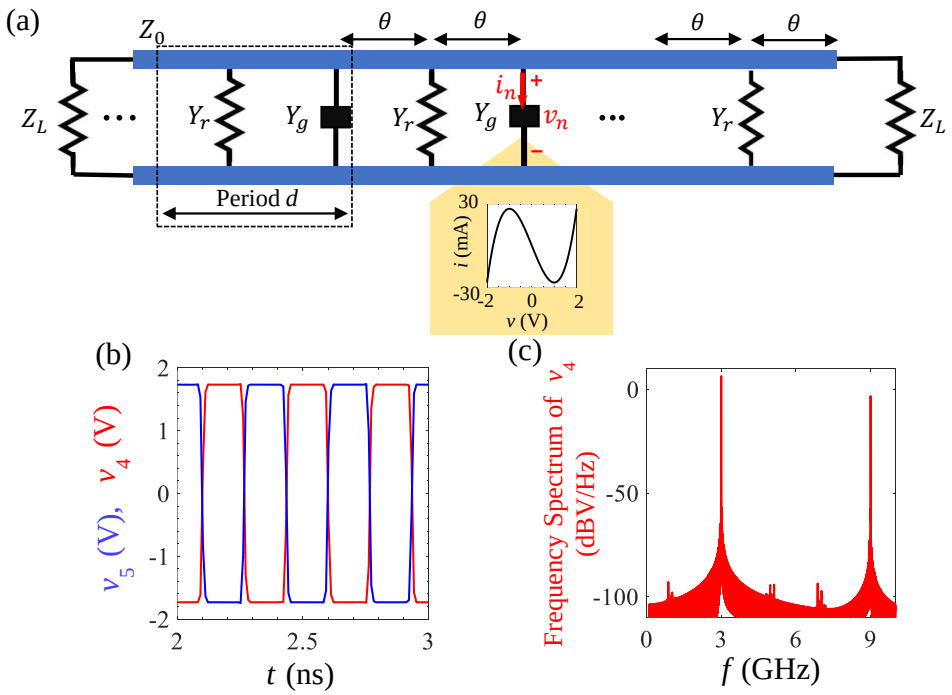

Figure 7.1: (a) Schematic of a periodically loaded waveguide represented by its equivalent transmission line (TL). Each unit cell is made of two TL segments with characteristic impedance Z_0 and same electrical lengths θ, loaded with a lossy shunt element Y_r representing a radiator (e.g., an antenna) and a shunt nonlinear gain element Y_g. (b) Time-domain voltage signals $v_4(t)$ and $v_5(t)$ are evaluated at the two middle unit cells' active elements, for an array with $N = 8$. Radiation is given by $Y_r Z_0 = 2.5$ and the nonlinear small-signal gain is $gZ_0 = 0.5$. (c) Frequency spectrum of the voltage $v_4(t)$ in dB scale shows the oscillation at the fundamental frequency $f_{osc} = 3$ GHz.

factor [26, 248], loading independency [12], and high output power [27]. The EPD concept with gain and loss has been proposed to enhance the performance of distributed oscillators in various ways [128, 30, 246]. A method to design distributed oscillators with EPD is through the utilization of waveguide loaded with periodic nonlinear gain and loss [128]. In this approach, losses represent the arrayed radiating elements, e.g., antennas. This chapter does not focus on providing a theoretical analysis of the nonlinear modes and bifurcation dynamics [119] of the system, but rather shows its dynamics as a result of numerical experiments fully accounting for nonlinearities.

This chapter presents a waveguide system modeled as a transmission line (TL), periodically loaded with discrete nonlinear gain and radiating elements as shown in Fig. 7.1(a). Rather

than the general EPD conditions discussed already in [128], here we explore the resonances of the finite-length array with gain and radiating elements, and the nonlinear features of the same structure, including the saturation from a nonuniform distribution of nonlinear gain elements. The analysis of nonuniform distribution of gain is extremely important in practice because it is impossible to guarantee that the active elements have the same value of gain along a waveguide, at both RF and optical frequencies. Variation in nonlinear gains over the arrayed structure, due to device tolerances, may alter the oscillator operation and affect the power extraction from radiating elements. Therefore, we show that when utilizing the EPD concept in waveguide oscillators, even nonuniform distributions of nonlinear gain elements along the array lead to a stable oscillation regime, and this stationary regime leads to a uniform *saturated* gain distribution. To confirm the full degeneracy of the eigenmodes, we employ the "coalescence parameter" tool to demonstrate the coalescence of the eigenvectors. Also, we show that the system maintains a stable oscillation frequency even when varying the length of the structure (number of unit cells), and also when the nonlinear small-signal gains or radiation losses are not uniform along the array, and when loads on the two sides are varied. Finally, we discuss the degeneracy condition in the presence of an additional small reactance in parallel to the gain element, and identify the EPD using the coalescence parameter tool. We provide an example where a small capacitance is added to each gain element, and we demonstrate that the system exhibits stable oscillation at a different EPD. This approach shows that we can create a tunable oscillator by adding a small tunable capacitor in each unit cell. Additionally, we confirm that the system tends to oscillate at a state where the nonlinear saturated gain is diminished, bring the system to another EPD.

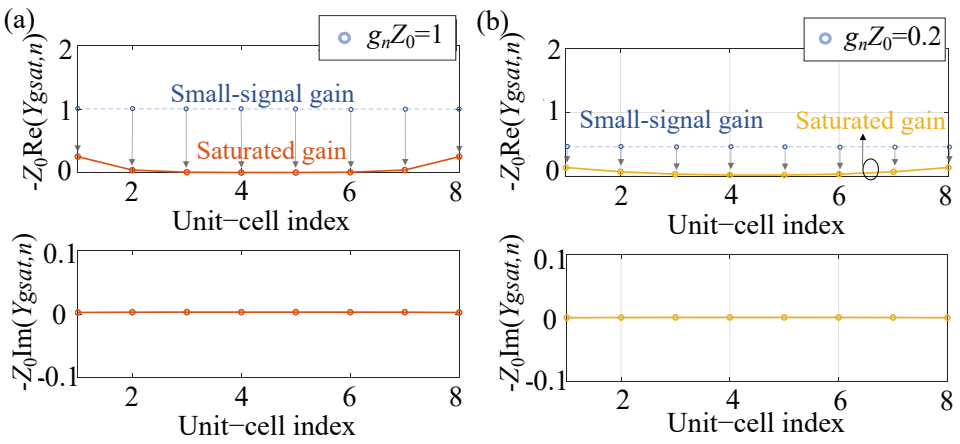

Figure 7.2: (a) Saturated gain calculated at each unit cell, found by Eq. 7.2, for two arrays with different nonlinear small-signal gain. Radiation losses are $Y_rZ_0 = 2.5$ in both cases. For two cases of arbitrary uniform nonlinear small-signal gain values $gZ_0 = 1$ (orange line) and $gZ_0 = 0.2$ (yellow line), the real and imaginary part of the *saturated* gain will end up at $Y_{gsat,n}Z_0 \approx 0$ in each unit cell.

7.2 Oscillatory Regime with Nonlinear Gain

The array oscillator consists of a waveguide, modeled as a TL with characteristic impedance $Z_0 = 50\,\Omega$, with a periodic distribution of N lumped nonlinear gain elements, described by shunt admittances $Y_{g,n}$ with $n = 1, 2, ..., N$ (not necessarily equal to each other), and $N + 1$ radiating elements described by shunt admittances Y_r (all equal to each other), both arranged periodically with period d as shown in Fig. 7.1(a). This assumption reflects realistic scenarios where it is easy to make radiators that are very similar to each other, hence exhibiting the same admittance (e.g., dielectric resonator antennas, patch antennas, slot antennas, etc.) whereas it is almost impossible to ensure that the gain of each element is the same when using active components like transistors or even in the case of optically or electrically pumped lasers. Impinging signals of a certain strength may have an effect on the oscillation operation, but we did not consider their effects on the array in this chapter.

For brevity, we only consider the case where radiating and gain lumped elements are separated by $d/2$. Therefore, each TL segment has electric length $\theta = k_w d/2$, where $k_w = 2\pi f/v_w$

is the wave propagation constant in the uniform TL segments where f is the frequency, and the phase velocity v_w is assumed to be dispersionless for simplicity. The array structure is symmetric, i.e., we terminate the left and right ends with loads $Z_L = Y_r/2$, and on the right side there is an extra shunt radiating element Y_r. Thus, the structure with N unit cells has N nonlinear gain elements, $N+1$ radiating elements, and left and right load terminations. Each gain element is described by a negative small-signal conductance $Y_{g,n} = -g_n$ and saturation effect, where the current i_n and voltage v_n, with $n = 1, 2, ..., N$, are related by the $i - v$ cubic model

$$i_n = -g_n v_n + \alpha_n v_n^3, \tag{7.1}$$

and $\alpha_n = g_n/3$ (unit of $\mathrm{S/V^2}$) describes the saturation level. This cubic model provides a negative conductance $Y_{g,n} = -g_n$ for small voltage in the range between $-1\,\mathrm{V} < v_n < 1\,\mathrm{V}$. At RF, the active component with the small-signal negative conductance can be realized in various ways, including a Gunn diode [249], a cross-coupled transistor pair [250], an op-amp [251], and other possible approaches. Due to the 3rd-order nonlinearity, each active element saturates to an admittance value $Y_{gsat,n}$ that provides a gain $-\mathrm{Re}(Y_{gsat,n})$ to the system, which differs from the small-signal gain g_n. We implicitly assume the time convention $e^{j\omega t}$. The saturated gain admittance (magnitude and phase) is found numerically by looking at the frequency components of the voltage and current, selecting the oscillation frequency f_{osc}, by using the fast Fourier Transform (FFT) as

$$\begin{cases} |Y_{gsat,n}| = \frac{|\mathrm{FFT}(i_n)|_{f_{osc}}}{|\mathrm{FFT}(v_n)|_{f_{osc}}} \\ \\ \angle Y_{gsat,n} = \left(\angle \mathrm{FFT}\left(i_n\right) - \angle \mathrm{FFT}\left(v_n\right)\right)\big|_{f_{osc}} \end{cases}, \tag{7.2}$$

where $||$ represents the magnitude, and $\angle$ represents the phase. Numerical simulations

are carried out in the time domain using the Keysight Advanced Design System (ADS) circuit simulator. We first assume that the uniform (i.e., $g_n = g$, constant along the array) normalized nonlinear small-signal gain and radiating element are $gZ_0 = 0.5$ and $Y_r Z_0 = 2.5$, respectively. Figure. 7.1(b) shows the time domain oscillatory signals v_4 and v_5 in the middle of the array. We observe that the time domain signal at the two consecutive unit cells has a π phase shift. Figure 7.1(c) shows the frequency spectrum of v_4 with the fundamental frequency of oscillation of 3 GHz, calculated by using the built-in fast Fourier transform (FFT) in the Keysight ADS simulator of the saturated signal in the time window from 2 μs to 12 μs, with 10^6 points. We observe the presence of higher harmonics of the oscillating voltage in this structure because of the nonlinearity in the gain. Simulation results show that the fundamental frequency carries the highest power in the array, and the next harmonic (9 GHz) is 9.7 dB smaller than the fundamental one.

To understand the observed oscillatory regime, we consider two other uniform cases with initial small-signal gain values of $gZ_0 = 1$ and $gZ_0 = 0.2$, and we calculate the cells' saturated gain using Eq. (7.2) after reaching saturation. Importantly, we observe that in both cases, after reaching saturation, the system *still* oscillates at $f = 3\,\mathrm{GHz}$, as observed in the previous case with $gZ_0 = 0.5$. Furthermore, we observe that the time domain voltages on the gain elements in consecutive unit cells still have a π phase shift, as in the previous case with $gZ_0 = 0.5$. For the cases of $gZ_0 = 1$ and $gZ_0 = 0.2$, Figs. 7.2(a) and (b) show the real and imaginary parts of the saturated gain $-Y_{gsat,n}$ in each unit cell, which is mainly real positive. The real part $-\mathrm{Re}(Y_{gsat,n})$ of the saturated gain at steady state regime are smaller than g, in both cases. At this stage, it seems that the system tends to work at the point that has a saturated gain such that $-\mathrm{Re}(Y_{gsat,n}) << (1/Z_0)$. In the following, we analyze the modes of the structure to determine the characteristics of this specific point.

7.3 Formulation of a waveguide periodically loaded with discrete linear gain

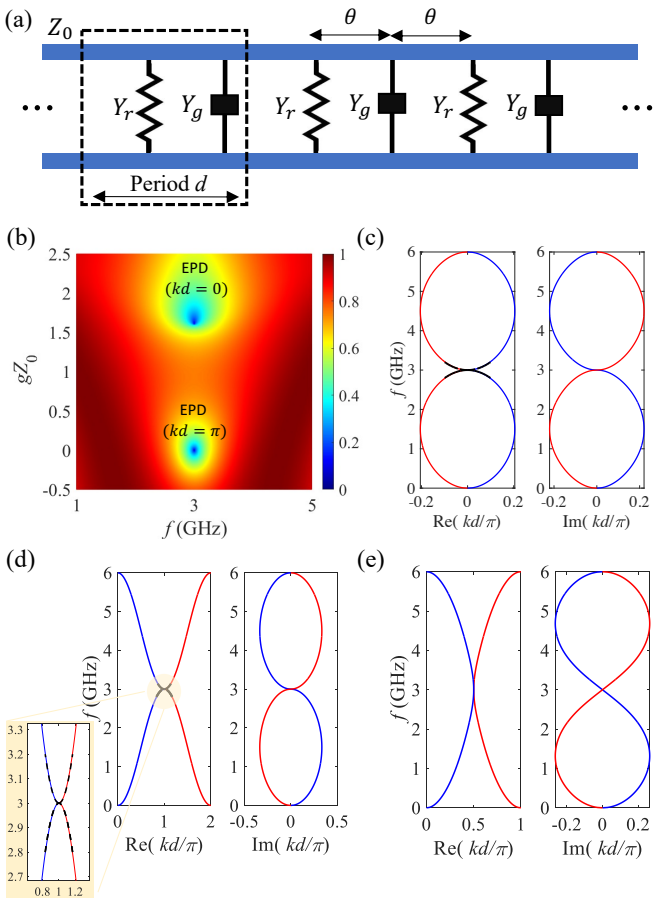

Figure 7.3: (a) Schematic of a periodic waveguide represented in terms of an equivalent TL with characteristic impedance $Z_0 = 50\,\Omega$, loaded periodically with a lumped loss Y_r and linear gain Y_g admittances. We assume $Y_r Z_0 = 2.5$ and $\theta = \pi/2$ at 3 GHz. (b) The vanishing of the coalescence parameter shows two EPDs calculated from Eq. 7.6, for varying small-linear gain g. The two EPs are at $kd = 0$ (for $gZ_0 = 1.6$) and $kd = \pi$ (for $gZ_0 = 0$). Dispersion relation of the real and imaginary parts of the complex-valued wavenumber k versus frequency for (c) $gZ_0 = 1.6$ and (d) $gZ_0 = 0$. In the inset, the dispersion diagram is fit with the quadratic equation $(f - f_e) = \pm\eta(k - k_e)^2$ denoted by the black dashed line, with $\eta \approx 7.153 \times 10^4\ \mathrm{m}^2/\mathrm{s}$. (e) A case without supporting EPD ($gZ_0 = 0.8$).

Second order EPDs can occur in the waveguide under study. We find the system's eigenmodes by using the transfer matrix approach as in [9, 128, 252]. We define the state-vector $\mathbf{\Psi}(z) = [V(z), I(z)]^{\mathrm{T}}$ with voltage $V(z)$ and current $I(z)$ along the waveguide, and T is the transpose

action. The state vector in the periodic structure with a period of d changes as

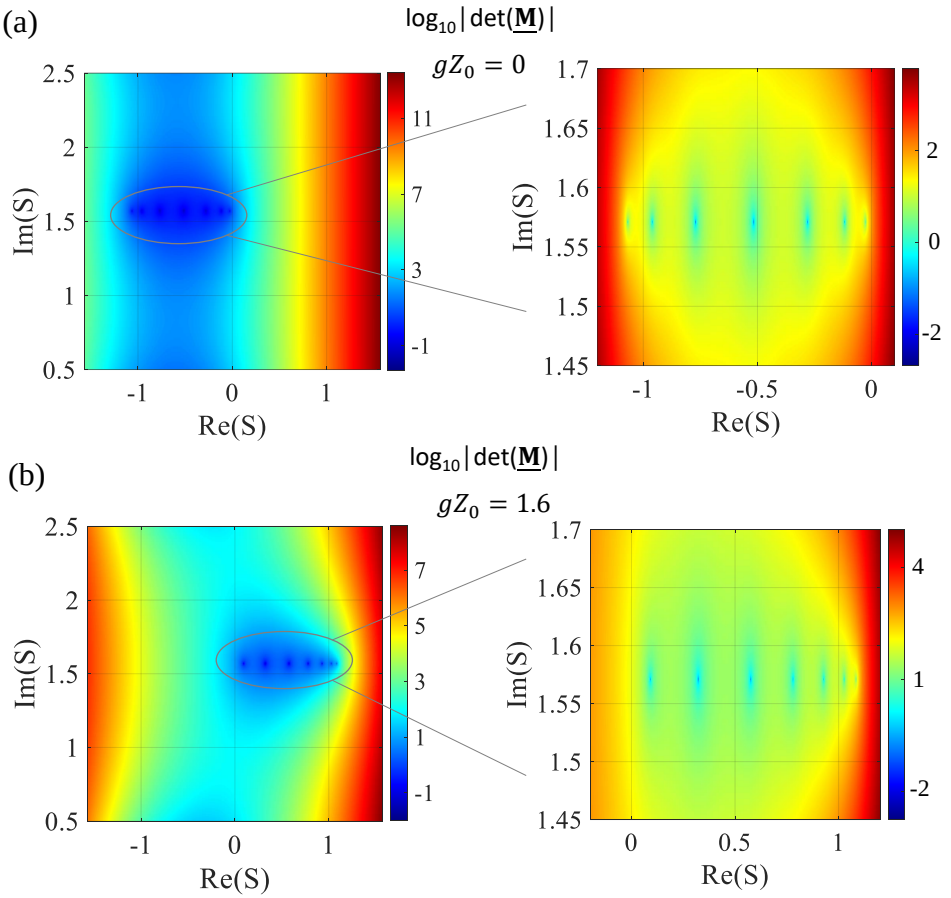

Figure 7.4: The vanishing of the determinant provides the complex resonances of the finite-length array in the complex $s = j\omega$ plane, with a zoomed-in version around the resonances. We consider two cases of gain, both with losses $Y_r Z_0 = 2.5$. They pertain to the two EPDs in Fig. 7.3: (a) $gZ_0 = 0$ and (b) $gZ_0 = 1.6$. Instability occurs when poles have $\mathrm{Re}(s) > 0$.

$$\mathbf{\Psi}(z + d) = \underline{\mathbf{T}}_{\mathrm{U}} \mathbf{\Psi}(z), \tag{7.3}$$

where $\underline{\mathbf{T}}_{\mathrm{U}}$ is the 2×2 transfer matrix relative to a unit cell denoted by a dashed line in Fig. 7.1(a). It is built using the sub blocks relative to shunt gain $\underline{\mathbf{T}}_{\mathrm{gain}}$, shunt loss $\underline{\mathbf{T}}_{\mathrm{loss}}$, and two lossless transmission lines with electric length $\theta = k_w d/2$, $\underline{\mathbf{T}}_{\mathrm{TL}}$. Multiplying each segment's transfer matrix yields the unit-cell's transfer matrix

$$\underline{\mathbf{T}}_{\mathrm{U}} = \underline{\mathbf{T}}_{\mathrm{gain}}\underline{\mathbf{T}}_{\mathrm{TL}}(\theta)\underline{\mathbf{T}}_{\mathrm{loss}}\underline{\mathbf{T}}_{\mathrm{TL}}(\theta). \tag{7.4}$$

The eigenmodes supported by the waveguide system are found by solving the eigenvalue problem

$$(\underline{\mathbf{T}}_{\mathrm{U}} - \lambda\underline{\mathbf{I}})\,\boldsymbol{\Psi}(z) = 0, \tag{7.5}$$

in which $\underline{\mathbf{I}}$ is the identity matrix of order two [128]. Eigenvalues are in the form of $\lambda_i = e^{-jk_i d}$, with $i = 1, 2$, and k_i is the Floquet–Bloch modal wavenumber in the periodic waveguide.

The eigenvalues are obtained by calculating the roots of the characteristic equation $\det(\underline{\mathbf{T}}_{\mathrm{U}} - \lambda\underline{\mathbf{I}}) = 0$ that is

$$\begin{aligned}\lambda^2 + \Big[&- 2\cos(2\theta) + Y_g Y_r Z_0^2 \sin^2(\theta) \\ &-jZ_0 Y_r (1 + Y_g/Y_r)\sin(2\theta)\Big]\lambda + 1 = 0.\end{aligned} \tag{7.6}$$

The characteristic equation is a second-order polynomial that results in $k_2 = -k_1$. In the Eq. 7.6, the λ's coefficient equal to ± 2 is a sufficient and necessary condition to have a second order degeneracy of the eigenvalues at λ_e, leading to the two EPD conditions

$$\begin{aligned}-2\cos(2\theta) + Y_g Y_r Z_0^2 \sin^2(\theta) &= \pm 2 \\ jZ_0 Y_r (1 + Y_g/Y_r)\sin(2\theta) &= 0,\end{aligned} \quad . \tag{7.7}$$

where $+2$ corresponds to an EPD at $kd = \pi$ and the -2 corresponds to an EPD at $kd = 0$. The degeneracy conditions are discussed in [128] with more details. Here, we just provide a brief summary of the conditions to obtain the EPD for the special case with $\theta = \pi/2$ at 3 GHz where the phase velocity to unit-cell period ratio is $v_w/d = 6 \times 10^9\ \mathrm{s}^{-1}$. There are three possible degeneracy conditions with real $Y_g = -g$: (i) no linear gain or loss ($Y_r = 0$ or $g = 0$);

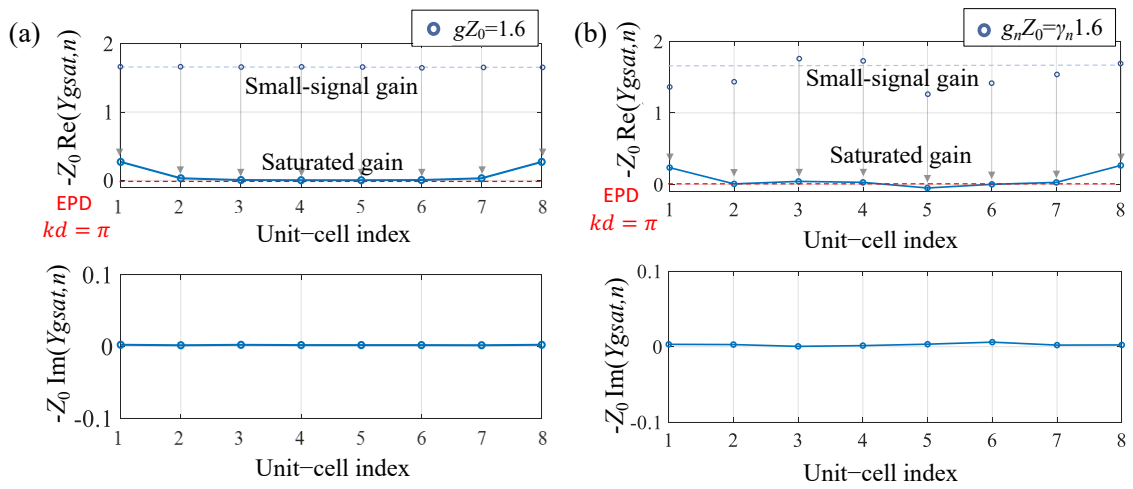

Figure 7.5: Saturated gain admittance $-Y_{gsat,n}$ calculated at each unit cell (blue curve), for an array with $N = 8$ unit cells. The radiating elements have conductance $Y_rZ_0 = 2.5$. We consider two cases: (a) all unit cells have the same small-signal gain $gZ_0 = 1.6$; and (b) each unit cell has a different small-signal gain $g_nZ_0 = \gamma_n 1.6$, with factors γ_n equal to 85%, 90%, 110%, 105%, 82%, 89%, 95%, 101%, respectively, of the EPD small-signal gain. The saturated gain $-Y_{gsat,n}$ (blue) converged to a much smaller value than the initial small-signal gain, and tends to vanish for longer arrays. For infinite arrays it converges to $Y_{gsat,n}Z_0 = 0$ that is associated to an EPD at 3 GHz with $kd = \pi$, shown with a dashed red line.

(ii) Symmetric linear gain and loss ($Y_rZ_0 = gZ_0 = 2$) results in an EPD at $kd = \pi$; (iii) Asymmetric linear gain and loss where the EPD at $kd = 0$ happens when $gZ_0 = 4/(Y_rZ_0)$ and the EPD at $kd = \pi$ happens when $g = 0$. In this chapter, we focus on the EPD condition (iii), i.e., the asymmetric linear gain and loss case, and analyze the nonlinear effects. To confirm the coalescence of the eigenvectors in our system, we use the concept of coalescence parameter C (also called hyperdistance) [2]. The coalescence parameter is a mechanism to measure the separation between the eigenvectors and how close they are to their degeneracy. The coalescence parameter vanishes when the eigenvectors collide. Thus, the Hermitian angle ϕ between the eigenvectors $\mathbf{\Psi}_1$ and $\mathbf{\Psi}_2$ is defined as [90, 93].

$$C = |\sin(\phi)|, \qquad \cos(\phi) = \frac{|\langle \mathbf{\Psi}_1, \mathbf{\Psi}_2 \rangle|}{\|\mathbf{\Psi}_1\| \, \|\mathbf{\Psi}_2\|}. \tag{7.8}$$

The $\cos(\phi)$ is found by using the inner product of the two eigenvectors $\langle \mathbf{\Psi}_1, \mathbf{\Psi}_2 \rangle =$

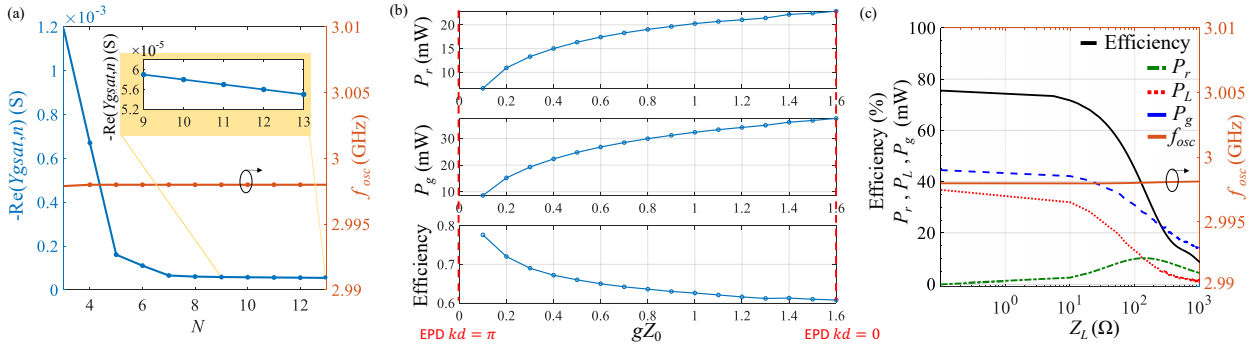

Figure 7.6: (a) Saturated nonlinear gain at the middle of the structure ($-Y_{gsat,n}$) (blue) and oscillation frequency (orange) versus the total number of unit cells N.(b) Radiated power P_r delivered to the periodic elements with conductance Y_r. The total power P_g is delivered by the nonlinear gain elements $Y_{gsat,n}$. The efficiency is P_r/P_g. The array has $N = 8$ unit cells and $Z_0 = 50\,\Omega$. The small-signal is $gZ_0 = 1.6$, and the radiation conductances have $Y_rZ_0 = 2.5$. (c) Delivered power to the radiating elements P_r, to the loads on the left and right P_L, and delivered by the nonlinear gain elements P_g, versus load variation Z_L. We also show the efficiency P_r/P_g and the oscillation frequency f_{osc}.

$\sum_{q=1}^{2}\psi_{1,q}\psi_{2,q}^{*}$, absolute value $||$ and norm of a complex vector $\|\mathbf{\Psi}\| = \sqrt{\langle\mathbf{\Psi},\mathbf{\Psi}\rangle}$. When the $\sin(\phi) = 0$ two eigenvector coalesce at the eigenvectors $\mathbf{\Psi}_e$ defining the EPD corresponding to the eigenvalue λ_e. Different combinations of the loss Y_r and gain g lead to EPDs at various frequencies. Here, we choose the parameters to find an EPD that occurs at 3 GHz. Figure. 7.3 (b) shows the coalescence parameter for different normalized gain values with a fixed loss $Y_rZ_0 = 2.5$, showing two degeneracies of the eigenvectors at $kd = \pi$ (when $gZ_0 = 0$) and $kd = 0$ (when $gZ_0 = 1.6$). Figure 7.3(c) shows the dispersion relation of complex-valued wavenumber versus frequency for the case with $Y_rZ_0 = 2.5$ and $gZ_0 = 1.6$, where the EPD happens at $f = 3$ GHz at $kd = 0$. The dispersion is fitted by the quadratic curve $(f - f_e) \propto \eta(k - k_e)^2$, where f_e is the frequency at which the two modes coalesce, and k_e is the wavenumber at the degeneracy point (black dashed line). The flatness coefficient η (m/s^2) shows the flatness of the dispersion in proximity of the degeneracy and it is related to $\partial^2 f/\partial k^2$. A lower value of η means a flatter dispersion, and by engineering the structure, the desired parameters could be achieved. In the studied case we have $\eta \approx 2.06 \times 10^5$ m^2/s.

Note that Figs. 7.3(b) and (d) exhibit another EPD at $f = 3$ GHz and $kd = \pi$. The EPD

is found for loss and gain at $Y_r Z_0 = 2.5$ and $gZ_0 = 0$, respectively. The dispersion is fitted by the quadratic formula $(f - f_e) = \pm\eta(k - k_e)^2$ with $\eta \approx 7.153 \times 10^4$ m^2/s, denoted by the black dashed line. As a reference, we also show in Fig. 7.3(e) a dispersion relation for a case without EPD with gain $gZ_0 = 0.8$ and loss $Y_r Z_0 = 2.5$. We see that the eigenvalues are crossing but we do not have a degeneracy and the relation $(f - f_e) \propto \eta(k - k_e)^2$ is not satisfied. The results shown in Fig. 7.3 are numerically calculated with MATLAB.

To predict the self-oscillation of the system, we look at the poles of the finite-length system ($N = 8$) by imposing boundary conditions (i.e., the loading) at the two array terminations. We first define the two-state vectors at the left and right terminations, $\mathbf{\Psi}_l = [V_l,\ I_l]^{\mathrm{T}}$ and $\mathbf{\Psi}_r = [V_r,\ I_r]^{\mathrm{T}}$, respectively. Assuming the loading on two ends $Z_L = 1/Y_r$ and applying the two boundary conditions, leads to

$$\begin{array}{l} \mathbf{\Psi}_r = \underline{\mathbf{T}}_{\mathrm{U}}^N \mathbf{\Psi}_l, \\ V_l + I_l Z_L = 0, \\ V_l - I_l Z_L = 0, \end{array} \rightarrow \underline{\mathbf{M}} \begin{pmatrix} \mathbf{\Psi}_r \\ \\ \mathbf{\Psi}_l \end{pmatrix} = 0. \tag{7.9}$$

The three equations are combined in a linear system with the 4×4 system matrix of $\underline{\mathbf{M}}$. The resonances are found by solving $|\det(\underline{\mathbf{M}})| = 0$ for $s = j\omega$, assuming a uniform $Y_r Z_0 = 2.5$ for the two cases supporting EPD, at $gZ_0 = 0$ and $gZ_0 = 1.6$. Figure 7.4 shows the $\log_{10}|\det(\underline{\mathbf{M}})|$ to demonstrate the resonances in the $s = j\omega$ complex plane. The system with no gain ($g = 0$) has all the poles such that $\mathrm{Re}(s) < 0$. The case with gain ($gZ_0 = 1.6$) shows that the poles are such that $\mathrm{Re}(s) > 0$, i.e., they are all unstable. The finite-length array is stable at the EPD with $gZ_0 = 0$; however, it becomes unstable with a relatively tiny nonlinear small-signal gain and oscillates close to the EPD frequency with $gZ_0 = 0$, as demonstrated in Fig. 7.6 in the next section that focuses on the array oscillatory regime.

7.4 Oscillator Operating at Second Order EPD

We now consider the waveguide with EPD at $kd = 0$ at 3 GHz, by selecting small-signal gain $gZ_0 = 1.6$ and radiation loss $Y_rZ_0 = 2.5$, while each segment has the same electric length as previously, with $\theta = \pi/2$ at 3 GHz. Then, we set the number of unit cells to be $N = 8$, and when using nonlinear gain as in Eq. (7.1) and we observe that the system oscillates at $f_{osc} = 3$ GHz. Since the system was designed at the EPD with $kd = 0$ (based on the small-signal gain value), one would expect the signal of each unit cell to have the same phase of oscillation. But, in reality, we observe that contiguous unit cells have a π phase difference. In other words, under the small-signal condition, the system should operate at the EPD with $kd = 0$, but we observe that after reaching saturation it operates at another point.

To gain physical insight, we calculate the saturated gain $Y_{gsat,n}$ on each unit cell as shown in Fig. 7.5 (a). For example, the saturated gain of the 4th active element of the array was found to be $-Y_{gsat,4}Z_0 = 0.003$, which is very far away from the starting small-signal one ($g_nZ_0 = 1.6$). The other saturated gains $Y_{gsat,n}$ follow an analogous behavior, as shown in Fig. 7.5 (a). We then look at the color map in Fig. 7.3(b) and observe that there is another point where the coalescence parameter C vanishes, at $gZ_0 = 0$, yielding a different EPD condition. From Fig. 7.3(d), we also observe that the phase shift associated to this EPD has $kd = \pi$, which is what we are observing in the saturated regime, even if the system started from the other EPD condition associated with $kd = 0$. Further investigation is needed to study the stability of these EPDs by looking at the Lyapunov exponents and nonlinear dynamics, as discussed in Refs. [121, 120, 105].

In summary, results from an array with a finite number N of elements indicate that the system tends to work at the point where the real and imaginary parts of the saturated gain is close to zero (as verified next). From the dispersion diagram of the complex-valued wavenumber k versus frequency, we have verified that the saturation point is at a gain value

that corresponds to another EPD condition with $kd = \pi$, which explains the observed π phase shift in the time-domain waveform. Numerical investigations show that the nonlinearity in the gain elements and their saturation raise an interesting point regarding the circuit's behavior; the system reaches a point where the oscillation frequency is insensitive to gain variations. A deeper theoretical investigation should be carried out in the future.

As further confirmation of these interesting dynamic properties, we also investigate the case where the nonlinear small-signal gain in each unit cell is *nonuniform*, i.e., varies as $g_n Z_0 = \gamma_n 1.6$ from the EPD value $g_n Z_0 = 1.6$. For the case shown in Fig. 7.5 (b), small-signal gain varies with an arbitrary value $-15\% < \gamma_n < 15\%$. Specifically for the mentioned arbitrary case, nonlinear active elements with small-signal gains are set on each unit cell with γ_n as 85%, 90%, 110%, 105%, 82%, 89%, 95%, 101%, respectively. After the system reaches saturation, the time domain waveforms show that the system tends again to work at the point where the saturated gain in each unit cell tends to be uniform and such that $-Y_{gsat,n} Z_0 << 1$. The saturated gain values in Fig. 7.5 (b) are very close to those in Fig. 7.5 (a). Thus, random variations in small-signal gain in each unit cell do not affect the system's saturation regime at the EPD. Moreover, even the implementation of actual radiators in the array might have an imperfection, therefore we have analyzed a deviation from the uniform array assuming that the actual radiators are $\zeta_n Y_r Z_0$, where $Y_r Z_0 = 2.5$. For a given arbitrary value $-5\% < \zeta_n < 5\%$, we consider the particular example with ζ_n as 95%, 98%, 102%, 101%, 96%, 102%, 99%, 97%, when $n = 1, .., 8$. After conducting time domain simulation with ADS with fixed small-signal gain $gZ_0 = 1.6$, we tracked the oscillation frequency on each unit cell, and the array still oscillates at 3 GHz.

We have performed time domain calculations on arrays with various lengths N and observed how the length affects the saturation regime. We considered nonlinear active elements with small-signal gain of $gZ_0 = 2$. Figure 7.6 (a), shows the saturated gain in the middle of the array $-Y_{gsat,n}$ in the middle of the array (where n is either $(N+1)/2$ or $N/2$ for odd or even

N, respectively) for different array lengths N (blue line), and the corresponding oscillation frequency after reaching the saturated regime (orange line). As N increases, the saturated gain has a monotonic decrease, as shown in the inset of Fig. 7.6 (a), indicating that the saturated system seems to converge to the EPD at $kd = \pi$ that occurs at 3 GHz. Indeed, in the saturation regime, the array exhibits stable oscillations at $f_{osc} = 3\,\text{GHz}$. The oscillation frequency is almost stable at the EPD frequency by only a 0.003% deviation ($\sim$100 KHz) when changing the structure length from $N = 3$ to $N = 13$.

We then investigate the efficiency of the system in terms of radiating power with respect to the power arising from the gain elements for the case of an array with $N = 8$ gain elements. In the saturated regime, we calculated the power P_r radiated by the radiating elements, and the one delivered by the nonlinear gain elements P_g. The efficiency of the system is defined as the ratio P_r/P_g evaluated in the saturated regime. Simulations are performed for different values of uniform nonlinear small-signal gains, ranging from $gZ_0 \approx 0$ to $gZ_0 = 1.6$, as shown in Fig. 7.6(b). These two values represent the two small-signal gains that are associated to the two EPDs in Fig. 7.3(b). The results reveal that when the system starts from a small-signal gain close to zero, after reaching saturation it operates with maximum efficiency. The efficiency decreases when the system starts from a larger value of small-signal gain; the efficiency is low even in the case when the system starts from the EPD associated with $gZ_0 = 1.6$ and $kd = 0$. Overall, the oscillating array system offers stable frequency of oscillation for all small-signal gain values, and high efficiency in radiating power for the lower end of small-signal gain values.

Additionally, we investigate the impact of the two load impedances Z_L on the saturation regime, displayed in Fig. 7.6(c). Time-domain simulations have been performed for Z_L ranging from 0.1 Ω to 1 kΩ, and then the power in the saturated regime has been evaluated. We still assume $N = 8$ nonlinear gain elements with $gZ_0 = 1.6$ and radiating elements with $Y_r Z_0 = 2.5$. Figure 7.6(c) shows the power P_r radiated by the arrayed radiating elements

(dashed green), the power P_L delivered to the two load terminations (dashed red), and the power delivered by the nonlinear gain elements in saturation (solid blue). Additionally, the figure presents the efficiency of the structure defined as P_r/P_g (solid black), and the oscillation frequency (solid orange). These outcomes demonstrate that remarkably the oscillation frequency at $f_{osc} = 3\,\text{GHz}$ remains almost constant, i.e., almost equal to the EPD one, with a negligible shift of only 0.006% ($\sim$200 KHz) when varying Z_L from 0.1 Ω to 1 kΩ. The stability of the oscillation frequency over a wide range of variations of the load resistance and also of the array length (number of unit cells) shows the robustness of the proposed array oscillator whose saturated regime always converges to an EPD state.

7.5 Tunability

The effect of the reactive part in the active element components Y_g is analyzed here. Such reactance can be present because of parasitic effects (e.g., in the solid state device or in its packaging, because of the way they are mounted, etc.) or because it can be added for tuning purposes. Therefore, even for small signals, we assume that the uniform linear gain elements Y_g are not a purely real negative conductance and we consider the effect of an additional inductive/capacitive susceptance as $Y_g = -g + jb$. The EPD condition corresponding to $kd = \pi$ (i.e, the λ coefficient in Eq. (7.6) is equal to +2) is discussed in the following. Accounting for the reactive part b, the EPD condition leads to these two new equations by setting both the imaginary and real parts equal to zero:

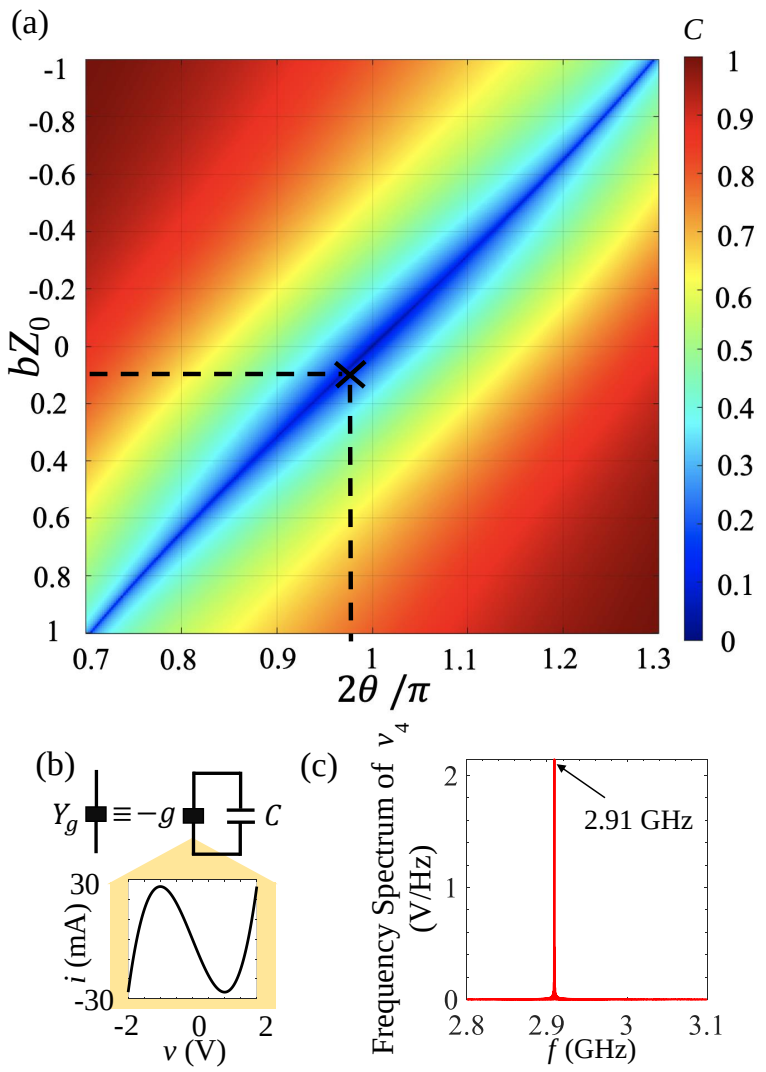

Figure 7.7: (a) The vanishing of the coalescence parameter shows different values for reactance satisfies the EPD condition. The EPs happen in different θ for different reactive susceptance b. (b) The frequency spectrum of the nonlinear gain voltage $v_4(t)$, which shows the oscillation frequency shifts when we added a small reactance to all nonlinear gain through the structure at $f_{osc} = 2.91$ GHz

$$bY_r \sin^2(\theta) + Y_r(1 - g/Y_r)\sin(2\theta) = 0$$
$$-Y_r g \sin^2(\theta) - b\sin(2\theta) - 4\cos^2(\theta) = 0 \tag{7.10}$$

Therefore, by setting $g = 0$ and $b = -2\cos\theta/\sin\theta$, the degeneracy condition at $kd = \pi$ is

satisfied. Hence, we can still find an EPD if the active reactance value is $b = -2\cos\theta/\sin\theta$, which implies that $\theta \neq \pi/2$ anymore, hence the EPD frequency is not at 3 GHz anymore. This analysis also clarifies why the results of Sec. 7.4, based on assuming that $\theta = \pi/2$ at 3 GHz, implied that the imaginary part of the saturated nonlinear gain approached zero.

Figure 7.7(a) shows the vanishing of the coalescence parameter C by varying x and $\theta = k_w d/2$, where $k_w = 2\pi f/v_w$, assuming $\mathrm{Re}(Y_g) = -g = 0$. Since the vanishing of the coalescence parameter indicates the occurrence of an EPD, the results illustrate how EPDs occur at frequencies $f = \theta v_w/(\pi d)$ that depend on b. The EPD frequency decreases/increases for larger capacitive/inductive b. For instance, we assumed that the uniform nonlinear small-signal gain admittance $Y_g = -g + jb$ comprises a capacitive reactive susceptance $b = j2\pi fC$ ($C = 0.1$ pF) equal to $bZ_0 = 0.091$ at 2.91 GHZ.

We then perform the nonlinear time-domain simulation for an array of $N = 8$ gain elements, assuming a small capacitor of 0.1pF in parallel to the nonlinear small-signal gain conductance g in each unit cell as depicted in Fig. 7.7(b). Time domain results obtained by the Keysight ADS simulator show that after saturation the oscillation frequency is $f_{osc} = 2.91$ GHz, corresponding to the EPD point denoted by the cross symbol in Fig. 7.7(a). Analogously to what has been demonstrated in the last section, here we start from a given value of small-signal gain, and after reaching saturation the admittance is $Y_{gsat,n}Z_0 \approx 0 + jb$. For example, assuming the nonlinear small-signal gain conductance of $gZ_0 = 0.3$, the saturation gain on $4th$ unit cell calculated at the oscillation frequency $f_{osc} = 2.91\,\mathrm{GHz}$ is $Y_{gsat,4}Z_0 = -0.009 + j0.093$ where the reactive part mostly comes from the added capacitor. Thus, the numerical result confirms that the system once again after starting from a given small-signal admittance value (including a reactance) converges to the limiting value associated to the EPD at $kd = \pi$ where the saturated admittance is $Y_{gsat,n} = 0 + jb$. In summary, an additional reactive part of the nonlinear gain can be adjusted to achieve tunability of the frequency of the stable oscillation.

7.6 Conclusions

We have investigated the effect of nonlinear active elements in a waveguide with a periodic array of radiating elements and discrete gain elements that supports EPDs. Importantly, by using a nonlinear gain for each active element in a finite-length array, we have demonstrated that for arbitrary choices of gain values, the array reaches a stable oscillation regime operating at a specific EPD at $kd = \pi$, independently of the number of array elements. Our results showed that even a 15% arbitrary variation in small-signal gain in each of the nonlinear elements does not alter the overall performance and the saturated gain is uniform and independent of the initial choice of the small-signal gain because the saturated gain is associated to an EPD. In other words, we have demonstrated the concept that the saturated system tends to operate at the exceptionally degenerate eigenmode. However, the initial choice of nonlinear small-signal gain affects the radiation power efficiency. We have also demonstrated that not all EPD are desirable points of operation, indeed in one representative example the initial choice of small-signal gain was an EPD but the system migrated to another EPD after reaching saturation. Further studies are needed to provide a more comprehensive analysis of nonlinear dynamics of systems with EPDs.

The proposed strategy to conceive coherent arrays of oscillators based on EPD operation provides a stable oscillation frequency (even when there is an unbalanced nonlinear gain across the array). Furthermore, the oscillation frequency does not change when varying the array length and the impedance loading at the two array ends. Numerical simulation results show that the array dynamics collapses onto a regime based on the EPD with $kd = \pi$, even when the gain elements are nonuniform along the array. Moreover, we have shown also the EPD condition in the presence of reactance in the active elements and justify the EPD occurrence by using the vanishing of the coalescence parameter. Our analysis revealed that the EPD occurs at a frequency that depends on the shunt capacitive or inductive reactance values. Nonlinear time-domain simulation has shown that a tunable EPD oscillator with a

stable oscillation frequency is conceived by adding small shunt capacitances to all the gain elements.

This proposed EPD oscillating array scheme may have diverse applications, including radiating arrays of active integrated antennas, and distributed high-power oscillators. The fundamental principles analyzed in this chapter are valid for a synchronized array of oscillators, from radio frequency to optics. The demonstrated concept is applicable also to high-power lasers with distributed power extraction (like in a vertically emitting laser). The proposed strategy is general, and it focuses on demonstrating possible advantages of EPD-based distributed oscillators in the robustness of oscillation, coherence of radiation with small phase noise, and high power in large apertures of radiators.

Acknowlegment

The text of Chapter 7 of this dissertation is a reprint of the material as it appears in Alireza Nikzamir, and Filippo Capolino. Exceptional Point Degeneracy as Desirable Operation Point of Oscillator Array with Discrete Nonlinear Gain and Radiating Elements. Phys. Rev. Appl., 21, 024037, Feb 2024. The coauthor listed in this publication is Filippo Capolino. Filippo Capolino directed and supervised research which forms the basis for the dissertation. This material is based upon work supported by the USA National Science Foundation under Award NSF ECCS-1711975.

Chapter 8

Array oscillator in coupled waveguides with nonlinear gain and radiation resistances saturating at exceptional point

A periodically loaded waveguide composed of periodic discrete nonlinear gain and radiating elements supports a stable oscillation regime related to the presence of an exceptional point of degeneracy (EPD). After reaching saturation, the EPD in the system establishes the oscillation frequency. We demonstrate a synchronization regime at a stable oscillation frequency, resulting in uniform saturated gain across the array and uniform radiating power. Unlike conventional one-dimensional cavity resonances, the oscillation frequency is independent of the array length. Our investigations further show that when small-signal gain is non-uniformly distributed across the array, the saturated gain results in having a uniform distribution at a gain value that generates an EPD. Experimental validation using the measured board confirmed that the system saturates at an EPD, with a measured spectrum exhibiting very

low phase noise. This low noise allows for operation at a clean oscillation frequency. Additionally, the measured uniform power across the array corresponds to the simulation results. The proposed scheme can pave the way for a new generation of high-power radiating arrays with distributed active elements.

8.1 Motivation and State of the Art

Exceptional points of degeneracy (EPD) in a system are singular points in a parameter space where some eigenstates experience a "full" degeneracy, i.e., when their eigenvectors and eigenvalues experience degeneracy [31, 32, 33, 34, 35]. We stress that we deal with an exceptional "degeneracy" as noted in Ref. [66], and that is the reason we have added the "D" in EPD. In the waveguide implementation studied in this paper, the eigenvalues correspond to the modal wavenumbers, and the eigenvectors represent the associated polarization states, here in terms of voltages and currents, that coalesce at an EPD. In general, an EPD occurs in systems that are periodic in space [39, 2, 55], in time [78, 174], in systems that are uniform and have spatial dispersion [74], or that have gain and loss [72, 2]. The class of EPD structures that have been mainly studied in the literature is based on parity-time (PT) symmetry [40, 44, 36, 76, 240, 71, 235] with balanced gain and loss [241, 76, 36, 70, 97].

The general conditions for EPD formation in a periodically loaded waveguide with discrete lossy elements and saturable gain were studied in Ref. [128], showing self-standing oscillations. Subsequent studies including nonlinearity in the array through discrete gain elements [253] focused on the saturation regime performance. It was found that the system converges to an EPD while undergoing saturation. However, the saturated gain value would vanish when increasing the length of the array. The purpose of this paper is to show that there are array oscillators where the saturated gain converges to a *nonvanishing value* related to an EPD. This demonstration has strong implications for high-power radiation when the length

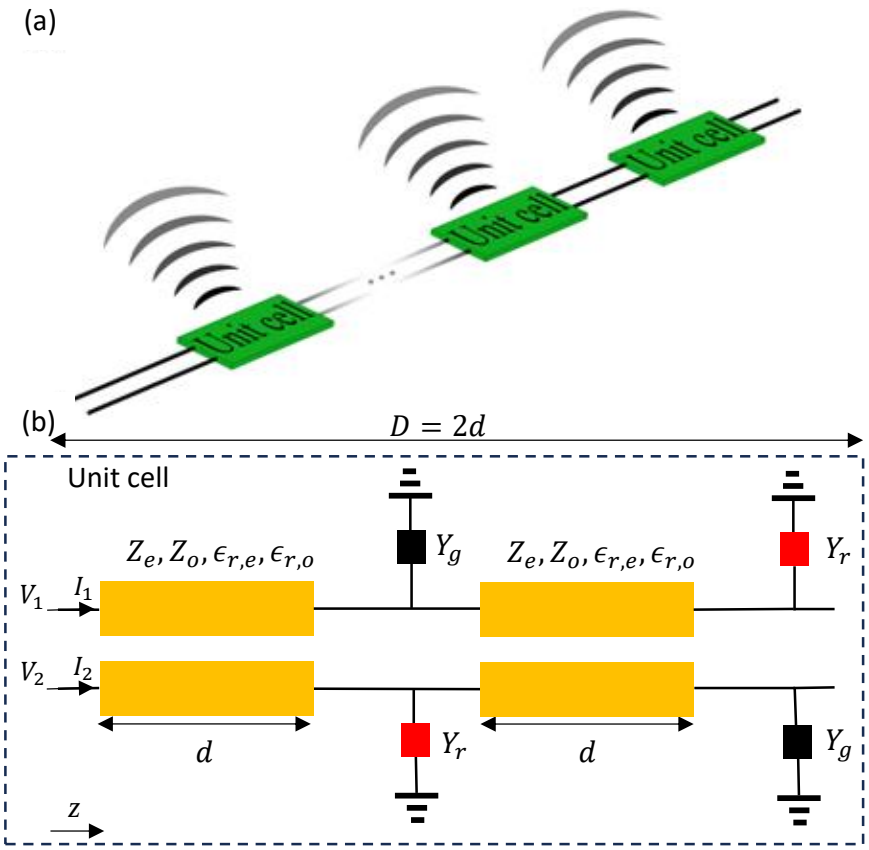

Figure 8.1: (a) Periodic array with elements radiating synchronously while oscillating. Power is radiated by the Y_r elements, two per unit cell, representing antennas. (b) Schematic of a unit cell with length $D = 2d$ made of two coupled transmission line (CTL) segments. The CTLs are characterized by even and odd mode impedances and effective permittivities Z_e, Z_o and $\epsilon_{r,e}$, $\epsilon_{r,o}$, respectively. The CTL is periodically loaded with both a lossy shunt element Y_r representing a radiator (e.g., an antenna) and a shunt nonlinear gain element Y_g at the same position z. The glide symmetry shift length is d. Voltages V_1 and V_2 are given with respect to the ground, not shown for simplicity.

of the array of antennas increases.

Recently, there has been an increasing interest in exploring the effects of nonlinearities in systems that support different kinds of EPD conditions. Studies have examined how nonlinear effects impact PT symmetry in lasing systems [118], EPD-based sensors with saturable gain [98, 86], oscillator arrays [253, 12], oscillator arrays based on degenerate band edge in microstrip circuit [8], and noise-resilient systems based on operation near an EPD [105]. Among these EPD-based applications, our focus is on the exceptional degeneracy conditions

in waveguides and on what possible advantages they offer. Specifically, we aim to explore the effects of nonlinearities in the saturation regime to design a periodic oscillator based on a waveguide with an array of antennas for efficient high-power radiation with a narrow spectral linewidth. Furthermore, it is important to confirm that such an array system should effectively operate under challenging conditions, such as system tolerances and partial failure. This situation includes the case where all the array elements do not have the same gain or one of the array elements fails or is damaged. To use the proposed concept in real life, the study of robustness and the system's resistance to failed components and perturbations is essential.

To address these challenges of robust stable oscillation, some of the present authors recently introduced a waveguide with loaded discrete nonlinear gain and antennas (simply represented by linear lossy elements for simplicity) that supports steady oscillation at a second-order EPD [253]. The EPD was the favorable regime of operation after reaching saturation. However, the saturated gain would vanish when the array length was growing to infinity. That finding raised a question that would be important for high-power radiating arrays: is it possible to have an array system supporting EPD with loss and gain where the saturated gain does not decrease with increasing array length?

This paper provides an affirmative answer to such a question that may lead to important applications. We propose a new method of designing arrays that saturate at an EPD with a non-vanishing saturated gain value, resulting in a stable oscillation frequency with increasing radiated power for longer arrays. Remarkably, while undergoing saturation, the gain in the radiating and oscillating array converges to operate at an EPD frequency at steady-state. We also show that this dynamic is independent of the value of the small-signal gain of the discrete active elements. Additionally, we also investigate the resilience of the oscillation frequency to element failure and variations in the small-signal gain and loss values. This feature is important for practical applications where guaranteeing a constant small-signal

gain level across the array is very challenging. Operating at an EPD generally leads to high radiation power and high synchronization of the signal over the radiating elements of the waveguide. It is due to the excitation of an exceptionally degenerate mode, which also leads to a low phase noise performance.

8.2 Active Waveguide Array in Saturated Oscillatory Regime

We analyze the self-oscillation mechanism due to instability in a waveguide made of two coupled microstrips periodically loaded with discrete nonlinear gain and radiating elements (modeled simply as lossy loads), as shown in Fig. 8.1(b). In each unit cell of length D, there are two nonlinear gain elements Y_g and two linear lossy loads Y_r, which alternate locations along the waveguide. Hence, the periodic waveguide has glide symmetry as defined in Ref. [254], with an effective period of $d = D/2$. Indeed, the structure is equal to itself when a half unit cell shift d is followed by a mirror operation in a transverse plane [254]. The first array case treated in Secs. 8.3 and 8.4 is neither PT symmetric nor glide-time (GT) symmetric. The concept of GT symmetry is defined and further explored in Ref. [9]. In Secs. 8.3 and 8.4, we study the tendency of the steady-state system to operate at an EPD associated to the gain values after reaching saturation. In simulations, the nonlinearity is provided by a cubic $i - v$ curve. In the following, we show that this waveguide ensures stable oscillation frequency at an EPD related to a non-zero saturated gain Y_{gsat} of the active elements, overcoming the challenges outlined above. Additionally, the "radiated" power (i.e., the power dissipated at the lossy loads Y_r) is mostly uniform across the array. The waveguide's unit cell is depicted in Fig. 8.1(b). In Sec. 8.5 we analyze a fabricated prototype to experimentally prove the discovered concepts. The experimented array in Sec.8.5 is GT-symmetric in the linear small-signal regime, and we show that it converges to a non GT-symmetric satu-

rated regime. Gain is provided by negative resistances built using operational amplifiers (op amps). For convenience, the experiment in Sec. 8.5 is carried out at lower frequencies than the design introduced in Sec. 8.3, and the coupling between the two microstrips is enhanced by adding a capacitance Y_c in each unit cell of the array. Furthermore, we investigate the stability of the oscillation frequency and system performance when the system is subjected to element failure and under variations in loss and gain values across the array.

8.3 Nonlinear Simulation Results

Nonlinearities play an important role in radio-frequency (RF) and microwave systems and bring both complexity and benefits [255]. In our theoretical analysis, we use time-domain simulations by Keysight Advanced Design System (ADS) circuit simulator to study the operation of the periodic waveguide in the saturated regime. The nonlinearity of the nth element is modeled via the $i - v$ cubic model, as described in Ref. [253], through a negative small-signal conductance $Y_{g,n} = -g_n$. The current i_n and voltage v_n relationship at the discrete nonlinear gain elements in the ADS simulator is defined as

$$i_n = -g_n v_n + \alpha_n v_n^3, \tag{8.1}$$

where $\alpha_n = g_n/3$ (unit of S/V^2) describes the saturation level with a 1 volt turning point. As it will become clear later on, the system is unstable and it oscillates at a frequency f_{osc} after reaching saturation. With the time-domain results obtained from ADS, we calculate the complex saturated gain admittance in the phasor domain using the Fourier transform of the voltage and current at the oscillation frequency f_{osc}. We implicitly assume the time convention $e^{j\omega t}$. Using the fast Fourier transform (FFT), the magnitude and phase of the admittance are calculated as

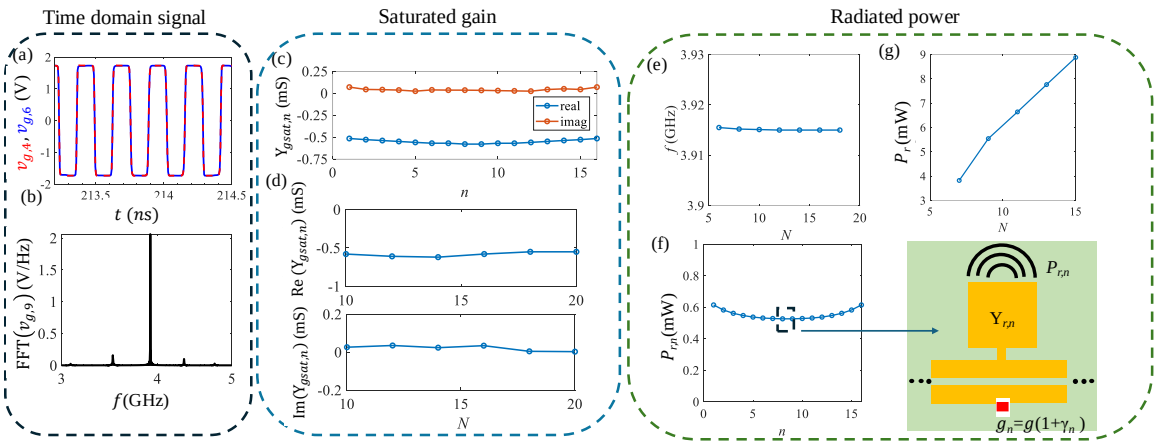

Figure 8.2: (a) Time domain signal in the saturation regime for a system with 16 unit cells in the array showing zero phase shift between voltages of nonlinear gain elements $v_{g,4}$ and $v_{g,6}$ with small signal gain $g = 10\,\text{mS}$. (b) The frequency spectrum of voltage $v_{g,9}$ (near the middle position of the system) showing an oscillation frequency of $f_{\text{osc}} = 3.91\,\text{GHz}$ in the saturation regime. (c) Calculated real and imaginary parts of the saturated gain along the structure highlighting a uniform saturated gain around $g_{sat} = 0.51\,\text{mS}$ and near negligible imaginary part. (d) The calculated real and imaginary parts of the saturated gain in the middle position of the structure ($n = N/2$) for different structure lengths N, showing a trend where the saturated gain approaches $g_{sat} = 0.51\,\text{mS}$ and $\text{Im}(Y_{gsat} \approx 0)$. (e) Oscillation frequency with respect to structure length, showing a remarkably stable frequency. A total change of 0.01% in oscillation frequency was observed when increasing the number of array elements from $N = 6$ to $N = 18$. (g) Total radiated power from the arrays for longer structure lengths shows that the radiated power more than doubles when increasing the array length from $N = 6$ to $N = 15$. (f) The radiated power of each array element along the structure for $N = 16$. There is near uniform power in the middle of the array. In the inset, half of the unit cell is displayed schematically and the radiation power from the n^{th} array is denoted as $P_{r,n}$.

$$|Y_{gsat,n}| = \frac{|\text{FFT}(i_n)|_{fosc}}{|\text{FFT}(v_n)|_{f_{\text{osc}}}} \quad , \qquad (8.2)$$

$$\angle Y_{gsat,n} = \left(\angle\text{FFT}\left(i_n\right) - \angle\text{FFT}\left(v_n\right)\right)\big|_{f_{\text{osc}}}$$

where $||$ represents the absolute value, and $\angle$ represents the phase. We performed time-domain simulations for a waveguide consisting of 8 unit cells (equivalent to $N = 16$ nonlinear elements) with a small-signal gain of $g = 10\,\text{mS}$ and a loss of $Y_r = 40\,\text{mS}$ (representing radiation).

In our design, we set the microstrips to have a width $W = 10\,\text{mm}$, a length $d = 198\,\text{mm}$, and spacing between the CTL pair to be $S = 0.3\,\text{mm}$. The waveguide is implemented on an FR4 substrate with a relative permittivity $\epsilon_r = 4.2$ and a substrate height $h = 2\,\text{mm}$. The microstrip is designed using 1 ounce copper, equivalent to a thickness $t \approx 35\,\mu\text{m}$. Using the Lincalc tool in Keysight ADS for coupled microstrip lines, we calculated the electrical values of the even and odd modes in the CTL at a frequency of 1 GHz. The relative permittivities for the even and odd modes are $\epsilon_{r,e} = 3.75$, $\epsilon_{r,o} = 3.02$, derived from $\epsilon_{r,e} = (c/v_{p,e})^2$ and $\epsilon_{r,o} = (c/v_{p,o})^2$, where c is the speed of light and v_p is the phase velocity of the respective mode. The corresponding characteristic impedances are $Z_e = 29.8\,\Omega$, and $Z_o = 19.8\,\Omega$. Additional information on the electrical parameters of coupled microstrip lines derived from their physical dimensions is discussed in Ref. [256].

To perform the finite-length simulation in Keysight ADS, the array is constructed by connecting the unit cells in series. An additional coupled transmission line segment with a length of d is added at the right end of the structure. Consequently, the array begins and ends with coupled transmission lines of length d, both terminated with open circuits. After conducting the time domain simulation in Keysight ADS, the voltage signals of the system are shown in Fig. 8.2(a), with the corresponding frequency spectrum shown in Fig. 8.2(b). The transient period is when a system transitions to a steady state, while the rising time indicates how long it takes to reach saturation. The time duration of the transient regime of the system is directly related to the initial small-signal gain. For a value of $g = 10\,\text{mS}$, it takes 150 ns for the system to reach saturation.

The time domain result in Fig. 8.2(a) shows zero phase shift between the nonlinear gain voltages $v_{g,4}$ and $v_{g,6}$ (out of 16 of them) in two consecutive unit cells (of size D) in the saturated regime. This means the periodic waveguide operates with zero Floquet-Bloch wavenumber, i.e., $k = 0$, at that frequency. The frequency spectrum of the middle nonlinear gain element $v_{g,8}$ in the saturation regime shows an oscillation frequency of 3.91 GHz. The

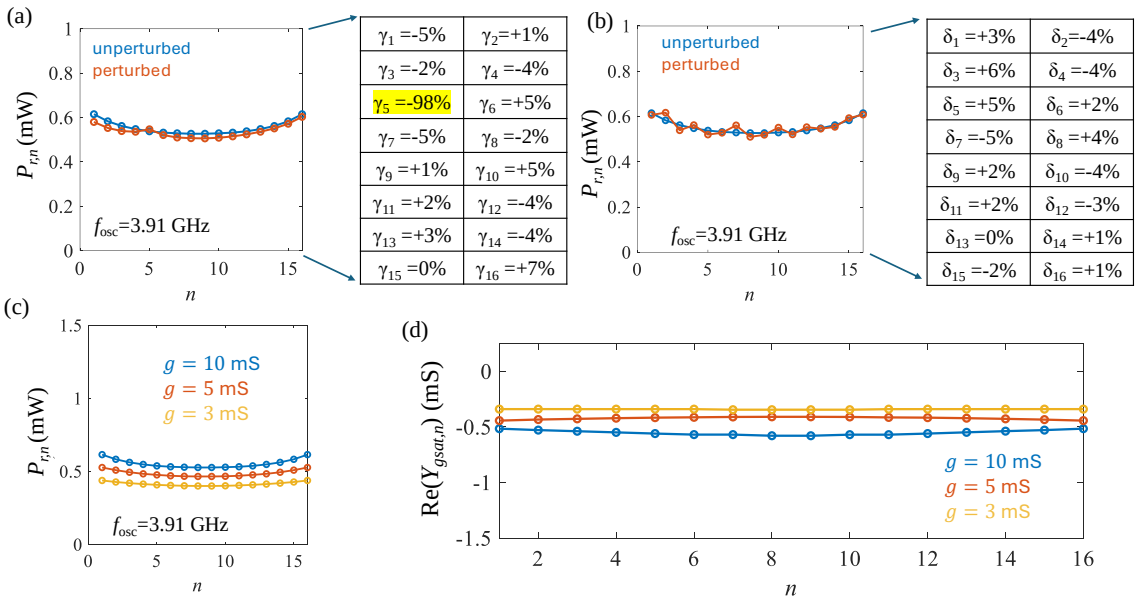

Figure 8.3: (a) Radiated power along the structure when the small-signal gain is nonuniform with random values γ_n shown as an inset. The $\gamma_5 = -98\%$ value is associated with a faulty nonlinear element. (b) Radiated power along the structure with a random perturbation on the array's admittances $-5\% < \delta_n < 5\%$ for the small gain $g = 10$mS. Radiated power for the perturbed array's admittances in orange follows the uniform one in blue well. (c) Radiated power for different small-signal gain values along the structure. (d) Saturated gain of each nonlinear gain element for different small-signal gain values. The calculated saturated gains are uniform along the structure, with the calculated value closely approaching the reported saturated gain of $g = 0.51$ mS in the middle of the structure.

frequency spectrum is calculated by applying the FFT on the saturated signal in the time window from 0.1 μs to 1 μs. We used 10^6 points in a frequency window of 0.1 GHz to 5 GHz.

To better characterize the saturated oscillation regime, in Fig. 8.2(c) we show the real and imaginary parts of saturated gain $Y_{gsat,n}$, where $n = 1, 2, ..., N$, over the $N = 16$ active elements using Eq. (8.2). The saturated gain is mostly uniform across all the nonlinear active elements, suggesting a high level of synchronization across the structure. While the system starts with all elements having a small-signal gain of $g = 10$ mS, it operates with a saturated gain g_{sat} close to 0.51 mS.

To further investigate this behavior, in Fig. 8.2(d) we examine the saturated gain in the middle array element, $Y_{gsat,n}$, where $n = N/2$, varying the total (even) number of nonlinear

elements N. There are $N/2$ unit cells, each with two gain elements. For the longer structures, the saturated gain tends to a purely real value, $g_{sat} = 0.51$ mS and the saturated reactance vanishes.

Additionally, this array displays an exceptionally stable oscillation frequency. This feature is depicted in Fig. 8.2(e), which shows the oscillation frequency at the middle of the array for lengths ranging from $N = 6$ to $N = 18$ nonlinear elements. The oscillation frequency only changes by 0.01% when the array length is tripled, thus demonstrating its stability against variations in the overall array length.

We analyze the power performance of the array by defining the total time-average "radiated" power of the array as the sum of the emitted powers at each radiating element, i.e., $P_r = \sum_{n=1}^{N} P_{r,n}$, where $P_{r,n}$ is the time-average power radiated from each array in the steady-state regime. In the saturated regime (i.e., the steady-state regime), we calculate the total time-average power P_r radiated by the radiating elements Y_r, for growing array length N. The results are depicted in Fig. 8.2(g), showing that longer structures radiate more power. Moreover, the power distribution along the length of an array is very important for many applications. Figure 8.2(f) and its inset show the time-average radiated power $P_{r,n}$ by each element n in an array of $N = 16$ nonlinear gain elements. The radiating power tends to be uniform in the middle of the array, and it does not vary much over the whole array, in agreement with the observed uniform saturated gain shown in Fig. 8.2(c).

As outlined in Ref. [253], the EPD of the infinitely long array (in this limit, the eigenvalue *is* the wavenumber) was the desirable point of operation after saturation. In Ref. [253], it was observed that when the system saturates at an EPD, the associated saturated gains of the array elements approached zero when the array length N was increasing. For that array system, the total radiated power grows with array length, but it tends to flatten with growing N because the saturated gain values in the whole array vanish. Notably, we have demonstrated here that it is possible to have systems where the power grows linearly with

array length (Fig. 8.2(g)), hence with saturated gain values that tend to a constant for growing array length N. And, importantly, the saturated regime is still associated to an EPD of the infinitely long array. This leads to a stable frequency of oscillation and low phase noise, as demonstrated next.

8.3.1 Gain and Loss Perturbation and Failure Analysis

RF or microwave oscillator schemes are required to have a stable oscillation frequency [25, 247], a high-quality factor [26, 248], a strong independence with respect to the loads [12], and a high output power [27]. To confirm these dynamic properties and to confirm the robustness of our proposed structure with respect to fabrication errors and tolerances, we examine a scenario where the small-signal gain g in each unit cell varies randomly within a certain range. The reason for this study is due to the greater difficulty in designing active elements than the passive ones. Therefore, we initially focus on perturbations of the values of the active elements, i.e., the nonlinear gain. Specifically, the gain varies as $g_n = 10 \times (1 + \gamma_n)$ mS, with $n = 1, 2, ..., N$ and where the $-10\% < \gamma_n < 10\%$ values are shown in Fig. 8.3(a). The γ_n values follow a uniform random distribution, as assumed in Ref. [253].

We also study the resilience of the system to a damaged active element by setting $\gamma_5 = -98\%$, which is equivalent to an element with near-zero small-signal gain. The resulting power delivered to each radiating element Y_r, depicted in Fig. 8.3(a), shows that even with tolerances in the small-signal gain g_n and with faulty elements, the array operates at the desired oscillation frequency $f_{\text{osc}} = 3.91$ GHz, and power delivered to all the loads Y_r follows a similar pattern as the unperturbed case where $\gamma_n = 0$. Also, the power radiated by $Y_{r,5}$, the lossy element adjacent to the faulty gain element, does not change.

Since lossy elements generally display lower tolerances than active elements, we assume that the arrays' admittances have a 5% variation around a nominal value $Y_r = 40$ mS, i.e., they

are $Y_{r,n} = (1 + \delta_n) \times 40\,\text{mS}$. Even with the values displayed in Fig. 8.3(b) for the perturbed array elements, we observe roughly uniform power radiation along the system.

Additionally, we studied changes in structure performance when the small-signal gain g is chosen to be constant over the entire array, but assuming three different values. Figure 8.3(c) shows the power delivered to the array elements Y_r, and Fig. 8.3(d) shows the saturated gain values over the discrete array elements. These results were obtained by performing time-domain simulations with three different values of the small-signal gain: $g = 10\,\text{mS}$, $g = 5\,\text{mS}$, and $g = 3$ mS for all the elements across the array. In all cases, the system oscillates and retains the same stable oscillation frequency of $f_{\text{osc}} = 3.91$ GHz regardless of the chosen small-signal gain value, and it displays roughly the same power distribution across the array. Moreover, the saturated gain values shown in Fig. 8.3(d) are approximately the same as the $g = 0.51$ mS in the original design. These results demonstrate that systems with different initial small-signal gain values still saturate close to the same gain value as the original design.

The saturation behavior of the system is intricately connected to the behavior of its modes. The results described in Sec. 8.3 suggest the saturated system operates at or near an EPD, as previously shown in Ref. [253]. Oscillators operating at an EPD show a very stable oscillation frequency, that is roughly independent of waveguide length [12]. Additionally, EPD-based oscillators display synchronized radiation across the array, caused by operation at the center or edge of the first Brillouin zone of the Bloch mode dispersion diagram, i.e., with $k = 0$ or $k = \pi/D$, as shown in the next section. We investigate the relationship between the system's modes, their degeneracy, and the overall performance.

8.4 Coupled Transmission Lines with Discrete Gain and Radiation Admittances

Exploiting the concept of EPDs to improve the performance of oscillators with distributed gain and loss has been explored in the past (see Refs. [128, 30, 246] for details). Here, as in Ref. [128], the array's radiating elements are simply represented by periodic radiation admittances Y_r along the TL. Though gain elements are nonlinear, in this section we assume they are linear and have their saturated gain value. We analyze the modes supported by the unit cell discussed in Fig. 8.1(b). The transfer matrix of the CTLs of given length d requires introducing even and odd modes, with propagation constants $\beta_e = 2\pi f\sqrt{\epsilon_{r,e}}/c$ and $\beta_o = 2\pi f\sqrt{\epsilon_{r,o}}/c$, where c is the speed of light, and characteristic impedances Z_e and Z_o. Their mode propagation is synonymously described in Ref. [257], but using the forward transfer matrix formalism, we have

$$\begin{pmatrix} V(d) \\ I(d) \end{pmatrix} = \begin{pmatrix} \cos(\beta d) & -jZ\sin(\beta d) \\ -j\sin(\beta d)/Z & \cos(\beta d) \end{pmatrix} \begin{pmatrix} V(0) \\ I(0) \end{pmatrix}, \tag{8.3}$$

where $\beta = \beta_{e,o}$, and $Z = Z_{e,o}$. Furthermore, $V = V_{e,o}$ and $I = I_{e,o}$ are the voltage and currents of the even and odd modes, defined by

$$\begin{aligned} V_e &= \tfrac{V_1+V_2}{2}, I_e = \tfrac{I_1+I_2}{2} \\ V_o &= \tfrac{V_1-V_2}{2}, I_o = \tfrac{I_1-I_2}{2} \end{aligned}. \tag{8.4}$$

It is convenient to define the waveguide state vector as $\Psi(z) = \Big(V_1, I_1, V_2, I_2\Big)^{\mathrm{T}}$, where the superscript T denotes transpose operation, and the parameters are defined in Fig. 8.1(b). This formulation is analogous to the one used for electric fields in optical waveguides [258]. The "evolution" of the state vector across the CTL segment of length d is given by

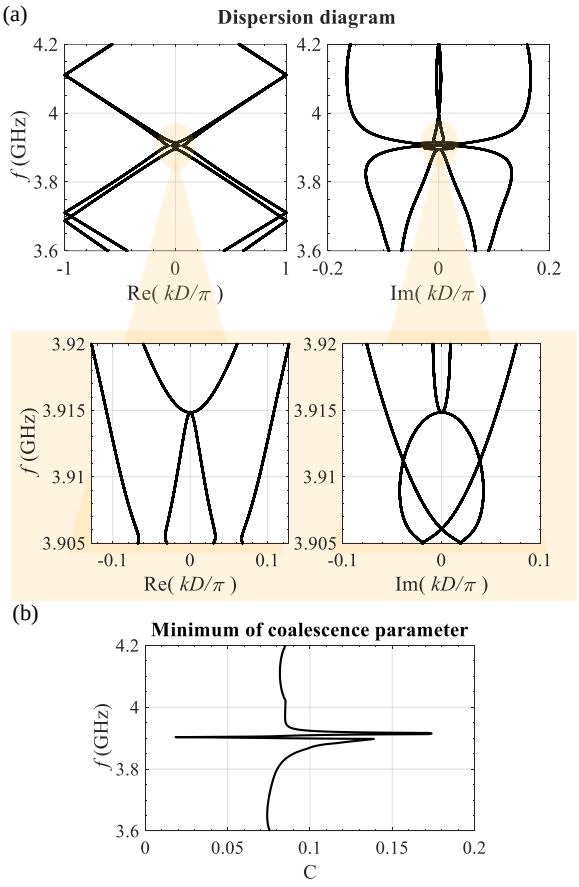

Figure 8.4: (a) Real and imaginary parts of the complex wavenumber k of the modes supported by the infinitely long array versus frequency with a zoomed-in version around the degeneracy at $kD/\pi = 0$. Branches coalesce at a second-order EPD at 3.915 GHz. This is the same steady-state oscillation frequency of the array of finite length in the steady state regime (i.e., after saturation), obtained from time domain simulations. (b) The vanishing of the coalescence parameter confirms the coalescence of two eigenvectors at 3.915 GHz.

$$\begin{pmatrix} V_1(d) \\ I_1(d) \\ V_2(d) \\ I_2(d) \end{pmatrix} = \begin{pmatrix} T_{11} & T_{12} & T_{13} & T_{14} \\ T_{21} & T_{11} & T_{23} & T_{13} \\ T_{13} & T_{14} & T_{11} & T_{12} \\ T_{23} & T_{13} & T_{21} & T_{11} \end{pmatrix} \begin{pmatrix} V_1(0) \\ I_1(0) \\ V_2(0) \\ I_2(0) \end{pmatrix}, \tag{8.5}$$

where the 4x4 matrix represents the transfer matrix $\mathbf{T}_{\mathrm{CTL}}$ of the CTL segment. Its elements are

$$
\begin{aligned}
T_{11} &= (\cos\theta_e + \cos\theta_o)/2 \\
T_{12} &= -j(Z_e \sin\theta_e + Z_o \sin\theta_o)/2 \\
T_{13} &= (\cos\theta_e - \cos\theta_o)/2 \\
T_{14} &= -j(Z_e \sin\theta_e - Z_o \sin\theta_o)/2 \\
T_{21} &= -j(\sin(\theta_e)/Z_e + \sin(\theta_o)/Z_o)/2 \\
T_{23} &= -j(\sin(\theta_e)/Z_e - \sin(\theta_o)/Z_o)/2,
\end{aligned}
$$

where $\theta_e = \beta_e d$ and $\theta_o = \beta_o d$ are the electric lengths of the even and odd modes of the two uniform waveguide segments, respectively. The transfer matrix of the unit cell, depicted in Fig. 8.1(b), is defined as

$$
\mathbf{T}_{\mathrm{U}} = \begin{pmatrix} \mathbf{T}_{\mathrm{loss}} & \mathbf{0} \\ \mathbf{0} & \mathbf{T}_{\mathrm{gain}} \end{pmatrix} \mathbf{T}_{\mathrm{CTL}} \begin{pmatrix} \mathbf{T}_{\mathrm{gain}} & \mathbf{0} \\ \mathbf{0} & \mathbf{T}_{\mathrm{loss}} \end{pmatrix} \mathbf{T}_{\mathrm{CTL}}, \tag{8.6}
$$

where $\mathbf{0}$ is a 2×2 matrix of zeros and $\mathbf{T}_{\mathrm{gain}}$, $\mathbf{T}_{\mathrm{loss}}$ are the transfer matrices of the shunt gain and loss elements, i.e.,

$$
\mathbf{T}_{\mathrm{gain}} = \begin{pmatrix} 1 & 0 \\ -Y_g & 1 \end{pmatrix}, \qquad \mathbf{T}_{\mathrm{loss}} = \begin{pmatrix} 1 & 0 \\ -Y_r & 1 \end{pmatrix}. \tag{8.7}
$$

In the small signal regime, we would have $Y_g = -g$. However, for us it is more important to analyze the state of the system after reaching saturation, hence we assume $Y_g = Y_{gsat}$. The analysis in the previous section tells us that $Y_{gsat} = -g_{sat}$ and we can neglect the reactance since it is almost zero.

The evolution equation for the state vector across a unit cell is given by $\Psi(z+D) = \mathbf{T}_{\mathrm{U}}\Psi(z)$. The modes supported by the periodic guiding structure are found by applying the Floquet-Bloch theorem [259], resulting in $\mathbf{\Psi}(z+D) = e^{-jkD}\mathbf{\Psi}(z)$ where $D = 2d$ is the unit-cell period and k is the Floquet-Bloch wavenumber. Note that d is the length of the CTL segments. The eigenmodes are found by solving the eigenvalue problem, i.e.,

$$(\mathbf{T}_{\mathrm{U}} - \zeta \underline{\mathbf{I}})\, \boldsymbol{\Psi} = 0, \tag{8.8}$$

where $\underline{\mathbf{I}}$ is the identity matrix of order four, $\zeta = e^{-jkD}$ is the eigenvalue of a mode, and $\boldsymbol{\Psi}$ is its associated eigenvector. The four eigenvalues are found by solving the characteristic equation $\det(\mathbf{T}_{\mathrm{U}} - \zeta \underline{\mathbf{I}}) = 0$. After some algebra, we obtain

$$\zeta^4 + b\zeta^3 + c\zeta^2 + b\zeta + 1 = 0, \tag{8.9}$$

where the coefficients b and c are given in Appendix A. Because of reciprocity, discussed in Appendix A, the characteristic equation is equivalent to

$$(\zeta^2 - a_1\zeta + 1)(\zeta^2 - a_2\zeta + 1) = 0, \tag{8.10}$$

where $a_1 = \zeta_1 + 1/\zeta_1$, $a_2 = \zeta_2 + 1/\zeta_2$. The terms ζ_1 and ζ_2 are the eigenmode solutions for Eq. (8.9), as well as $1/\zeta_1$ and $1/\zeta_2$ leading to the four wavenumbers k_1 and $-k_1$, and k_2 and $-k_2$.

In the remainder of this section, we discuss the EPD condition based on the characteristic equation with the coefficients shown in Appendix A. The relationship between the coefficients in the full dispersion equation in Eq. (8.9) and in the general polynomial in Eq. (8.10) are

$$\begin{aligned} b &= -a_1 - a_2 \\ c &= 2 + a_1 a_2 \end{aligned}. \tag{8.11}$$

The four modes that satisfy Eq. (8.10) are

$$\zeta_{1,3} = \frac{a_1 \pm \sqrt{a_1^2 - 4}}{2}, \quad \zeta_{2,4} = \frac{a_2 \pm \sqrt{a_2^2 - 4}}{2} \ . \tag{8.12}$$

Based on the above Eq. (8.12), this structure can support exceptional degeneracies (i.e., EPDs) of orders 2 and 4 (involving either 2 or 4 coalescing modes, respectively). An EPD of order 2 or 4 is formed when the modes of the system fall into one of the following cases: (I) when either $\zeta_1 = \zeta_3$ or $\zeta_2 = \zeta_4$, that is, when either $a_1 = \pm 2$ or $a_2 = \pm 2$, and $a_1 \neq a_2$. In this case, there is one EPD of order 2, represented as the point in the dispersion diagram where the slope vanishes, at the center or edges of the Brillouin Zone (BZ), i.e., $k = 0$ when either a_1 or a_2 is 2, or $k = \pi/D$ when either a_1 or a_2 is -2. The remaining two modes do not merge. (II) When $\zeta_1 = \zeta_3$ and $\zeta_2 = \zeta_4$, yet $\zeta_1 \neq \zeta_2$. This is equivalent to the condition that $a_1 = \pm 2$, $a_2 = \pm 2$, with $a_1 \neq a_2$. There are then two EPDs of order 2 at the same frequency, where one occurs at the center of the BZ and the other one at its edges. In this case, the dispersion diagram denotes two distinct EPDs at the same frequency, one at $k = 0$ and at $k = \pm\pi/D$. (III) When $\zeta_1 = \zeta_2$ and $\zeta_3 = \zeta_4$, namely, when $a_1 = a_2 \neq \pm 2$. In this instance, there are two EPDs of order 2 which occur at reciprocal positions off the center or edges of the BZ, i.e., $k_1 = k_2$, $k_3 = k_4$, and $k_n \neq 0, \pm\pi/D$. (IV) When $\zeta_1 = \zeta_2$ and $a_1 = a_2 = \pm 2$, the four eigenvalues become degenerate, potentially leading to the formation of a fourth-order EPD at the center or edges of the BZ. In this work, we focus on the formation of EPDs of order 2 belonging to case I, so cases II, III and IV are not considered in the following.

Figure 8.4(a) displays the dispersion diagram of the periodic waveguide with the same parameter values in the saturation regime as in Sec. 8.3, namely, $g_{sat} = 0.51\,\text{mS}$, $Y_r = 21.3\,\text{mS}$, $d = 198$ mm, $\epsilon_{r,e} = 3.75$, $\epsilon_{r,o} = 3.02$, $Z_e = 29.8\ \Omega$ and $Z_o = 19.8\ \Omega$. As expected from the results in Ref. [253], the saturated periodic system displays a second-order EPD, and the frequency at which it occurs corresponds to the frequency at which the finite-length array discussed in the previous section operates after reaching saturation, namely

$f_{\text{EPD}} = f_{\text{osc}} = 3.915\,\text{GHz}$. At this frequency, we calculate $a_1 = 2$ and $a_2 = 1.912 + 0.228i$, which show that the EPD is at $k = 0$.

The occurrence of the exceptional degeneracy is confirmed by using the concept of coalescence parameter C, introduced in Ref. [2] where it is referred to as hyperdistance. This parameter C is a figure of merit to assess how close the infinitely-long array is to an EPD by observing the degree of coalescence of the system's eigenvectors. The coalescence parameter of two eigenvectors m and n is defined as

$$\text{C}_{mn} = |\sin\theta_{mn}|,\ \cos\theta_{mn} = \frac{|\langle \mathbf{\Psi}_m, \mathbf{\Psi}_n \rangle|}{\|\mathbf{\Psi}_m\|\,\|\mathbf{\Psi}_n\|}, \tag{8.13}$$

where θ_{mn}, with any choice of $n = 1, ..., 4$ and $m = 1, ..., 4$, with $m \neq n$, represents the angle between 2 eigenvectors m and n in a four-dimensional complex vector space via the inner product $\langle \mathbf{\Psi}_m, \mathbf{\Psi}_n \rangle = \mathbf{\Psi}_m^{\dagger} \mathbf{\Psi}_n$, where the dagger symbol † denotes the complex conjugate transpose operation, and $\|\mathbf{\Psi}\| = \sqrt{\langle \mathbf{\Psi}, \mathbf{\Psi} \rangle}$ represents the norm of a complex vector [90, 260].

The coalescence parameter defined in Eq. (8.13) is always positive and smaller than one with small values indicating that the eigenvectors of the structure are close to degeneracy. At an EPD, the transfer matrix of the unit cell $\mathbf{T_U}$ is similar to a Jordan Block matrix [261, 39]. Since the transfer matrix is a 4x4 matrix, it supports four eigenmodes and eigenvectors. We are searching for a minimum coalescence parameter between each pair of eigenvectors $\text{C} = \min_{m,n}(\text{C}_{mn})$. The coalescence parameter is equal to zero when two eigenvectors in the waveguide coalesce, i.e., when the CTL system experiences a second-order EPD. In physical systems and numerical studies, the coalescence will never be exactly zero. Figure 8.4(b) shows the minimum of the coalescence parameter versus frequency. A degeneracy is clearly identified at $f = 3.915\,\text{GHz}$, which is the same oscillation frequency associated with the steady-state regime of oscillation with saturated nonlinear gain values shown in Fig. 8.2(b). In conclusion, we have demonstrated via simulations that the finite-length periodic array

with nonlinear gain elements saturates and oscillates at an EPD frequency of the waveguide dispersion. The EPD condition can be thought of as a "destination" the nonlinear system approached upon saturation.

8.5 Experimental Confirmation of EPD-Based Stable Oscillation

To provide an experimental confirmation of a periodic array system that oscillates at an EPD related to saturated nonlinear gain, as shown in the previous sections, we create another design at a lower frequency in the MHz range, instead of the $f_{\text{osc}} = 3.91\,\text{GHz}$ previously considered. By operating at lower frequencies, we can neglect several parasitic capacitances and small lengths, and therefore we can test the array using standard wiring.

The new design shows that the array oscillates at $f_{\text{osc}} = 21.67\,\text{MHz}$. To build an array that achieves uniform power distribution across the structure, we consider the same configuration discussed in Fig. 8.1. Due to the long period of the original unit cell, here we reduce the period D in experimental verification because of fabrication limitations. When decreasing the unit-cell period while maintaining differences between the even and odd modes, a strong coupling between CTLs is needed. Since it is difficult to operate with a very large difference in even and odd mode permittivities $\epsilon_{r,e}$ and $\epsilon_{r,o}$, respectively, here we include additional capacitances between the CTLs next to the lossy and active loads as shown in Fig. 8.5(a). After this modification, we first numerically verify the system's performance, followed by experimental results that validate our findings in Sec. 8.3 and Sec. 8.4.

8.5.1 Theory and Simulation of Experimental board

The theoretical investigation slightly differs from that in the previous sections because of the two extra capacitances per unit cell shown in Fig. 8.5. We will first show the time-domain simulation results by modeling the nonlinear gain as described earlier in Eq. (8.1) using ADS Keysight. Then, the modal dispersion and EPD are verified using the transfer matrix accounting for the coupling capacitors, given by

$$\mathbf{T}_{\mathrm{U}} = \begin{pmatrix} & & 0 & 0 \\ \mathbf{T}_{\mathrm{loss}} & & Y_c & 0 \\ 0 & 0 & & \\ Y_c & 0 & \mathbf{T}_{\mathrm{gain}} & \end{pmatrix} \mathbf{T}_{\mathrm{CTL}} \begin{pmatrix} & & 0 & 0 \\ \mathbf{T}_{\mathrm{gain}} & & Y_c & 0 \\ 0 & 0 & & \\ Y_c & 0 & \mathbf{T}_{\mathrm{loss}} & \end{pmatrix} \mathbf{T}_{\mathrm{CTL}}, \tag{8.14}$$

where $\mathbf{T}_{\mathrm{gain}}$ and $\mathbf{T}_{\mathrm{loss}}$ are the transfer matrices of the shunt gain and loss with the added capacitor, i.e.,

$$\mathbf{T}_{\mathrm{gain}} = \begin{pmatrix} 1 & 0 \\ -(Y_g + Y_c) & 1 \end{pmatrix}, \qquad \mathbf{T}_{\mathrm{loss}} = \begin{pmatrix} 1 & 0 \\ -(Y_r + Y_c) & 1 \end{pmatrix}, \tag{8.15}$$

where $Y_c = j\omega C$ is the coupling capacitive admittance. We use the Rogers RO4350B grounded dielectric substrate with relative permittivity $\epsilon_r = 3.48$ and height $h = 2\,\mathrm{mm}$, covered by 1 ounce copper. It has low loss, characterized by $\tan\delta = 0.003$ for frequencies ranging from 0.1 MHz to 1 GHz. We design the microstrips with a width $W = 10\,\mathrm{mm}$ and a length $d = 50\,\mathrm{mm}$. The spacing between the CTL segments is $S = 1\,\mathrm{mm}$. The unit-cell period is $D = 2d = 100\,\mathrm{mm}$, roughly a quarter of the value in the original design. The coupled microstrips are characterized by $\epsilon_{r,e} = 3.2$, $\epsilon_{r,o} = 2.7$, $Z_e = 32\,\Omega$, and $Z_o = 24.4\,\Omega$, at a frequency of 1 GHz. The loads representing the radiation admittance are $Y_r = 21.3\,\mathrm{mS}$.

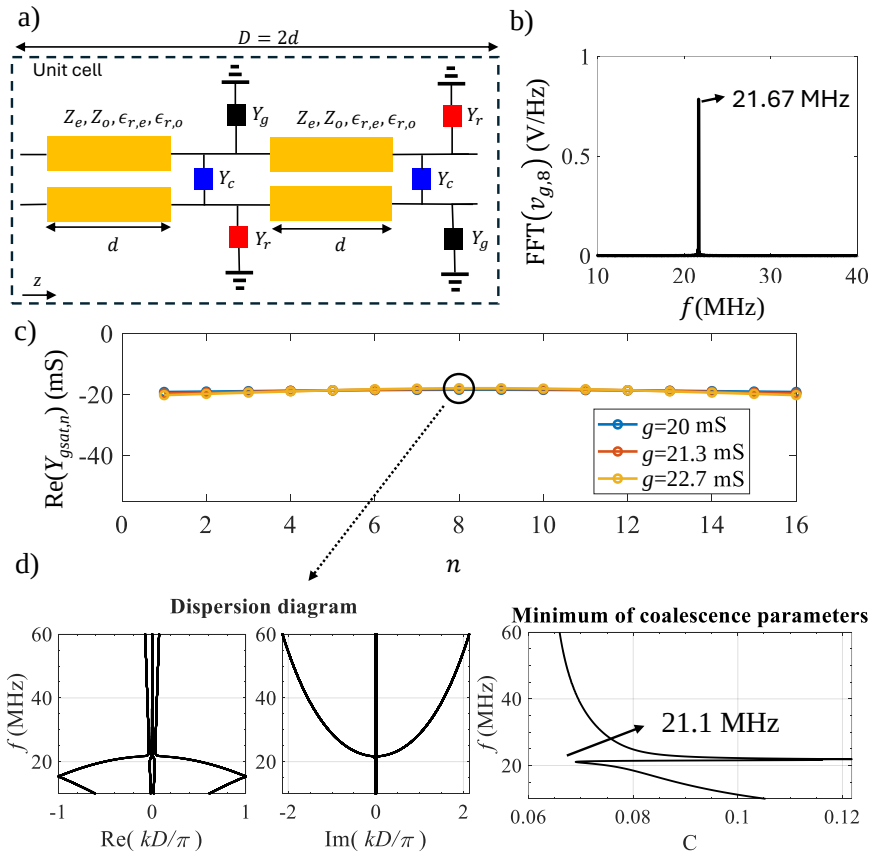

Figure 8.5: (a) Proposed circuit with a coupling capacitive admittance $Y_c = j\omega C$ between the two TLs. (b) Frequency spectrum of the voltage $v_{g,8}$ (near the middle position of the system) after reaching the saturation regime. (c) Saturated gain calculated in the saturation regime over the structure for $N = 16$. (d) Calculated dispersion diagram and coalescence parameter for the structure using $g_{sat} = 18.1$ mS as gain, showing an EPD close to the spectrum maximum in (b).

To conduct the finite-length simulation in Keysight ADS and ensure consistency with the experimental board being tested later on, the array starts with a coupled transmission line of length $d/2$ in the first unit cell instead of d. Similarly, an additional CTL of length $d/2$ is included at the other end. As a result, the system begins and ends with coupled transmission lines of length $d/2$, both terminated with open circuits. Via ADS Keysight simulations, we found that increasing the coupling capacitance from $C = 1$ nF to 16 nF, with a small-signal gain of $g = 21.3$ mS, leads to a significant reduction in the oscillation frequency. To make fabrication and measurement feasible, we chose a coupling capacitance of $C = 16$ nF, which

significantly lowers the oscillation frequency to $f_{\text{osc}} = 21.67\,\text{MHz}$ for $N = 16$ nonlinear gain elements as seen as the first peak in Fig. 8.5(b) that shows the frequency spectrum of the system. Based on the theoretical investigation and time-domain simulation results in Sec. 8.3, we expect uniformly saturated gain values across the array.

Figure 8.5(c) shows the real part of the saturated gain along the array for three different small-signal gains: $g = 20\,\text{mS}$, $g = 21.3\,\text{mS}$, and $g = 22.7\,\text{mS}$. These results show the expected behavior for the oscillation frequency at $f_{\text{osc}} = 21.67\,\text{MHz}$, with a saturated gain value close to $g_{sat,8} = 18.1\,\text{mS}$, in all cases, *independently of the value of the small-signal gain* considered. The array primarily oscillates at the fundamental frequency, with the third harmonic appearing 20.4 dB below the peak at the fundamental frequency $f_{\text{osc}} = 21.67\,\text{MHz}$ in the obtained simulated frequency spectrum for Keysight ADS. Using the calculated value of the eighth element's saturated gain, $g_{sat,8} = 18.1\,\text{mS}$, in Fig. 8.5(d), we plot the wavenumber dispersion of the modes in the infinitely long array, and the coalescence parameter C whose minimum reveals how close the system is to the ideal EPD. It is important to note that this coalescence is determined by finding the minimum among six possible combinations of the four eigenvectors, as outlined in Sec. 8.4. The system exhibits a second-order EPD at 21.1 MHz based on the calculated coalescence parameter, which is close to the frequency of oscillation of the finite-length array with nonlinear elements. In these results, the coalescence parameter does not completely vanish, but it is very close to zero, revealing that the system approaches the ideal EPD of the infinitely long array. By analyzing the dispersion of this updated design, we see that it is a second-order EPD of case (I) as in the previous design.

8.5.2 Experimental Results

The experimental board is shown in Fig. 8.6(a). This board implements the structure shown in Fig. 8.5(a), where the nonlinear gain is created with an op amp-based inverter

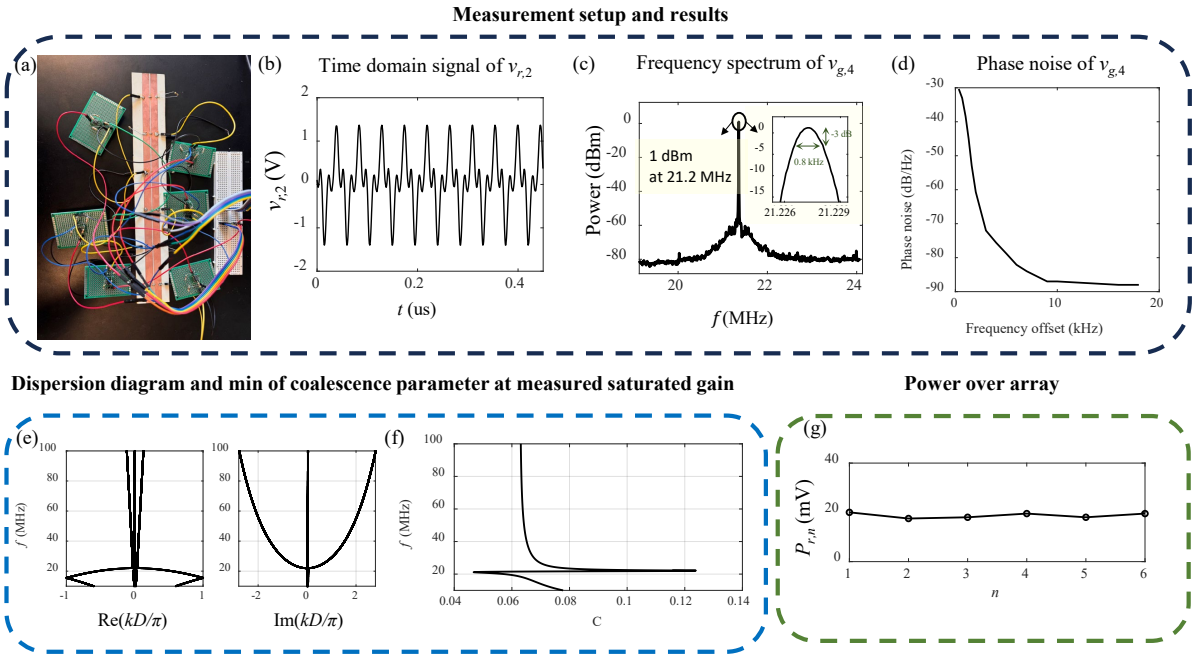

Figure 8.6: (a) Assembled array with a length of $N = 6$ (three unit cells). (b) Measured time-domain voltage signal at the fourth array element $Y_{r,2}$ using an oscilloscope. (c) Measured spectrum using a spectrum analyzer (Rigol DSA832E) with the fundamental frequency of oscillation at 21.2MHz at the fourth gain element. (d) The phase noise of the power spectrum measured by the spectrum analyzer at frequency offsets from a few Hertz to 20 kHz, with a resolution bandwidth of 100Hz and a video bandwidth of 30Hz to fully capture the spectrum. (e) Real and imaginary parts of the complex wavenumber k as a function of frequency, showing a second-order EPD at 21.1 MHz using the saturated gain value $g_{sat} = 19$ mS. (f) Coalescence parameter confirming at least two eigenvectors coalescence at 21.1 MHz. (g) Measured radiated power along the array.

circuit (Texas Instruments, model LMH6702MAX/NOPB), as depicted in Fig. 8.10(a) in Appendix D. To achieve a small-signal gain of $g = 21.3$ mS, we used a 47 Ω resistor in series with a 1Ω resistor. The additional 1Ω resistor was added to compensate for the loss produced by the dummy 1 Ω resistor placed in series with the inverter. This dummy resistor allows us to measure the current entering the inverter system, enabling us to calculate the active admittance in the saturated regime as detailed in Appendix D. By setting $g = 21.3$ mS, we measure the time domain of $v_{r,2}$ and frequency spectrum signal of $v_{g,4}$, as shown in Fig. 8.6(b) and (c), respectively. Based on the measurements discussed in Appendix D, the negative gain admittance achieved by the inverter circuit is mainly real valued. We measured

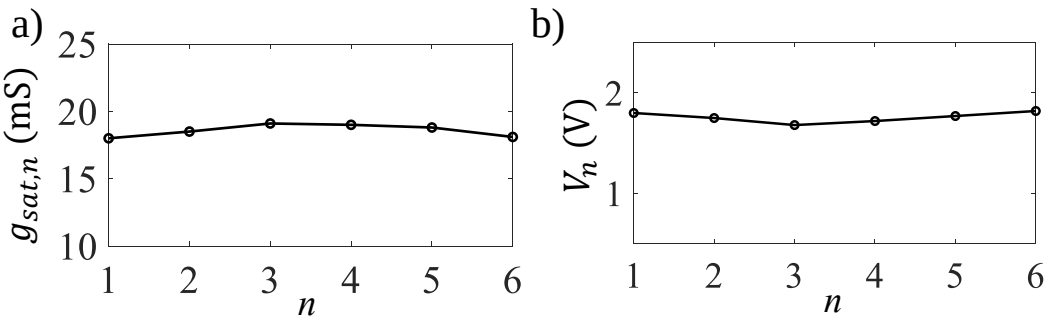

Figure 8.7: (a) Measured saturation gain distribution across the array for $N = 6$. (b) Voltage amplitudes corresponding to each gain element. They are both more or less constant across the array.

the oscillation frequency to be $f_{\text{osc}} = 21.2\,\text{MHz}$, noting a slight shift from the simulation results. We suspect this small difference between the simulated and measured oscillation frequencies can be attributed to different nonlinearity and saturation models.

To confirm that the system tends to oscillate at an EPD in the saturation regime, we measured the saturated gain of the active elements. Using the technique discussed in Appendix D, we measured $g_{sat,4} \approx 19\,\text{mS}$, which is close to the real value found via ADS time-domain simulations. The measured saturation gain g_{sat} across the arrayed active elements and the corresponding voltage amplitudes are shown in Fig. 8.7(a) and (b), respectively. The measured $g_{sat,n}$ shows a uniform gain distribution across the array.

An essential feature of any oscillator is its ability to produce a near-perfect periodic time-domain signal, which is quantified in terms of phase noise [262, 263]. The phase noise refers to the random fluctuations in the phase of an oscillator's output, and it plays a critical role in determining the stability and quality of the output signal. Minimizing phase noise ensures reliable performance in applications where precise frequency control is necessary [264]. The measured power spectrum and phase noise up to a 20 kHz frequency offset are shown in Fig. 8.6(c) and (d). Despite the presence of electronic noise (which is significant in the op amp) and thermal noise, the proposed oscillator exhibits stable oscillation with notably small harmonics. The low phase noise of -89dB/Hz at a 10kHz offset from the oscillation frequency

confirms the oscillator's stability and precision. A key indicator of clean oscillation is the narrow linewidth of the oscillation spectrum in Fig. 8.6(c). We used a resolution bandwidth of 100 Hz and a video bandwidth of 100 Hz. All the measured frequency spectra of gain over the array remain clean, approximately down to -81 dB from the peak value. At the fourth gain element, the linewidth, measured at -3 dB from the peak, is around 0.8 kHz, indicating the very narrow linewidth relative to the oscillation frequency.

To confirm the saturated system supports an EPD at the oscillation frequency, we calculate the Bloch mode dispersion diagram using the gain of $g_{sat} = 19$ mS measured in the saturation regime. The real and imaginary parts of the complex Bloch wavenumber k as a function of frequency are shown in Fig. 8.6(e). The plot highlights the presence of a second-order EPD with $k = 0$ at 21.1 MHz, which is very close to the oscillation frequency obtained from both the time-domain simulations and the experimental measurements. To further validate the EPD occurrence, we calculate the coalescence parameter C using the measured saturated gain of $g_{sat} = 19$ mS. As shown in Fig. 8.6(f), the coalescence parameter reaches its minimum at 21.1 MHz, verifying the existence of an EPD in the system.

Figure 8.6(g) shows the measured time-average power delivered to each array element. The power $P_{r,n} = Y_r|V_{r,n}|^2/2$ is determined by measuring the voltage $V_{r,n}$ on each real-valued radiation admittance $Y_r = 21.3$ mS. Here, $|V_{r,n}|$ represents the phasor magnitude, calculated as the peak value of the measured time-domain signal. For example, the measured time-average power $P_{r,4} = 19.4$ mW delivered to the fourth array element is more or less close to the power generated by the fourth active element $P_{g,4} = g_{sat,4}|V_{g,4}|^2/2 = 26.8$ mW.

The plot in Figure 8.6(g) also shows that the power over the array elements is more or less constant across the array. We have used resistors with a 1% tolerance, while the active elements may have an ever larger small-signal gain variation across the array. The uniform power distribution delivered to the admittances $Y_{r,n}$ implies that arrayed antennas working at an EPD will maintain constant radiated power across the array, highlighting the robustness of

the design in practical scenarios with elements' variability. These findings show the important result that the array radiates power at a stable, low-noise, oscillation frequency, as discussed in Sec. 8.5.1, even when perturbations occur.

8.6 Conclusions

We have demonstrated that the proposed array of active nonlinear elements and loads (representing antennas), achieves a stable oscillation frequency and uniform power distribution over the lossy elements with a non-zero saturated gain across the array. The work in Ref. [253] showed a degenerate active array structure that saturated gain that decreases when increasing the array length, converging to an EPD. In this work, we overcome that limitation by achieving a periodic array system with non-zero saturated gain across the array, oscillating at a stable frequency, with a narrow linewidth, and with uniform power distribution across the array. The active array consistently operates near an EPD in its steady state, regardless of the initial small-signal gain values. This inherent stability, along with the resilience to variations in gain or loss variations and discrete element failure, underscores the robustness of the new concept. These concepts have been verified via simulations for two array designs, and experimentally for the second design.

Our findings indicate that the EPD is the desirable operational regime, because of the nonlinear gain dynamics. Indeed, the saturated gain is predominantly uniform across all nonlinear active elements and equal to the one that leads to an EPD in the infinitely long array. The system's tendency to reach a purely real saturated gain, especially in longer structures, further supports the effectiveness of the proposed design in maintaining the exceptional degenerate regime under various conditions.

By operating at an EPD, the array oscillator not only stabilizes the oscillation frequency

with respect to the array length but also provides radiation power that increases with the array length, making it highly suitable for high-power radiation applications requiring a stable frequency with low noise.

8.7 Appendix A: Coefficients for the Dispersion Relation

The coefficients b and c in Eq. (8.9) are

$$\begin{aligned}
\mathrm{Re}(b) &= (Y_r - g)^2 \left(Z_o \sin\theta_o - Z_e \sin\theta_e\right)^2 /4 \\
&-2Y_r g Z_e Z_o \sin\theta_e \sin\theta_o + 4\left(1 - \cos^2\theta_e - \cos^2\theta_o\right) \\
\mathrm{Im}(b) &= (g - Y_r)\left(Z_e \sin(2\theta_e) + Z_o \sin(2\theta_o)\right) \\
\mathrm{Re}(c) &= (Y_r - g)^2 \left(Z_o \sin\theta_o - Z_e \sin\theta_e\right)^2 /2 - (Y_r - g)^2 \left(Z_e \sin\theta_e \cos\theta_o + Z_o \sin\theta_o \cos\theta_e\right)^2 \\
&+(Y_r g Z_e Z_o \sin\theta_e \sin\theta_o + 4\cos\theta_e \cos\theta_o)^2 - 4Z_e Z_o \sin\theta_e \sin\theta_o Y_r g - 8\cos^2(\theta_o) - 8\cos^2\theta_e + 6 \\
\mathrm{Im}(c) &= (Y_r - g)[Y_r g Z_o Z_e \left(Z_e \sin(2\theta_o)\sin^2\theta_e + Z_o \sin(2\theta_e)\sin^2\theta_o\right) + 2Z_o \sin(2\theta_o)\cos(2\theta_e) \\
&+2Z_e \sin(2\theta_e)\cos(2\theta_o)],
\end{aligned} \tag{8.16}$$

where Z_e and Z_o are characteristic impedances and $\theta_e = \beta_e d$ and $\theta_o = \beta_o d$ are the electric lengths of the even and odd modes of the uniform coupled waveguide segments, respectively.

Because of reciprocity, if a complex wavenumber k is a solution to the characteristic equation, $-k$ is also a solution. Therefore, we simplify the characteristic equation as follows: the eigenvalues ζ_1, $1/\zeta_1$, ζ_2 and $1/\zeta_2$ are the four solutions of the characteristic equation that is

rewritten as

$$\begin{aligned}&(\zeta-\zeta_1)(\zeta-1/\zeta_1)(\zeta-\zeta_2)(\zeta-1/\zeta_2)\\&=(\zeta^2-a_1\zeta+1)(\zeta^2-a_2\zeta+1)=0,\end{aligned}\tag{8.17}$$

where

$$a_1=\zeta_1+1/\zeta_1,\quad a_2=\zeta_2+1/\zeta_2.\tag{8.18}$$

Expanding this equation, we write

$$\zeta^4-\zeta^3(a_1+a_2)+\zeta^2(2+a_1a_2)-\zeta(a_1+a_2)+1=0,\tag{8.19}$$

which coincides with 8.9, whose solutions are the four Bloch eigenmodes.

8.8 Appendix B: Resilience to Small-Signal Gain Variations

To ensure the experiment's resilience to tolerances, we consider scenarios where there are variations in the active elements and investigate via simulations the resilience of the system to such perturbations. We examine two different initial small-signal gains, $g = 21.3\,\text{mS}$ and $22.7\,\text{mS}$. In each case, we assume a large variation of the small-signal gain values from array element to element. Specifically, the small-signal gain varies, for each of the two different scenarios, as $g_n = g \times \gamma_n$, where $-5\% < \gamma_n < 5\%$ or $-10\% < \gamma_n < 10\%$. These variations are illustrated in Fig. 8.8. For the cases with maximum perturbation of 5% or 10%, the γ_n values are shown as an inset. In each scenario, the resulting saturated gain value, obtained via ADS time-domain simulations, is more or less the same and it leads to an EPD at roughly the same frequency. Furthermore, the oscillation frequency in the steady state regime is maintained at $f_{\text{osc}} = 21.67\,\text{MHz}$ in all six cases.

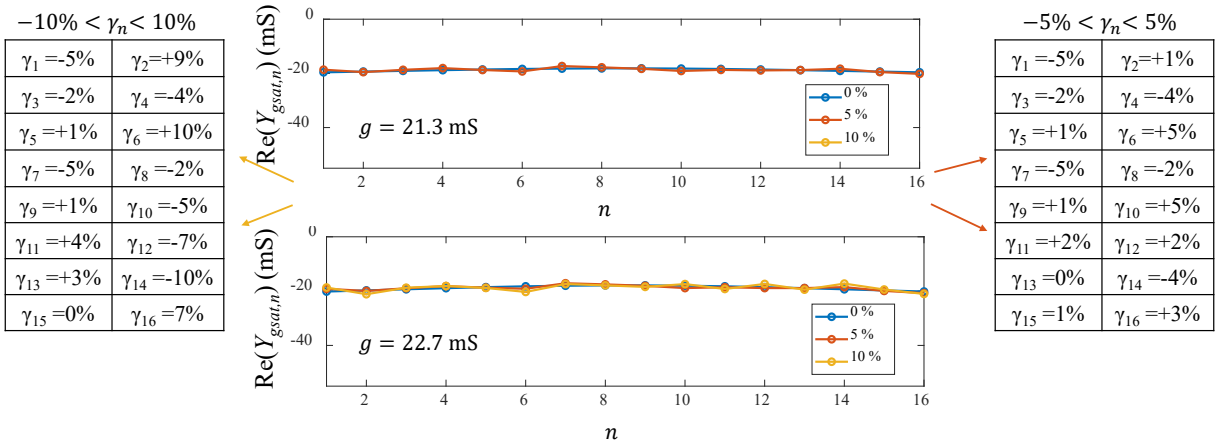

Figure 8.8: Simulated saturated gain of each nonlinear gain element for two small-signal gain values $g = 21.3\,\text{mS}$ and $g = 22.7\,\text{mS}$. In each case, we apply a random perturbation of the array's small-signal admittances $Y_{g,n} = -g_n$ across the array with relative variation $-5\% < \gamma_n < 5\%$ and $-10\% < \gamma_n < 10\%$. The saturated gains are basically the same for all the six cases considered, confirming that the array saturates at and EPD independently of the variations and perturbations of small-signal gain.

8.9 Appendix C: Power Extraction and Oscillation Frequency Stability Varying Array Length

Here, we demonstrate how the power extraction (i.e., delivered to the loads Y_r) increases when the array length increases, while maintaining a stable oscillation frequency. To do this, we conducted time-domain simulations using Keysight ADS to determine the total power, and oscillation frequency versus array length. All the results in this Appendix are based on simulations, assuming the small-signal gain is $g = 21.3\,\text{mS}$. Additionally, we analyze the saturated gain in the middle of the structure as a function of N. Our goal is to confirm that the structure operates at the EPD, independently of the array length.

Figure 8.9(a) illustrates the *total* power delivered to all the N elements Y_r, showing a clear increase in radiated power as the array lengthens. Moreover, in Fig. 8.9(b) we present the saturated gain in the middle of the structure, i.e., for $n = N/2$, as a function of N, revealing a more or less constant $g_{sat,n} \approx 18\,\text{mS}$, with $n = N/2$, after $N = 12$. Furthermore, Fig. 8.9(c)

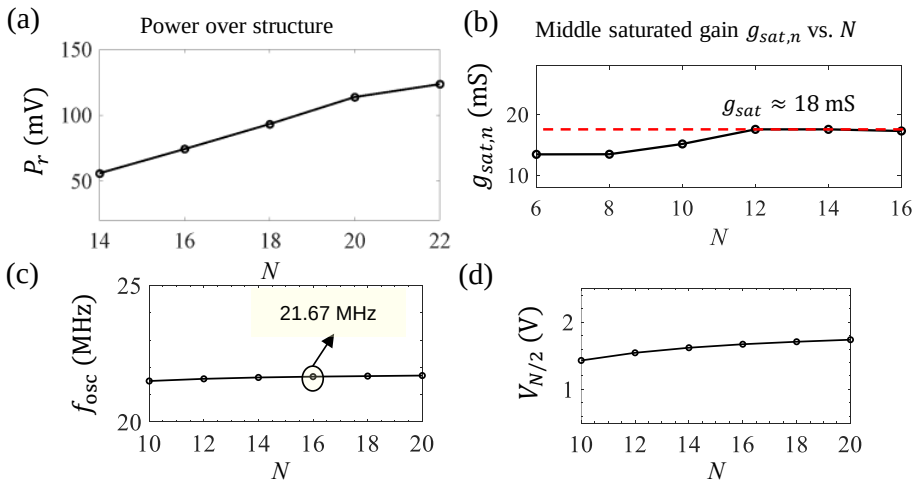

Figure 8.9: (a) Total "radiated" power increases with array length, where N is the number of active elements. (b) Calculated real part of the saturated gain in the middle of the array ($n = N/2$) versus array length N, which shows a trend where the saturated gain approaches a constant value $g_{sat} \approx 18\,\text{mS}$ independently of the array length. (c) The oscillation frequency remains stable with changes in array length, showing less than 1% variation when the number of array elements doubled from $N = 10$ to $N = 20$. (d) Oscillation signal's voltage amplitude at the active elements at the center of the array ($n = N/2$), from $N = 10$ to $N = 20$.

demonstrates that the oscillation frequency within the array is $f_{\text{osc}} = 21.67\,\text{MHz}$, confirming that the concept of extracting more power from a longer array with stable oscillation is feasible. The result shows that the oscillation frequency changes by less than 1 % as the system length increases from $N = 10$ to $N = 20$.

Figure 8.9(d) shows the voltage amplitude of the oscillation signal at the middle gain element ($n = N/2$) for array lengths ranging from $N = 10$ to $N = 20$. For instance, in an array with $N = 14$, the voltage amplitude at the center element is $V_{g,7} = 1.6\,\text{V}$. To further validate the measurement results, the power provided by this active element in the steady state regime is calculated as $P_{g,7} \approx 23\,\text{mW}$, which corresponds to the measured power $P_{r,4}$ delivered on Y_r shown in Fig. 8.6(g). Furthermore, since the system operates in a saturated gain regime with approximately constant gain across the array, the total power produced by all the active elements is expected to follow $P_g \approx N \times P_{g,N/2}$, where P_g is the total power and $P_{g,N/2}$ represents the power delivered by the middle gain element. By analyzing the voltage distribution for different array lengths and the total power, we confirm that the

system maintains a uniform operational state due to the EPD.

8.10 Appendix D: Measurement of Negative Conductance in the Saturated Regime

Several approaches can provide the negative conductances for the proposed array. In the experiment, we have used the circuit shown in Fig. 8.10(a) that utilizes an operational amplifier (op amp) to generate a negative impedance. The converter circuit modifies the impedance such that $Z_{\text{in}} = -(1/g + 1) + 1\,\Omega$. In our experiment, we used $1/g = 47\,\Omega$ and $R_2 = 1\,\text{k}\Omega$ to achieve the small-signal gain of $g = 21.3\,\text{mS}$.

To measure the gain in the saturated regime, we first measured the voltage $v_{\text{in}} = v_1$ at the nonlinear active element in Fig. 8.10(a) in the saturation regime. We also measured the voltage across a dummy $1\,\Omega$ resistor that leads to the calculation of the input current of the active element. Note that we have added another $1\,\Omega$ in the inverter in series to $1/g$ to compensate for the dummy resistance $1\,\Omega$, resulting in $Z_{\text{in}} = -1/g = -1/21.3\,(1/\text{mS})$. In Fig. 8.10(b), we show the measured v_1 and v_2 for the fourth nonlinear gain element with respect to the ground using an oscilloscope. The voltage difference is measured to estimate the current $i_{\text{in}} = (v_1 - v_2)/(1\,\Omega)$; the measured saturated gain is calculated, in phasor terms, as $Y_{gsat} = I_{\text{in}}/V_{\text{in}}$. As expected, the phase shift observed between the voltage v_2 and v_1 across the $1\,\Omega$ resistor is negligible, as shown in Fig. 8.10(b), leading to an almost real-valued Y_{gsat}. To further analyze the voltages v_1 and v_2, we used a spectrum analyzer to measure their spectrum in Fig. 8.10(c), that confirm that their oscillation frequency is 21.2 MHz. These measurements are done using a resolution bandwidth of 300 kHz and a video bandwidth of 300 kHz. Based on the measured voltages, we obtained a saturated gain admittance $g_{sat,4} \approx 19\,\text{mS}$.

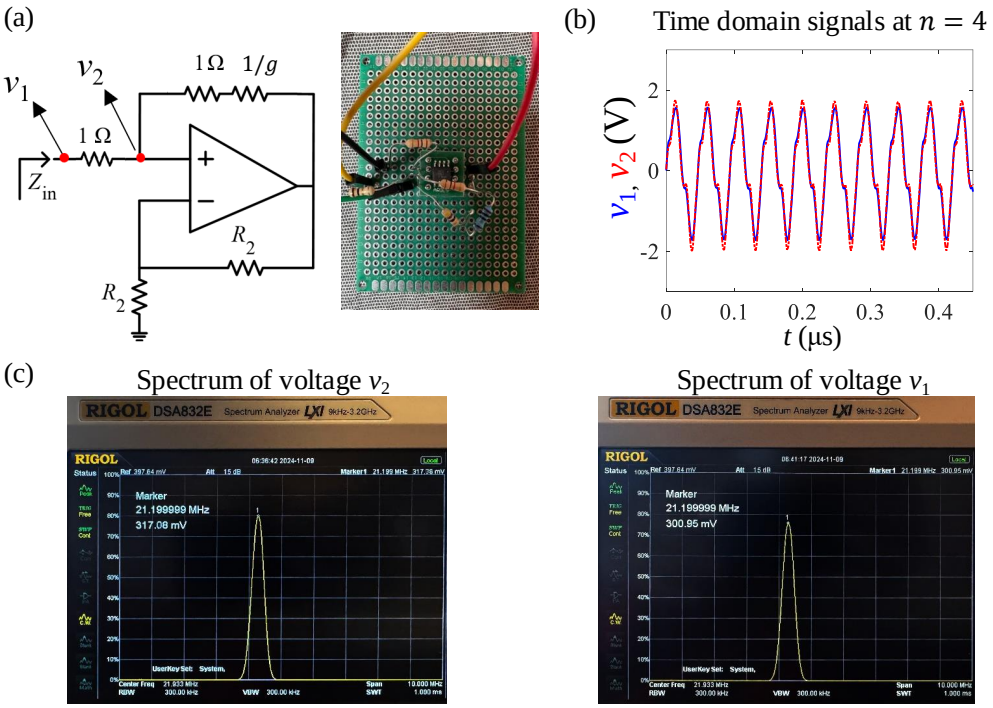

Figure 8.10: (a) Schematic of the circuit using an op amp to provide a negative conductance $Y_g = -g$. (b) Measured time-domain signals v_1 and v_2 in phase, showing that $Y_{gsat,4}$ is mainly real. (c) The measured frequency spectrum of v_1 and v_2, showing the oscillation frequency is 21.2 MHz when $N = 6$.

Bibliography

[1] Mohamed Y. Nada, Mohamed A. K. Othman, and Filippo Capolino. Theory of coupled resonator optical waveguides exhibiting high-order exceptional points of degeneracy. *Phys. Rev. B*, 96:184304, Nov 2017.

[2] A. F. Abdelshafy, M. A. K. Othman, D. Oshmarin, A. T. Almutawa, and F. Capolino. Exceptional points of degeneracy in periodic coupled waveguides and the interplay of gain and radiation loss: Theoretical and experimental demonstration. *IEEE Transactions on Antennas and Propagation*, 67(11):6909–6923, Nov 2019, doi: 10.1109/TAP.2019.2922778.

[3] Joseph Schindler, Ang Li, Mei C. Zheng, F. M. Ellis, and Tsampikos Kottos. Experimental study of active lrc circuits with $\mathcal{PT}$ symmetries. *Phys. Rev. A*, 84:040101, Oct 2011.

[4] Hamidreza Kazemi, Mohamed Y. Nada, Tarek Mealy, Ahmed F. Abdelshafy, and Filippo Capolino. Exceptional points of degeneracy induced by linear time-periodic variation. *Phys. Rev. Applied*, 11:014007, Jan 2019, doi: 10.1103/PhysRevApplied.11.014007.

[5] Hossein Hodaei, Absar U. Hassan, Steffen Wittek, Hipolito Garcia-Gracia, Ramy El-Ganainy, Demetrios N. Christodoulides, and Mercedeh Khajavikhan. Enhanced sensitivity at higher-order exceptional points. *Nature*, 548(7666):187–191, 2017.

[6] Pai-Yen Chen, Maryam Sakhdari, Mehdi Hajizadegan, Qingsong Cui, Mark Ming-Cheng Cheng, Ramy El-Ganainy, and Andrea Alù. Generalized parity–time symmetry condition for enhanced sensor telemetry. *Nature Electronics*, 1(5):297–304, May 2018, doi: 10.1038/s41928-018-0072-6.

[7] Dmitry Oshmarin, Farshad Yazdi, Mohamed A.K. Othman, Jeff Sloan, Mohammad Radfar, Michael M. Green, and Filippo Capolino. New oscillator concept based on band edge degeneracy in lumped double-ladder circuits. *IET Circuits, Devices & Systems*, 13(7):950–957, Jul 2019, doi: 10.1049/iet-cds.2018.5048.

[8] Dmitry Oshmarin, Ahmed F Abdelshafy, Alireza Nikzamir, Michael M Green, and Filippo Capolino. Experimental demonstration of a new oscillator concept based on degenerate band edge in microstrip circuit. *arXiv:2109.07002. [Online]. Available: http://arxiv.org/abs/2109.07002*, 2021.

[9] Farshad Yazdi, Tarek Mealy, Alireza Nikzamir, Robert Marosi, and Filippo Capolino. Third order modal exceptional degeneracy in waveguides with glide-time symmetry. *Phys. Rev. A*, 105:052230, May 2022.

[10] Farshad Yazdi, Mohamed AK Othman, Mehdi Veysi, Alexander Figotin, and Filippo Capolino. A new amplification regime for traveling wave tubes with third-order modal degeneracy. *IEEE Transactions on Plasma Science*, 46(1):43–56, 2017.

[11] Hao Wang, Abbas Jasim, and Xiaodan Chen. Energy harvesting technologies in roadway and bridge for different applications–a comprehensive review. *Applied energy*, 212:1083–1094, 2018.

[12] Ahmed F. Abdelshafy, Dmitry Oshmarin, Mohamed A. K. Othman, Michael M. Green, and Filippo Capolino. Distributed degenerate band edge oscillator. *IEEE Transactions on Antennas and Propagation*, 69(3):1821–1824, Mar 2021.

[13] Mohamed A. K. Othman, Farshad Yazdi, Alex Figotin, and Filippo Capolino. Giant gain enhancement in photonic crystals with a degenerate band edge. *Phys. Rev. B*, 93:024301, Jan 2016.

[14] Mohamed AK Othman, Mehdi Veysi, Alexander Figotin, and Filippo Capolino. Giant amplification in degenerate band edge slow-wave structures interacting with an electron beam. *Physics of plasmas*, 23(3), 2016.

[15] Mehdi Veysi, Mohamed A. K. Othman, Alexander Figotin, and Filippo Capolino. Degenerate band edge laser. *Phys. Rev. B*, 97:195107, May 2018.

[16] Weijian Chen, Sahin Kaya Ozdemir, Guangming Zhao, Jan Wiersig, and Lan Yang. Exceptional points enhance sensing in an optical microcavity. *Nature*, 548(7666):192–196, Aug 2017.

[17] T. Stehmann, W. D. Heiss, and F. G. Scholtz. Observation of exceptional points in electronic circuits. *Journal of Physics A: Mathematical and General*, 37(31):7813, 2004, doi: 10.1088/0305-4470/37/31/012.

[18] Behzad Razavi. Rf microelectronics. *Prentice Hall New Jersey*, pages 206–246, 1998.

[19] B. Van der Pol. The nonlinear theory of electric oscillations. *Proceedings of the IRE*, 22(9):1051–1086, sep 1934.

[20] George W. Pierce. Piezoelectric crystal resonators and crystal oscillators applied to the precision calibration of wavemeters. *Proceedings of the American Academy of Arts and Sciences*, 59(4):81, 1923.

[21] Edwin H Colpitts. Oscillation generator, apr 12 1927. US Patent 1,624,537.

[22] Hui Wu and A. Hajimiri. Silicon-based distributed voltage-controlled oscillators. *IEEE Journal of Solid-State Circuits*, 36(3):493–502, Mar 2001, doi: 10.1109/4.910488.

[23] H.-A. Tanaka, A. Hasegawa, H. Mizuno, and T. Endo. Synchronizability of distributed clock oscillators. *IEEE Transactions on Circuits and Systems I: Fundamental Theory and Applications*, 49(9):1271–1278, Sep 2002, doi: 10.1109/tcsi.2002.802361.

[24] A. Hajimiri, S. Limotyrakis, and T.H. Lee. Jitter and phase noise in ring oscillators. *IEEE Journal of Solid-State Circuits*, 34(6):790–804, Jun 1999, doi: 10.1109/4.766813.

[25] Marvin E. Frerking. Oscillator frequency stability. In *Crystal Oscillator Design and Temperature Compensation*, pages 14–19. Springer Netherlands, 1978.

[26] An-Sun Hyun, Hoon-Seok Kim, Ji-Yong Park, Jong-Heon Kim, Jong-Chul Lee, Nam-Young Kim, Bok-Ki Kim, and Ui-Seok Hong. K-band hair-pin resonator oscillators. *999 IEEE MTT-S International Microwave Symposium Digest (Cat. No.99CH36282)*, vol.2:pp. 725–728, 1999.

[27] Kouhei Kasagi, Safumi Suzuki, and Masahiro Asada. Large-scale array of resonant-tunneling-diode terahertz oscillators for high output power at 1 THz. *Journal of Applied Physics*, 125(15):151601, Apr 2019.

[28] A. Figotin and I. Vitebsky. Nonreciprocal magnetic photonic crystals. *Physical Review E*, 63(6), May 2001.

[29] Mohamed A. K. Othman, Xuyuan Pan, Georgios Atmatzakis, Christos G. Christodoulou, and Filippo Capolino. Experimental demonstration of degenerate band edge in metallic periodically loaded circular waveguide. *IEEE Transactions on Microwave Theory and Techniques*, 65(11):4037–4045, Nov 2017.

[30] Tarek Mealy, Ahmed F. Abdelshafy, and Filippo Capolino. Exceptional point of degeneracy in a backward-wave oscillator with distributed power extraction. *Phys. Rev. Appl.*, 14:014078, Jul 2020.

[31] Marko Iosifovich Vishik and Lazar Aronovich Lyusternik. The solution of some perturbation problems for matrices and selfadjoint or non-selfadjoint differential equations i. *Russian Mathematical Surveys*, 15(3):1–73, 1960.

[32] P. Lancaster. On eigenvalues of matrices dependent on a parameter. *Numerische Mathematik*, 6(1):377–387, Dec 1964, doi: 10.1007/bf01386087.

[33] Tosio Kato. *Perturbation Theory for Linear Operators*. Springer-Verlag New York Inc., New York, 1966, doi: 10.1007/978-3-662-12678-3.

[34] W D Heiss and A L Sannino. Avoided level crossing and exceptional points. *Journal of Physics A: Mathematical and General*, 23(7):1167–1178, apr 1990.

[35] Alexander P. Seyranian. Sensitivity analysis of multiple eigenvalues. *Journal of Structural Mechanics*, 21(2):261–284, Jan 1993, doi: 10.1080/08905459308905189.

[36] A. Guo, G. J. Salamo, D. Duchesne, R. Morandotti, M. Volatier-Ravat, V. Aimez, G. A. Siviloglou, and D. N. Christodoulides. Observation of $\mathcal{PT}$-symmetry breaking in complex optical potentials. *Phys. Rev. Lett.*, 103:093902, Aug 2009.

[37] WD Heiss. The physics of exceptional points. *Journal of Physics A: Mathematical and Theoretical*, 45(44):444016, 2012.

[38] A. Figotin and I. Vitebskiy. Oblique frozen modes in periodic layered media. *Phys. Rev. E*, 68:036609, Sep 2003.

[39] Alex Figotin and Ilya Vitebskiy. Gigantic transmission band-edge resonance in periodic stacks of anisotropic layers. *Phys. Rev. E*, 72:036619, Sep 2005.

[40] Carl M. Bender and Stefan Boettcher. Real spectra in non-Hermitian Hamiltonians having PT symmetry. *Phys. Rev. Lett.*, 80:5243–5246, Jun 1998.

[41] Carl M Bender. Making sense of non-Hermitian Hamiltonians. *Reports on Progress in Physics*, 70(6):947–1018, May 2007, doi: 10.1088/0034-4885/70/6/r03.

[42] Ali Mostafazadeh. Exact pt-symmetry is equivalent to hermiticity. *Journal of Physics A: Mathematical and General*, 36(25):7081, 2003.

[43] A Ruschhaupt, F Delgado, and J G Muga. Physical realization of -symmetric potential scattering in a planar slab waveguide. *Journal of Physics A: Mathematical and General*, 38(9):L171, Feb 2005.

[44] R. El-Ganainy, K. G. Makris, D. N. Christodoulides, and Ziad H. Musslimani. Theory of coupled optical PT-symmetric structures. *Optics Letters*, 32(17):2632, Aug 2007.

[45] Mohamed A. K. Othman, Vincenzo Galdi, and Filippo Capolino. Exceptional points of degeneracy and PT symmetry in photonic coupled chains of scatterers. *Physical Review B*, 95(10):104305, Mar 2017, doi: 10.1103/PhysRevB.95.104305.

[46] Viktar S Asadchy, Mohammad Sajjad Mirmoosa, Ana Díaz-Rubio, Shanhui Fan, and Sergei A Tretyakov. Tutorial on electromagnetic nonreciprocity and its origins. *Proceedings of the IEEE*, 108(10):1684–1727, 2020.

[47] Maryam Sakhdari, Nasim Mohammadi Estakhri, Hakan Bagci, and Pai-Yen Chen. Low-threshold lasing and coherent perfect absorption in generalized pt-symmetric optical structures. *Physical Review Applied*, 10(2):024030, 2018.

[48] Rüdiger Seydel. *Practical bifurcation and stability analysis*, volume 5. Springer Science & Business Media, 2009.

[49] George W Hanson, Alexander B Yakovlev, Mohamed AK Othman, and Filippo Capolino. Exceptional points of degeneracy and branch points for coupled transmission lines—linear-algebra and bifurcation theory perspectives. *IEEE Transactions on Antennas and Propagation*, 67(2):1025–1034, 2018.

[50] E Hernández, A Jáuregui, and A Mondragón. Exceptional points and non-hermitian degeneracy of resonances in a two-channel model. *Physical Review E—Statistical, Nonlinear, and Soft Matter Physics*, 84(4):046209, 2011.

[51] Alexander B Yakovlev and George W Hanson. On the nature of critical points in leakage regimes of a conductor-backed coplanar strip line. *IEEE transactions on microwave theory and techniques*, 45(1):87–94, 1997.

[52] Alex Figotin and Ilya Vitebskiy. Slow-wave resonance in periodic stacks of anisotropic layers. *Physical Review A*, 76(5):053839, 2007.

[53] A Nikzamir, N Furman, A Herrero, T Mealy, and F Capolino. Exceptional points of degeneracy in waveguides with or without loss and gain. In *2022 Sixteenth International Congress on Artificial Materials for Novel Wave Phenomena (Metamaterials)*, pages 326–328. IEEE, 2022.

[54] Mohamed AK Othman, Mehdi Veysi, Alexander Figotin, and Filippo Capolino. Low starting electron beam current in degenerate band edge oscillators. *IEEE Transactions on Plasma Science*, 44(6):918–929, 2016.

[55] Farshad Yazdi, Alireza Nikzamir, Tarek Mealy, Mohamed Y. Nada, and Filippo Capolino. Triple ladder lumped circuit with sixth order modal exceptional degeneracy. *IEEE Transactions on Circuits and Systems I: Regular Papers*, 69(5):1910–1918, May 2022.

[56] Mohamed A. K. Othman and Filippo Capolino. Demonstration of a degenerate band edge in periodically-loaded circular waveguides. *IEEE Microwave and Wireless Components Letters*, 25(11):700–702, Nov 2015, doi: 10.1109/lmwc.2015.2479845.

[57] Dmitry Oshmarin, Alireza Nikzamir, Michael M Green, and Filippo Capolino. Pulse generation based on a microstrip circuit with fourth order degenerate band edge. *arXiv preprint arXiv:2206.13564*, 2022.

[58] Aodong Li, Heng Wei, Michele Cotrufo, Weijin Chen, Sander Mann, Xiang Ni, Bingcong Xu, Jianfeng Chen, Jian Wang, Shanhui Fan, et al. Exceptional points and non-hermitian photonics at the nanoscale. *Nature Nanotechnology*, 18(7):706–720, 2023.

[59] Rajendra Nayak, Iman Kianpoor, and Pydi Ganga Bahubalindruni. Low power ring oscillator for IoT applications. *Analog Integrated Circuits and Signal Processing*, 93(2):257–263, jun 2017.

[60] Heng-Chia Chang, Xudong Cao, U.K. Mishra, and R.A. York. Phase noise in coupled oscillators: theory and experiment. *IEEE Transactions on Microwave Theory and Techniques*, 45(5):604–615, may 1997.

[61] Tetsuro Endo and S. Mori. Mode analysis of a multimode ladder oscillator. *IEEE Transactions on Circuits and Systems*, 23(2):100–113, Feb 1976, doi: 10.1109/tcs.1976.1084183.

[62] Carl M Bender, M V Berry, and Aikaterini Mandilara. Generalized PT symmetry and real spectra. *Journal of Physics A: Mathematical and General*, 35(31):L467–L471, jul 2002.

[63] W D Heiss. The physics of exceptional points. *Journal of Physics A: Mathematical and Theoretical*, 45(44):444016, oct 2012.

[64] Bo Peng, Şahin Kaya Özdemir, Fuchuan Lei, Faraz Monifi, Mariagiovanna Gianfreda, Gui Lu Long, Shanhui Fan, Franco Nori, Carl M Bender, and Lan Yang. Parity–time-symmetric whispering-gallery microcavities. *Nature Physics*, 10(5):394–398, 2014.

[65] A P Seyranian, O N Kirillov, and A A Mailybaev. Coupling of eigenvalues of complex matrices at diabolic and exceptional points. *Journal of Physics A: Mathematical and General*, 38(8):1723–1740, feb 2005.

[66] M.V. Berry. Physics of nonhermitian degeneracies. *Czechoslovak Journal of Physics*, 54(10):1039–1047, Oct 2004, doi: 10.1023/b:cjop.0000044002.05657.04.

[67] Maryam Sakhdari, Mohamed Farhat, and Pai-Yen Chen. PT-symmetric metasurfaces: wave manipulation and sensing using singular points. *New Journal of Physics*, 19(6):065002, jun 2017.

[68] Kasra Rouhi, Alireza Nikzamir, Alexander Figotin, and Filippo Capolino. Exceptional point in a degenerate system made of a gyrator and two unstable resonators. *Phys. Rev. A*, 105:032214, Mar 2022.

[69] Alireza Nikzamir, Kasra Rouhi, Alexander Figotin, and Filippo Capolino. How to achieve exceptional points in coupled resonators using a gyrator or pt-symmetry, and in a time-modulated single resonator: high sensitivity to perturbations. *EPJ Applied Metamaterials*, 9:14, 2022.

[70] Hamidreza Kazemi, Alireza Nikzamir, Tarek Mealy, Ahmed Abdelshafy, and Filippo Capolino. High-sensitive parity-time symmetric oscillator in coupled transmission lines with nonlinear gain. *IEEE Journal of Microwaves*, 2(3):389–400, Jul 2022.

[71] Hossein Hodaei, Mohammad-Ali Miri, Matthias Heinrich, Demetrios N. Christodoulides, and Mercedeh Khajavikhan. Parity-time symmetric microring lasers. *Science*, 346(6212):975–978, Nov 2014, doi: 10.1126/science.1258480.

[72] M. A. K. Othman and F. Capolino. Theory of Exceptional Points of Degeneracy in Uniform Coupled Waveguides and Balance of Gain and Loss. *IEEE Transactions on Antennas and Propagation*, 65(10):5289–5302, Oct 2017, doi: 10.1109/TAP.2017.2738063.

[73] J. T. Sloan, M. A. K. Othman, and F. Capolino. Theory of Double Ladder Lumped Circuits With Degenerate Band Edge. *IEEE Transactions on Circuits and Systems I: Regular Papers*, 65(1):3–13, Jan 2018, doi: 10.1109/TCSI.2017.2690971.

[74] Tarek Mealy and Filippo Capolino. General conditions to realize exceptional points of degeneracy in two uniform coupled transmission lines. *IEEE Transactions on Microwave Theory and Techniques*, 68(8):3342–3354, Aug 2020, doi: 10.1109/TMTT.2020.2999498.

[75] Shachar Klaiman, Uwe Günther, and Nimrod Moiseyev. Visualization of branch points in $\mathcal{PT}$-symmetric waveguides. *Phys. Rev. Lett.*, 101:080402, Aug 2008.

[76] Christian E. Rüter, Konstantinos G. Makris, Ramy El-Ganainy, Demetrios N. Christodoulides, Mordechai Segev, and Detlef Kip. Observation of parity–time symmetry in optics. *Nature Physics*, 6(3):192–195, Jan 2010.

[77] Jan Schnabel, Holger Cartarius, Jörg Main, Günter Wunner, and Walter Dieter Heiss. $\mathcal{PT}$-symmetric waveguide system with evidence of a third-order exceptional point. *Phys. Rev. A*, 95:053868, May 2017.

[78] Hamidreza Kazemi, Mohamed Y Nada, Alireza Nikzamir, Franco Maddaleno, and Filippo Capolino. Experimental demonstration of exceptional points of degeneracy in linear time periodic systems and exceptional sensitivity. *Journal of Applied Physics*, 131(14):144502, 2022.

[79] Hamidreza Kazemi, Amirhossein Hajiaghajani, Mohamed Y. Nada, Manik Dautta, Muhannad Alshetaiwi, Peter Tseng, and Filippo Capolino. Ultra-sensitive radio frequency biosensor at an exceptional point of degeneracy induced by time modulation. *IEEE Sensors Journal*, 21(6):7250–7259, Mar 2021, doi: 10.1109/JSEN.2020.3047886.

[80] Youngsun Choi, Choloong Hahn, Jae Woong Yoon, and Seok Ho Song. Observation of an anti-PT-symmetric exceptional point and energy-difference conserving dynamics in electrical circuit resonators. *Nature Communications*, 9(1), jun 2018.

[81] Zhenya Dong, Zhipeng Li, Fengyuan Yang, Cheng-Wei Qiu, and John S. Ho. Sensitive readout of implantable microsensors using a wireless system locked to an exceptional point. *Nature Electronics*, 2(8):335–342, aug 2019.

[82] Zhicheng Xiao, Huanan Li, Tsampikos Kottos, and Andrea Alù. Enhanced sensing and nondegraded thermal noise performance based on $\mathcal{PT}$-symmetric electronic circuits with a sixth-order exceptional point. *Phys. Rev. Lett.*, 123:213901, Nov 2019.

[83] Chao Zeng, Yong Sun, Guo Li, Yunhui Li, Haitao Jiang, Yaping Yang, and Hong Chen. Enhanced sensitivity at high-order exceptional points in a passive wireless sensing system. *Optics Express*, 27(20):27562, sep 2019.

[84] W D Heiss. Exceptional points of non-hermitian operators. *Journal of Physics A: Mathematical and General*, 37(6):2455, jan 2004.

[85] Jan Wiersig. Robustness of exceptional-point-based sensors against parametric noise: The role of hamiltonian and liouvillian degeneracies. *Phys. Rev. A*, 101:053846, May 2020.

[86] Siavash Kananian, George Alexopoulos, and Ada S.Y. Poon. Coupling-independent real-time wireless resistive sensing through nonlinear $\mathcal{PT}$ symmetry. *Phys. Rev. Applied*, 14:064072, Dec 2020.

[87] Omer Kotlicki, Jacob Scheuer, and M.S. Shahriar. Theoretical study on brillouin fiber laser sensor based on white light cavity. *Optics Express*, 20(27):28234, dec 2012.

[88] Jacob Scheuer. White light cavity formation and superluminal lasing near exceptional points. *Optics Express*, 26(24):32091, nov 2018.

[89] Aaron Welters. On explicit recursive formulas in the spectral perturbation analysis of a Jordan block. *SIAM journal on matrix analysis and applications*, 32(1):1–22, 2011.

[90] K. Scharnhorst. Angles in complex vector spaces. *Acta Applicandae Mathematicae*, 69(1):95–103, 2001, doi: 10.1023/a:1012692601098.

[91] David M Pozar. Microwave engineering. *John Wiley & Sons*, 2009.

[92] Sophocles J. Orfanidis. *Electromagnetic waves and antennas*. Rutgers University New Brunswick, NJ, 2002.

[93] A. Galántai and Cs. J. Hegedűs. Jordan's principal angles in complex vector spaces. *Numerical Linear Algebra with Applications*, 13(7):589–598, 2006, doi: 10.1002/nla.491.

[94] Jan Wiersig. Sensors operating at exceptional points: General theory. *Physical Review A*, 93(3):033809, Mar 2016, doi: 10.1103/PhysRevA.93.033809.

[95] Julio Moro, James V. Burke, and Michael L. Overton. On the lidskii–vishik–lyusternik perturbation theory for eigenvalues of matrices with arbitrary Jordan structure. *SIAM Journal on Matrix Analysis and Applications*, 18(4):793–817, Oct 1997, doi: 10.1137/s0895479895294666.

[96] Alireza Nikzamir, Kasra Rouhi, Alexander Figotin, and Filippo Capolino. Time modulation to manage and increase the power harvested from external vibrations. *Applied Physics Letters*, 123(21):211701, 11 2023.

[97] Camilo Moncada, Franco Ramírez, and Almudena Suárez. Frequency-domain analysis of an oscillator with an exceptional point of degeneracy. *IEEE Transactions on Microwave Theory and Techniques*, 2024.

[98] Alireza Nikzamir and Filippo Capolino. Highly sensitive coupled oscillator based on an exceptional point of degeneracy and nonlinearity. *Phys. Rev. Appl.*, 18:054059, Nov 2022.

[99] Jan Wiersig. Enhancing the sensitivity of frequency and energy splitting detection by using exceptional points: application to microcavity sensors for single-particle detection. *Physical Review Letters*, 112(20):203901, 2014.

[100] Kasra Rouhi, Robert Marosi, Tarek Mealy, Ahmed F. Abdelshafy, Alexander Figotin, and Filippo Capolino. Exceptional degeneracies in traveling wave tubes with dispersive slow-wave structure including space-charge effect. *Applied Physics Letters*, 118(26):263506, 2021.

[101] Kasra Rouhi, Filippo Capolino, and Alexander Figotin. Simple reciprocal electric circuit exhibiting exceptional point of degeneracy. *Journal of Physics A: Mathematical and Theoretical*, 2024.

[102] WW Chow, J Gea-Banacloche, LM Pedrotti, VE Sanders, Wo Schleich, and MO Scully. The ring laser gyro. *Reviews of Modern Physics*, 57(1):61, 1985.

[103] Satoshi Sunada and Takahisa Harayama. Design of resonant microcavities: application to optical gyroscopes. *Optics express*, 15(24):16245–16254, 2007.

[104] P Djorwe, Y Pennec, and B Djafari-Rouhani. Exceptional point enhances sensitivity of optomechanical mass sensors. *Physical Review Applied*, 12(2):024002, 2019.

[105] Arunn Suntharalingam, Lucas Fernández-Alcázar, Rodion Kononchuk, and Tsampikos Kottos. Noise resilient exceptional-point voltmeters enabled by oscillation quenching phenomena. *Nature Communications*, 14(1):5515, 2023.

[106] Kai Bai, Tian-Rui Liu, Liang Fang, Jia-Zheng Li, Chen Lin, Duanduan Wan, and Meng Xiao. Observation of nonlinear exceptional points with a complete basis in dynamics. *Phys. Rev. Lett.*, 132:073802, Feb 2024.

[107] Alexander Figotin. Synthesis of lossless electric circuits based on prescribed Jordan forms. *Journal of Mathematical Physics*, 61(12):122703, 2020.

[108] Alexander Figotin. Perturbations of circuit evolution matrices with Jordan blocks. *Journal of Mathematical Physics*, 62(4):042703, 2021.

[109] Kasra Rouhi, Alireza Nikzamir, Alexander Figotin, and Filippo Capolino. High-sensitivity in various gyrator-based circuits with exceptional points of degeneracy. *EPJ Applied Metamaterials*, 9:8, 2022.

[110] Carson R. White, Jason W. May, and Joseph S. Colburn. A variable negative-inductance integrated circuit at UHF frequencies. *IEEE Microwave and Wireless Components Letters*, 22(1):35–37, Jan 2012.

[111] E. H. Kopp. Negative impedance inverter circuits. *in Proceedings of the IEEE*, 53(12):2125–2126, Dec 1965.

[112] Paul Horowitz and Winfield Hill. *The art of electronics*. Cambridge Univ. Press, 1989.

[113] M. Ershov, H.C. Liu, L. Li, M. Buchanan, Z.R. Wasilewski, and A.K. Jonscher. Negative capacitance effect in semiconductor devices. *IEEE Transactions on Electron Devices*, 45(10):2196–2206, 1998.

[114] Bernard DH Tellegen. The gyrator, a new electric network element. *Philips Res. Rep*, 3(2):81–101, 1948.

[115] R.M. Inigo. Gyrator realization using two operational amplifiers. *IEEE Journal of Solid-State Circuits*, 6(2):88–89, Apr 1971.

[116] C. L. Hogan. The ferromagnetic faraday effect at microwave frequencies and its applications. *Bell System Technical Journal*, 31(1):1–31, Jan 1952.

[117] B Shenoi. Practical realization of a gyrator circuit and rc-gyrator filters. *IEEE Transactions on Circuit Theory*, 12(3):374–380, 1965.

[118] Vladimir V. Konotop, Jianke Yang, and Dmitry A. Zezyulin. Nonlinear waves in $\mathcal{PT}$-symmetric systems. *Rev. Mod. Phys.*, 88:035002, Jul 2016.

[119] Yuri A Kuznetsov, Iu A Kuznetsov, and Y Kuznetsov. *Elements of applied bifurcation theory*, volume 112. Springer, 1998.

[120] Yertay Zhiyenbayev, Yannis Kominis, Constantinos Valagiannopoulos, Vassilios Kovanis, and Anastasios Bountis. Enhanced stability, bistability, and exceptional points in saturable active photonic couplers. *Phys. Rev. A*, 100:043834, Oct 2019.

[121] Sunkyu Yu, Xianji Piao, and Namkyoo Park. Neuromorphic functions of light in parity-time-symmetric systems. *Advanced Science*, 6(15):1900771, 2019.

[122] Norman Balabanian, Sundaram Seshu, and Theodore A Bickart. *Electrical network theory*. Wiley, 1969.

[123] Peter Lancaster. On eigenvalues of matrices dependent on a parameter. *Numerische Mathematik*, 6(1):377–387, 1964.

[124] W-H Steeb and WD Heiss. Energy eigenvalue levels and singular point analysis. *Physics Letters A*, 152(7):339–342, 1991.

[125] W. D. Heiss. Repulsion of resonance states and exceptional points. *Physical Review E*, 61(1):929–932, jan 2000.

[126] Alex Figotin and Ilya Vitebskiy. Frozen light in photonic crystals with degenerate band edge. *Physical Review E—Statistical, Nonlinear, and Soft Matter Physics*, 74(6):066613, 2006.

[127] Alireza Nikzamir, Kasra Rouhi, Alexander Figotin, and Filippo Capolino. Demonstration of exceptional points of degeneracy in gyrator-based circuit for high-sensitivity applications. *arXiv:2107.00639. [Online]. Available: http://arxiv.org/abs/2107.00639*, 2021.

[128] Ahmed F. Abdelshafy, Tarek Mealy, Ehsan Hafezi, Alireza Nikzamir, and Filippo Capolino. Exceptional degeneracy in a waveguide periodically loaded with discrete gain and radiation loss elements. *Applied Physics Letters*, 118(22):224102, May 2021, doi: 10.1063/5.0051238.

[129] Po-Jui Chen, Saloomeh Saati, Rohit Varma, Mark S Humayun, and Yu-Chong Tai. Wireless intraocular pressure sensing using microfabricated minimally invasive flexible-coiled lc sensor implant. *Journal of Microelectromechanical Systems*, 19(4):721–734, 2010.

[130] Tran Quang Trung, Subramaniyan Ramasundaram, Byeong-Ung Hwang, and Nae-Eung Lee. An all-elastomeric transparent and stretchable temperature sensor for body-attachable wearable electronics. *Advanced materials*, 28(3):502–509, 2016.

[131] Yi Feng, Li Xie, Qiang Chen, and Li-Rong Zheng. Low-cost printed chipless rfid humidity sensor tag for intelligent packaging. *IEEE Sensors Journal*, 15(6):3201–3208, 2014.

[132] Qian Yi, Sahar Najafikhoshnoo, Prativa Das, Sangjun Noh, Emily Hoang, Taeil Kim, and Rahim Esfandyarpour. All-3d-printed, flexible, and hybrid wearable bioelectronic tactile sensors using biocompatible nanocomposites for health monitoring. *Advanced Materials Technologies*, 7(5):2101034, 2022.

[133] Po-Jui Chen, Damien C Rodger, Saloomeh Saati, Mark S Humayun, and Yu-Chong Tai. Microfabricated implantable parylene-based wireless passive intraocular pressure sensors. *Journal of Microelectromechanical Systems*, 17(6):1342–1351, 2008.

[134] Simon R Corrie, JW Coffey, J Islam, KA Markey, and MAF Kendall. Blood, sweat, and tears: developing clinically relevant protein biosensors for integrated body fluid analysis. *Analyst*, 140(13):4350–4364, 2015.

[135] Peter Tseng, Bradley Napier, Logan Garbarini, David L Kaplan, and Fiorenzo G Omenetto. Functional, rf-trilayer sensors for tooth-mounted, wireless monitoring of the oral cavity and food consumption. *Advanced Materials*, 30(18):1703257, 2018.

[136] Yun Jing Zhang, Hoyeong Kwon, Mohammad-Ali Miri, Efthymios Kallos, Helena Cano-Garcia, Mei Song Tong, and Andrea Alu. Noninvasive glucose sensor based on parity-time symmetry. *Physical Review Applied*, 11(4):044049, 2019.

[137] Zhong-Peng Liu, Jing Zhang, Şahin Kaya Özdemir, Bo Peng, Hui Jing, Xin-You Lü, Chun-Wen Li, Lan Yang, Franco Nori, and Yu-xi Liu. Metrology with pt-symmetric cavities: enhanced sensitivity near the pt-phase transition. *Physical review letters*, 117(11):110802, 2016.

[138] Mohammad-Ali Miri and Andrea Alu. Exceptional points in optics and photonics. *Science*, 363(6422):eaar7709, 2019.

[139] L. Feng, Z. J. Wong, R.-M. Ma, Y. Wang, and X. Zhang. Single-mode laser by parity-time symmetry breaking. *Science*, 346(6212):972–975, oct 2014.

[140] Athanasios Antoniou. Gyrators using operational amplifiers. *Electronics Letters*, 3(8):350–352, 1967.

[141] Mehrdad Ehsani, Iqbal Husain, and Mehmet Oruç Bilgiç. Power converters as natural gyrators. *IEEE Transactions on Circuits and Systems I: Fundamental Theory and Applications*, 40(12):946–949, 1993.

[142] WH Holmes, S Gruetzmann, and WE Heinlein. High-performance direct-coupled gyrators. *Electronics Letters*, 2(3):45–46, 1967.

[143] A Nikzamir, K Rouhi, A Figotin, and F Capolino. Exceptional points of degeneracy in gyrator-based coupled resonator circuit. In *2021 Fifteenth International Congress on Artificial Materials for Novel Wave Phenomena (Metamaterials)*, pages 302–304. IEEE, 2021.

[144] Shahab Ramezanpour and Andrey Bogdanov. Tuning exceptional points with kerr nonlinearity. *Physical Review A*, 103(4):043510, 2021.

[145] J.A. Richards. Analysis of periodically time-varying systems. *Springer, Berlin Heidelberg*, 1983.

[146] Shashank Priya. Modeling of electric energy harvesting using piezoelectric windmill. *Applied Physics Letters*, 87(18):184101, 2005.

[147] Adam M Wickenheiser and Ephrahim Garcia. Power optimization of vibration energy harvesters utilizing passive and active circuits. *Journal of Intelligent Material Systems and Structures*, 21(13):1343–1361, 2010.

[148] Neil G Stephen. On energy harvesting from ambient vibration. *Journal of Sound and Vibration*, 293(1-2):409–425, 2006.

[149] In-Ho Kim, Hyung-Jo Jung, Bo Mi Lee, and Seon-Jun Jang. Broadband energy-harvesting using a two degree-of-freedom vibrating body. *Applied Physics Letters*, 98(21):214102, 2011.

[150] Yasuyuki Naito and Keisuke Uenishi. Electrostatic mems vibration energy harvesters inside of tire treads. *Sensors*, 19(4):890, 2019.

[151] Hiroshi Toshiyoshi, Suna Ju, Hiroaki Honma, Chang-Hyeon Ji, and Hiroyuki Fujita. Mems vibrational energy harvesters. *Science and Technology of Advanced Materials*, 20(1):124–143, 2019.

[152] Joseph A Paradiso and Thad Starner. Energy scavenging for mobile and wireless electronics. *IEEE Pervasive computing*, 4(1):18–27, 2005.

[153] Soon-Duck Kwon. A t-shaped piezoelectric cantilever for fluid energy harvesting. *Applied Physics Letters*, 97(16):164102, 2010.

[154] SC Sinha and A David. Parametric excitation. In S. Braun, editor, *Encyclopedia of Vibration*, pages 1001–1009. Elsevier, 2001.

[155] Jerzy Warminski. Nonlinear dynamics of self-, parametric, and externally excited oscillator with time delay: van der pol versus rayleigh models. *Nonlinear Dynamics*, 99(1):35–56, 2020.

[156] Mehrdad Aghamohammadi, Vladislav Sorokin, and Brian Mace. Dynamic analysis of the response of duffing-type oscillators subject to interacting parametric and external excitations. *Nonlinear Dynamics*, 107(1):99–120, 2022.

[157] AF Arrieta, P Hagedorn, Alper Erturk, and Daniel J Inman. A piezoelectric bistable plate for nonlinear broadband energy harvesting. *Applied Physics Letters*, 97(10):104102, 2010.

[158] Seok-Min Jung and Kwang-Seok Yun. Energy-harvesting device with mechanical frequency-up conversion mechanism for increased power efficiency and wideband operation. *Applied Physics Letters*, 96(11):111906, 2010.

[159] Michele Zilletti, Stephen J Elliott, and Emiliano Rustighi. Optimisation of dynamic vibration absorbers to minimise kinetic energy and maximise internal power dissipation. *Journal of Sound and Vibration*, 331(18):4093–4100, 2012.

[160] Francesco Di Monaco, Maryam Ghandchi Tehrani, Stephen J Elliott, Elvio Bonisoli, and Stefano Tornincasa. Energy harvesting using semi-active control. *Journal of Sound and Vibration*, 332(23):6033–6043, 2013.

[161] Maryam Ghandchi Tehrani and Stephen J Elliott. Extending the dynamic range of an energy harvester using nonlinear damping. *Journal of Sound and Vibration*, 333(3):623–629, 2014.

[162] Matteo Scapolan, Maryam Ghandchi Tehrani, and Elvio Bonisoli. Energy harvesting using parametric resonant system due to time-varying damping. *Mechanical Systems and Signal Processing*, 79:149–165, 2016.

[163] Weijian Jiao and Stefano Gonella. Intermodal and subwavelength energy trapping in nonlinear metamaterial waveguides. *Physical Review Applied*, 10(2):024006, 2018.

[164] Dibin Zhu, Michael J Tudor, and Stephen P Beeby. Strategies for increasing the operating frequency range of vibration energy harvesters: a review. *Measurement Science and Technology*, 21(2):022001, 2009.

[165] Xiudong Tang and Lei Zuo. Enhanced vibration energy harvesting using dual-mass systems. *Journal of Sound and Vibration*, 330(21):5199–5209, 2011.

[166] Roszaidi Ramlan, MJ Brennan, BR Mace, and I Kovacic. Potential benefits of a nonlinear stiffness in an energy harvesting device. *Nonlinear Dynamics*, 59(4):545–558, 2010.

[167] H Laalej, Zi Qiang Lang, Stephen Daley, I Zazas, SA Billings, and GR Tomlinson. Application of non-linear damping to vibration isolation: an experimental study. *Nonlinear Dynamics*, 69:409–421, 2012.

[168] Marco Ferrari, Vittorio Ferrari, Michele Guizzetti, Bruno Ando, Salvatore Baglio, and Carlo Trigona. Improved energy harvesting from wideband vibrations by nonlinear piezoelectric converters. *Sensors and Actuators A: Physical*, 162(2):425–431, 2010.

[169] Junyi Cao, Wei Wang, Shengxi Zhou, Daniel J Inman, and Jing Lin. Nonlinear time-varying potential bistable energy harvesting from human motion. *Applied Physics Letters*, 107(14):143904, 2015.

[170] WT Van Horssen, AK Abramian, et al. On the free vibrations of an oscillator with a periodically time-varying mass. *Journal of Sound and Vibration*, 298(4-5):1166–1172, 2006.

[171] WT Van Horssen, OV Pischanskyy, and JLA Dubbeldam. On the forced vibrations of an oscillator with a periodically time-varying mass. *Journal of Sound and Vibration*, 329(6):721–732, 2010.

[172] Miodrag Zukovic and Ivana Kovacic. An insight into the behaviour of oscillators with a periodically piecewise-defined time-varying mass. *Communications in Nonlinear Science and Numerical Simulation*, 42:187–203, 2017.

[173] Giuseppe Giorgi and Nicolás Faedo. Performance enhancement of a vibration energy harvester via harmonic time-varying damping: A pseudospectral-based approach. *Mechanical Systems and Signal Processing*, 165:108331, 2022.

[174] Kasra Rouhi, Hamidreza Kazemi, Alexander Figotin, and Filippo Capolino. Exceptional points of degeneracy directly induced by space–time modulation of a single transmission line. *IEEE Antennas and Wireless Propagation Letters*, 19(11):1906–1910, 2020.

[175] SP Beeby, MJ Tudor, and NM White. Energy harvesting vibration sources for microsystems applications. *Measurement Science and Technology*, 17(12):R175–R195, 2006.

[176] Steve P Beeby, Russel N Torah, M John Tudor, Peter Glynne-Jones, Terence O'Donnell, Chitta R Saha, and Saibal Roy. A micro electromagnetic generator for vibration energy harvesting. *Journal of Micromechanics and Microengineering*, 17(7):1257–1265, 2007.

[177] Sushanta Kundu and Harshal B Nemade. Modeling and simulation of a piezoelectric vibration energy harvester. *Procedia Engineering*, 144:568–575, 2016.

[178] Alper Erturk, J Hoffmann, and Daniel J Inman. A piezomagnetoelastic structure for broadband vibration energy harvesting. *Applied Physics Letters*, 94(25):254102, 2009.

[179] Sebastien Boisseau, Ghislain Despesse, and Bouhadjar Ahmed Seddik. Nonlinear h-shaped springs to improve efficiency of vibration energy harvesters. *Journal of Applied Mechanics*, 80(6):061013, 2013.

[180] Philippe Basset, Elena Blokhina, and Dimitri Galayko. *Electrostatic kinetic energy harvesting*. John Wiley & Sons, 2016.

[181] Peter Spies, Markus Pollak, and Loreto Mateu. *Handbook of energy harvesting power supplies and applications*. CRC Press, 2015.

[182] John A Richards. *Analysis of periodically time-varying systems*. Springer Science & Business Media, 1983.

[183] Joseph W Matiko, Neil J Grabham, Steve P Beeby, and Michael J Tudor. Review of the application of energy harvesting in buildings. *Measurement Science and Technology*, 25(1):012002, 2013.

[184] Philippe Le Corbeiller and Ying-Wa Yeung. Duality in mechanics. *The Journal of the Acoustical Society of America*, 24(6):643–648, 1952.

[185] CB Williams and Rob B Yates. Analysis of a micro-electric generator for microsystems. *sensors and actuators A: Physical*, 52(1-3):8–11, 1996.

[186] Shad Roundy, Paul K Wright, and Jan Rabaey. A study of low level vibrations as a power source for wireless sensor nodes. *Computer communications*, 26(11):1131–1144, 2003.

[187] Chongfeng Wei and Xingjian Jing. A comprehensive review on vibration energy harvesting: Modelling and realization. *Renewable and Sustainable Energy Reviews*, 74:1–18, 2017.

[188] Neil White. *Energy harvesting for autonomous systems*. Artech House, 2010.

[189] Niell Elvin and Alper Erturk. *Advances in energy harvesting methods*. Springer Science & Business Media, 2013.

[190] Samuel C Stanton, Clark C McGehee, and Brian P Mann. Reversible hysteresis for broadband magnetopiezoelastic energy harvesting. *Applied Physics Letters*, 95(17), 2009.

[191] Yunus Uzun and Erol Kurt. The effect of periodic magnetic force on a piezoelectric energy harvester. *Sensors and Actuators A: Physical*, 192:58–68, 2013.

[192] D. Karnopp, M. J. Crosby, and R. A. Harwood. Vibration control using semi-active force generators. *Journal of Engineering for Industry*, 96(2):619–626, 1974.

[193] S. Rakheja and S. Sankar. Vibration and shock isolation performance of a semi-active on-off damper. *Journal of Vibration, Acoustics, Stress, and Reliability in Design*, 107(4):398–403, 1985.

[194] Yanqing Liu, Hiroshi Matsuhisa, and Hideo Utsuno. Semi-active vibration isolation system with variable stiffness and damping control. *Journal of sound and vibration*, 313(1-2):16–28, 2008.

[195] S. Hurlebaus and L. Gaul. Smart structure dynamics. *Mechanical Systems and Signal Processing*, 20(2):255–281, 2006.

[196] Yanqing Liu, Hiroshi Matsuhisa, Hideo Utsuno, and Jeong Gyu Park. Vibration isolation by a variable stiffness and damping system. *JSME International Journal Series C Mechanical Systems, Machine Elements and Manufacturing*, 48(2):305–310, 2005.

[197] Yanqing Liu, Hiroshi Matsuhisa, Hideo Utsuno, and Jeong Gyu Park. Variable damping and stiffness vibration control with magnetorheological fluid dampers for two degree-of-freedom system. *JSME International Journal Series C Mechanical Systems, Machine Elements and Manufacturing*, 49(1):156–162, 2006.

[198] Yanqing Liu, Hiroshi Matsuhisa, Hideo Utsuno, and Jeong Gyu Park. Vibration control by a variable damping and stiffness system with magnetorheological dampers. *JSME International Journal Series C Mechanical Systems, Machine Elements and Manufacturing*, 49(2):411–417, 2006.

[199] N.H. McClamroch, D.S. Oritz, H.P. Gavin, and R.D. Hanson. Electrorheological dampers and semi-active structural control. In *Proceedings of 1994 33rd IEEE Conference on Decision and Control*, volume 1, pages 97–102, 1994.

[200] N.H. McClamroch and H.P. Gavin. Electrorheological dampers and semi-active structural control. In *Proceedings of 1995 34th IEEE Conference on Decision and Control*, volume 4, pages 3528–3533, 1995.

[201] K.W. Wang, Y.S. Kim, and D.B. Shea. Structural vibration control via electrorheological-fluid-based actuators with adaptive viscous and frictional damping. *Journal of Sound and Vibration*, 177(2):227–237, 1994.

[202] Sha Zhou and Tianjun Yu. Performance comparisons of piezoelectric energy harvesters under different stochastic noises. *AIP Advances*, 10(3), 2020.

[203] Son Duy Nguyen, Einar Halvorsen, and Geir U Jensen. Wideband mems energy harvester driven by colored noise. *Journal of microelectromechanical systems*, 22(4):892–900, 2013.

[204] RL Harne and KW Wang. Prospects for nonlinear energy harvesting systems designed near the elastic stability limit when driven by colored noise. *Journal of Vibration and Acoustics*, 136(2):021009, 2014.

[205] Qifan He and Mohammed F Daqaq. New insights into utilizing bistability for energy harvesting under white noise. *Journal of Vibration and Acoustics*, 137(2):021009, 2015.

[206] Li Haitao, Qin Weiyang, Lan Chunbo, Deng Wangzheng, and Zhou Zhiyong. Dynamics and coherence resonance of tri-stable energy harvesting system. *Smart Materials and Structures*, 25(1):015001, 2015.

[207] Di Liu, Yong Xu, and Junlin Li. Probabilistic response analysis of nonlinear vibration energy harvesting system driven by gaussian colored noise. *Chaos, Solitons & Fractals*, 104:806–812, 2017.

[208] IS Mokem Fokou, C Nono Dueyou Buckjohn, M Siewe Siewe, and Clément Tchawoua. Probabilistic distribution and stochastic p-bifurcation of a hybrid energy harvester under colored noise. *Communications in Nonlinear Science and Numerical Simulation*, 56:177–197, 2018.

[209] Sovan Sundar Dasgupta, Vasudevan Rajamohan, and Abhishek Kumar Jha. Dynamic characterization of a bistable energy harvester under gaussian white noise for larger time constant. *Arabian Journal for Science and Engineering*, 44:721–730, 2019.

[210] Subramanian Ramakrishnan and Connor Edlund. Stochastic stability of a piezoelectric vibration energy harvester under a parametric excitation and noise-induced stabilization. *Mechanical Systems and Signal Processing*, 140:106566, 2020.

[211] Hang Deng, Jimin Ye, and Dongmei Huang. Design and analysis of a galloping energy harvester with v-shape spring structure under gaussian white noise. *Chaos, Solitons & Fractals*, 175:113962, 2023.

[212] Marek Borowiec, Grzegorz Litak, and Stefano Lenci. Noise effected energy harvesting in a beam with stopper. *International Journal of Structural Stability and Dynamics*, 14(08):1440020, 2014.

[213] Meng Su, Wei Xu, Ying Zhang, and Guidong Yang. Response of a vibro-impact energy harvesting system with bilateral rigid stoppers under gaussian white noise. *Applied Mathematical Modelling*, 89:991–1003, 2021.

[214] Xingbao Huang. Stochastic resonance in a piecewise bistable energy harvesting model driven by harmonic excitation and additive gaussian white noise. *Applied Mathematical Modelling*, 90:505–526, 2021.

[215] Wen-An Jiang and Li-Qun Chen. Energy harvesting of monostable duffing oscillator under gaussian white noise excitation. *Mechanics Research Communications*, 53:85–91, 2013.

[216] Wen-An Jiang and Li-Qun Chen. An equivalent linearization technique for nonlinear piezoelectric energy harvesters under gaussian white noise. *Communications in Nonlinear Science and Numerical Simulation*, 19(8):2897–2904, 2014.

[217] Yong-Ge Yang and Wei Xu. Stochastic analysis of monostable vibration energy harvesters with fractional derivative damping under gaussian white noise excitation. *Nonlinear Dynamics*, 94:639–648, 2018.

[218] O Foupouapouognigni, C Nono Dueyou Buckjohn, M Siewe Siewe, and C Tchawoua. Hybrid electromagnetic and piezoelectric vibration energy harvester with gaussian white noise excitation. *Physica A: Statistical Mechanics and Its Applications*, 509:346–360, 2018.

[219] Yanxia Zhang, Yanfei Jin, and Pengfei Xu. Dynamics of a coupled nonlinear energy harvester under colored noise and periodic excitations. *International Journal of Mechanical Sciences*, 172:105418, 2020.

[220] GJ Fezeu, IS Mokem Fokou, C Nono Dueyou Buckjohn, M Siewe Siewe, and C Tchawoua. Resistance induced p-bifurcation and ghost-stochastic resonance of a hybrid energy harvester under colored noise. *Physica A: Statistical Mechanics and its Applications*, 557:124857, 2020.

[221] Shu-Ling Guo, Yong-Ge Yang, and Ya-Hui Sun. Stochastic response of an energy harvesting system with viscoelastic element under gaussian white noise excitation. *Chaos, Solitons & Fractals*, 151:111231, 2021.

[222] Qinyuan Liu, Zidong Wang, Hongli Dong, and Changjun Jiang. Remote estimation for energy harvesting systems under multiplicative noises: A binary encoding scheme with probabilistic bit flips. *IEEE Transactions on Automatic Control*, 68(1):343–354, 2022.

[223] Vicenç Méndez, Daniel Campos, and Werner Horsthemke. Efficiency of harvesting energy from colored noise by linear oscillators. *Physical Review E*, 88(2):022124, 2013.

[224] Miquel Lopez-Suarez, Gabriel Abadal, Luca Gammaitoni, and Riccardo Rurali. Noise energy harvesting in buckled bn nanoribbons from molecular dynamics. *Nano Energy*, 15:329–334, 2015.

[225] Nuanyang Cui, Long Gu, Jinmei Liu, Suo Bai, Jiawen Qiu, Jiecai Fu, Xinli Kou, Hong Liu, Yong Qin, and Zhong Lin Wang. High performance sound driven triboelectric nanogenerator for harvesting noise energy. *Nano Energy*, 15:321–328, 2015.

[226] Ali Ghodsi, Hamid Jafari, Saber Azizi, and Mohammad Reza Ghazavi. On the dynamics of a novel energy harvester to convert the energy of the magnetic noise into electrical power. *Energy*, 207:118268, 2020.

[227] Christian Wolff, Christos Tserkezis, and N Asger Mortensen. On the time evolution at a fluctuating exceptional point. *Nanophotonics*, 8(8):1319–1326, 2019.

[228] Changdong Chen and Lina Zhao. The effect of thermal-induced noise on doubly-coupled-ring optical gyroscope sensor around exceptional point. *Optics Communications*, 474:126108, 2020.

[229] Jan Wiersig. Review of exceptional point-based sensors. *Photonics Research*, 8(9):1457–1467, 2020.

[230] Robert Duggan, Sander A Mann, and Andrea Alu. Limitations of sensing at an exceptional point. *ACS Photonics*, 9(5):1554–1566, 2022.

[231] Rodion Kononchuk, Jizhe Cai, Fred Ellis, Ramathasan Thevamaran, and Tsampikos Kottos. Exceptional-point-based accelerometers with enhanced signal-to-noise ratio. *Nature*, 607(7920):697–702, 2022.

[232] William Tuxbury, Rodion Kononchuk, and Tsampikos Kottos. Non-resonant exceptional points as enablers of noise-resilient sensors. *Communications Physics*, 5(1):210, 2022.

[233] Zhipeng Li, Chenhui Li, Ze Xiong, Guoqiang Xu, Yongtai Raymond Wang, Xi Tian, Xin Yang, Zhu Liu, Qihang Zeng, Rongzhou Lin, et al. Stochastic exceptional points for noise-assisted sensing. *Physical Review Letters*, 130(22):227201, 2023.

[234] Michael G. Wood, Justin R. Burr, and Ronald M. Reano. Degenerate band edge resonances in periodic silicon ridge waveguides. *Opt. Lett.*, 40(11):2493–2496, Jun 2015.

[235] Jan Schnabel, Holger Cartarius, Jörg Main, Günter Wunner, and Walter Dieter Heiss. $\mathcal{PT}$-symmetric waveguide system with evidence of a third-order exceptional point. *Phys. Rev. A*, 95:053868, May 2017.

[236] Changqing Wang, William R Sweeney, A Douglas Stone, and Lan Yang. Coherent perfect absorption at an exceptional point. *Science*, 373(6560):1261–1265, 2021.

[237] Jérôme Sol, Malte Röntgen, and Philipp del Hougne. Covert scattering control in metamaterials with non-locally encoded hidden symmetry. *Advanced Materials*, n/a(n/a):2303891, 2023.

[238] Mohammad P Hokmabadi, Alexander Schumer, Demetrios N Christodoulides, and Mercedeh Khajavikhan. Non-hermitian ring laser gyroscopes with enhanced sagnac sensitivity. *Nature*, 576(7785):70–74, 2019.

[239] Carl M. Bender and Philip D. Mannheim. PT symmetry and necessary and sufficient conditions for the reality of energy eigenvalues. *Physics Letters A*, 374(15):1616–1620, 2010.

[240] I. V. Barashenkov, L. Baker, and N. V. Alexeeva. $\mathcal{PT}$-symmetry breaking in a necklace of coupled optical waveguides. *Phys. Rev. A*, 87:033819, Mar 2013.

[241] W D Heiss. The physics of exceptional points. *Journal of Physics A: Mathematical and Theoretical*, 45(44):444016, Oct 2012.

[242] Nadav Gutman, Andrey A. Sukhorukov, Falk Eilenberger, and C. Martijn de Sterke. Bistability suppression and low threshold switching using frozen light at a degenerate band edge waveguide. *Opt. Express*, 20(24):27363–27368, Nov 2012.

[243] Nil Apaydin, Lanlin Zhang, Kubilay Sertel, and John L. Volakis. Experimental validation of frozen modes guided on printed coupled transmission lines. *IEEE Transactions on Microwave Theory and Techniques*, 60(6):1513–1519, Jun 2012.

[244] A. Figotin and I. Vitebskiy. Slow wave phenomena in photonic crystals. *Laser & Photonics Reviews*, 5(2):201–213, 2011.

[245] W. Tuxbury, L. J. Fernandez-Alcazar, I. Vitebskiy, and T. Kottos. Scaling theory of absorption in the frozen mode regime. *Opt. Lett.*, 46(13):3053–3056, Jul 2021.

[246] Tarek Mealy, Ahmed F. Abdelshafy, and Filippo Capolino. High-power X-band relativistic backward-wave oscillator with exceptional synchronous regime operating at an exceptional point. *Phys. Rev. Appl.*, 15:064021, Jun 2021.

[247] F.L. Walls and D.W. Allan. Measurements of frequency stability. *Proceedings of the IEEE*, 74(1):162–168, 1986.

[248] K. Hosoya, S. Tanaka, Y. Amamiya, T. Niwa, H. Shimawaki, and K. Honjo. A low phase-noise 38-GHz HBT MMIC oscillator utilizing a novel transmission line resonator. *2000 IEEE MTT-S International Microwave Symposium Digest (Cat. No.00CH37017)*, vol. 1:pp. 47–50, 2000.

[249] J.A. Copeland. Theoretical study of a gunn diode in a resonant circuit. *IEEE Transactions on Electron Devices*, 14(2):55–58, 1967.

[250] Kyu-Nam Lim. Cross-coupled transistor pair, August 26 2003. US Patent 6,611,009.

[251] Leon Chua and Guo-Qun Zhong. Negative resistance curve tracer. *IEEE transactions on circuits and systems*, 32(6):569–582, 1985.

[252] Siddharth Buddhiraju, Alex Song, Georgia T. Papadakis, and Shanhui Fan. Nonreciprocal metamaterial obeying time-reversal symmetry. *Phys. Rev. Lett.*, 124:257403, Jun 2020.

[253] Alireza Nikzamir and Filippo Capolino. Exceptional-point degeneracy as a desirable operation point for an oscillator array with discrete nonlinear gain and radiative elements. *Physical Review Applied*, 21(2):024037, 2024.

[254] A. Hessel, Ming Hui Chen, R.C.M. Li, and A.A. Oliner. Propagation in periodically loaded waveguides with higher symmetries. *Proceedings of the IEEE*, 61(2):183–195, 1973.

[255] Stephen A Maas. *Nonlinear microwave and RF circuits*. Artech house, 2003.

[256] E. Hammerstad and O. Jensen. Accurate models for microstrip computer-aided design. In *1980 IEEE MTT-S International Microwave symposium Digest*, pages 407–409, 1980.

[257] David M. Pozar. *Microwave Engineering*. WILEY, 4 edition, 2011.

[258] Mohamed Y. Nada, Tarek Mealy, Md Shafiqul Islam, Ilya Vitebskiy, Ricky Gibson, Robert Bedford, Ozdal Boyraz, and Filippo Capolino. Design of a Modified Coupled Resonators Optical Waveguide Supporting a Frozen Mode. *Journal of Lightwave Technology*, 41(17):1–15, 2023.

[259] A. Gómez-León and G. Platero. Floquet-bloch theory and topology in periodically driven lattices. *Phys. Rev. Lett.*, 110:200403, May 2013.

[260] Mohamed Y. Nada, Tarek Mealy, and Filippo Capolino. Frozen mode in three-way periodic microstrip coupled waveguide. *IEEE Microwave and Wireless Components Letters*, 31(3):229–232, 2021.

[261] Leslie Hogben. *Handbook of linear algebra*. CRC press, 2006.

[262] A. Hajimiri and T.H. Lee. A general theory of phase noise in electrical oscillators. *IEEE Journal of Solid-State Circuits*, 33(2):179–194, 1998.

[263] Mohammad Oveisi, Seyedali Hosseinisangchi, and Payam Heydari. A study of out-of-band emission in digital transmitters due to pll phase noise, circuit non-linearity, and bandwidth limitation. *IEEE Open Journal of Circuits and Systems*, 2023.

[264] Thomas H Lee and Ali Hajimiri. Oscillator phase noise: A tutorial. *IEEE journal of solid-state circuits*, 35(3):326–336, 2000.